THE DESIGN AND OPTIMISATION OF FABRIC REINFORCED POROUS PROSTHETIC GRAFTS USING FINITE ELEMENT METHODS AND GENETIC ALGORITHMS

MARK S YEOMAN

January 2004

Thesis submitted for the degree of Doctor of Philosophy

Department of Mechanical Engineering
University of Cape Town
Rondebosch
7700
South Africa

In memory of Penny Wilson

[20 October 1975 – 5 December 1996]

Elegance and Fortitude,
Emanating from an abundant Nature,
Which is touching to the Heart,
And a blessing to the Soul,
These words are not Enough.

We shall always remember you with Immortal Affection.

M. S. YEOMAN (1996)

Declaration

I, Mark Simpson Yeoman, declare that the work set out in this thesis is essentially my own work and that no part has been submitted for a degree at any academic institution.

Mark S. Yeoman

Acknowledgements

I thank the following people and organisations for their valued and committed help throughout this project:

Prof. Peter Zilla (aka GodZilla) and Dr. Deon Bezuidenhout (Bez) for the initiative to this work and their continued support and efforts. Even though at times I was stubborn, I hope you have learnt as much as I have from our interesting times working together. ("Even though I walk a difficult path, I shall proceed, indifferent to the world around me and unchanged from the uncarved block to which I owe my being!" M S Yeoman @ 00:36am on the 28 May 2002)

My supervisor, Prof. B.D. Reddy for his help, guidance, supervision and constructive criticism of the work.

Medtronic Inc. USA for the generous funding for the Project. In particular Mike Wolf for his assistance, guidance and ensuring the works commercial value.

Secant Medical (Pvt) Ltd., especially Skott Greenhalgh and Tom Moltz.

The Staff of the Radiology Departments of Groote Schoor and Vincent Pallotti Hospitals for their generous help and allowing me to use their ultrasound machines. Special thanks go to Dr. Kamilla Padi and Prof. Benningfield of Groote Schuur Hospital.

Hellmut Bowles for his encouragement, technical assistance and continued help.

Alex Seifalian and George Hamilton from the Royal Free Hospital, University College London for kindly letting me use there compliance test equipment at such short notice.

Richard Steventon at the Centre for Research in Computational and Applied Mechanics (CERECAM) for his initial help on the genetic algorithms.

The Cardiovascular Research Unit, which include; Lab Mom (Elria Collocott), Dotty (Dorothy Daws, don't hurt me for saying "Dotty"), Ohh Sister! (Mona Bracher), Noddy (Lars Schilling), Dude (Neil Davies), Zeee (Zelda Vergotine), Little T and Big T (Melanie Black and Jenny Molde), Nazzz (Nazlia Samodien), Dr. H (Dr. Paul Human), Boss (Anel Oosthuysen), Big-Boy (Lawerence Higham), Ryce (opps Reece Marillier), The Man (Bruno Orlandi), Ditscunt (Dr. Matthius Fittkau), Giggles (Ronnett Seldon), Kung Fu King (Richard Han), Ronaldo (Raymond Michaels) Ferdie Barends, Boggy babe (Letchemie Hesqua) and obviously Big Ma Ma (Patricia) and those who have left, but will always be a part of the "Church" no matter how hard they try not to be (Ross Millam, Cristoph, Woong, Arthur Marsden, Jaco, Phil). Finally to Ragga-man (Dmitri Lennert), for his ever eager presence and damn funny/cool/mind-bending statements.

Mr. Plankermann of Finitex (Pvt.) Ltd., Cape Town, for the fabric samples used in the uniaxial tensile tests.

Special thanks go to the following individuals:

Lara Atkinson (Gutter Girl) for kicking my butt and making me finish this!

Caryn Maxwell (aka. Evil Landlord, Snuggles, Pooky Bear, Puff Daddy, Snookums, Snuggle

Muffin) for making her home, my home, for several months of absolute fun, laughter and; "I'm like a bird, dum dee dum dee dee dum, I'll only fly away!".

Rainer Lehr and James Lockley for the countless hours spent at Divas and Cool Runnings looking at the future, smoking bongs, and basically playing pool until the early hours of the morn.

My family including; my two brothers, Gary and Denis, for their continued support throughout this work. My parents, "the Fossils" yeah, yeah, I tried! My grandfather, Ian R. Yeoman, the greatest man ever!

Kris Zacny and Eric Yan (Kia Hu Ki) for the humour.

Peter Lenton and Rob Wakeford for the days of our lives.

The Wilsons (John, Lorraine and Mark), thanks for all the great biscuits.

Chanti and Caroline McGahey and my second mom, Lorraine Leonard.

Lucy Barnes for deserving so much more and being a true companion.

TK and RB (Thorsten Koch and Ryan Benjamin) for the brilliant statements about life, fish and marbles and their help in designing the Instron tensile test jaws for the porous structures and fabrics.

The Sousters, for trying to show me God, but failed dismally.

Nicola Sloan (High Maintenance Women), for making me a minger!

The people of Villa Kuntabunt and SCUMFF (Ulla Worthmann, Shamim Tehradzadeh, Crystal "Tiddle" Englebrecht, Fiona Donald and Frank Spencer) you guys gave me the greatest roller coaster ride ever, I'll always remember '95 as the year of colour and love!

Omid Kassiri, Nava Bastani and Joa Tehradzadeh (Johumsborte) you guys carry on, I need some red wine.

Stefan Rotter and Neil Courtney-Clark, you guys rock, carry on regardless and may the "Marquard Crawl" live on forever, and Stef the cartoon is just for you!

Finally, to Mac (Andrew McBride) for adding his comments and help with LaTex..

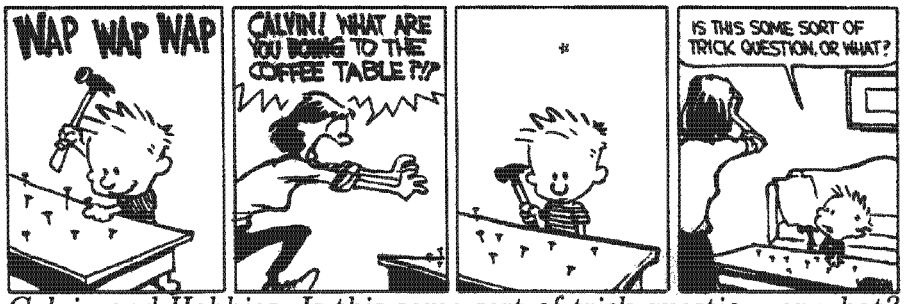

Calvin and Hobbies: Is this some sort of trick question, or what?

Synopsis

Small to medium diameter vascular grafts have met with little success over the past 50 years, in-spite of increased research and available technology. This low success has been attributed to two main areas, namely; surface thrombogenecity and anastomotic intimal hyperplasia (exuberant muscle and tissue growth at the interface between host artery and graft).

The main factors believed to influence these areas are compliance mismatching between graft and host vessel, and the graft's inability to promote endothelialisation. Consequently, tissue engineers are looking toward closely matched compliant grafts which promote tissue ingrowth through the prosthetic wall. Among these are compliant polyurethane (PU) grafts containing well defined, interconnected pores which allow for cellular regeneration. Problems encountered by such grafts under physiological conditions include high viscoelastic effects, ballooning, and low burst strength. Thus, a support structure is required which does not adversely affect the interconnecting pores.

Many reinforcing techniques have been investigated, most of which involve externally wound or ring-type structures. Problems encountered by such methods include low compliance, high stress, and wall compression. Thus, an external (adventitial) fabric support is proposed which is highly porous, evenly distributes load along the graft wall, and displays nonlinear stiffening.

The work presented here is a collaborative venture between the Cardiovascular Research Unit (CVRU) at the University of Cape Town (UCT) and Medtronic USA Inc., to design and develop a porous PU graft which has an adventitial fabric support. Finite element methods and genetic algorithms are used to facilitate the design process through the use of computational simulation and optimisation.

A commercially available finite element software package is used to numerically model the porous PU graft and adventitial fabric reinforcing. A hyperfoam strain energy material model is used to represent the nonlinear isotropic elastic behaviour of the porous grafts, using relevant experimental data, while a modified soft tissue material model is used to describe the general mechanical characteristics of the fabric reinforcing. The fabric model coefficients are optimised, using a genetic algorithm (GA1), to obtain a 6 %/100 mmHg diameter compliance (C_d), a 4.0 mm diastolic diameter and nonlinear stiffening in a graft computational model. The fabric model solutions obtained from GA1 are then used in circumferential and longitudinal tensile finite element simulations to acquire mutually orthogonal (warp and weft) stress-strain characteristics for the required reinforcing fabrics.

Validation of the fabric material model has been carried out using four distinct knit structures with desirable characteristics such as high porosity and nonlinear stiffening. These knit structures were physically tested in the warp and weft directions to obtain uniaxial tensile test data. A

second genetic algorithm (GA2) in conjunction with an equivalent uniaxial tensile finite element model was used to optimise the fabric material model to the obtained test data. It was found that some of the solutions obtained from GA2 were weak. The weak solutions were not due to a deficiency of the genetic algorithm, but rather the inability of the exponential fabric material model to adequately describe the extreme differences between the warp and weft directions and linear stress-strain relations.

It was not possible to develop and manufacture fabric structures with the desired warp and weft stress-strain characteristics obtained from GA1 due to cost and time constraints, thus direct correlations could not be made. Instead, two of the fabric reinforcing structures developed were used. A third genetic algorithm (GA3) was utilised to gain the fabric model coefficients which best described these reinforcing fabrics in the circumferential and longitudinal directions.

One of the fabrics was then physically tested on the porous grafts and compliance data obtained. The fabric model solutions obtained from GA3 were used in the graft computational model to obtain comparative numerical data. Close correlations between static pressure-diameter numerical solutions and experimental results were observed. Correlations between numerical and physical compliance were poor, where the numerical models predicted higher compliance values. This was attributed to:

- the use of bead cast rods rather than graft samples to obtain the hyperfoam material models used to describe the porous structures
- the inconsistent graft test samples used
- the high mechanical contribution of the luminal latex liner used to prevent pressure loss through the porous grafts
- the error in analytically subtracting the latex liner from the static compliance curves obtained
- the error in assuming no compression through the porous graft wall to obtain internal diameter measurements from external diameter data,
- and the failure of the obtained fabric models from GA3 to accurately describe the behaviour of the fabric reinforcing samples.

In conclusion, a fabric material model is utilised and tested and has been shown to describe the general mechanics of coarse knitted fabrics. Optimised circumferential and longitudinal tensile stress-strain requirements for adventitial fabric reinforcing structures were found by finite element and genetic algorithm techniques for grafts of various pore sizes. The genetic algorithm utilised found fabric model solutions quickly for the required compliance C_d, diastolic diameter ϕ^{dia}, and nonlinear stiffening. Correlations were drawn from graft model solutions and physical tests; however, these were not from the optimal solutions obtained from GA1 but rather from available reinforcing fabrics.

Table of Contents

List of Figures

List of Tables

Glossary of Terms

Tensors		Description
B	-	Left Cauchy-Green deformation tensor
C	-	Right Cauchy-Green deformation tensor
D	-	Rate of deformation tensor
E	-	Green (Lagrangian) strain tensor
F	-	Deformation gradient tensor
I	-	Identity tensor
J	-	Jacobian tensor
K	-	Tangent moduli tensor
L	-	Velocity gradient tensor
N	-	Nominal stress tensor
P	-	First Piola-Kirchhoff stress tensor
R	-	Rigid body rotation tensor
S	-	Second Piola-Kirchhoff stress tensor
T	-	Traction tensor
U	-	Right stretch tensor
V	-	Left stretch tensor
W	-	Spin tensor
∇U	-	Displacement gradient tensor
Ω	-	Angular velocity tensor
σ	-	Cauchy stress tensor
τ	-	Kirchhoff stress tensor
ε	-	Strain tensor, logarithmic strain tensor
ϵ	-	Biot strain (nominal strain) tensor
e	-	Eulerian strain tensor
$\Psi^{(i)}$	-	Elasticity tensors ($i = 1, 2, 3$ or 4)
χ	-	Transformation tensor

Matrices		Description
M	-	Mass matrix
N	-	Interpolation matrix
d	-	Displacement matrix
f	-	Force matrix
r	-	Residual matrix

Vectors		Description
b	-	Force per unit mass vector
n	-	Unit normal vector
p	-	Linear momentum vector
t	-	Traction (force vector per unit area) vector
u	-	Displacement vector
v	-	Velocity vector
x, X	-	Position vectors (spatial and material)

Scalars		Description
I_1, I_2, I_3	-	Tensor invariants
J	-	Jacobian (det F)
L	-	Length
P	-	Pressure
T	-	Temperature
V	-	Volume
d	-	Displacement
m	-	Mass
$\mathbf{q}$	-	Heat flux per unit area
s	-	Heat source per unit mass
t	-	Time
ρ	-	Density

Symbols		Description
$f(x)$	-	Function, fitness function
$\phi(x)$	-	Objective function
$p(x)$	-	Penalty function
C	-	Compliance, material model coefficient
E_P	-	Pressure strain elastic modulus
G	-	Shear modulus
H	-	Schema
J_{el}	-	Elastic volume strain
K	-	Bulk modulus
S	-	Surface
T_M	-	Melt temperature
T_G	-	Glass transition temperature
U	-	Strain energy
a_i	-	Material model coefficients
l	-	Length of bit strings
p	-	Probability
Ω	-	Domain of continuous body
Γ	-	Boundary/plane in domain Ω
δP	-	Virtual power
α	-	Fibre twist angle
β, μ	-	Temperature dependent material parameters
γ	-	Shear stress
δ	-	Kronecker-delta
λ	-	Principal stretch or stretch ratios, eigenvalues
$\jmath$	-	Non-linear stiffening characteristic
ϕ	-	Diameter
υ	-	Poisson's ratio
w	-	Weighting
ω	-	Frequency
ψ, w	-	Stored (strain) energy function
Δt	-	Time step

Operators		Description
$\det A$	-	Determinant of tensor A
$\text{div}\, A$, $\text{div}\, a$	-	Divergence of tensor A, divergence of vector a
$\text{tr}(A)$	-	Trace of tensor A
$\|a\|$	-	Modulus of a
∇A, ∇a	-	Gradient of a tensor A, gradient of a vector a

Superscripts		Description
-1	-	Inverse
G	-	Green-Naghdi rate
J	-	Jaumann rate
T	-	Transpose, Truesdell rate
$\bigtriangledown$	-	Objective rate
g	-	Global
n	-	Increment n, n^{th} order differentiable
$o(f)$	-	Order of f
dev	-	Deviatoric
dyn	-	Dynamic
end	-	End state
hyd	-	Hydrostatic
int	-	Initial state
kin	-	Kinetic
$normalised$	-	Normalised
$stat$	-	Static
vol	-	Volumetric

Subscripts		Description
$1, 2, 3, i, j, k, l$	-	Tensor indices
I	-	Node number
φ	-	Iteration number
max	-	Maximum
min	-	Minimum
c	-	Crossover
m	-	Mutation
0	-	Zero pressure/initial/reference
v	-	Volume compliance
d	-	Diameter compliance
p	-	Pressure
ID	-	Internal diameter
OD	-	External diameter
H	-	Hoop
R	-	Radial
dia	-	Diastolic
sys	-	Systolic

Superposed		Description
$\bar{}$	-	Boundary values, average
$\hat{}$	-	Corotational components, observed average
$\dot{}$	-	Derivative
$\ddot{}$	-	Second derivative

List of Abbreviations

Abbreviation		Description
AAMI	-	American association of medical implants
bpm	-	Beats per minute
CABG	-	Coronary artery bypass graft
CCV	-	Closed circuit video
CERECAM	-	Centre for Research in Computational and Applied Mechanics
CO_2	-	Carbon dioxide
CPU	-	Central processing unit
CVRU	-	Cardiovascular research unit
d.o.f	-	Degree/s of freedom
EC	-	Endothelial cell
EEL	-	External elastic lamina
ETO	-	Ethylene oxide
e-PTFE	-	Expanded polytetraflouroethelene
FBGC	-	Foreign body giant cell
FE, FEM, FEA	-	Finite element/method/model/s/analysis
GA	-	Genetic algorithm
H&E	-	Hematoxylin and eosin
ID	-	Internal diameter
IEL	-	Inner elastic lamina
ISO	-	International standards organisation
LDT	-	Linear displacement transducer
MRI	-	Magnetic imaging resonance
NMP	-	*N*-methyl pyrollidone
OD	-	Outside (external) diameter
O_2	-	Oxygen
PAL	-	Phase alternating line
PBS	-	Phosphate buffered saline
PC	-	Personal computer
PDE	-	Partial differential equation
PEG	-	Polyethylene glycol (hydrogel)
PET	-	Polyethylene terephthalate (Dacron®)
PPS	-	polyphenylene sulfide
PTFE	-	Polytetraflouroethelene (Teflon®)
PU	-	Polyurethane
RF	-	Radio-frequency
rms	-	Root mean square
SMC	-	Smooth muscle cell
SEM	-	Scanning electron microscope
TE	-	Tissue engineered
UCT	-	University of Cape Town
UMAT	-	User material subroutine

List of Medical Definitions

Term		Description
Adventitia	-	Outer membranous layer of a blood vessel
Anastomosis	-	The surgically connected ends of a blood vessel to form a continuos channel
Aneurysm	-	A fluid-filled sac in the wall of an artery that can weaken the wall and lead to excess localised vessel enlargement
Arteriosclerosis	-	Arterial disease where raised areas of cholesterol deposits (plaques) form on the lumen of the artery
Autologous	-	Derived from the same persons body
Bifurcation	-	A split or branch into two parts
Bypass	-	A surgical procedure to redirect blood around an occlusion via a grafted vessel
Carotid artery	-	Large artery which supplies blood to the head via the left and right side of the neck
Compliance	-	The percentage diameter or volume change of a blood vessel per unit increase in internal pressure
Clot	-	The binding of blood cells to form a solid mass through platelet action
Distal	-	Anatomically; a point which is located further from a point of reference
Desiccation	-	Degradation of tissue, due to the lack of nutrients and oxygen
Endothelium	-	Inner layer of cells that line blood vessel lumen
Endothelial cells	-	Cell type which forms Endothelium
Femoral Artery	-	Artery located in thigh
Graft	-	Blood vessel replacement which can be made of synthetic material or living tissue
Heterogenous	-	Containing dissimilar elements or parts, not homogenous
Heterograft (Xenograft)	-	A living tissue graft which is obtained from another species
Homograft	-	Graft or tissue from one organism to another of the same species
Homologous	-	Corresponding in structure, position and origin
Hyperplasia	-	Abnormal growth in part of body, caused by excessive cellular growth
Heparin	-	Polysaccharide present in living tissue which functions naturally as an anticoagulant and used medically to treat thrombosis
Intima	-	The innermost membrane of an organ or a part
Intima hyperplasia	-	The proliferation of smooth muscles and endothelial cells to the inside of a blood vessel
In vitro	-	Experiment done in an artificial environment
In vivo	-	Experiment done in a living creature
Ischemia	-	Inadequate supply of blood to a vessel caused by vessel blockage
Lumen	-	Inner surface of a blood vessel, which is in contact with blood
Ligation	-	Tying of vessel with surgical ligature
Media	-	Mid-section of blood vessel wall
Occlusion, occluded	-	Blockage or blocked

Term		Description
Patency, patent	-	Measure of a graft's ability to function effectively
Pathological	-	Relating to or arising from disease
Pathology	-	Study of origin, nature and cause of disease
Proximal	-	Anatomically, a point which is located nearer to a point of reference
Saphenous vein	-	Vein that runs from foot to thigh near surface of skin
Smooth muscle cells	-	Involuntary functioning muscle cell type which is found in blood vessels
Suture	-	Thread used for securing, tying and sowing of body organs, vessels
Transanastomotic	-	An event occurring across the anastomosis
Transmural	-	An event occurring through the wall of the prosthesis
Thrombogenetic	-	Description of materials, bodies ability to form thrombosis
Thromboresistant	-	Material or body which prevents or reduces thrombosis
Thrombosis	-	Formation or presence of blood clots which may partially or completely block a blood vessel
Xenograft	-	Crosslink treated or fixed heterograft

Chapter 1

Introduction

Arteries are complex blood vessels which not only carry blood to the various organs of the body but also help maintain blood pressure and flow. With the increasing number of people suffering from arterial problems, it is no wonder that vascular disease in medium to small diameter arteries is of great concern.

The impediment of blood flow through arteries is either caused by occlusion due to a thrombosis (fibrous/cholesterol build up) or from aneurysm (acute dilation) of the vessel. Such impediments in a vessel normally require reconstructive or bypass surgery. Reconstructive surgery is either in the form of a synthetic or autologous (arteries and veins taken from the host or animal) grafts. Of the synthetic replacements it has been found that large diameter artery replacements are successful where blood flow is high and resistance is relatively low [1], however in the small to medium diameter range success has been low. Approximately 1.4 million surgical procedures requiring arterial prostheses are preformed annually in the United States of America (USA) where, most of these procedures concern small to medium diameter arterial replacement for which synthetic graft materials are not generally suitable [2]. For this reason much research is being conducted in the development of a reliable small to medium diameter synthetic graft.

Vascular surgery has developed rapidly over the last century from the first work published by Carrel and Gutherie on the topic in 1902 [3]. Goyeses performed the first vascular graft surgery in 1906 by using popliteal vein to replace a section of diseased artery, after which the reversed saphenous vein became popular as an autologous graft replacement and was successfully shown to replace femoral arteries by Kunlin in 1949 [3]. While Gross *et al.* worked on hetero- and homografts (human or animal blood vessels), Voorhees in 1952 discovered that cells grew on silk threads exposed to blood [3]. This encouraged the development of synthetic textile tubes as arterial replacements.

Current materials used in vascular implants are natural blood vessels, textile tubes made from Dacron® or e-PTFE. These grafts have a high success rate in large diameter artery replacement [1]. However, with small to medium diameter grafts a significant proportion eventually fail by occlusion due to thrombosis or intimal hyperplasia.

Although autologous grafts are still considered the best vascular prosthetics for small to medium diameter arteries [4], they tend to be diseased or unsuitable for use. Up to 30 % of autologous veins are unsuitable in patients due to poor quality, or insufficient length [5]. In addition 20 % fail within the first year. Currently commercially available synthetic grafts (Dacron® and e-PTFE) are also unsuccessful over long periods where 40 % thrombose within six months [3].

New porous polyurethane grafts are being developed and have shown to be initially compliant [6–9], however the long term success of these grafts still remains to be seen.

The patency (long term indicator of a graft's performance) of small to medium diameter grafts has been shown to be unsuccessful over long periods, and although the mechanics behind these failures is not well understood, it is clear that compliance mismatching and the thrombogenetic nature play a large role in determining the success of a graft [10].

Work done by Burkel [3] and How *et al.* [11] showed that the thrombogenetic nature of the graft material, surface roughness, the mechanical and hemodynamic properties of the replacement graft compared to the host artery greatly influenced success. Although the failure of grafts is not fully understood, it is generally agreed that compliance mismatch between artery and graft plays a major role in failure [1, 7, 11–17]. To date current small diameter vascular prostheses, which are not autologous, are greatly mismatched and require extensive medical treatment after implantation. This physical discontinuity between the artery and graft alters the blood flow, contributing to thrombosis and eventual failure [3,4,14,18]. Furthermore, compliance mismatch between the host artery and the graft causes unnatural stresses to occur on the anastomotic sites (proximal and distal points of graft attachment), thus enhancing the development of anastomotic intimal hyperplasia. Therefore much emphasis has been placed on the mechanics of natural arteries in the hope of finding a patent graft which would mimic the properties of the host vessel [13,19].

It was shown by Burkel [3] that the ingrowth of endothelial cells on the inner surface of a vascular prosthesis greatly increased patency by reducing the thrombogenetic reaction of blood with the graft. Much of the current research in polymer grafts utilise biological coatings to reduce this thrombogenetic reaction of the grafts' luminal wall. One such method of inducing endothelium growth on the luminal surface is to allow for cellular ingrowth through the graft wall, leading to musculogenesis (re-growth of muscular cells), angiogenesis (arterioles development) and the eventual endothelialisation [1,6,11,20]. One method of encouraging this is by utilising a porous graft structure, which has defined channels and micro-pores to the luminal surface [6–10].

The control mechanism of the arterial tree is maintained primarily by the endothelium layer where endothelial cells monitor shear and flow forces on the luminal surface. When these forces change endothelial cells respond accordingly by releasing growth factors within the arterial wall, controlling cellular growth and structure and thus blood vessel mechanical responses. Therefore, when a vessel becomes diseased or blocked, or a replacement graft is implanted, blood flow patterns are affected causing an eventual change in arterial wall structure and mechanical response. This control mechanism, although there to control blood flow patterns and pressure within the arterial tree under normal conditions, becomes the mechanism which reduces the success of grafts. Thus, a graft with the same mechanical behaviour as the host vessel would ensure that blood flow patterns are not affected.

Thus, the development of a long-term patent graft would have to allow for cellular ingrowth

as well as display the right mechanical characteristic to ensure success. With this comes the need to find fast, efficient and effective replacements for these vessels, which are readily available and do not require great resources, expense or time. Ideally a synthetic vascular replacement would not require preservation, would be readily available at any length, and have a high patency where the host does not require extensive medication after implantation.

Much work has been done developing porous polymeric graft superstructures in the Cardiovascular Research Unit (CVRU) at the University of Cape Town (UCT) which has a defined microstructure [9]. These structures however have been found to be too weak and display large viscoelastic properties. Past research within the CVRU has considered ways of reinforcing these structures. Work by MacKellar [21] and Hughes [22] investigated the effects of wound external reinforcing. It was found that even though much of the wound reinforcing helped strengthen the graft, it did cause compression through the graft wall and high stress concentrations in the region of the reinforcing. It was also shown that in most cases the wound reinforcing stiffened the structure, excessively reducing compliance.

Thus, a better method of reinforcing is required, one which will not cause localised stress concentrations and hence excessive localised compression of the porous structure while still allowing for tissue regeneration through to the porous structure.

It is proposed that a fabric structure be used to externally reinforce the porous graft. The fabric construction and structure should be fine enough to ensure that stress concentrations are not observed, while course enough to ensure that tissue ingrowth is allowed.

1.1 Aim of work

The aim of this work is to develop a method of finding the requirements of a fabric reinforced porous prosthetic graft to give a specific dynamic diameter compliance (C_d), using finite element methods (FEM) and optimisation techniques. Existing porous graft structures from the CVRU are to be used, and the method should be general enough to be utilised for other porous material properties and graft structures.

1.2 Specific objectives

The specific objectives of the work are to:

- develop a fabric constitutive relation and implement it in a general purpose finite element package
- develop an optimisation routine which can interact with the finite element package and optimise the fabric model coefficients for specific criteria
- use the developed fabric constitutive relation and optimisation routine in a graft finite element model and optimise the fabric model coefficients to produce an externally reinforced fabric graft which has a 6 %/100 mmHg dynamic diameter compliance and displays non-linear stiffening characteristics

- utilise the optimised fabric coefficients to find the warp and weft (mutually orthogonal directions) mechanical requirements of the fabric reinforcing, by making use of computational simulations of longitudinal and circumferential tests
- correlate the results obtained from the finite element models against experimental data
- develop the fabric reinforced graft using numerical, computational and optimisation tools.

1.3 Overview of dissertation

The work starts out in Chapter 2 by describing the structure and mechanics of natural arteries and the requirements of a successful prosthetic graft. Chapter 3 reviews the mechanical characteristics of polymers and fabrics. In Chapters 4 and 5 the relevant aspects of continuum mechanics and the finite element method are examined. Chapter 6 is devoted to optimisation techniques with specific reference to genetic algorithms (GA). Chapter 7 considers the various methods of measuring the compliance of natural blood vessels and synthetic grafts. This chapter also describes the method used to measure compliance in the work and makes a comparative study between various groups and techniques. Chapter 8 sets out the constitutive material models, the approximations and simplifications used in the finite element simulations. Uniaxial tensile finite element simulations are also considered for the validation of the fabric constitutive model.

Chapter 9 describes the particular genetic algorithms used in optimising the fabric model coefficients: GA1 for compliance and non-linear stiffening of the graft simulations and GA2 for uniaxial tensile test data. This is followed by Chapter 10 which examines the validation of the fabric, porous and latex continuum material models used in the finite element procedures. Chapter 11 describes the optimised solutions obtained from GA1 and the graft finite element simulations. The fabric model solutions from GA1 are then utilised in circumferential and longitudinal tensile finite element simulations where the transverse mechanical requirements are obtained for the reinforcing fabrics. Chapter 12 investigates the iterative development and manufacture of the adventitial fabric reinforcing tubes by a medical fabrics specialist. A further genetic algorithm (GA3) is utilised to find the fabric model coefficients to these developed reinforcings. Chapter 13 studies the physical compliance tests and results obtained for the non-reinforced and reinforced grafts. These compliance results are compared to finite element model solutions using the fabric coefficients obtained from GA3. Finally Chapters 14 and 15 conclude the work by discussing the results of the previous chapters, drawing conclusions based on observations and making recommendations.

Chapter 2

The Structure and Mechanics of Arteries and the Requirements of a Prosthetic Graft

2.1 Introduction

The structure and mechanics of natural blood vessels are complex and vary according to the position of the vessel within the body. Much work has been done [12, 23–36] to quantify the mechanical characteristics of these vessels within the body.

This chapter reviews the constituent tissue and the various wall structures found in blood vessels. It details the structure of large and small to medium diameter arterial walls and their variation, depending upon the location within the body. The chapter also discusses the requirements of a good prosthetic graft and its relationships to these structures.

2.2 Biomechanics of the circulatory system

The human circulatory system consists of three major vessel types namely; arteries, veins and capillaries. The arteries, in addition to supplying blood to the various organs from the heart, are also responsible for controlling a steady blood flow and pressure distribution throughout the body. Capillaries are responsible for distributing and allowing for the transmission of the nutrient-rich, oxygenated blood to the various organs and cells. The veins are responsible for returning the deoxygenated blood from the capillaries back to the lungs and heart. Figure 2.1 shows the major arteries and veins of the human circulatory system.

2.3 Diastolic and systolic pressures across the body

Due to the pump action of the heart, a pressure pulse is set up within the vessels of the body. The peak value is called the systolic pressure and the lower bound, the diastolic pressure. Figure 2.2 shows the typical pressure and flow waves experienced in the arterial tree for an average adult human.

The shape of the pressure wave and the systolic and diastolic pressure values greatly depend on the position of the vessel in the body. For an adult the systolic and the diastolic pressures of the ascending aorta can range from 100-150 mmHg to 60-100 mmHg respectively [37].

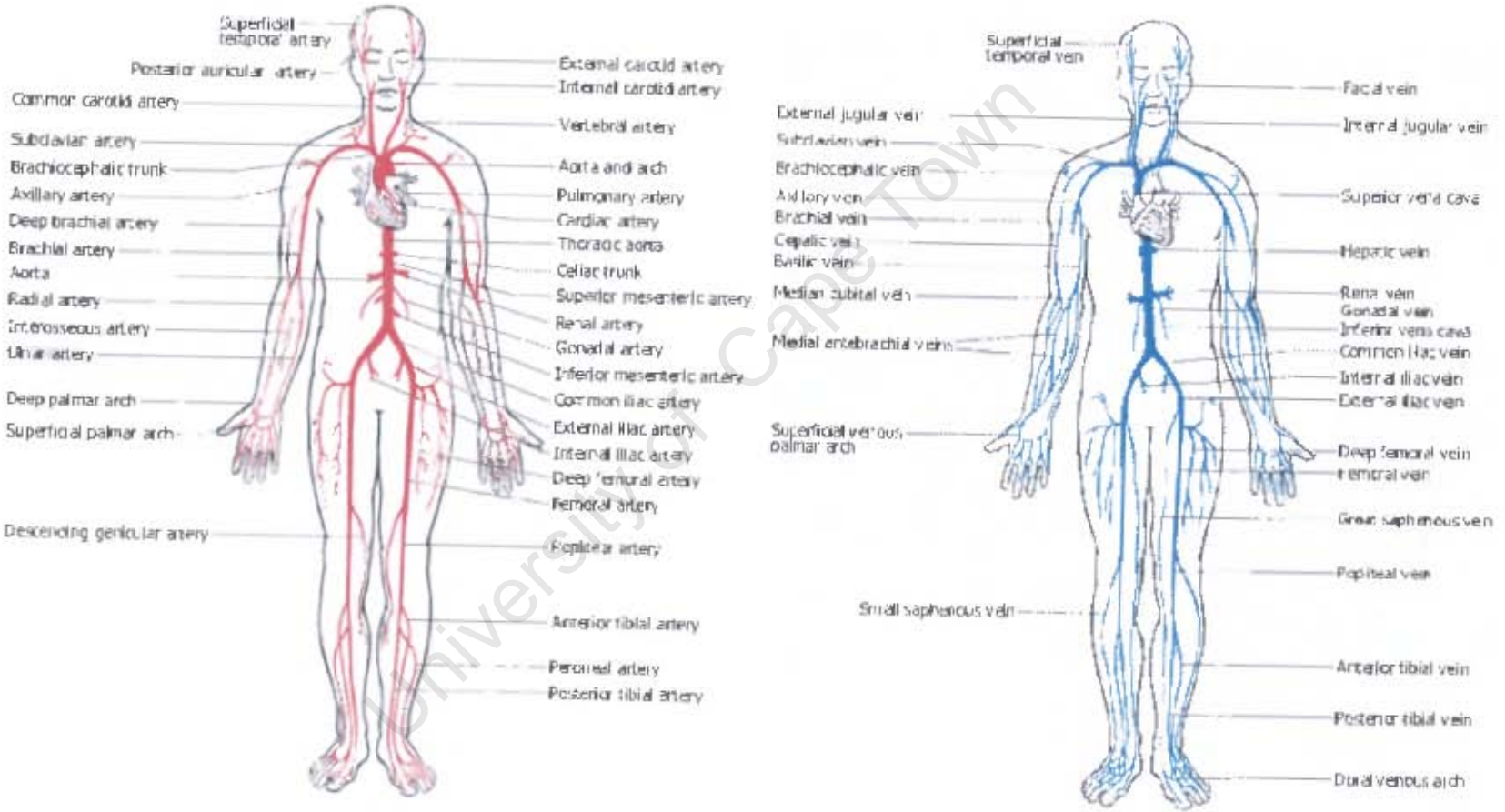

Figure 2.1: Arteries and veins of the human circulatory system

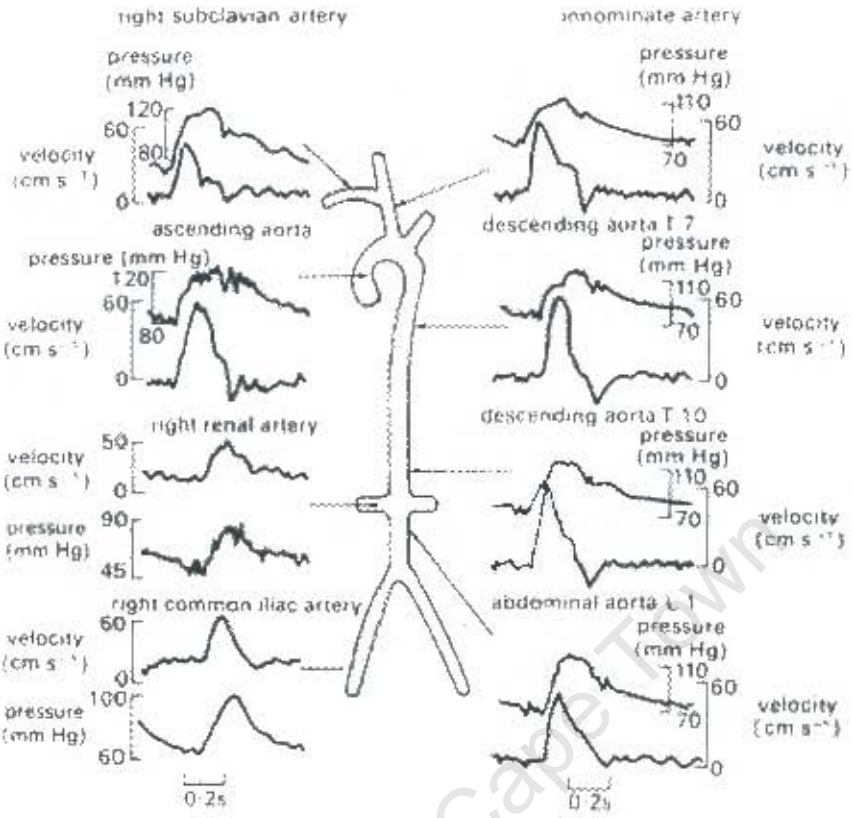

Figure 2.2: Pressure and flow waveforms in the human arterial tree [38]

Figure 2.3 shows the variation of mean blood pressure in both arteries and veins through the body. The bar on the right of the human figure shows the variation of mean blood pressure up the human body in the veins (left scale) and the arteries (right scale) .The higher up the body, the lower the mean blood pressure.

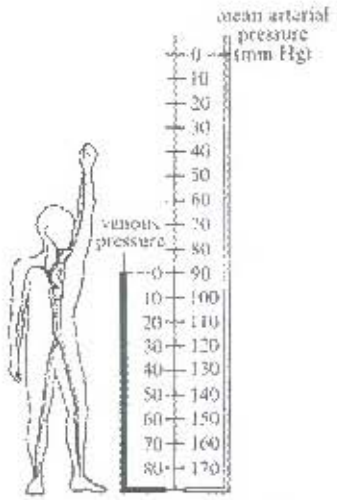

Figure 2.3: Mean blood pressure distribution across the human body [39]

2.4 Histology of blood vessels

The histology of blood vessels is an important aspect to consider before studying synthetic replacements, which are intended to match the properties of the native blood vessel.

2.4.1 Tissue types found in blood vessels

Blood vessels consist of six major cell/tissue types. The cellular components include endothelial cells (EC), smooth muscle cells (SMC), and fibroblasts. The extracellular components include collagen, elastin, and ground substance. Each plays a specific role in the blood vessel and all but the EC contribute to the mechanical properties of the artery.

Collagen (Stiffening) typically forms long fibres, bound together in bundles which have a serpigious (wavy) form. Collagen has a high elastic modulus about 1 GPa and a low extensibility, where a maximum strain of 2-4 % can be observed. Due to the serpigious (wavy) form, length change can be seen without strain due to the initial alignment.

Elastin (Rubber-like) is a typical protein which has a low elastic modulus in the region of 0.300-0.6 MPa and a high extensibility where strains of up to 130 % are commonly observed. Elastin has similar properties to that of rubber.

Smooth muscle cells, SMC *(Pre-tensioning and responsive)* are the major cellular component of a vessel wall and are spindle shaped with typical lengths of 20-50 μm and diameters of 5-10 μm. This cell type helps pre-stress the blood vessel wall. Some smooth muscles respond to the pressure wave by contracting periodically.

Ground substance (Nodules) are mainly mucopolysaccharides and are cement-like nodules which hold components in some regular configuration. This is similar to the action of carbon in steel.

Endothelial cells, EC *(Regulating)* are highly sophisticated cells, which have no apparent effect on the mechanical properties of the blood vessels apart from regulating the shear stress on the lumen wall. The release of growth and response factors by the EC achieves this regulation, controlling SMC contraction and wall tissue growth and structure.

2.4.2 Typical structures of various blood vessels

A typical blood vessel wall is composed of three major concentric layers (tunics): namely; tunica adventitia (the outermost layer or tunica external), tunica media (internal to the adventitia) and the tunica intima (found nearest the lumen). Separating these layers in some blood vessels are elastic laminae. Figure 2.4 shows diagrammatically these layers and their location within a blood vessel wall.

The *tunica intima (Endothelial Layer)* is the layer of endothelium cells covering the lumen as well as a basement membrane of sub-endothelial connective tissue with fibroblasts and connective tissue fibres, some of which run longitudinally. The *inner elastic lamina (*IEL*)* is a layer composed of an accumulation of elastic fibres. This is the outermost component of the tunica

intima and is found in arterioles greater than 62 μm in size.

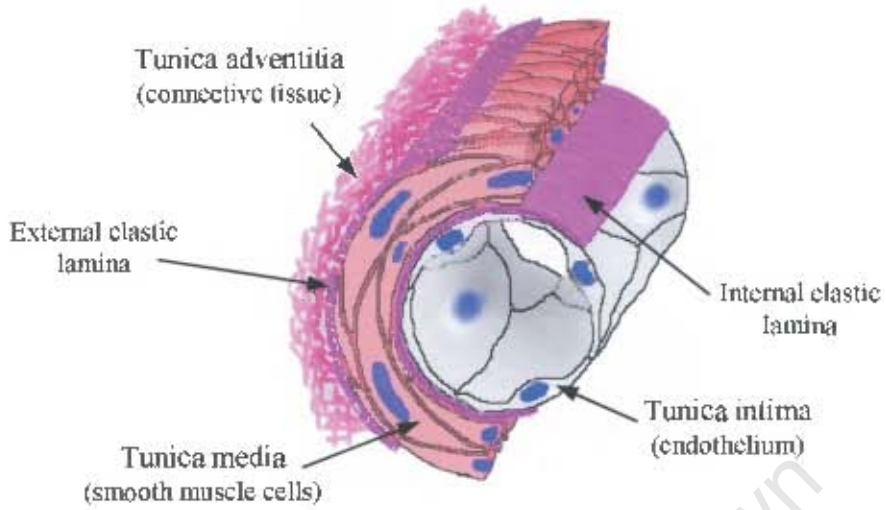

Figure 2.4: General structure of blood vessels

The *tunica media* is composed primarily of circumferentially arranged SMC and connective tissue fibres, where fibroblasts are sometimes present. These fibres are formed by specialised SMC. The *external elastic lamina (*EEL*)* is a concentration of elastic fibres forming the outermost component of the tunica media. While the *tunica adventitia* is the outermost layer composed primarily of longitudinally-arranged, moderately dense, connective tissue, consisting of collagen bundles loosely connected by elastin.

2.4.3 Variation of vessel wall structure along the human circulatory system

The wall structure of blood vessels of different sizes (arterioles vs. arteries) and different types (arteries vs. veins) vary. These variations are the result of quantitative variations of the general structure described earlier with the exception of the capillaries. These differences and the percentage make-up of each layer within the vessel wall depend on the location and size of the vessel within the body. Figure 2.5 below shows a simple schematic of the human blood vessel system with the variation of wall structure along the circulatory system.

Arteries. Arteries can be classified in three groups: large elastic arteries, small to medium-sized muscular arteries, and arterioles. The transition between these groups is not sharp, so intermediate types exist which possess the characteristics of two of the major types. In all arteries the media has the most well-developed wall structure. An IEL is nearly always present and an EEL is present in the larger vessels. Although some small arteries may resemble larger arteries in composition and vice versa, the following is a summary of the characteristic arrangement of the various artery sizes. *Large elastic arteries (ϕ = 10-25 mm, example: Aorta).* The EC of the intima may be polygonal. The sub-endothelial connective tissue is relatively thick with many fibres, and the IEL is not as distinct as in muscular arteries. The media contains SMC and

has much elastic fibre forming many thin tubular elastic membranes (elastic lamina). The high elastic content allows expansion to accommodate excess blood during ventricular contraction and diminishes pulsatile delivery to the peripheral vessels. The EEL is indistinct due to the high content of elastin in the media. The adventitia is thinner than the media, composed of loosely arranged collagen bundles which spiral around the vessel. Over-distention of the intima and media is prevented by the adventitia.

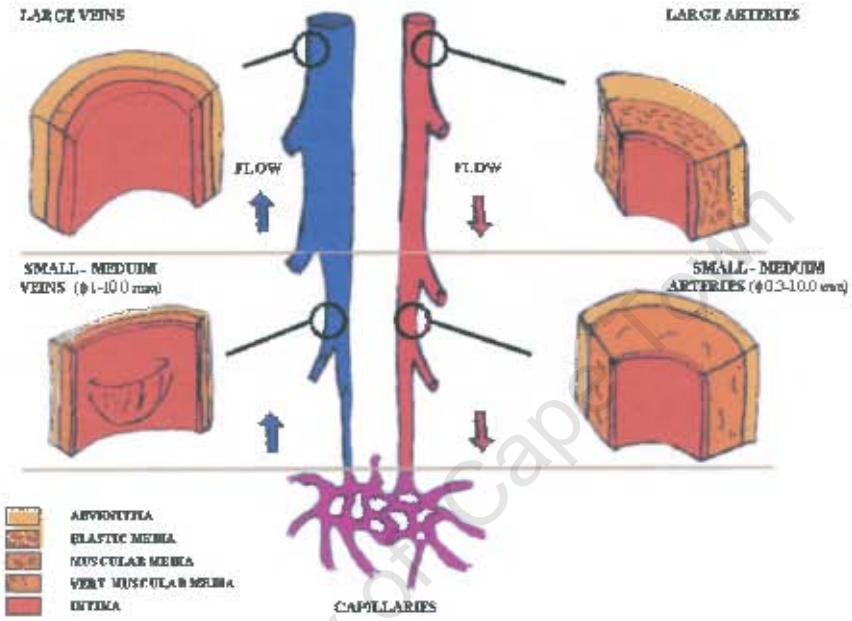

Figure 2.5: Variation of vessel wall properties along circulatory system [40]

Medium-sized muscular arteries (ϕ=0.5-10 mm, example: Femoral). The intima of these vessels has small amounts of sub-endothelial connective tissue present and the IEL is well developed and a prominent feature. The media is very thick and up to 40 layers of SMC can be seen. Collagen may also be present. Smaller arteries in this group have a relatively low elastic fibre content while the larger arteries have increasing quantities of elastin. Autonomic nervous control of the SMC in the media helps regulate the distribution of blood flow to the various tissues and organs. The EEL of these vessels is well developed. The adventitia of these vessels is usually thinner than the media and comprises mainly of collagen with some elastic fibres present.

Arterioles (ϕ=0.05-0.5 mm). The intima is very thin with little or no sub-endothelial connective tissue. The IEL is not distinct and consists of a fibre network only. The media is usually one to five layers of SMC and there is generally no defined EEL. Contraction and relaxation of SMC in arterioles is also important in controlling blood flow to the capillary beds and the regulation of blood pressure. The adventitia of these vessels are usually thinner than the media and are not well developed.

The largest artery in the human body is the aorta which in an adult has a diameter of ±25 mm

and a wall thickness of ± 1.2 mm, while the smallest arteriole has a diameter of $\pm 8\ \mu$m and a wall thickness of $\pm 0.2\ \mu$m.

Veins. Veins can be classified as venules, small-medium veins, and large veins. Generally, the boundaries between tunicae are not sharp in these vessels. The tunica intima is normally very thin where smooth muscle may be present, arranged longitudinally. An IEL can only be seen in larger veins. The media varies in size and tends to lack definition. Vein walls generally have more collagen than any other tissue component and are very thin compared with the lumen size. Very little smooth muscle and elastic fibre is present in veins and if found, they tend to be arranged in a spiral fashion. No distinct EEL is found, whereas the adventitia is thicker, consisting of fibrous connective tissue where longitudinally or spirally-oriented bundles of smooth muscle can be present. Medium-sized veins often have valves, which aid the movement of the blood under low pressure. Although great variability exists, the following is a summary of the components characteristically found in veins of various size. *Large Veins (ϕ=10-25 mm; examples: Vena Cavae, Portal vein).* In the intima of these vessels, sub-endothelial connective tissue is nearly always present as well as longitudinal smooth muscle. A delicate IEL can be observed while the media is generally very thin and has little or no circumferential smooth muscle. The adventitia is very thick in comparison to both the intima and media, and in addition to collagen bundles it consists of longitudinal or spiral smooth muscle bundles.

Small to medium veins (ϕ=0.2-10 mm; example: Saphenous). In the intima the EC may be polygonal where small amounts of sub-endothelial connective tissue may be present. Longitudinal or spiral smooth muscle fibres are also present, while elastic fibres, when present, form a diffuse internal elastic membrane. The media is thin with spiral bundles of smooth muscle separated by collagen. In the lower extremities of the body there is more longitudinal smooth muscle. The adventitia in these vessels is well developed, where collagen and elastic fibres predominate. Longitudinally or spirally-oriented smooth muscles may also be present near the media.

Venules(ϕ <0.2 mm). The intima in these veins is composed predominantly of endothelium. The media is very thin and contains one to three layers of SMC, where scattered elastic fibres are sometimes present. The adventitia is the thickest part of the vessel wall and is composed primarily of longitudinal collagen bundles.

Comparison of arteries and veins of the same size. The lumen of an artery is always smaller than that of the accompanying sized vein, while an artery's wall is always thicker and contains more smooth muscle and elastic fibres. Vein walls tend to contain more collagen, where typical elastin-collagen ratios of some blood vessels are 2.0 for the intrathoracic aorta, 0.5 for other arteries and 0.33 for veins [32]. An IEL is always present in arteries, while in smaller diameter veins, valves are present.

2.5 Mechanical properties of blood vessels

The mechanical behaviour of blood vessels is complex as a result of their complex composite structure. Generally, blood vessels can be idealised as nonlinear, anisotropic and incompressible elastic vessels. They are also pre-stressed, both longitudinally and circumferentially. Much work has been done [32, 41- 45] to quantify these mechanical properties; a summary follows.

Incompressibility. Carew *et al.*, Lawton, Dobrin and Rovick [46] have all shown that artery deformation is approximately isochoric (the volume remains constant). Choung and Fung [33] measured fluid extrusion during the compression of rabbit aortic walls and reported that the compression stiffness increased slightly due to small amounts of fluid being extruded. However, the amount of fluid dispelled (compressibility) is dependent on the extent of the loading. The results of these investigations have shown that it is reasonable to assume that arteries are incompressible under physiological loadings.

Pre-stressed state. Arteries have been observed to be in a pre-stressed state when no internal pressure is present [23, 47]. This is demonstrated in Figure 2.6 which shows the pre-stressed nature of a rat's pulmonary artery and a human's ileal artery. Figure 2.6 (a) shows the pressurised state (physiological pressure, rat & human), (b) the non-pressurised states (the arteries have a bunched-up, corrugated appearance due to internal compressive stress), and (c) the zero-stress state (when the vessel is sliced open longitudinally).

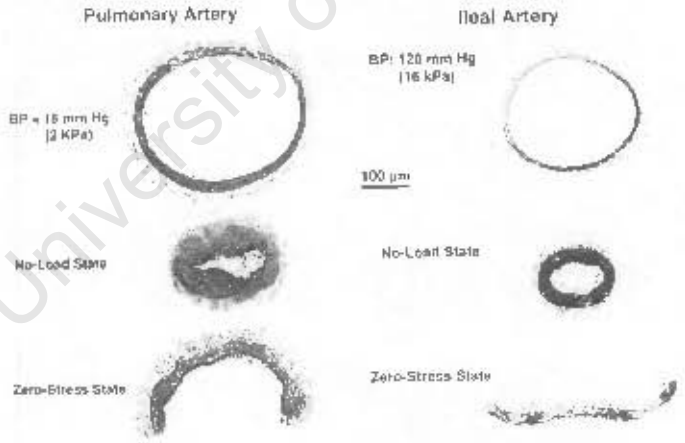

Figure 2.6: In vivo, no-load and zero stress states of a rats pulmonary and a humans ileal arteries [23]

Arteries can be regarded geometrically as thick-walled cylinders. For a typical elastic thick walled cylinder with an internal pressure, the circumferential stress decreases through the wall thickness to the outer surface with the inverse square of the radius, while the axial stress is constant throughout the wall, and the radial stress is a maximum compressive stress on the inner surface and reduces to zero at the outer surface [48].

To reduce the maximum circumferential stress experienced on the inner surface of a thick-

walled cylinder due to an internal pressure, one may pre-stress the inner section of a cylinder. This can easily be demonstrated in the case of a compound cylinder, where an outer cylinder is shrunk onto an inner sleeve, thereby inducing compressive stresses on the inner sleeve, under no load conditions. When an internal pressure is applied, the stress distribution through the compound cylinder wall in the circumferential direction is reduced due to the influence of the initial pre-stressed state. This is seen diagrammatically for the circumferential stress in Figures 2.7 (a), (b) and (c). This can also be observed in the longitudinal and radial directions, although pre-stressing in the radial direction can only be observed at the interface of the compound cylinders and does not help reduce the radial stress at the inner or outer surface, as demonstrated in Figures 2.7 (d) and (e).

Therefore, the pre-stressed state of arteries helps reduce the peak internal wall stresses and helps create a uniform stress state through the wall thickness, thus allowing the artery to operate at a lower stress state, similar to that observed at the interface of the compound cylinders in Figure 2.7.

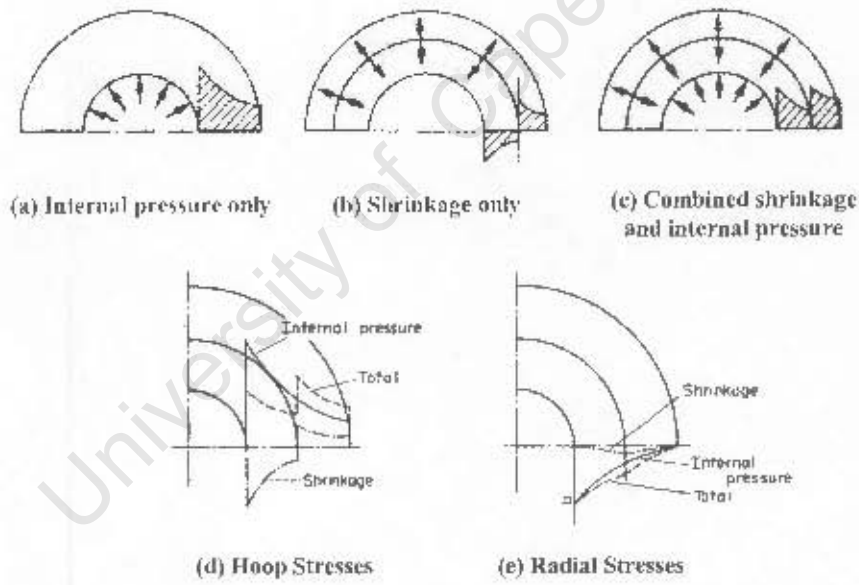

Figure 2.7: The effects of pre-stressing and the difference in circumferential and radial stress through compound cylinder walls [49]

Much work has been done in the way of measuring and observing the pre-stressed states of arteries [23, 47, 50]. The degree of pre-stressing is normally determined by the opening angles made by the artery wall when sliced open longitudinally and in the zero-stress state. Figure 2.8 schematically defines these angles.

Pre-stressing of the artery is also found in the longitudinal direction. During growth from infancy arteries stretch longitudinally, causing tension, which helps regulate length changes during the cardiac cycle due to pressure and viscous drag forces. The length increase of the abdomi-

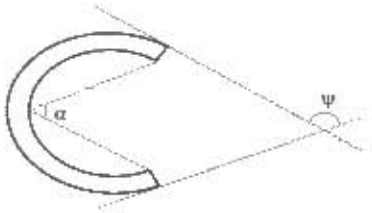

Figure 2.8: Angles used to measure pre-stressed states of blood vessels [32]

nal aorta is usually 1% while the pulmonary and the ascending aorta increase by 5-11% during the cardiac cycle [50]. It should also be noted from the histology of the blood vessels that at the extremities smooth muscles are longitudinally orientated to curb this response.

Nonlinear mechanical behaviour. The mechanical behaviour of most biological tissue, including blood vessels is nonlinear. Figure 2.9 shows the pressure-strain relationship of a typical blood vessel and the existence of hysteresis as shown by the area between the loading and off-loading curves.

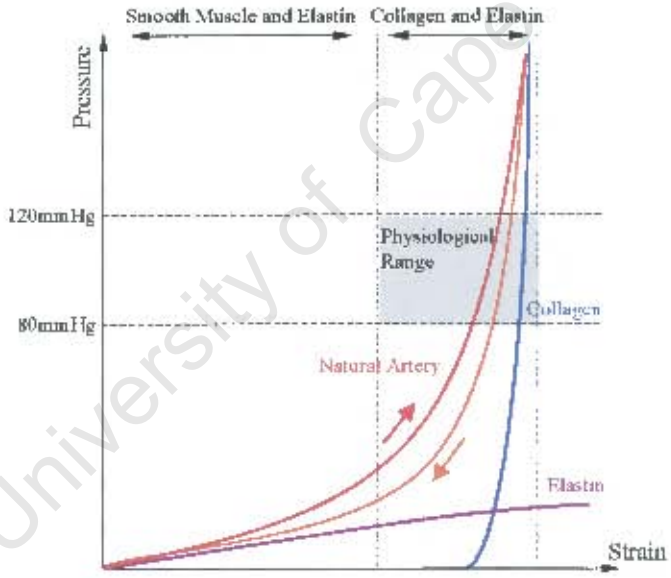

Figure 2.9: The nonlinear elastic and viscoelastic behaviour of blood vessel tissue and the interaction between collagen and elastin.

Since the mechanical effects of the intima can be considered negligible in comparison to those of the media and adventitia, the blood vessel can be treated as a compound vessel of the media and the adventitia (as shown in Figure 2.7).

Due to its high collagen content the adventitia has a higher elastic modulus than the media with its predominant elastin content. In the physiological pressure range, arteries are under cyclic loading between 10.6-16.0 kPa (80-120 mmHg), where the response of the artery can be regarded as largely linear and the energy is absorbed mainly in the elastin and smooth muscles of the media. At higher pressures the load is seen to transfer to the adventitia and the stress-

strain curve becomes steeper. This energy transfer from the media to the adventitia is achieved through the alignment of the wavy bundles of collagen fibres. As the vessel distends the collagen bundles in the adventitia re-orientate and align themselves circumferentially. This re-orientation and alignment of the collagen bundles causes the adventitia to play a larger role in the mechanics of the artery at higher pressures, making the vessel circumferentially stiffer and resulting in a nonlinear response. This effect helps prevent aneurysms (over-inflation) occurring in blood vessels.

Anisotropic behaviour. The behaviour of arteries is anisotropic (the mechanical behaviour is different in different directions). It is reasonable to assume transverse anisotropy, with orthogonal planes of symmetry corresponding to the circumferential, radial and longitudinal directions.

Viscoelasticity. In the absence of active SMC, arteries exhibit hysteresis under cyclic loading (as shown in Figure 2.9), stress relaxation under constant extension, and creep under constant load. These all point to the viscoelastic nature of arteries. Fung [51] found that arteries exhibited a delayed response to loading and that the stiffness increased with increased load rate. He also found that the change in strain rate had little effect. From test data of canine aortas Fung postulated a simple continuous modulus function for arterial behaviour that used a linear response, where viscoelastic parameters vary insignificantly with varying strain. Studies by Hutchinson [52], Newman [53] and Greenwald [54] were in agreement with Fung [51]. However, more recent works by Langewousters *et al.* [31, 43] have shown that the human arterial wall tissue has a nonlinear response in which viscoelastic parameters vary significantly with varying strain.

There now appears to be a consensus in the literature [25,35,36,55,56] that the true viscoelastic behaviour of biological soft tissue is nonlinear.

2.6 Factors in the design of a prosthetic graft

The success of a graft depends on the mechanical matching of its behaviour with the host artery. Much work has been done in graft design to increase patency, the graft's long term ability to function in the circulatory system. Factors that affect patency include the promotion of endothelialisation on the luminal surface, the correct matching of compliance to the host vessel, the reduction in stress energy across the anastomosis, the reduction of the blood flow disruptions, and the biological reaction of the host to the graft. Apart from the biological reactions, the above-mentioned factors affecting patency are dependent on matching the mechanical properties of the graft to the host vessel. Factors which affect patency are:

Compliance. Compliance matching of the graft is an important part of graft design [13, 17, 57–59]. The correct matching of the graft's compliance to that of the host vessel helps blood flow, reduces thrombotic build up, allows for a steady transfer of the pressure pulse and windkessel effect [60] (the elastic return of arteries aiding the steady flow of blood) and reduces the elastic

stress-strain difference between the graft and artery. Compliance is the inverse of stiffness and is widely used in the medical field to describe the mechanical properties of arteries [61]. Two forms of compliance are generally used: diameter compliance (C_d) and volume compliance (C_v). These are defined by

$$C_d = \frac{\Delta d}{d\Delta P} \times 100 \times 100\,\text{mmHg} \tag{2.1}$$

$$C_v = \frac{\Delta V}{V\Delta P} \times 100 \times 100\,\text{mmHg} \tag{2.2}$$

where d and V are the internal diameter and internal volume of the vessel respectively, ΔP is the pressure difference (static or dynamic), and Δd and ΔV the change in diameter and volume induced by this pressure difference. It can be shown that C_v is twice C_d, assuming no change in vessel length and second order changes in diameter are negligible (see Appendix G for derivation). Compliance is expressed in percentage change of diameter or volume over 100 mmHg pressure (%/100 mmHg). Table 2.1 below shows the variation in compliance for grafts and natural blood vessels.

Description	**Diameter** mm	**Compliance Type** Diameter C_d/Volume C_v	**Compliance** %/100 mmHg	**Reference**
Human Femoral Artery	–	C_d	5.9	[62]
Human Common Femoral Artery	–	C_d	14.1	[63]
Human Popliteal Artery	–	C_d	4.7	[63]
Human Common Carotid Artery	–	C_d	6.6	[64]
Human Saphenous Vein	–	C_d	4.4	[62]
Human Superficial Femoral Artery	–	C_d	1.8	[64]
Human Fixed Umbilical Vein	–	C_d	3.7	[62]
Woven Dacron®	10	C_d	0.08	[65]
Knitted Dacron®	8	C_d	2.0	[65]
Reinforced PU with PET Fibers	4 – 6	C_v	0.31 – 0.43	[65]
Expanded PTFE	6	C_d	1.2	[66]
Polyurethane Grafts				
PU	3 – 8	C_d	7.0 – 19.0	[66]
PU	–	C_d	8.1	[67]
PEUU	3 – 8	C_v	2.8 – 4.8	[68]
Tecoflex 80A	3 – 6	C_v	4.9	[69]
PU/Siloxane copolymer	4	C_d	13.2	[70]
Biomer	4	C_d	10.3	[71]
Chronoflex	5 – 6	C_v	5 – 10	[72]
Segmented PU	4.9 – 5.2	C_d^{static} C_d^{dyn}	4.2 – 9.5 4.4 – 9.7	[73]

Table 2.1: Compliance values for various grafts and blood vessels

There are a further two ways of characterising the compliance of a vessel, namely static (C^{stat}) and dynamic (C^{dyn}) compliance. Static compliance testing entails the step-wise, incremental increase in internal pressure and a corresponding diameter change. The advantage of this method is the ease with which a pressure-diameter relation can be found for a vessel and characterised over the full pressure range of the vessel. The drawback to this method however is that it does

not take into account strain rate effects on the vessel, which may have a large influence on compliance. If the material is highly viscoelastic, at higher strain rates the material will appear "stiffer", due to slow strain response [74].

Dynamic compliance is carried out under pulsatile pressure conditions over a period of time; thus a more realistic response is observed, where physiological conditions are taken into account. Research has shown that compliance is strain rate dependent [75], where at higher strain rates (pulse rates), arteries show a decreased compliance. MacWilliams *et al.* [76] also showed that compliance varies within the pressure pulse while Hamiltons' group [67, 77] have done step-wise dynamic compliance testing over a pressure range, showing that compliance is pressure dependent. Conti *et al.* [78] showed that in latex tubing, compliance decreased by nearly 50 % when tested at 72 and 1600 bpm, however, it was also observed to increase at higher frequencies (strain rates). It was postulated that possible instrumental harmonics or the material's natural frequency cause complex relations between material properties, strain rate and compliance.

Pressure strain elastic modulus (K). The pressure strain modulus K is the inverse of diameter compliance, and is defined by

$$K = \frac{d\Delta P}{\Delta d}. \tag{2.3}$$

This is measured in mmHg or Pa.

Nonlinear stiffening index (β). The nonlinear stiffening effect of an artery is important and helps prevent aneurysms occurring in blood vessels. Figure 2.9 shows the stress strain relation between collagen and elastin and its role in the mechanics of arteries. A stiffness index β has been defined by Hayashi *et al.* [79], and is given by

$$\beta = \frac{\ln(P/P_0)}{(d - d_0)/d_0}, \tag{2.4}$$

where d is the diameter of the vessel at a pressure P, and d_0 is the diameter at a standard pressure P_0 (100 mmHg). Hayashi *et al.* showed that β was a constant in the physiological range of pressure. This was modified to β' by Kawasaki *et al.* [80] to include the diastolic and systolic pressures (P_{dia} and P_{sys}) and diameters (d_{dia} and d_{sys}) where,

$$\beta' \simeq \beta = \frac{\ln(P_{sys}/P_{dia})}{(d_{sys} - d_{dia})/d_{dia}}. \tag{2.5}$$

Kawasaki *et al.* showed that the modulus K increased linearly with systolic pressure, while β' values remained independent of arterial pressure. Thus β' values can be regarded as a reliable measure of elasticity within the physiological pressure range.

Porosity and gel fill. It has been shown by Burkel [3] that the ingrowth of EC on the inner surface of a vascular prosthesis greatly increases the patency of the graft by reducing the thrombogenetic reaction of the blood with the graft. A means of increasing such ingrowth is to induce cellular ingrowth through the walls of the graft, leading to the eventual endothelialisation

of the inner surface [1, 6, 11, 20]. Therefore, maximising this endothelialisation of the lumen surface would greatly increase the success of the graft. This may be achieved by increasing porosity and introducing defined micro-channels to the lumen surface through the graft wall. By filling these pores with growth matrices, further tissue ingrowth can be promoted. Thus a highly porous graft with defined channels from the outer surface to the lumen will greatly promote the grafts self-healing abilities and increase patency.

Thrombogenecity and surface treatment. Thrombogenecity refers to the nature of a vessel to thrombose (i.e. the build-up of blood clotting). This is related to the surface smoothness of the lumen wall and the shear stress at those points. As mentioned earlier, EC are responsible for regulating the shear stresses on the lumen by controlling the response and structure of the vessel wall. At high shear stresses EC try to slow the blood flow by making the smooth muscles dilate, while, if low, they induce the SMC to contract. In cases where muscular response does not curb the change in shear stress, growth factors are released, changing the tissue make-up and structure of the vessel wall, and thus its mechanical properties. This tissue growth can however be excessive at the anastomosis where sharp mechanical changes occur, and where blood flow is disrupted and invariably turbulent, so that high shear forces occur. The perturbed endothelium reacts by releasing substances which aid thrombosis. Therefore, to ensure that the thrombogenecity of a graft is low, a covering endothelium should be present on the lumenal surface, and the disruption of blood flow patterns at the anastomosis should be minimised.

Kink resistance. Small to medium sized arteries in the human body tend to be located at the extremities of the body. These parts of the body are continually in active motion (for example at the knee and elbow). Therefore, if a replacement graft is to be successful it would need to be kink resistant. Novel ideas for increasing kink resistance include the placement of external support rings or the use of corrugated structures, which prevents the vessel wall from collapsing.

Suturability. The suturability of a graft pertains to the ability of the graft to resist suture (stitch) pullout. Due to the active nature of both the host and the blood vessel, a graft once implanted needs to remain intact. A graft which pulls out will cause massive hemorrhaging and various complications.

Geometry. The geometry of the replacement graft is significant. Traditionally grafts with a larger diameter than that of the host artery have been found to have a higher patency. A diameter of $1.5\times$ the host vessel was found to be optimal in small to medium diameter grafts [81]. However, this work is based on using currently available synthetic grafts which do not match the mechanical characteristics of the host vessel, where a large diameter vessel would smooth out blood flow and reduce turbulence. An exact match of wall thickness and vessel diameter should be attempted as far as possible.

2.7 Prosthetic grafts

Two groups of prosthetic grafts, biological and synthetic, are currently available. The merits of biological grafts far outweigh those of the synthetic in terms of patency and success; however, biological grafts are often difficult to obtain. Figure 2.10 below shows the graft types and the trend towards combining the two distinct groups to obtain a combined biosynthetic graft.

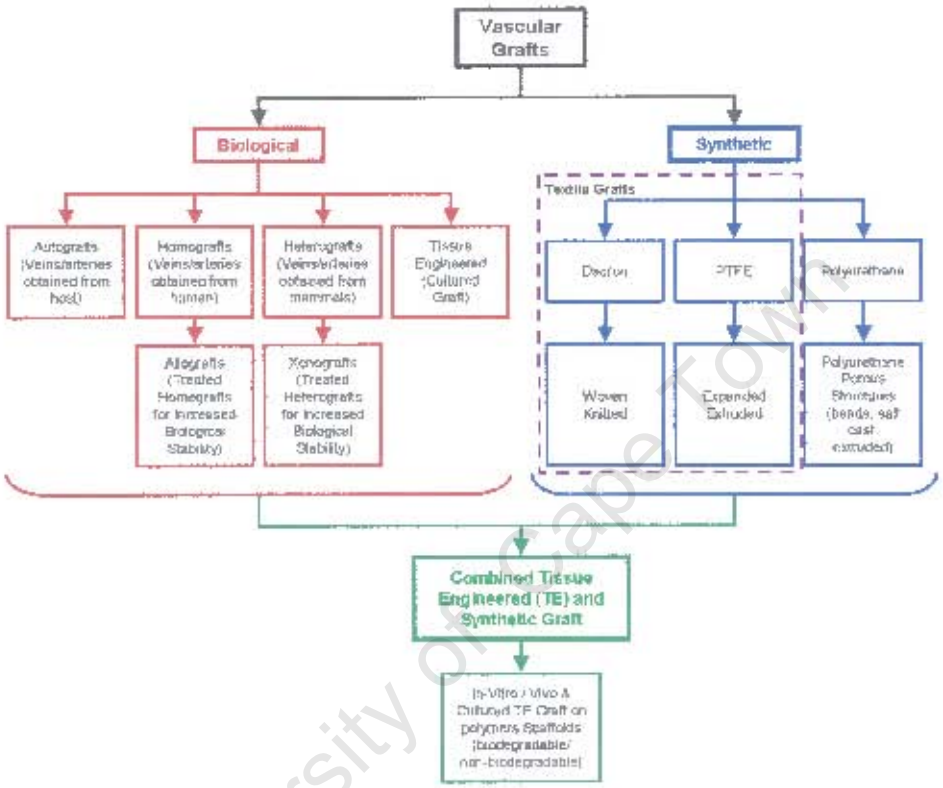

Figure 2.10: Prosthetic graft types

2.7.1 Biological grafts

The body of biological grafts include; autografts (veins or arteries obtained from the host), homografts (veins and arteries obtained from another human being), heterografts (veins and arteries obtained from mammals), and tissue engineered grafts (cultured). Autografts currently have the highest success; however, as described earlier it is not always feasible to obtain good undiseased samples from the host in the right length [5]. Homo- and heterografts tend to be rejected by the host unless the host is heavily treated against biological reactions. Allografts and xenografts are crosslink treated or fixed homo- and heterografts, giving a more biostable graft. This fixing, however, causes a reduction in graft patency as cross-linking causes stiffening and a marked reduction in compliance.

Recent biological graft developments include the novel tissue engineered (TE) grafts. These were pioneered by Weinburg and Bell [82] who cultured SMC and bovine collagen in annular molds over one month with an external Dacron® sleeve. Further work includes that of Aúger *et*

al. [83, 84], who utilised a completely biological approach where SMC from the umbilical cord and fibroblasts from adult dermis (skin) were combined. The SMC and collagen were cultured and then wrapped around a mandrel in sequential layers. This was then placed in a bio-reactor for further culturing, taking a total of one to two months to manufacture. Figure 2.11 shows the biological graft produced by Aüger *et al.* and the three distinct layers of lamina, media and adventitia through the wall.

Figure 2.11: Tissue engineered graft; (a) complete specimen and (b) wall cross-section showing distinct layers of lamina, media and adventitia [84]

These grafts have well structured layers and organised collagen and elastin which resemble those of a natural vessel. Preliminary tests on dogs have shown that these grafts are suitable for suturing, and exhibit a 50% patency after seven days when inter-layer blood infiltrations are observed (small blood vessel integration through the wall structure) [84]. The compliance of these grafts has been found to be high, but less than that of saphenous veins. However, these tissue engineered grafts are costly, require great lengths of time to manufacture, and need to be carefully stored, making them undesirable.

As can be seen, biological grafts have a high patency, unfortunately they are not readily available. The cross-linking of naturally occurring biological grafts causes a drastic reduction in compliance. With the advanced state of tissue engineered grafts and the initial results, these show great promise, however, manufacturing time and cost is high.

2.7.2 Synthetic grafts

Dacron®, e-PTFE (expanded Teflon®), Nylon, and other biomedically stable polymers form the body of synthetic grafts. The advantages of synthetic over biological grafts are, they are readily available, can be manufactured to any length, and can be varied in strength and structure by varying their specifications. However, so far these grafts have shown limited success if used as small diameter conduits. Manufacturing technology and a detailed understanding of blood vessel mechanics is lacking. Dacron®, e-PTFE and polyurethane structures form the majority of the synthetic group. Figures 2.12 a), b) and c) show the micro-structures of each of these synthetic graft groups.

Figure 2.12: Various synthetic graft micro-structures

Expanded Teflon grafts. Expanded Teflon® (e-PTFE) is an exceptionally strong, chemically inert, gas permeable, hydrophobic and biocompatable material, making it useful as a synthetic graft. Expanded Teflon® grafts were first introduced in 1975, and were produced by extruding PTFE tubes which are then expanded at high temperature, resulting in a highly porous graft structure. The porous structure consists of a series of solid nodes of PTFE with interconnecting small fibrils (see Figure 2.12 a)). The pores are elliptical splines with a dimension of 5-10 μm wide and 5-100 μm long with interconnecting fibrils having a diameter of less than 0.5 μm. This microstructure leads to an anisotropic material behaviour which is strong in tension while weak in compression. The pore structure is created during the expansion process, where orientated pores are produced in the direction of expansion. Initial problems with e-PTFE grafts included material creep and dilation; these were overcome by reinforcing or increasing the wall thickness, which invariably reduced compliance. These grafts are sometimes seeded with EC to help reduce the thrombogenetic nature of the graft surface.

Dacron grafts. Following the discovery that cells grew on silk threads exposed to blood by Voorhees in 1952, woven and knitted grafts were introduced in the early 1970's [3]. Dacron® grafts are part of the textile grafts available and are formed from polyester multifilament yarns. Two forms of textile grafts are available, viz. woven and knitted. Woven Dacron® grafts tend to be stiff both radially and longitudinally and are thus structurally sound, but their compliance is poor. These woven grafts tend to have a low porosity and therefore do not require pre-clotting. Woven grafts tend to fray and have a low suturability.

Knitted Dacron® grafts tend to be highly porous compared to woven grafts and thus require pre-clotting before use. The size of yarn and type of knit define porosity and with this variation of knit structure a certain amount of variation in the mechanical response can be achieved. Knitted grafts tend to be more compliant and do not fray to the extent of woven structures, this makes them highly suturable.

Table 2.2 compares the characteristics of woven and knitted Dacron® grafts to a typical artery.

Novel designs in the line of textile grafts include a solution spinning technique used by Cooman *et al.* [85] to create an orientated fibre porosity. Ze Zhang *et al.* [86] developed a fibrous prosthesis made from a polycarbonate urethane. The technique creates communicating

Structure Type	Porosity (cc/cm^2-min)	Radial Strength ($N/m \times 10^4$)	Handling
Woven (Warp & Weft)	50 – 3800	2.8 – 3.5	Difficult to Suture Little Conformability
Knit (Weft)	1300 – 4000	0.7 – 1.5	Moderate-Easy to Suture Excellent Conformability
Velour Knit (Warp)	1300 – 1800	0.7 – 1.8	Moderate-Easy to Suture Excellent Conformability
Typical Artery	0	0.2 – 0.3	Difficult to Suture Little Conformability

Table 2.2: Properties of various graft wall structures

pores in the wall structure but no orientation. Lyman *et al.* [57] produced a Dacron® reinforced porous prosthesis using a coagulation process. Gupta *et al.* [65] developed a hybrid woven textile graft; the graft had a two-layer construct made from two different elastic materials: an inner fabric layer of low elastic modulus polyurethane yarn and an outer layer of high modulus polyester yarn.

Figure 2.13 shows a comparison of load-elongation curves for Dacron® and e-PTFE grafts, and natural blood vessels. As can be seen, current Dacron® and Teflon® grafts are highly non-compliant, thus reducing patency.

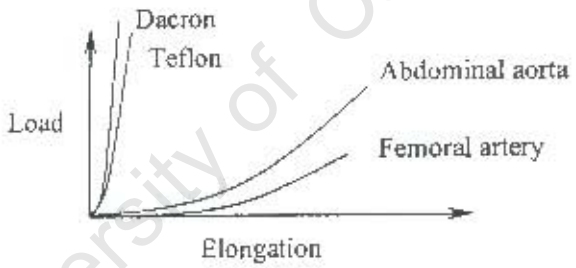

Figure 2.13: Comparison of synthetic grafts with natural blood vessels

Polyurethane grafts. The most recent developments in prosthetic design include porous polymer grafts. These grafts are advantageous, since well-developed, orientated pore structures can be produced relatively easily. Early work in porous prosthetics includes that of Hayashi *et al.* [6] where a polyurethane porous prosthesis was produced using silicon rubber additives; a phase separation technique was used to form the pores and a polyester net externally reinforced the structure. Lyman [57] used a precipitation method in the formation of a polyurethane foam, and a polyester mesh was introduced to reinforce the structure. This graft structure showed a linear elastic response with a relatively low elastic modulus compared to other synthetic grafts. The wall thickness thus had to be increased to obtain the correct compliance and an external reinforcing added to ensure the grafts integrity. Polyurethane grafts are advantageous as they can be moulded into any form with a high degree of porosity (up to 90% [87]), giving greater compliance and making them well-suited for small vessel replacement. However, they are structurally

weak and invariably require some form of strengthening.

2.8 The adventitial graft

The various factors in graft design described above and the current failure of commercial grafts to incorporate all these factors demonstrates the need for further research into small diameter prosthetic graft design. With these factors in mind, a porous polymer structure with well-established channels has been developed, in the hope of producing a self-healing synthetic graft [9]. However, the structure has been found to be weak and requires strengthening. Wound reinforcing was initially investigated by MacKellar [21] and Hughes [22], where regions of concentrated stress and compression were observed. This reduced the grafts compliance and locally affected the porous scaffold. To ensure that the prosthetic scaffold remains highly porous and retains its well-defined channels to the lumen surface, an adventitial style graft is proposed, in which a loosely attached, highly porous fabric supports the porous structure externally. It is hoped that this fabric structure will mimic the mechanical behaviour of the natural host vessel and distribute the stress uniformly over the porous scaffold.

This thesis is concerned with the development of such a reinforcing structure. Figure 2.14 shows the concept, in which a well established inner porous structure with little mechanical strength provides a scaffold for tissue regeneration, and the fabric externally reinforces this scaffold, providing the graft's integrity and mechanical requirements, while permitting cellular activity to take place through it.

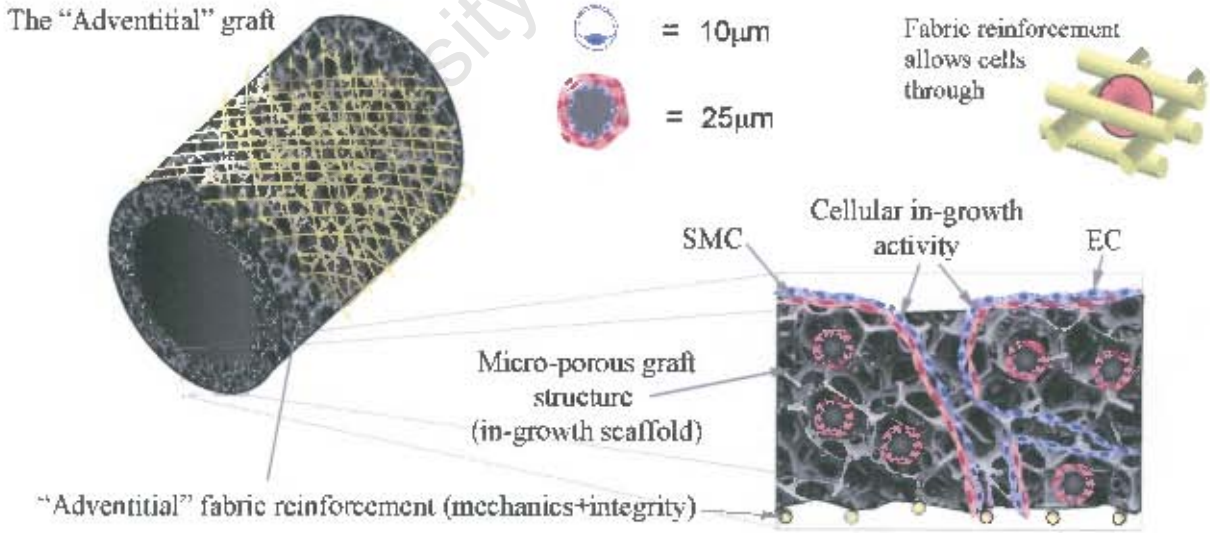

Figure 2.14: The fabric reinforced adventitial graft concept

Chapter 3

The Structure and Mechanics of Polymers and Fabrics

3.1 Introduction

The mathematical description of a material requires a sound understanding of the material and its structure. In this Chapter the physical characteristics of polymers and fabrics, including structure and mechanical properties, are described.

3.2 Polymers

Polymers have been utilised in the medical field since the 1960s. Yet, the extent to which all polymers integrate with and affect the body is still poorly understood. Extensive testing is thus required before a polymer can be safely implemented in the human body. Many biomaterials, especially heart valve and blood vessel replacements, are made from polymers like Dacron®, Teflon® and various polyurethanes.

Polymers are materials containing a large number of repetitive parts, chemically bonded together to form a solid. Polymers are divided into two groups; natural and synthetic (Figure 3.1). Examples of natural polymers are protein chains such as collagen, sugar chains such as cellulose, and natural rubbers. Examples of synthetic polymers are polyethylene, Nylon® and Teflon®. From these, polymers with properties optimised for strength, stiffness, abrasion resistance, density and creep requirements can be produced. The following sections describe the various polymers available and their properties.

3.2.1 Polymer morphology

The molecular shape and the arrangement of the molecules in a polymer are important factors in determining its properties. Crystalline and amorphous structures coexist in polymers. Amorphous structures are random, while crystalline structures are ordered and orientated. Figure 3.2 shows a polymer with the molecules in this dualistic state.

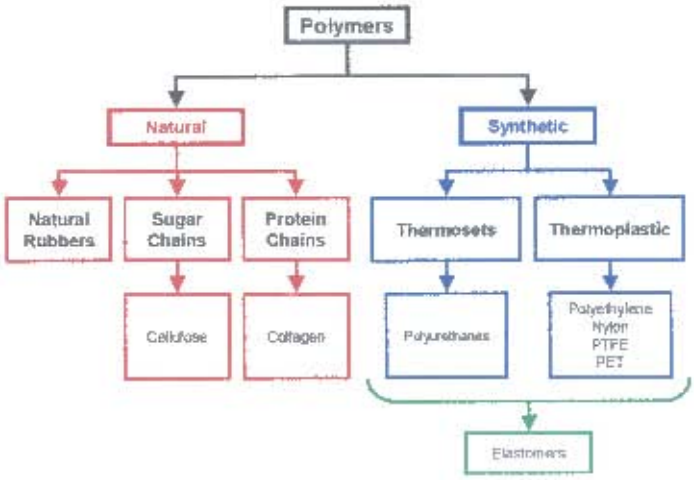

Figure 3.1: Division of the polymer groups

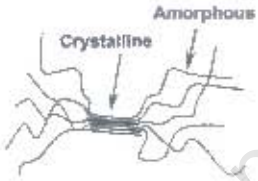

Figure 3.2: Crystalline and amorphous structures

3.2.2 Synthetic polymers

Synthetic polymers can be subdivided into two groups, namely, thermoplastics and thermosets. Due to the difference in structure and chemical bonds, thermoplastics and thermosets display different mechanical properties. Elastomers, which can be either thermoplastics or thermosets, are rubber-like materials which are highly elastic.

Thermoplastics. Thermoplastics are those polymers which soften on heating and harden on cooling. These processes can be repeated many times without changing the polymers' chemical and mechanical properties once cooled. Thermoplastics account for the majority of plastics available; examples include polyethylene, PTFE (Teflon®), PET (Dacron®) and Nylon®. Thermoplastics are extremely ductile, have a high strain to failure, have good impact and chemical resistance and a low friction coefficient, however, they have a low creep resistance and are difficult to form.

Thermosets. In contrast to thermoplastics, thermosets flow and cross-link upon heating, forming a rigid polymer structure which after cooling cannot be softened by further heating. These plastics are produced from a two-stage chemical procedure: the first stage produces large molecules while the second cross-links these molecules under heat and pressure. This process makes thermosets suitable for moulding. These polymers are quite rigid due to the strong bonds produced between the molecular chains from cross-linking. Thermosets are not affected by tem-

perature once cross-linked, have a low shrinkage, adhere well to fibres and show high static and dynamic strengths, yet they are not easily reformed. Table 3.1 shows the variation of properties between thermosets and thermoplastics.

Description	Thermoplastics	Thermosets
Processing	poor	excellent
Adherence	nil	high
Shelf Life	indefinite	definite
Shrinkage	low	fair
Cure Cycle	short	long
Solvent Resistance	fair - excellent	good
Re-processability	good	nil
Creep Resistance	low	good

Table 3.1: Comparison of thermosets and thermoplastics

Elastomers. Elastomers are rubber-like materials which can be classified as either thermosets or thermoplastics, of which rubber is the most well-known. They consist of very long amorphous chain-like molecules which are cross-linked and cured in a vulcanisation process, in which natural rubber is cross-linked by heating it in sulphur. Cross-linked elastomers can undergo large elastic deformation and regain their original shape on unloading. This is achieved through the uncoiling of these amorphous molecular chains, which orientate and align themselves, and upon unloading return to their original form due to the cross-links. Examples of elastomers are natural rubber, Lycra® (Spandex®) and elastomester.

Forming processes. Polymer products are formed through a variety of processes, such as injection moulding, blow moulding, compression moulding, melt cast, thermo-forming, and extrusion. In injection moulding, the polymer (only thermoplastics) is heated above its glass transition temperature (flow melted) and then forced into a mould. Blow moulding and thermo-forming are techniques which expand a polymer into a mould by making use of blowing agents. Blowing agents are dissolved gases which expand into bubbles through pressure reduction or by utilising chemical reactions within the molten polymer.

Compression moulding and melt cast are processes where the molten polymer (normally in paste form) is compressed or heat pressed into shape. Pores are introduced into these processing forms either through a forming process such as blow moulding, or by utilising a solid fill within the molten polymer, which is then dissolved off once the polymer has cured (hardened).

Glass transition (T_G) and melt temperatures (T_M). When a polymer is cooled, it passes through a certain temperature at which it changes from a viscous rubber-like material to a hard, brittle material. This point is known as the glass transition temperature (T_G). Glass transition occurs predominantly in amorphous polymers. Polymers can either be used above or below this glass transition temperature. Plastics like perspex are used below their glass transition temperature and so are hard and brittle, while rubber elastomers like Lycra® are used above their glass transition temperature and so have a rubber-like formable nature. The melting temperature

(T_M) of a polymer is the transition which occurs in a highly crystalline polymer, where the molecular chains move from a dominant crystalline structure to an amorphous structure.

3.3 General mechanical properties of polymers

Many polymers can be described as isotropic elastic materials which display viscoelastic behaviour. The elastic and viscoelastic behaviour varies depending on the glass transition temperature, the operation temperature, the load rate and time scale. A polymer's elastic properties can either be almost linear, in the case of polymers which are used below their glass transition temperature (Perspex®), or highly nonlinear, in the case of polymers which operate above their glass transition temperature (Elastomers). This variation in elasticity can be seen in the different stress-strain curves obtained for a polymer with increasing temperature (Figure 3.3).

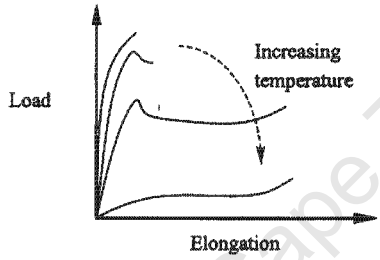

Figure 3.3: Stress-strain properties of polymers [21]

The viscoelastic (creep) nature of polymers depends heavily on time scales, load rates, temperature, and the glass transition temperature [88]. This can be seen in Figure 3.4, where with increased temperature a polymers viscoelastic properties vary.

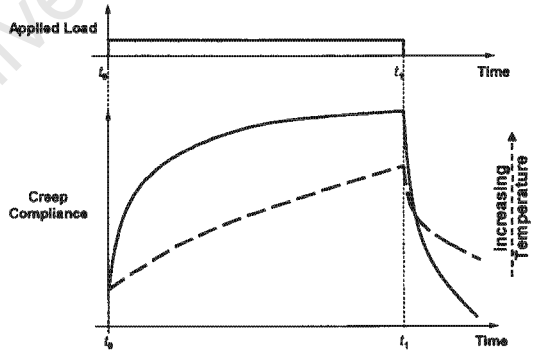

Figure 3.4: Creep properties of polymer with increased temperature [21]

At low temperatures and high frequencies (load rates) a polymer may display glass-like characteristics (low breaking strains and high elastic modulus), and at higher temperatures and low frequencies it displays rubber-like qualities (large strains and low elastic modulus), while at normal temperatures it acts like a viscous fluid. These characteristics make a polymer's behaviour difficult to describe generally and therefore each has to be categorised individually as either a

brittle-glass-like polymer, a highly deformable rubber-like polymer, or a highly viscous polymer, depending on the structure and conditions under which the polymer is used.

3.4 Textiles

Textile structures have been utilised in the medical field for centuries in the form of bandages and sutures, with the discovery that cells grew on silk threads exposed to blood by Voorhees *et al.* [3] in 1952, textiles have been used for arterial and skin grafts. Fibres and fabrics have great scope in the medical field, not only for their mechanical similarities to biological tissue but also due to the ability to be formed with desired characteristics by simply altering the fibre construction and assembly.

Fibres and filaments. Fibres and filaments are formed from polymers, and like polymers, can be divided into two groups, namely, natural and synthetic. Examples of natural fibres are cellulosics (linen, cotton, rayon, acetate) and proteins (wool, silk). Examples of synthetic fibres are polyamides, polyester, vinyls, acrylics, PTFE, polyphenylene sulfide (PPS), aramids (Kevlar®, Nomex®) and polyurethanes (Lycra®, Pellethane, Biomer). Each has different mechanical properties; Lycra®, for example, is an elastomer which is highly deformable and can be compared to elastin, while polyester is highly stiff and can be compared to collagen. The manufacture of synthetic fibres is achieved by extrusion through wet, dry or melt spinning; these fibres are then processed to obtain the desired fibre size, shape and texture. Through the careful control of morphology, fibres can be manufactured with specific mechanical properties. Tensile strengths of fibres can vary from 2-30 grams/denier, while most industrial fibres range between 2-6 grams/denier. The breaking strain can vary between 10 % in standard textile fibres to 500 % in elastomeric fibres. The denier system is employed internationally to measure the size of silk, man-made fibres and filaments and indicates the weight in grams of 9000 m of fibre or filament. The higher the denier value the coarser the fibre; for example, a 15 denier fibre is finer than a 100 denier fibre.

Yarns. Yarns are fibres or filaments which are twisted into larger sections to improve strength, abrasion resistance, and handling. Yarn properties (y) depend on the fibre or filaments properties (f) and the twist angle (α) of the yarn; for example the Young's modulus and strain of a yarn in terms of the filament properties is given by

$$E_y \cong E_f \cos^2 \alpha \ . \tag{3.1}$$

The formation of fibres and yarns is shown in Figure 3.5.

The denier system described earlier is not convenient for the measurement of a yarn's weight per unit length, as their greater weight would mean large denier values. Therefore the Tex system was developed for yarns; it is also applicable to fibres and filaments, and is based on the weight in grams of 1000 m of yarn.

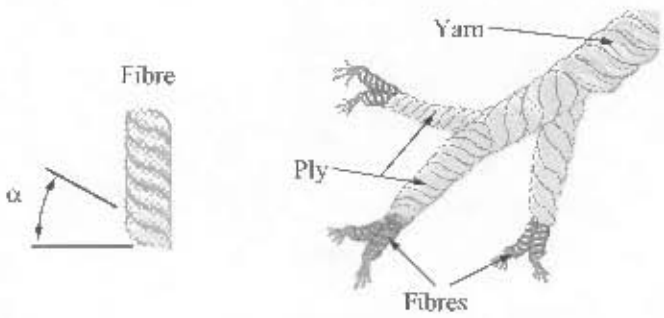

Figure 3.5: Fibre and yarn construction

3.4.1 Fabrics

Fabrics are yarns which are interlaced together in various forms to produce a desired structure. Yarns are interlaced either in woven, knitted, braided or non-woven structures. Weaves, knits and braided structures are all made from yarns, while non-woven structures can be directly spun from fibres. The properties of a fabric depend on the characteristics of the yarn used and the geometry of the formed structure. The following describes the various fabrication techniques.

Weaves. Weaves are sets of yarns interlaced at right angles to each other; the yarns aligned lengthwise are warp yarns and perpendicular to these are the weft yarns. Figure 3.6 (a) shows the basic weave structure. Weaves tend to be very stiff and structurally sound, and due to the tight interlaced yarns these tend to be less porous than other structures. A disadvantage of woven fabrics is their tendency to fray and unravel at the edges, which greatly reduces the suturability of these structures. However, a weave known as the leno weave, where two warp threads twist around a weft, substantially reduces fraying and unraveling. Many weave variations are possible, some of which are shown in Figures 3.6 (b) and (c).

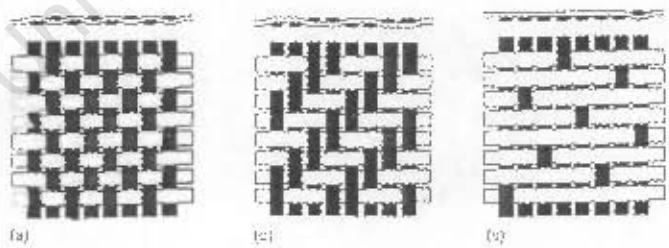

Figure 3.6: Weave constructions: (a) plain, (b) twill and (c) satin

Knits. Knits are fabrics where yarns are inter-meshed through the use of loops. Generally, knitted structures are not as stiff as their woven counterparts and are highly porous. Knitted fabrics encompass two groups, namely weft and warp knits (Figures 3.7 (a) and (b) respectively). Warp knits are highly complex compared to weft, many of the medically implanted fabrics are warp knits. Weft knit structures tend to be highly extendable but are structurally unstable, unless interlocking occurs. This interlocking tends to reduce extensibility but does help with elastic

recovery. Advantages of knitted fabrics include their flexible, comfortable nature, and their tendency not to fray and unravel at the edges. Many knit patterns are possible. Figures 3.7 (c) and (d) show two variations in knit construction.

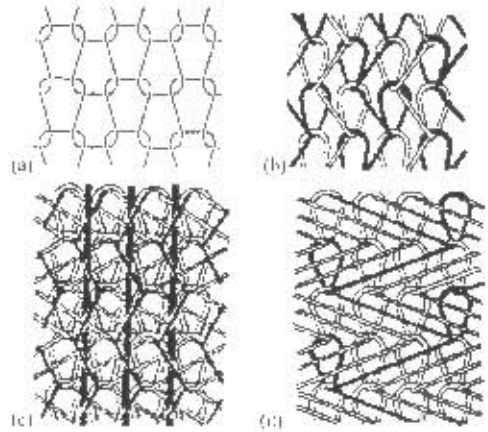

Figure 3.7: Knit constructions: (a) weft, (b) warp (tricot), (c) warp knit with underlaps and (d) warp knit with weft inserted yarns

Braids. Braids are a simple method of forming fabric structures involving three or more yarns crossed over each other sequentially at 45 degrees. These are typically used in cords and sutures but are not extensively used as fabrics for medical purposes.

Non-woven. These fabrics are formed by tangling fibres and/or yarns into fabric form. They can be processed directly from fibres and are needle-felted, hydro-entangled or bonded through thermal, chemical and or adhesive methods. Non-woven properties are determined directly from the fibre, the yarns, and the bonding process between them. Polyurethane-based non-wovens produce a product that resembles a collagenous material in both structure and mechanical application. The porosity of these structures can be controlled directly by the manufacturing process.

3.5 General mechanical properties of textiles

In general, fabrics possess mechanical properties that are nonlinear, anisotropic, and inelastic. Figures 3.8 (a), (b) and (c) show the typical responses of fabrics under various deformations. From these it can be seen the behaviour of fabrics is complex compared to conventional engineering materials.

Stiffness and strength. Stiffness and strength govern the handling characteristics and the conformability of a fabric, which is critical in medical applications. A low stiffness is generally required. Factors affecting stiffness are fibre shape, modulus, linear density, and specific gravity. Generally, the higher the denier, the higher the stiffness. Monofilament fabrics tend to be stiffer than multifilament; with all factors being the same, the bending stiffness of a monofilament of

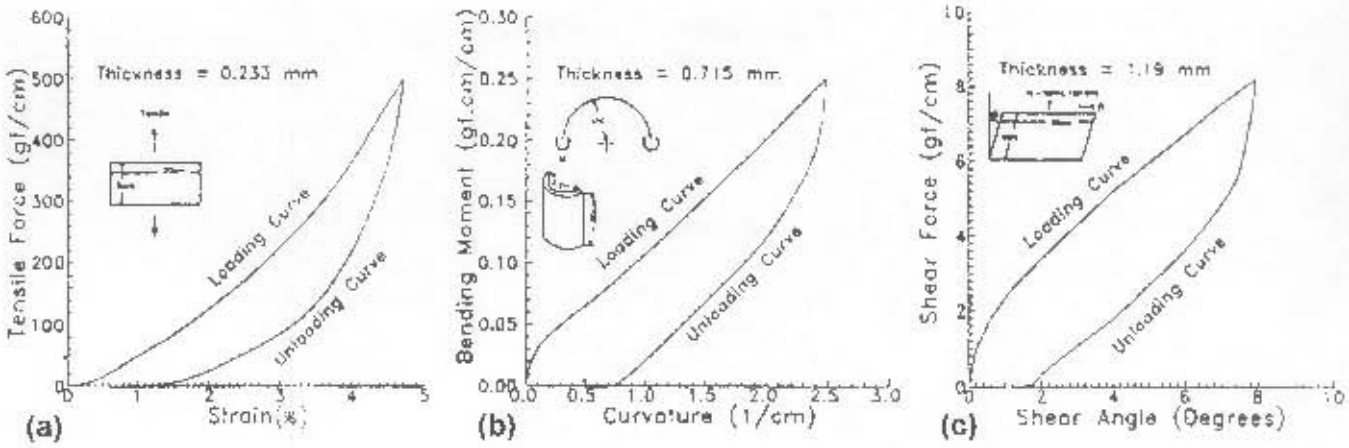

Figure 3.8: Fabric stress-strain curves in: (a) tensile, (b) bending and (c) shear [89]

denier T, will be roughly n times greater than a multifilament with n filaments and denier T/n. The ratio of a yarn's bending stiffness compared to that of a solid rod of the same diameter can be shown to be [89]

$$\alpha(r/R)^2 \ , \tag{3.2}$$

where α is the ratio of summed area of fibres to the yarn's cross-section, R the radius of yarn, and r is the radius of yarn's constituent fibres. This makes it possible to produce thick yarns with a high degree of flexibility. Coupled with the fact that fabrics are very thin, this makes a fabric's bending stiffness much lower and sometimes insignificant compared to its tensile strength. Fabrics generally have a high stiffness in tension, while their shear stiffness is low, and in bending, much lower. For example, a typical fabric in tension is 30 MPa, while in shear, 0.4 MPa and in bending, 0.001 MPa.

Large deformability. Figure 3.8 (a) shows a typical tensile stress-strain curve for a fabric, and shows that large strains are achievable under small loads. This is achieved by the alignment of crimped yarns within the fabric structure. At larger deformations this diminishes when alignment of fibre and yarn is achieved and the stress is taken up in straining the yarns. An initial tensile modulus of a fabric is of the order 10 MPa, which compared to steel (2×10^5 MPa) is orders of magnitude smaller. Fabrics display even greater compliance in bending. Fabrics can under their own weight deform considerably and buckle at very small in-plane compressive stresses. It is this highly deformable nature that gives fabrics the requirements of human body movement and physiological effects.

Nonlinear elastic behaviour. The stress-strain relation of a fabric is highly nonlinear in the low stress region and then becomes linear after a critical point. This critical point varies from fabric to fabric and the various deformation modes, and is dependent on a number of factors: fibre material, the number of fibres in a yarn, yarn density and fabric structure. However, this critical point is generally high in tension and low in bending and shear. This nonlinear behaviour

is also attributed to the porous, crimped and loosely connected construction of fabrics. Under tension, the crimped yarns straighten under small stresses, while at the higher strains, where decrimping is complete, inter-fibre friction increases and the fabric structure becomes orientated. Thus at these higher strains the stress-strain relation becomes almost linear. For bending and shear, when stresses are low, inter-fibre friction causes a high initial resistance, but as the applied stress is increased, this frictional resistance is overcome and yarn slippage occurs which causes a reduction in stiffness [90]. This behaviour is shown in Figures 3.8 (b) and (c).

Inelastic and viscoelastic behaviour. From Figures 3.8 (a), (b) and (c) hysteresis loops occur where, generally, permanent deformation occurs upon unloading. This demonstrates the inelastic nature of the fabric. Conventional engineering materials show plasticity after a plastic limit is reached where yielding occurs and permanent deformation achieved. With fabrics an elastic limit is reached where the kinking of yarns becomes permanent, and this elastic limit can be directly related to the bending stiffness of a fabric's constitutive yarn [89]. Thus, the inelastic and viscoelastic properties of a fabric can easily be reduced by simply utilising fibres with a high elastic content or a low modulus, such as Lycra®. Such materials have been successfully used in the garment industry to provide elastic fabrics which conform to the body and can extend to strains of 200 % without suffering from permanent deformation, examples are cycling shorts and tights.

Chapter 4

Continuum Mechanics

4.1 Introduction

In this chapter a review of those aspects of continuum mechanics that are relevant to the development of a mathematical model for describing the mechanical behaviour of fabrics and grafts is given. For more details on the subject the reader is referred to the works by Lai *et al.* [91], Malvern [92] and Holzapfel [93].

4.2 Kinematics

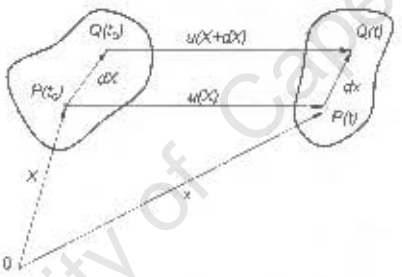

Figure 4.1: Motion of a continuous body

Consider the motion of a continuous body, denoted in Figure 4.1. A material particle initially located at some reference position X will move to a new position x; this may be described by a one-to-one, invertible mapping χ, so that

$$x = \chi(X, t)\,, \tag{4.1}$$

and

$$X = \chi^{-1}(x, t)\,. \tag{4.2}$$

Thus, field quantities such as density and velocity can be given as functions of X and t, known as the material or Lagrangian description, or of x and t, known as the spatial or Eulerian description.

Consider two neighbouring particles P and Q, located at X and $X + dX$ in the reference configuration. The body undergoes a displacement u, so that $x = X + u(X, t)$ for point P and $x + dx = X - dX - u(X + dX, t)$ for point Q. Subtracting these two equations, we obtain

$$dx = dX + (\nabla U)\, dX\,, \tag{4.3}$$

where ∇U is the displacement gradient; that is,

$$(\nabla U)_{ij} = \frac{\partial u_i}{\partial X_j} . \tag{4.4}$$

Alternatively, one has

$$dx = F\, dX \tag{4.5}$$

where $F = \nabla x = I + \nabla U$, I is the identity tensor, and F is the deformation gradient tensor; that is,

$$F_{ij} = \frac{\partial x_i}{\partial X_j} . \tag{4.6}$$

Both F and ∇U characterise local deformation. The deformation gradient F contains information on both rigid body motion and deformation. If F is a proper orthogonal tensor (i.e. $F^T F = I$ and $\det F = +1$) then it corresponds to a rigid body motion only (translation and/or rotation), and no deformation occurs at X.

The Jacobian J, defined by

$$J = \det F > 0 , \tag{4.7}$$

describes the ratio of current to reference volume at a point.

Any real tensor F with a non-zero determinant can be decomposed according to

$$F = RU = VR , \tag{4.8}$$

where U, V and R are unique, U and V are positive definitive symmetric tensors, and R is a proper orthogonal tensor. Equation (4.8) is known as the polar decomposition theorem, where motion is decomposed into pure stretch and rotation; U and V are the right and left stretch tensors which contain information about deformation, and R is the rotation tensor.

From equation (4.8) it follows that:

$$U = R^T V R . \tag{4.9}$$

Also

$$F^T F = (RU)^T (RU) = U^T R^T R U = U^T U , \tag{4.10}$$

so that

$$C = U^2 = F^T F . \tag{4.11}$$

It can also be shown that

$$B = V^2 = F F^T . \tag{4.12}$$

U^2 or C is known as the Right Cauchy-Green deformation tensor and V^2 or B, the Left Cauchy-Green deformation tensor; these are measures of deformation only.

The principal invariants I_1, I_2 and I_3 of a second-order tensor A are given by

$$I_1(A) = \mathrm{tr}(A) \tag{4.13}$$

$$I_2(A) = \frac{1}{2}\left\{(\mathrm{tr}(A))^2 - \mathrm{tr}(A^2)\right\} \tag{4.14}$$

$$I_3(A) = \det A \tag{4.15}$$

If A is symmetric it possesses three real principal values, or eigenvalues $\lambda_1, \lambda_2, \lambda_3$, and

$$I_1(A) = \lambda_1 + \lambda_2 + \lambda_3 \ , \tag{4.16}$$

$$I_2(A) = \lambda_1\lambda_2 + \lambda_2\lambda_3 + \lambda_3\lambda_1 \ , \tag{4.17}$$

$$I_3(A) = \lambda_1\lambda_2\lambda_3 \ . \tag{4.18}$$

Strain is a measure of deformation and is independent of rotation R. Various strain measures exist; for example,

Green Lagrangian strain

$$E = \frac{1}{2}(U^2 - I) \ , \tag{4.19}$$

Eulerian strain

$$e = \frac{1}{2}(I - V^{-2}) \ , \tag{4.20}$$

nominal strain (Biot strain)

$$\epsilon = U - I \ , \tag{4.21}$$

and logarithmic strain

$$\varepsilon = \ln(U) \ . \tag{4.22}$$

The velocity v of a material particle is defined by

$$v = \frac{\partial x}{\partial t} \ . \tag{4.23}$$

The time rate change of a quantity associated with a material particle is known as the material time derivative or material derivative and for a quantity $f(x,t)$ is given by

$$\dot{f} = \frac{Df}{Dt} = \frac{\partial f}{\partial t} + (v \cdot \nabla) f \ . \tag{4.24}$$

The velocity gradient L is defined by

$$L = \nabla v = \frac{\partial v}{\partial x} \ . \tag{4.25}$$

By using the identities $dv = Ldx = LFdX$, as $dx = FdX$, it can be shown that

$$\dot{F} = LF \ . \tag{4.26}$$

L can be decomposed into symmetric and skew-symmetric or antisymmetric parts according to

$$L = \frac{1}{2}(L + L^T) + \frac{1}{2}(L - L^T) \ . \tag{4.27}$$

The rate of deformation D is defined to be the symmetric part of L, and the spin tensor W is the skew-symmetric part; that is,

$$D = \frac{1}{2}(L + L^T) \ , \tag{4.28}$$

$$W = \frac{1}{2}(L - L^T) \ . \tag{4.29}$$

For the Green (Lagrangian) Strain E, we have

$$\dot{E} = \frac{1}{2}\left(F^T\dot{F} + \dot{F}^T F\right) \tag{4.30}$$

or, using (4.26),

$$\dot{E} = \frac{1}{2}\left(F^T L F + F^T L^T F\right) \ . \tag{4.31}$$

Therefore,

$$\dot{E} = F^T D F \ . \tag{4.32}$$

4.3 Stress measures

Consider a continuous body Ω_0 with a plane Γ_0 passing through an arbitrary point Q which has a unit normal vector n_0 in the undeformed state, and in the deformed state Ω, Γ and n, as shown in Figure 4.2.

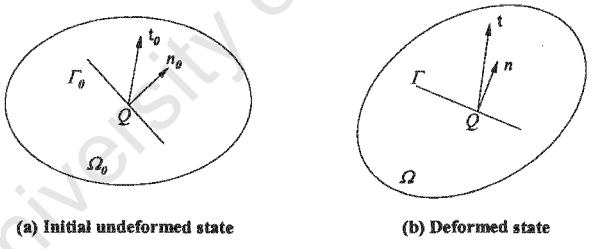

Figure 4.2: Initial undeformed and deformed stress states of a body

Cauchy (true) stress. The Cauchy stress tensor σ at point Q is defined through Cauchy's relation

$$\mathrm{t} = \sigma n \ , \tag{4.33}$$

where t is the traction (force per unit area) in the deformed position acting on the surface Γ with normal n at point Q.

Kirchhoff stress. Another form of stress measure is the Kirchhoff stress τ, defined by

$$\mathrm{t} = \tau n_0 \ . \tag{4.34}$$

The Kirchhoff stress can be thought of as the force per unit area related to the material's undeformed state, and is a useful stress measure in the development of constitutive models for large

elastic strain [94].

First Piola-Kirchhoff (Lagrangian) stress. The first Piola-Kirchhoff stress P is such that

$$t_0 = Pn_0 \,, \tag{4.35}$$

where t_0 is the traction (force per unit area) in the undeformed position.

Second Piola-Kirchhoff stress. The second Piola-Kirchhoff stress S is defined by

$$S = JF^{-1}\sigma F^{-T} = F^{-1}P \,. \tag{4.36}$$

This is commonly used in constitutive models and is a convenient stress measure as it is the conjugate stress (see Section 4.5.4) for the Green (Lagrangian) strain, E, which is readily interpreted physically. It is also useful from a numerical point of view as it is a symmetric tensor and the Green strain is directly computed from the deformation gradient, F. The different stress tensors are related by functions of the deformation; these relations can be obtained by using (4.33) to (4.36) and Nanson's relation [92] which relates the deformed normal n to the undeformed normal n_0 by

$$nd\Gamma = Jn_0 F^{-1} d\Gamma_0 \,. \tag{4.37}$$

The relations between the stress forms are

$$\tau = J\sigma \tag{4.38}$$

and the Piola transformation

$$P = J\sigma F^{-T} = FS \,. \tag{4.39}$$

4.4 Corotational coordinate framework

With deformations involving rotations, it is often difficult to work with a fixed coordinate system. This is especially true when material properties are non-isotropic and are highly dependent on the orientation of the body. Thus, it is often simpler to work with a coordinate system which rotates with the body; such systems are called corotational coordinates. The components of the base vector e in the corotational system are related to the global components by

$$\hat{e}_i = R_{ji}e_j \tag{4.40}$$

where R is the rotation tensor and the superposed "hat" indicates the corotational components. The components of Cauchy stress and the rate of deformation in the corotational system are then given by

$$\hat{\sigma}_{ij} = R_{ki}\sigma_{kl}R_{lj} \tag{4.41}$$

and

$$\hat{D}_{ij} = R_{ki}D_{kl}R_{lj} \,. \tag{4.42}$$

4.5 Conservation equations

The conservation or balance equations relevant to isothermal mechanical behaviour are the conservation of mass, momentum, angular momentum and energy.

In the derivation of the conservation equations we need Gauss's theorem, which states that for a piecewise continuously differentiable function $f(x,t)$,

$$\int_{\Omega} \nabla f \, d\Omega = \int_{\Gamma} n f \, d\Gamma \tag{4.43}$$

where Ω denotes the domain and Γ its surface, with unit outward normal n. This can be used to relate a volume integral to a surface integral as in (4.43), or an area integral to a contour integral.

Reynold's transport theorem. Reynold's transport theorem is also required. Reynold's transport theorem states that the rate of change of an integral over a material volume is equal to the volume integral of the rate of change of a variable $f(x,t)$, keeping the material domain fixed, plus the surface integral of the rate of the variable moving due to surface velocity. This is given by

$$\frac{D}{Dt}\int_{\Omega} f \, d\Omega = \int_{\Omega} \frac{\partial f}{\partial t} \, d\Omega + \int_{\Gamma} f v \, n \, d\Gamma \ , \tag{4.44}$$

where v is the velocity.

4.5.1 Conservation of mass

The mass $m(\Omega)$ of a material domain Ω is given by

$$m(\Omega) = \int_{\Omega} \rho(X,t) \, d\Omega \tag{4.45}$$

where $m(\Omega)$ is a constant greater than zero and $\rho(X,t)$ is the mass density with respect to the current configuration. Mass conservation requires that the mass over a material domain remains constant; thus

$$\frac{Dm}{Dt} = \frac{D}{Dt}\int_{\Omega} \rho \, d\Omega = 0 \, . \tag{4.46}$$

Using Reynolds transport theorem it can be shown that

$$\frac{D\rho}{Dt} + \rho \, \mathrm{div}\, v = 0 \, , \tag{4.47}$$

which is the equation of mass conservation, or the continuity equation.

4.5.2 Conservation of linear momentum

Consider a domain Ω with a boundary Γ, and subjected to body force b and surface traction t, the total force f is given by

$$\mathrm{f}(t) = \int_{\Omega} \rho \mathrm{b}(x,t) \, d\Omega + \int_{\Gamma} \mathrm{t}(x,t) \, d\Gamma \, , \tag{4.48}$$

and linear momentum p is given by

$$\mathrm{p}(t) = \int_{\Omega} \rho v(x,t)\, d\Omega\,, \tag{4.49}$$

where ρv is the linear momentum per unit volume.

The momentum conservation principle for a continuum states that the material time derivative of the linear momentum p equals the net force. This gives

$$\mathrm{f}(t) = \frac{D\mathrm{p}(t)}{Dt} = \frac{D}{Dt}\int_{\Omega} \rho v\, d\Omega\,. \tag{4.50}$$

Using (4.48) we get

$$\frac{D}{Dt}\int_{\Omega} \rho v\, d\Omega = \int_{\Omega} \rho \mathrm{b}\, d\Omega + \int_{\Gamma} \mathrm{t}\, d\Gamma\,. \tag{4.51}$$

Using Reynold's transport theorem, Cauchy's relation and Gauss's theorem it can be shown that

$$\int_{\Omega} \left(\rho\frac{Dv}{Dt} - \nabla\cdot\sigma - \rho\mathrm{b}\right)\, d\Omega = 0\,. \tag{4.52}$$

Since Ω is arbitrary,

$$\rho\frac{Dv}{Dt} = \nabla\cdot\sigma + \rho\mathrm{b} \equiv \mathrm{div}\,\sigma + \rho\mathrm{b}\,. \tag{4.53}$$

This is the equation of conservation of momentum.

In many problems loads are applied slowly and so inertia forces are small and can be neglected. Thus, the acceleration term in (4.53) is neglected giving the equilibrium equation

$$\nabla\cdot\sigma + \rho\mathrm{b} = 0\,. \tag{4.54}$$

4.5.3 Conservation of angular momentum

The balance of angular momentum states that the rate of change of angular momentum must be equal to the total torque applied; that is,

$$\frac{D}{Dt}\int_{\Omega} x\times\rho v\, d\Omega = \int_{\Omega} x\times\rho\mathrm{b}\, d\Omega + \int_{\Gamma} x\times\mathrm{t}\, d\Gamma\,. \tag{4.55}$$

From this it can be shown that the conservation of angular momentum requires that the Cauchy stress be a symmetric tensor; that is,

$$\sigma = \sigma^{T}\,. \tag{4.56}$$

Therefore the Cauchy stress tensor has six distinct independent components in three-dimensional problems.

4.5.4 Conservation of energy

The principle of conservation of energy states that the rate of change of total energy is equal to the rate of work done by the body forces and surface tractions plus the heat energy delivered

to the body. The internal energy per unit volume is denoted by ρw^{int} where w^{int} is the internal energy per unit mass. The heat flux per unit area is denoted by q, and heat source per unit volume is denoted by ρs. Conservation of energy then requires that

$$P^{int} + P^{kinetic} = P^{ext} + P^{heat} \tag{4.57}$$

where

$$P^{int} = \frac{D}{Dt}\int_{\Omega} \rho w^{int}\, d\Omega \tag{4.58}$$

$$P^{kinetic} = \frac{D}{Dt}\int_{\Omega} \frac{1}{2}\rho v \cdot v\, d\Omega \tag{4.59}$$

$$P^{ext} = \int_{\Omega} v \cdot \rho \mathrm{b}\, d\Omega + \int_{\Gamma} v \cdot \mathrm{t}\, d\Gamma \tag{4.60}$$

$$P^{heat} = \int_{\Omega} \rho s\, d\Omega - \int_{\Gamma} n \cdot \mathrm{q}\, d\Gamma \tag{4.61}$$

By using Reynold's theorem, Cauchy's law and Gauss's theorem one can show that

$$\int_{\Omega} \left(\rho \frac{Dw^{int}}{Dt} - D : \sigma + \nabla \cdot \mathrm{q} - \rho s + v \cdot \left(\rho \frac{Dv}{Dt} - \nabla \cdot \sigma - \rho \mathrm{b} \right) \right) d\Omega = 0\,. \tag{4.62}$$

The last term of the integral can be recognised as the momentum equation (4.53), thus, using the fact that Ω is arbitrary, we have

$$\rho \frac{Dw^{int}}{Dt} = D : \sigma - \nabla \cdot \mathrm{q} + \rho s\ , \tag{4.63}$$

which is the equation of energy conservation. In purely mechanical processes the heat flux and heat source terms vanish thus leaving

$$\rho \frac{Dw^{int}}{Dt} = D : \sigma\,. \tag{4.64}$$

It can be seen that the internal power is given by the inner product of the rate of deformation with the Cauchy stress. These are said to be conjugate quantities or work conjugates. Work conjugacy is useful in the development of weak forms of the momentum equations. Other conjugate pairs can be derived from (4.64) [95]; for example, the first Piola-Kirchhoff stress and rate of deformation gradient

$$\rho \frac{Dw^{int}}{Dt} = \dot{F}_{ij} P_{ji}\,, \tag{4.65}$$

and the second Piola-Kirchhoff stress and rate of Green strain

$$\rho \frac{Dw^{int}}{Dt} = \dot{E}_{ij} S_{ij}\,. \tag{4.66}$$

4.6 Frame-invariance, objective rate formulations

The components of Cauchy stress in a fixed coordinate system will change during pure rotation. Thus, to account for the change in stress due to this rotation in a constitutive equation it is necessary to use an objective or frame invariant stress rate. Three invariant rates are presented: the Jaumann rate, the Truesdell rate, and the Green-Naghdi rate.

Jaumann rate. The Jaumann rate of Cauchy stress is given by

$$\sigma_{ij}^{\nabla J} = \frac{D\sigma_{ij}}{Dt} - W_{ik}\sigma_{kj} - \sigma_{ik}W_{jk} \,. \tag{4.67}$$

This can be written in the form

$$\frac{D\sigma_{ij}}{Dt} = \sigma_{ij}^{\nabla J} + (W_{ik}\sigma_{kj} + \sigma_{ik}W_{jk}) \tag{4.68}$$

Thus the material derivative of Cauchy stress consists of two parts: the rate of change due to material response and the change of stress due to rotation. With the objective rate, material rotations are taken into consideration.

Truesdell rate and Green-Naghdi rate. Two other common objective rates are the Truesdell rate and Green-Naghdi rate. These are similar to the Jaumann rate, however they use variations in the measure of rotation; the Truesdell rate uses velocity gradient (L) and the Green-Naghdi rate uses the angular velocity ($\Omega_{ij} = \dot{R}_{ik}R_{jk}$). These are defined as follows:

Truesdell rate:

$$\sigma_{ij}^{\nabla T} = \frac{D\sigma_{ij}}{Dt} + \operatorname{div} v\, \sigma_{ij} - L_{ik}\sigma_{kj} - \sigma_{ik}L_{jk} \tag{4.69}$$

Green-Naghdi rate:

$$\sigma_{ij}^{\nabla G} = \frac{D\sigma_{ij}}{Dt} - \Omega_{ik}\sigma_{kj} - \sigma_{ik}\Omega_{jk} \,. \tag{4.70}$$

4.7 Constitutive equations

4.7.1 Hyperelastic materials

Elastic materials for which a stored energy function exists are said to be hyperelastic. This behaviour is observed in most rubber-like materials. For a hyperelastic material with a stored (strain) energy function $\psi(F)$, the stress is given by

$$P_{ij} = \frac{\partial\psi(F_{ij})}{\partial F_{ij}} \,. \tag{4.71}$$

It can be shown that $\psi = \psi(C)$ and that alternative forms of (4.71) are

$$S_{ij} = 2\frac{\partial\psi(C)}{\partial C_{ij}} = \frac{\partial w(E_{ij})}{\partial E_{ij}} \,. \tag{4.72}$$

When this energy is written as a function of Green strain E, we use the notation w, where the

relation between ψ and w is

$$w(E_{ij}) = \psi(2E_{ij} + I) \,. \tag{4.73}$$

Hyperelastic materials provide a natural framework for frame-invariant formulations of anisotropic material properties by simply embodying this anisotropy in w. With the stored energy formulation it can be seen that the work done on a hyperelastic material is independent of deformation path, since

$$w = \int_{E^{end}}^{E^{int}} S_{ij}\, dE_{ij} = w(E^{end}) - w(E^{int}) \,. \tag{4.74}$$

Isotropic hyperelastic materials. For isotropic hyperelastic materials the stored strain energy depends on the principal invariants I_1, I_2 and I_3 of the right Cauchy-Green deformation tensor, C [92]. Thus, for an isotropic material,

$$\begin{aligned} S_{ij} &= 2\frac{\partial \psi}{\partial C_{ij}} && \text{(4.75a)} \\ &= 2\left(\frac{\partial \psi}{\partial I_1}\frac{\partial I_1}{\partial C_{ij}} + \frac{\partial \psi}{\partial I_2}\frac{\partial I_2}{\partial C_{ij}} + \frac{\partial \psi}{\partial I_3}\frac{\partial I_3}{\partial C_{ij}}\right) && \text{(b)} \\ &= 2\left(\frac{\partial \psi}{\partial I_1} + I_1\frac{\partial \psi}{\partial I_2}\right) I - 2\frac{\partial \psi}{\partial I_2}C_{ij} + 2I_3\frac{\partial \psi}{\partial I_3}C_{ij} \,. && \text{(c)} \end{aligned}$$

From this we can see that S has the same principal axes as C.

Neo-Hookean materials. A special case of isotropic hyperelastic materials is the Neo-Hookean model. The stored energy function for a compressible isotropic Neo-Hookean material is given by

$$\psi(C) = \frac{1}{2}\lambda_0(\ln J)^2 - \mu_0 \ln J + \frac{1}{2}\mu_0\left(\operatorname{tr}(C) - 3\right) \,, \tag{4.76}$$

where λ_0 and μ_0 are the Lamé constants. From equation (4.75a) the stress is given by

$$S_{ij} = \lambda_0 (\ln J) C^{-1}_{ij} + \mu_0\left(I_{ij} - C^{-1}_{ij}\right) \,. \tag{4.77}$$

The tangent modulus K^{SE} can be expressed as

$$4\frac{\partial S_{ij}}{\partial C_{kl}} = K^{SE}_{ijkl} = \lambda_0\left(C^{-1}_{ij}C^{-1}_{kl}\right) + (\mu_0 - \lambda_0 \ln J)\left(C^{-1}_{ik}C^{-1}_{jl} + C^{-1}_{il}C^{-1}_{kj}\right) \,. \tag{4.78}$$

Mooney-Rivlin materials. Rivlin and Saunders [96] developed a hyperelastic material model for the large deformations of rubber. The model is incompressible and isotropic. For an incompressible material $J = \det F = 1$, and therefore, $I_3 = \det C = J^2 = 1$. The strain energy can then be written as a series expansion of I_1 and I_2, in the form

$$\psi = \psi(I_1, I_2) = \sum_{i=0}^{\infty}\sum_{i=0}^{\infty} \bar{c}_{ij}\,(I_1 - 3)^i\,(I_2 - 3)^j \,, \tag{4.79}$$

where $\bar{c}_{ij}$, are constants and $\bar{c}_{00} = 0$. Mooney and Rivlin [97,98] showed that the simple form

$$\psi = \psi(I_1, I_2) = c_1(I_1 - 3) + c_2(I_2 - 3) \tag{4.80}$$

closely matched experimental results.

Other hyperelastic material models. Other hyperelastic strain energy functions range from high order polynomials such as the Swanson model [99], to exponential and logarithmic forms such as the Alexander [100] and Blatz-Ko [101] models. The use of these high order models improves the correlations between experimental and model results for a wide range of rubber-like materials. Their disadvantage is the greater number of coefficients to be fitted to experimental data. Other forms of strain energy functions involve the use of the principal stretch or stretch ratios λ_i, rather than the invariants. One such model is the Ogden model [94], given by

$$\psi = \psi(\bar{\lambda}_1, \bar{\lambda}_2, \bar{\lambda}_3) = \sum_{i=1}^{N} \frac{2\mu_i}{\alpha_i^2}\left(\bar{\lambda}_1^{\alpha_i} + \bar{\lambda}_2^{\alpha_i} + \bar{\lambda}_3^{\alpha_i} - 3\right) + \sum_{i=1}^{N} \frac{1}{D_i}(J_{el} - 1)^{2i}\,, \tag{4.81}$$

where $\bar{\lambda}_i = J^{-\frac{1}{3}}\lambda_i$, J_{el} is the elastic volume strain and D_i, μ_i and α_i are temperature dependent material parameters.

Hyperfoam material models fall into the category of hyperelastic materials. However, they have been developed for foam structures which display high compressibility, so that $J = \lambda_1\lambda_2\lambda_3 \neq 1$. A strain energy function for hyperfoam materials, due to Storåkers [102], is given by

$$\psi = \psi(\bar{\lambda}_1, \bar{\lambda}_2, \bar{\lambda}_3) = \sum_{i=1}^{N} \frac{2\mu_i}{\alpha_i^2}\left[\left(\bar{\lambda}_1^{\alpha_i} + \bar{\lambda}_2^{\alpha_i} + \bar{\lambda}_3^{\alpha_i} - 3\right) + 3\left(J_{el}^{\frac{1}{3}\alpha_i} - 1\right) + \frac{1}{\beta_i}\left(J_{el}^{-\alpha_i\beta_i} - 1\right)\right], \tag{4.82}$$

where β_i are temperature dependent material parameters. If all β_i are equal to a constant value β, one can define the effective Poisson's ratio

$$\upsilon = \frac{\beta}{1 + 2\beta}\,. \tag{4.83}$$

4.7.2 Elasticity tensors

Expressions for fourth order tensors which relate stress rates to relevant strain rates are required in the linearisation of the governing equations. These are known as elasticity tensors, and their form depends on the particular stress and deformation pair used.

First elasticity tensor. The first elasticity tensor $\Psi^{(1)}_{ijkl}$ is obtained by taking the time derivative of the nominal stress N, which is the transpose of the first Piola-Kirchhoff stress P. Since

$$N_{ij} = \frac{\partial w}{\partial F_{ji}}\,, \tag{4.84}$$

we have

$$\dot{N}_{ij} = \frac{\partial N_{ij}}{\partial F_{lk}} \dot{F}_{lk} = \frac{\partial^2 w}{\partial F_{ji} \partial F_{lk}} \dot{F}_{lk} = \Psi^{(1)}_{ijkl} \dot{F}_{lk} \,, \tag{4.85}$$

where

$$\Psi^{(1)}_{ijkl} = \frac{\partial^2 w}{\partial F_{ji} \partial F_{lk}} \,. \tag{4.86}$$

This elasticity tensor has the major symmetry $\Psi^{(1)}_{ijkl} = \Psi^{(1)}_{klij}$, but does not have minor symmetry i.e. $\Psi^{(1)}_{ijkl} \neq \Psi^{(1)}_{jikl}$ and $\Psi^{(1)}_{ijkl} \neq \Psi^{(1)}_{ijlk}$.

Second elasticity tensor. The second elasticity tensor $\Psi^{(2)}_{ijkl}$ is obtained by taking the time derivative of the second Piola-Kirchhoff stress S. Using

$$S_{ij} = \frac{\partial w}{\partial E_{ij}} \,, \tag{4.87}$$

we have

$$\dot{S}_{ij} = \frac{\partial S_{ij}}{\partial E_{kl}} \dot{E}_{kl} = \frac{\partial^2 w}{\partial E_{ij} \partial E_{kl}} \dot{E}_{kl} = \Psi^{(2)}_{ijkl} \dot{E}_{kl} \,, \tag{4.88}$$

so that

$$\Psi^{(2)}_{ijkl} = \frac{\partial^2 w}{\partial E_{ij} \partial E_{kl}} = K^{SE}_{ijkl} \,. \tag{4.89}$$

This elasticity tensor has both major and minor symmetries.

Third elasticity tensor. The third elasticity tensor is obtained from the relationship between the first two elastic tensors. From $N_{ij} = S_{ik} F_{jk}$, the time derivative of the nominal stress N gives

$$\dot{N}_{ij} = \dot{S}_{ik} F_{jk} + S_{ik} \dot{F}_{jk} \,. \tag{4.90}$$

Thus, substituting for $\dot{S}$ from equation (4.88) and using equation (4.30) and the minor symmetry of K^{SE} we obtain

$$\dot{N}_{ij} = \Psi^{(1)}_{ijkl} \dot{F}_{lk} = \left(K^{SE}_{inpk} F_{jn} F_{lp} + S_{ik} \delta_{lj} \right) \dot{F}_{lk} \,. \tag{4.91}$$

The third elasticity tensor is then defined from the push-forward of $\dot{N}$, that is,

$$\begin{aligned} F_{ir} \dot{N}_{rj} &= F_{ir} \left(K^{SE}_{inpk} F_{jn} F_{lp} + S_{ik} \delta_{lj} \right) \dot{F}_{lk} && \text{(4.92a)} \\ &= \left(F_{im} F_{jn} F_{kp} F_{lq} K^{SE}_{mnpq} + F_{im} F_{kn} S_{mn} \delta_{lj} \right) L_{lk} && \text{(b)} \\ &= \Psi^{(3)}_{ijkl} L_{lk} \,. && \text{(c)} \end{aligned}$$

Thus

$$\Psi^{(3)}_{ijkl} = F_{im} F_{jn} F_{kp} F_{lq} K^{SE}_{mnpq} + F_{im} F_{kn} S_{mn} \delta_{lj} \,. \tag{4.93}$$

Fourth elasticity tensor. This is given by the first term in equation (4.93), that is

$$\Psi^{(4)}_{ijkl} = F_{im}F_{jn}F_{kp}F_{lq}K^{SE}_{mnpq} \tag{4.94a}$$
$$= F_{im}F_{jn}F_{kp}F_{lq}\Psi^{(2)}_{ijkl}\,. \tag{b}$$

It should be noted here that the second part of the third elasticity tensor is the Kirchhoff stress, so that

$$\Psi^{(3)}_{ijkl} = \Psi^{(4)}_{ijkl} + \tau_{ik}\delta_{lj}\,. \tag{4.95}$$

The minor symmetry of $\Psi^{(4)}_{ijkl}$ allows us to write

$$\Psi^{(3)}_{ijkl}L_{lk} = \Psi^{(4)}_{ijkl}D_{kl} + \tau_{ik}\delta_{lj}L_{lk}\,. \tag{4.96}$$

The fourth elasticity tensor $\Psi^{(4)}_{ijkl}$ in equation (4.96) is the material tangent stiffness and the term involving $\tau_{ik}\delta_{lj}$ is the geometric stiffness. In the linearisation of the updated Lagrangian discretisation, the relation between the convected rate of the Kirchhoff stress and the rate of deformation is useful, where the convected rate of Kirchhoff stress (or Lie derivative of Kirchhoff stress) is given by

$$\ell_v\tau_{ij} = F_{ik}\dot{S}_{kl}F_{jl} \tag{4.97a}$$
$$= \tau^{\nabla c}\,. \tag{b}$$

Using this and the relation $\dot{E}_{ij} = F_{ki}D_{kl}F_{lj}$, we have

$$\ell_v\tau_{ij} = K^{\tau}_{ijkl}D_{kl}\,, \tag{4.98}$$

where

$$K^{\tau}_{ijkl} = F_{im}F_{jn}F_{kp}F_{lq}K^{SE}_{mnpq} = \Psi^{(4)}_{ijkl}\,. \tag{4.99}$$

Thus, in terms of the Truesdell rate of Cauchy stress we have

$$\sigma^{\nabla T}_{ij} = J^{-1}\tau^{\nabla c}_{ij} \tag{4.100a}$$
$$= J^{-1}F_{im}F_{jn}F_{kp}F_{lq}K^{SE}_{mnpq} \tag{b}$$
$$= J^{-1}\Psi^{(4)}_{ijkl} \tag{c}$$
$$= J^{-1}K^{\tau}_{ijkl}\,, \tag{d}$$

The elasticity tensors play an important role in stability and uniqueness of solutions in finite strain elasticity.

4.7.3 Relations between tangent moduli

In this section we show how the same constitutive can be written in terms of the various tangent moduli. Using equations (4.67) and (4.69), we have

$$\sigma^{\nabla T}_{ij} = K^{\sigma J}D - D\sigma - \sigma D^T + \mathrm{tr}\,(D)\,\sigma \tag{4.101a}$$
$$= (K^{\sigma J} - K' + \sigma\otimes I)D \tag{b}$$
$$= K^{\sigma T}D\,, \tag{c}$$

where

$$K'D = D\sigma + \sigma D \ . \tag{4.102}$$

Thus, the relation between the elasticity tensors is

$$\begin{aligned} K^{\sigma T} &= K^{\sigma J} - K' + \sigma \otimes I & \text{(4.103a)} \\ &= K^{\sigma J} - K^* \ , & \text{(b)} \end{aligned}$$

where

$$K^* = K' - \sigma \otimes I \ , \tag{4.104}$$

or

$$K^*_{ijkl} = \frac{1}{2}\left(\delta_{ik}\sigma_{jl} + \delta_{il}\sigma_{jk} + \delta_{jk}\sigma_{il} + \delta_{jl}\sigma_{ik}\right) - \sigma_{ij}\delta_{kl} \ . \tag{4.105}$$

We see that if $K^{\sigma J}$ is constant, the tangent moduli $K^{\sigma T}$ is not constant. K' also has major symmetry, while K^* does not, as $\sigma_{ij}\delta_{kl} \neq \delta_{ij}\sigma_{kl}$.

The relation between Truesdell and Green-Naghdi rate moduli is obtained from the Green-Naghdi rate of Cauchy stress; thus,

$$\begin{aligned} \sigma^{\nabla T} &= \sigma^{\nabla T} - (L - \Omega)\sigma - \sigma(L - \Omega)^T + \mathrm{tr}(D)\sigma & \text{(4.106a)} \\ &= K^{\sigma G}{:}D - (L - \Omega)\sigma - \sigma(L - \Omega)^T + \mathrm{tr}(D)\sigma & \text{(b)} \\ &= K^{\sigma G}{:}D - D\sigma - \sigma D - (W - \Omega)\sigma - \sigma(W - \Omega)^T + \mathrm{tr}(D)\sigma \ , & \text{(c)} \end{aligned}$$

where $\Omega = \dot{R}R^T$ is the angular velocity tensor. Through a complex derivation [103] we can show that

$$K^{\sigma T} = K^{\sigma G} - K^* - K^{spin} \ , \tag{4.107}$$

where K^{spin} is a function of the left stretch tensor V and the Cauchy stress, and is defined by

$$K^{spin}{:}D = (W - \Omega)\sigma + \sigma(W - \Omega)^T \ . \tag{4.108}$$

4.7.4 Incompressibility

In an incompressible material the volume remains constant. Therefore,

$$\det F = J = 1 \ , \tag{4.109}$$

and

$$\mathrm{div}\, v = 0 \tag{4.110}$$

since $\dot{J} = 0$ and $\dot{J} = J\mathrm{div}\, v$.

The stress and strain measures may be formulated in terms of the deviatoric and hydrostatic (volumetric) parts, according to

$$\sigma = \sigma^{dev} + \sigma^{hyd} \text{ where: } \sigma^{hyd} = \frac{1}{3}\mathrm{tr}(\sigma)I \tag{4.111}$$

$$S = S^{dev} + S^{hyd} \text{ where: } S^{hyd} = \frac{1}{3}(S{:}C)C^{-1} \tag{4.112}$$

and

$$D = D^{dev} + D^{vol} \text{ where: } D^{vol} = \frac{1}{3}\text{tr}(D)I \tag{4.113}$$

$$\dot{E} = \dot{E}^{dev} + \dot{E}^{vol} \text{ where: } \dot{E}^{vol} = \frac{1}{3}(\dot{E}{:}C^{-1})C \tag{4.114}$$

The deviatoric and hydrostatic/volumetric parts of a tensor are orthogonal, that is, $\sigma^{hyd}{:}D^{dev} = \sigma^{dev}{:}D^{vol} = 0$, and $S^{hyd}{:}\dot{E}^{dev} = S^{dev}{:}\dot{E}^{vol} = 0$. the power can thus be split into deviatoric and hydrostatic parts: that is,

$$\rho\dot{w} = \sigma{:}D = \sigma^{dev}{:}D^{dev} + \sigma^{hyd}{:}D^{vol}\,, \tag{4.115}$$

$$\rho\dot{w} = S{:}\dot{E} = S^{dev}{:}\dot{E}^{dev} + S^{hyd}{:}\dot{E}^{vol}\,. \tag{4.116}$$

A multiplicative decomposition is used to separate the volumetric part of the deformation, according to

$$F = F^{vol}F^{dev}, \tag{4.117}$$

where $F^{vol} = J^{\frac{1}{3}}I$ and $F^{dev} = J^{-\frac{1}{3}}F$. The determinant of the deviatoric part of the deformation gradient is unity, i.e. $\det(F^{dev}) = 1$; therefore, any function of F^{dev} is independent of the volumetric deformation.

4.8 Mathematical modelling of soft tissue

Numerous researchers have focused on the development of constitutive relations to describe the behaviour of soft tissue, including blood vessels [12, 26, 32, 104]. Their models are expressed in terms of strain energy functions. Three forms of strain energy functions have primarily been used to describe the behaviour of blood vessels: exponential, polynomial and logarithmic.

Fung *et al.* [32] proposed the exponential strain energy function

$$w(E) = \frac{C}{2}\exp(a_1E_{\theta\theta}^2 + a_2E_{zz}^2 + 2a_4E_{\theta\theta}E_{zz})\,. \tag{4.118}$$

Vaishnav *et al.* [104] have proposed the polynomial function,

$$w(E) = a_1E_{\theta\theta}^2 + a_2E_{zz}^2 + a_4E_{\theta\theta}E_{zz}\,, \tag{4.119}$$

and Takamizawa and Hayashi [12] the logarithmic function,

$$w(E) = -C\ln(1 - \frac{1}{2}a_1E_{\theta\theta}^2 - \frac{1}{2}a_2E_{zz}^2 - a_3E_{\theta z}^2)\,. \tag{4.120}$$

In (4.118) to (4.120), θ and z are the circumferential and axial coordinates in a cylindrical system and C, a_1, a_2, a_3 and a_4 are material coefficients which are determined experimentally.

Figure 4.3 shows the influence of increasing a_1 on the stress-strain relation in the θ direction. In a similar manner a_2 describes the stress-strain behaviour in the z direction, while a_3 describes the shear relation and a_4 the transverse coupling.

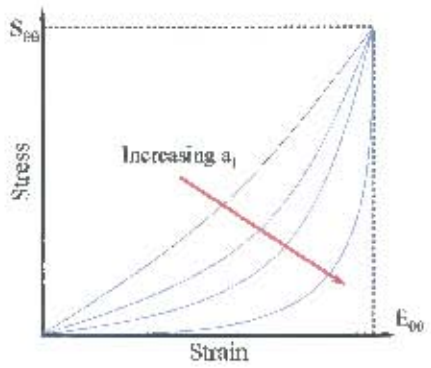

Figure 4.3: Effect of increasing coefficient a_1 on the stress-strain relation

4.9 The mathematical modelling of polymers (rubbers & foams)

Substantial work has been done in the development of constitutive relations for rubber-like elastic polymers (Ogden [95], Mooney-Rivlin [97, 98] and Treloar [105]). Mathematically the material behaviour of polymers is commonly referred to as hyperelastic or hyperfoam behaviour (see Section 4.7.1). Various relations have been proposed since the 1940s in the form of a strain energy potential U and formulated in terms of strain invariants, I_1, I_2 and I_3. The simplest of these is the Neo-Hookean model (equation (4.76)) proposed by Treloar in 1943 [105] and defined in terms of a single parameter. Mooney and Rivlin [97, 98] provided a strain energy function (equation (4.79)) in terms of two parameters and showed that results compared well with experimental data for uniaxial deformation modes. Ogden [95] proposed a strain energy function in terms of principal stretch ratios λ_i rather than strain invariants (equation (4.81)), and a number of coefficients dependent on the order of the function . This function can be reduced in special cases to form the Neo-Hookean and Mooney-Rivlin models. Hyperelastic materials describe generally incompressible materials, while hyperfoam models describe compressible polymers.

4.10 The mathematical modelling of fabrics

The study of fabric mechanics dates back to the first work done by Hass [106] in 1917 on the development of fabrics for airships. However, the first real model for fabric forces was presented by Perice [107] who simplified the structure of a woven fabric as ideal rods. His work has led the way for theories on the geometrical and mechanical behaviour of fabrics.

Much work has been done in forming mathematical relations for modelling the tensile deformation of fabrics: for example, Kageyama and Kawabata [108], Hu and Newton [109], Hearle [110], Grosberg *et al.* [111] and Alsawaf [112]. Kageyama and Kawabata [108] looked at a linearisation method in two zones to describe the tensile behaviour of fabrics. The predicted stress-strain relation presented by Hearle *et al.* [113] was based on strain energy principles, solving two systems of equations (geometric and mechanical) with physical yarn properties. Grosberg and associates presented a function which displayed an initially high modulus, yet lit-

erature does not confirm this. Alsawaf [112] characterised the tensile behaviour of fabrics into two straight segments, one with an initially low modulus where decrimping occurred and another with a higher modulus representing yarn extension which occurred after a critical point. Figure 4.4 shows the variation in tensile stress-strain behaviour for each proposed model.

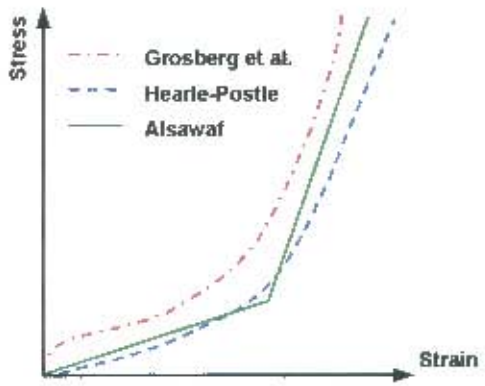

Figure 4.4: Proposed fabric tensile stress-strain relations [109]

Polynomial functions have also been used to describe nonlinear stress-strain tensile behaviour of fabrics [114]. However, the use of high degree polynomials for function fitting has given rise to polynomial "wiggling" [115], where a number of maxima and minima are observed. Due to this, alternate functions have been proposed, such as exponential and logarithmic functions, which do not suffer from polynomial "wiggling". Hu and Newton [109] established a number of exponential constitutive equations for woven fabrics under tension, of the form:

$$\sigma = \frac{e^{\alpha\varepsilon} - 1}{\beta}, \sigma = e^{\alpha\varepsilon} - 1 \text{ and } \sigma = \alpha\varepsilon^{\beta}. \tag{4.121}$$

These exponential expressions used one or two parameters to describe fabric behaviour. The resulting solutions compared well with experimental data. However, only simple tensile tests were modelled; thus these models only represent a specific deformation state. They also use two separate sets of parameters for the warp and weft directions, and hence do not include coupling effects between the fabric warp and weft behaviour. Since the early 1980s advancement in this field has slowed due to the complex nature of the mathematical expressions needed to describe fabric behaviour.

Work by Bias-Singh *et al.* [116, 117] looked at modelling the non-uniform deformation of spun-bound fabrics under uniaxial and biaxial tension, where a bilinear relation similar to that proposed by Alsawaf [112] is utilised, and which shows good comparisons with experimental data.

Other researchers such as Collier *et al.* [118], Kim [119], Gan *et al.* [120], Yu *et al.* [121] and Kang *et al.* [122] used an orthotropic linear elastic material models to analyse drape tests [123]. Collier *et al.* and Kim showed good correlations to experimental data, while Kim gave quantitative comparisons where predictions varied by 10%. However, drape tests exhibit small strains

and large deflection deformation which is not ideal for the large strain tensile deformation modes needed.

Due to the complexity of the problem these models have taken specific deformation modes into consideration and have ignored others. Thus, much work still needs to be done before an accurate and reliable model is developed to model all the deformation modes [89].

4.11 Proposed constitutive relation for coarse knit fabrics

Large strain constitutive relations are needed when modelling coarse knit fabrics under tension. Since the nonlinear stress-strain characteristics of fabrics and soft tissue are similar, it is proposed that Fung's model (equation (4.118)) be adapted and used to describe the general tensile behaviour of coarse knit fabrics.

Since a fabric's thickness is considerably small in comparison to its other dimensions it can be considered a membrane, and subject to plane stress conditions. By including shear and presenting the model in a general two-dimensional form, and increasing the order and the number of coefficients used to describe the fabric behaviour, the following strain energy function is obtained

$$\begin{aligned} w(E) &= \frac{C}{2}\exp[a_1(E_{11}^2) + a_2(E_{22}^2) + a_3(E_{12}^2 + E_{21}^2) + a_4(E_{11}E_{22}) - a_5(E_{11}^3) + a_6(E_{22}^3) \\ &\quad -a_7(E_{12}^3 + E_{21}^3) + a_8(E_{11}^3E_{22}) - a_9(E_{11}E_{22}^3)] \end{aligned} \tag{4.122}$$

Since the knitted fabrics are highly compressible, incompressibility will not be enforced.

Chapter 5

The Finite Element Method

5.1 Introduction

As structures become increasingly complex, not only in design but also in material use, pure analytical methods begin to fail in describing their behaviour. Essentially, analytical methods are rendered impossible. Thus, computer aided mathematical techniques have been developed to obtain approximate numerical solutions to these complex systems. One such numerical tool developed over the past 50 years is the finite element method (FEM).

A brief description of the finite element method and the underlying mathematics is described in this chapter. For more detailed texts on the subject one may consult Cook *et al.* [124], Burnett [125], Crisfield [126] and Belytschko *et al.* [127], for example.

5.2 The finite element method

Problems in solid mechanics generally take the form of systems of partial differential equations defined in terms of the spatial coordinates and time, as seen in Chapter 4. The finite element method is useful for solving such partial differential equations in cases involving complex geometry, boundary conditions, nonlinear behaviour, and contact.

The key feature of the finite element method is that of discretisation (Figures 5.1 and 5.2). The domain is partitioned into smaller regions of simple shapes. These are known as finite elements, and designated points in the elements are called nodes. A finite element solution is approximated inside the elements by interpolation functions or shape functions which are normally polynomial in form. Usually continuity of the field variables is enforced across neighbouring elements.

Figure 5.1: Discretisation of a solid into elements and nodes

Interpolation or shape functions are used to represent the field variables such as displacement and stress. The order of the interpolation functions is linked to the number of nodes in the

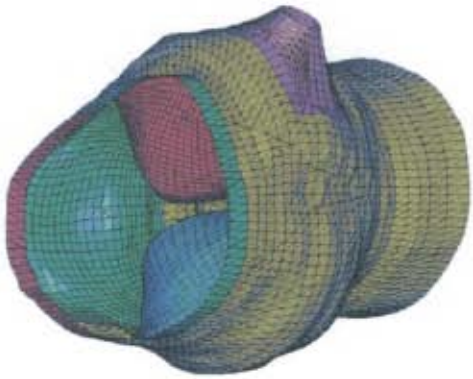

Figure 5.2: Discretised aortic heart valve (coloured elements represent different regions)

element. Accuracy of the solution normally increases with an increase in the order of the interpolation function. Figure 5.3 demonstrates how an exact solution or continuous field may be approximated by a piecewise linear interpolation over three elements, in the space dimension.

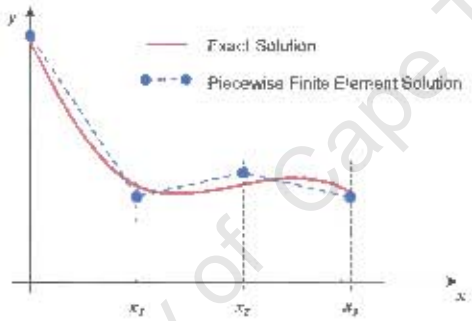

Figure 5.3: Finite element piecewise approximation for an exact solution

5.2.1 Spatial discretisation; Lagrangian and Eulerian meshes

Lagrangian meshes, are where the elements and nodes move with the material. Finite element discretisation using these meshes can be classified as updated and total Lagrangian formulations. The updated Lagrangian formulation involves derivatives and integrals taken with respect to the Eulerian coordinates x, while the total Lagrangian formulation is formulated with respect to the Lagrangian coordinates X. The development of both formulations are similar, and expressions in either formulation can be transformed to the other using transformations and mappings. Eulerian meshes on the other hand do not deform with the material; thus, Eulerian elements retain their shape.

The development of the Eulerian and updated Lagrangian formulations uses the principle of virtual power, while the development of the total Lagrangian formulation uses the principle of virtual work. These are termed weak forms as the differential requirements of the variables are reduced or weakened. We shall only consider finite element discretisations using updated Lagrangian meshes.

5.2.2 Governing equations

The governing equations for the mechanical behaviour of a continuous body are the conservation of mass, momentum (linear and angular) and energy, a measure of strain (strain-displacement equation) and the material constitutive equation. These have been considered in Chapter 4.

In Lagrangian meshes the conservation of mass (4.46) is used in its integrated form

$$\rho(X,t)J(X,t) = \rho_0(X)J_0(X) = \rho_0(X) \ . \tag{5.1}$$

A material's constitutive equation when it is expressed in rate form in terms of a rate of Cauchy stress, requires a frame-invariant rate such as the Jaumann and Truesdell rate. It is however, not necessary for the constitutive equation to be expressed in terms of Cauchy stress or its frame-invariant rate in the updated Lagrangian formulation. For example, a constitutive relation can be expressed in terms of the second Piola-Kirchhoff stress S and then transformed into Cauchy stress. The strain-displacement equation, or the measure of strain or strain rate used depends on the constitutive equation. Common strain-displacement equations used are Green strain (4.19), and the rate of deformation (4.28). We shall assume that the constitutive equation is in a frame-invariant rate form and is a function of the rate of deformation D and Cauchy stress σ.

Other governing conditions include the boundary and initial conditions. The boundary conditions for the tractions and velocities are described by

$$\sigma n = \bar{t} \ \text{ on } \ \Gamma_t \,, \tag{5.2}$$

$$v = \bar{v} \ \text{ on } \ \Gamma_v \,, \tag{5.3}$$

where

$$\Gamma_t \cap \Gamma_v = \phi \ \text{ and } \ \Gamma_t \cup \Gamma_v = \Gamma \,. \tag{5.4}$$

Prescribed values are designated by a superposed bar, and Γ_t and Γ_v are the traction and velocity boundaries. It should be noted that displacement can also be considered as it is the time integral of velocity.

The initial conditions are given as

$$v(X,0) = v_0(X) \ \text{ and } \ \sigma(X,0) = \sigma_0(X) \ . \tag{5.5}$$

Another consideration is the traction continuity condition, which requires that

$$\lceil \sigma n \rceil = 0 \ \text{ on } \ \Gamma_{\text{int}} \,, \tag{5.6}$$

where $\lceil \sigma n \rceil$ designates the jump in σn, i.e. $\lceil f(X) \rceil = \lim [f(X+\varepsilon) - f(X-\varepsilon)]$ as $\varepsilon \to 0$, and Γ_{int} is the union of all the surfaces on which the stresses are discontinuous in the body.

In the discretisation and the enforcing of the above equations and conditions the continuity of the dependent variables must be considered. A function f is C^n continuous if the n^{th} derivative is a continuous function. Thus for a C^1 function the first derivative exists and is continuous, while a C^0 function is continuous, however, its derivative is not.

5.2.3 Principle of virtual power

In this section the weak form of the momentum equation (4.52) is developed. From (4.52) the dependent variables are the velocity $v(X,t)$ and stress $\sigma(X,t)$. The trial functions $v_i(X,t)$ and test functions $\delta v_i(X)$ are such that

$$v_i(X,t) \in \Im, \quad \Im = \left\{ v_i \mid v_i \in C^0(X), \quad v_i = \bar{v}_i \text{ on } \Gamma_{v_i} \right\} , \tag{5.7}$$

$$\delta v_i(X) \in \Im_0, \quad \Im_0 = \left\{ \delta v_i \mid \delta v_i \in C^0(X), \quad \delta v_i = 0 \text{ on } \Gamma_{v_i} \right\} . \tag{5.8}$$

It should be noted that displacement $u_i(X,t)$ can also be considered as the trial function as it is the time integral of the velocity.

Integrating the product of a test function δv_i and (4.52) over the current configuration gives

$$\int_\Omega \delta v_i \left(\frac{\partial \sigma_{ji}}{\partial x_j} + \rho \mathrm{b}_i - \rho \dot{v}_i \right) d\Omega = 0 . \tag{5.9}$$

Using the product rule, Gauss's theorem, and the traction continuity and boundary conditions it can be shown that

$$\int_\Omega \delta v_i \frac{\partial \sigma_{ji}}{\partial x_j} = \int_{\Gamma_{t_i}} \delta v_i \bar{\mathrm{t}}_i \, d\Gamma - \int_\Omega \frac{\partial (\delta v_i)}{\partial x_j} \sigma_{ji} \, d\Omega . \tag{5.10}$$

Substituting this into (5.9) gives the weak form of the momentum equation, the traction boundary conditions and the traction continuity conditions in the form

$$\int_\Omega \frac{\partial (\delta v_i)}{\partial x_j} \sigma_{ji} \, d\Omega - \int_{\Gamma_{t_i}} \delta v_i \bar{\mathrm{t}}_i \, d\Gamma - \int_\Omega \delta v_i \rho \mathrm{b}_i - \int_\Omega \delta v_i \rho \dot{v}_i \, d\Omega = 0 . \tag{5.11}$$

The first term in (5.11) can be manipulated using (4.27)-(4.29) and (4.55), to give

$$\int_\Omega \frac{\partial (\delta v_i)}{\partial x_j} \sigma_{ji} \, d\Omega = \int_\Omega \delta L_{ij} \sigma_{ji} \, d\Omega = \int_\Omega (\delta D_{ij} + \delta W_{ij}) \sigma_{ji} \, d\Omega = \int_\Omega D_{ij} \sigma_{ji} \, d\Omega = \int_\Omega \delta D_{ij} \sigma_{ij} \, d\Omega . \tag{5.12}$$

Thus (5.11) can be rewritten and physically interpreted in the form

$$\delta P^{int} - \delta P^{ext} + \delta P^{kinetic} = 0 \tag{5.13}$$

where

$$\delta P^{int} = \int_\Omega \frac{\partial (\delta v_i)}{\partial x_j} \sigma_{ij} \, d\Omega = \int_\Omega \delta D_{ij} \sigma_{ij} \, d\Omega , \tag{5.14}$$

$$\delta P^{ext} = \int_\Omega \delta v \cdot \rho \mathrm{b} \, d\Omega + \int_{\Gamma_{t_i}} \delta v_i \bar{\mathrm{t}}_i \, d\Gamma , \tag{5.15}$$

$$\delta P^{kin} = \int_\Omega \delta v \cdot \rho \dot{v} \, d\Omega , \tag{5.16}$$

and δP^{int}, δP^{ext}, δP^{kin} are the virtual internal power, virtual external power and the virtual kinetic power, respectively.

5.2.4 The updated Lagrangian finite element discretisation

Assume a domain Ω is subdivided into elements Ω_e. Let the nodal coordinates in the current configuration be denoted by x_I, where the uppercase subscript denotes the nodes i.e. $I = 1$ to n_N, and n_N is the number of nodes in an element. The motion x is approximated by

$$x = \sum_{I=1}^{n_N} N_I(X) x_I(t) \ , \tag{5.17}$$

where $N_I(X)$ are the global interpolation or shape functions, and $x_I(t)$ is the position vector of node I at time t. The nodal displacements u are defined as

$$u_I(t) = x_I(t) - X_I \ . \tag{5.18}$$

Thus the displacement field is

$$u(X,t) = \sum_{I=1}^{n_N} u_I(t) N_I(X) \ . \tag{5.19}$$

The velocities and accelerations are obtained from the material time derivatives of the displacements where

$$\dot{u}(X,t) = v(X,t) = \sum_{I=1}^{n_N} \dot{u}_I(t) N_I(X) \ , \tag{5.20}$$

$$\ddot{u}(X,t) = \ddot{u}_I(t) N_I(X) = \sum_{I=1}^{n_N} \dot{v}_I(t) N_I(X) \ . \tag{5.21}$$

The velocity gradient is obtained from (5.20) and (4.25), where

$$L = \sum_{I=1}^{n_N} v_I \nabla N_I \ . \tag{5.22}$$

The rate of deformation D is then the symmetric part of L.

The test function is not a function of time; thus we can approximate the test function as

$$\delta v(X) = \delta v_I N_I(X) \ , \tag{5.23}$$

where δv_I are the virtual nodal velocities. This is then substituted into (5.13) giving

$$\delta P^{int} = \delta v_{iI} \int_\Omega \frac{\partial N_I}{\partial x_j} \sigma_{ji} \, d\Omega \ , \tag{5.24}$$

$$\delta P^{ext} = \delta v_{iI} \int_\Omega N_I \rho \mathrm{b}_i \, d\Omega + \delta v_{iI} \int_{\Gamma_{\mathrm{t}_i}} N_I \bar{\mathrm{t}}_i \, d\Gamma \ , \tag{5.25}$$

and

$$\delta P^{kinetic} = \delta v_{iI} \int_\Omega N_I \rho \dot{v}_i \, d\Omega \ . \tag{5.26}$$

The stresses in (5.24)-(5.26) are functions of the trial velocities and displacements and $\delta v_i = 0$

on Γ_{v_i}. From (5.24) the internal nodal forces are given by

$$\mathrm{f}_{iI}^{int} = \int_{\Omega} \frac{\partial N_I}{\partial x_j} \sigma_{ji} \, d\Omega \ . \tag{5.27}$$

These are internal as they represent the stresses in the body. The external nodal forces are obtained from (5.25) and are given by

$$\mathrm{f}_{iI}^{ext} = \int_{\Omega} N_I \rho \mathrm{b}_i \, d\Omega + \int_{\Gamma_{\mathrm{t}_i}} N_I \bar{\mathrm{t}}_i \, d\Gamma \ . \tag{5.28}$$

The inertial nodal forces are obtained from (5.26) and are

$$\mathrm{f}_{iI}^{kinetic} = \int_{\Omega} N_I \rho \dot{v}_i \, d\Omega \ . \tag{5.29}$$

Using (5.21) for acceleration and substituting it into the above gives

$$\mathrm{f}_{iI}^{kinetic} = \int_{\Omega} \rho N_I N_J \, d\Omega \, \dot{v}_{iJ} \ . \tag{5.30}$$

These inertial nodal forces are usually defined as a product of a mass matrix and nodal accelerations, i.e.

$$\mathrm{f}_{iI}^{kinetic} = M_{ijIJ} \, \dot{v}_{jJ} \ , \tag{5.31}$$

where the mass matrix is defined as

$$M_{ijIJ} = \delta_{ij} \int_{\Omega} \rho N_I N_J \, d\Omega \ . \tag{5.32}$$

Thus the discrete approximation to (5.13) can be re-written as

$$\delta v^T (\mathrm{f}^{int} - \mathrm{f}^{ext} + Ma) = 0 \ , \tag{5.33}$$

where δv, a, f^{int} and f^{ext} are column matrices of the unconstrained virtual velocities, accelerations and nodal forces, and M is the mass matrix of the unconstrained degrees of freedom. Thus,

$$\mathrm{f}^{int} - \mathrm{f}^{ext} + Ma = 0 \quad \text{or} \quad \mathrm{f} = Ma \tag{5.34}$$

where $\mathrm{f} = \mathrm{f}^{ext} - \mathrm{f}^{int}$. (5.34) are the discrete momentum equations or the equations of motion, and are a system of $n_{d.o.f}$ ordinary differential equations in time, where $n_{d.o.f}$ is the number of degrees of freedom. These are often termed semidiscrete, as they have been discretised in space but not in time.

5.2.5 Isoparametric element formulations

Instead of defining global shape functions for an element Ω_e, it is convenient to define local shape functions on a reference element, or isoparametric element $\hat{\Omega}_e$. The element coordinates are then mapped or transformed to the reference element using a transformation function. This allows for the use of simple interpolation functions on the reference element to describe the internal field. Isoparametric elements are particularly useful as they make it possible to generate elements that

are non-rectangular and have curved surfaces. They also offer computational advantages when performing numerical integration (see Section 5.2.6). The term "Isoparametric" means same-parameters, and comes from using the same transformation function to interpolate between nodal values for both the coordinates and field variables. The transformation maps an element in one space, xyz to another, $\xi\eta\zeta$, and is represented by

$$x(\xi) = \sum_{I=1}^{n_N} x_I(t)\hat{N}_I(\xi)\,, \tag{5.35}$$

where x represents either coordinates or a field variable and $\hat{N}_I(\xi)$ the reference interpolation function at node I. In one space dimension the reference element is defined on the domain $-1 \leqslant \xi \leqslant 1$, and there is a one to one or unique transformation from the reference space to the actual space. The Isoparametric transformation is illustrated in Figure 5.4 for a four node plane element which is mapped onto an arbitrary quadrilateral shape.

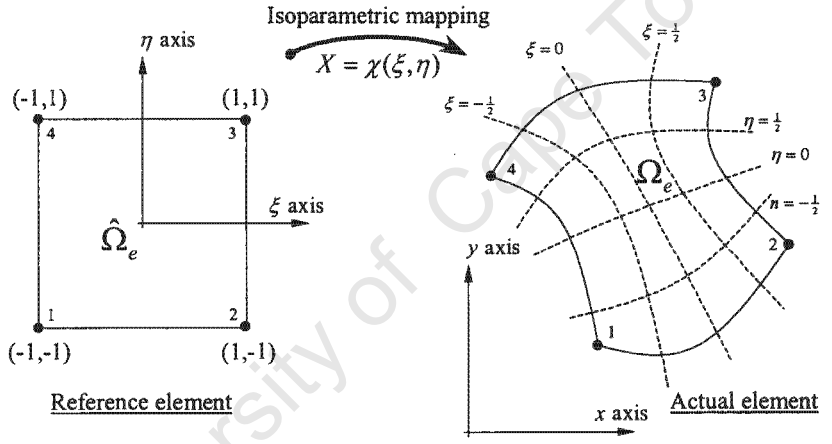

Figure 5.4: Isoparametric mapping for a four node plane element.

The interpolation function $\hat{N}_I$ is a continuous function, and is defined to be equal to one at node I and zero at all other nodes; that is,

$$\hat{N}_I(\xi_J) = \delta_{IJ} = \left\{ \begin{array}{l} 1 \text{ if } I = J \\ 0 \text{ otherwise} \end{array} \right\}\,, \tag{5.36}$$

where ξ_J is the set of coordinates of node J on the reference element. The reference shape function $\hat{N}_1(\xi,\eta)$ is illustrated in Figure 5.5 for a four node linear isoparametric quadrilateral.

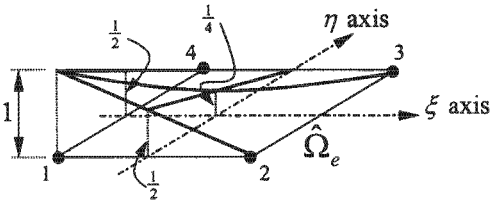

$$\hat{N}_I = \tfrac{1}{4}(1+\xi_I\xi)(1+\eta_I\eta)$$

Figure 5.5: Shape function $\hat{N}_1(\xi,\eta)$ for a four node linear isoparametric quadrilateral.

The derivative of the mapping is called the Jacobian matrix J, and is given by

$$J_{ij} = \frac{\partial x_i(\xi)}{\partial \xi_j} = x_{,\xi}(\xi) \ . \tag{5.37}$$

Given the mapping between $\hat{\Omega}_e$ and Ω_e, the chain rule and the Jacobian it is possible to evaluate the interpolation functions and their derivatives on $\hat{\Omega}_e$ where for the two dimensional case

$$\begin{Bmatrix} \frac{\partial \hat{N}_I}{\partial \xi} \\ \frac{\partial \hat{N}_I}{\partial \eta} \end{Bmatrix} = \begin{bmatrix} \frac{\partial x}{\partial \xi} & \frac{\partial y}{\partial \xi} \\ \frac{\partial x}{\partial \eta} & \frac{\partial y}{\partial \eta} \end{bmatrix} \begin{Bmatrix} \frac{\partial N_I}{\partial x} \\ \frac{\partial N_I}{\partial y} \end{Bmatrix} = J \begin{Bmatrix} \frac{\partial N_I}{\partial x} \\ \frac{\partial N_I}{\partial y} \end{Bmatrix} \ . \tag{5.38}$$

To find the derivatives of N_I, (5.38) can be inverted

$$\begin{bmatrix} \frac{\partial N_I}{\partial x} \\ \frac{\partial N_I}{\partial x} \end{bmatrix} = J^{-1} \begin{Bmatrix} \frac{\partial \hat{N}_I}{\partial \xi} \\ \frac{\partial \hat{N}_I}{\partial \eta} \end{Bmatrix} = \frac{1}{\det J} \begin{bmatrix} \frac{\partial y}{\partial \eta} & -\frac{\partial y}{\partial \xi} \\ -\frac{\partial x}{\partial \eta} & \frac{\partial x}{\partial \xi} \end{bmatrix} \begin{Bmatrix} \frac{\partial N_I}{\partial x} \\ \frac{\partial N_I}{\partial y} \end{Bmatrix} \ . \tag{5.39}$$

The determinant of the Jacobian matrix must be positive over the isoparametric element, that is

$$\det J > 0 \ . \tag{5.40}$$

5.2.6 Numerical integration (quadrature)

Integration on elements is done using numerical integration, or quadrature. There are many quadrature methods such as Simpson's and Gauss' rules [115, 128]. The integral of a function $\phi(\xi)$ on the interval $-1 \leqslant \xi \leqslant 1$ is approximated by evaluating the function at set sampling points ξ_i, more commonly referred to as Gauss points with appropriate weightings w_i, where

$$I = \int_{-1}^{1} \phi(\xi)\, d\xi \cong \sum_{i=1}^{n} w_i \phi(\xi_i) \ . \tag{5.41}$$

The number of Gauss points n, is determined by the rule that n Gauss points will integrate exactly a polynomial of degree $(2n-1)$. Figure 5.6 illustrates the Gauss rule for $n = 1$ and 2.

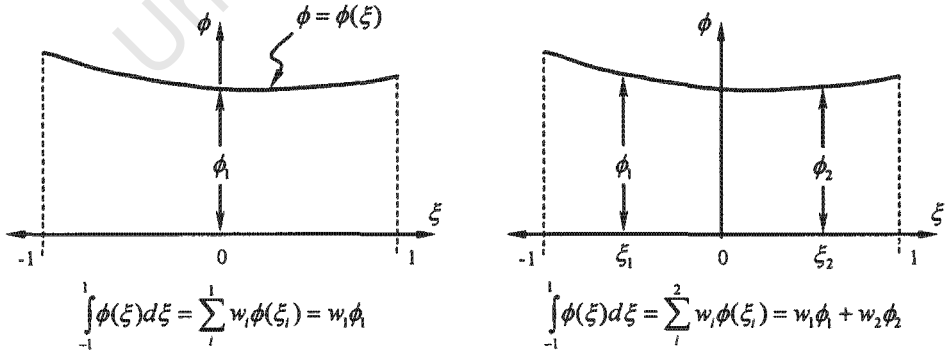

Figure 5.6: Gauss quadrature to compute area under curve ϕ using one and two Gauss points

The number of sampling points is determined by the order of integration, which is dependent on the order of the function being integrated. If the order of integration is less than required to provide the exact integral of all terms used, then this is referred to as "reduced integration".

Because of isoparametric mapping, it is convenient to carry out integration on the reference element. The Gauss rule for three dimensions is given by

$$I = \int_{-1}^{1}\int_{-1}^{1}\int_{-1}^{1} \phi(\xi,\eta,\zeta)\, d\xi d\eta d\zeta \cong \sum_{i=1}^{n_i}\sum_{j=1}^{n_j}\sum_{k=1}^{n_k} w_i w_j w_k \phi\left(\xi_i,\eta_j,\zeta_k\right) \quad . \tag{5.42}$$

5.2.7 Time discretisation

Let the time domain of a simulation be subdivided into $n\triangle t$ increments or time steps, where n is the number of time steps and $\triangle t$ is the size of the time step. Discretising (5.34) in time gives

$$Ma^n + \mathrm{f}^{int}(d^n, t^n) = \mathrm{f}^{ext}(d^n, t^n) \ , \tag{5.43}$$

where the superscript n denotes the time step and d^n is the displacement at time step t^n. In order to step from time t^n to time t^{n+1}, a numerical time integration method is required. This can either be implicit or explicit.

Implicit time integration. Implicit time integration has the form:

$$d^{n+1} = f(\ddot{d}^{n+1}, \dot{d}^{n+1}, \ddot{d}^{n}, \dot{d}^{n}, d^{n}, ...) \, . \tag{5.44}$$

Thus the calculation of d^{n+1} requires the time derivatives $\ddot{d}^{n+1}$ and $\dot{d}^{n+1}$ which are unknown. Most implicit methods are unconditionally stable, thus they have no restriction on time step size, unless required for accuracy. A common unconditionally stable implicit method is the Trapezoidal rule or average acceleration method. This relates displacements, velocities and accelerations according to

$$d^{n+1} = d^n + \frac{\triangle t}{2}(\dot{d}^n + \dot{d}^{n+1}) \ , \tag{5.45}$$

and

$$\dot{d}^{n+1} = \dot{d}^n + \frac{\triangle t}{2}(\ddot{d}^n + \ddot{d}^{n+1}) \, . \tag{5.46}$$

Equations (5.45) and (5.46) are obtained from a Taylor series expansion of d^{n+1} about time t^n and d^n about time t^{n+1}. Equations (5.45) and (5.46) can then be used to solve for $\ddot{d}^{n+1}$ and $\dot{d}^{n+1}$ in terms of $\ddot{d}^n$, $\dot{d}^n$, d^n and d^{n+1}. These are then substituted into the discretised equation of motion (5.43) at time t^{n+1} to form a set of simultaneous equations which are then solved by iterative methods to obtain d^{n+1}.

Explicit time integration. Explicit time integration has the form:

$$d^{n+1} = f(\ddot{d}^n, \dot{d}^n, d^n, \ddot{d}^{n-1}, ...) \, . \tag{5.47}$$

The main advantage of explicit time integration is that it only requires information from previous time steps to evaluate d^{n+1}. This makes this methods computationally faster and easier to work with. A common explicit method used is the central difference, this approximates the velocity

and acceleration by

$$\dot{d}^n = \frac{1}{2\,(\triangle t)}(d^{n+1} - d^{n-1}) \ , \tag{5.48}$$

and

$$\ddot{d}^n = \frac{1}{(\triangle t)^2}(d^{n+1} - 2d^n + d^{n-1}) \ . \tag{5.49}$$

Equations (5.48) and (5.49) are obtained from a Taylor series expansion of d^{n+1} and d^{n-1} about time t^n. These can then be used directly into the discretised equation of motion (5.43), at time t^n to form a set of equations where d^{n+1} is unknown. The central difference method is second-order accurate and thus any error is proportional to $\triangle t^2$. Compared to implicit methods, explicit methods are easy to implement and are computationally attractive as it is not necessary to solve a set of simultaneous equations. The draw back with explicit methods is that they are conditionally stable and require that the time step not exceed a critical value $\triangle t_{\text{crit}}$, i.e.

$$\triangle t \leq \triangle t_{\text{crit}} = \frac{2}{\omega_{\max}} \ , \tag{5.50}$$

where $\omega_{\max}$ is the maximum frequency of the linearised system (see Section 5.2.9). This can be a disadvantage when modelling long time periods.

5.2.8 Static and dynamic problems

When accelerations are neglected the system is said to be in equilibrium, thus from (5.43)

$$\mathrm{f}^{int}(d^{n+1}, t^{n+1}) = \mathrm{f}^{ext}(d^{n+1}, t^{n+1}) \ . \tag{5.51}$$

Equilibrium problems described by (5.51) are called static problems. In static problems, time t does not need to be real time when the material constitutive equations are rate-independent. Problems in which the accelerations are not negligible are termed dynamic.

5.2.9 Nonlinear iterative methods

The discretised nonlinear equations of motion require iterative procedures in order to be solved. Writing (5.43) at time step $n+1$ such that

$$0 = r(d^{n+1}, t^{n+1}) = Ma^{n+1} + \mathrm{f}^{int}(d^{n+1}, t^{n+1}) - \mathrm{f}^{ext}(d^{n+1}, t^{n+1}) \tag{5.52}$$

where the column matrix $r(d^{n+1}, t^{n+1})$ is called the residual, we require to solve (5.52) such that $r(d^{n+1}, t^{n+1}) = 0$.

Newton's or Newton-Raphson Method is commonly utilised to solve this system of nonlinear equations. This is an iterative procedure to find a better approximation to d^{n+1} such that $r(d^{n+1}, t^{n+1}) = 0$. Using the subscript φ to indicate the iteration number so that d_φ^{n+1} is the displacement in iteration φ and time step $n+1$. This is done by using a Taylor expansion of the residual about $d_\varphi^{n+1}$and ignoring the higher order terms such that

$$0 = r(d_{\varphi+1}^{n+1}, t^{n+1}) = r(d_\varphi^{n+1}, t^{n+1}) + \frac{\partial r(d_\varphi^{n+1}, t^{n+1})}{\partial d_\varphi}\triangle d \, , \tag{5.53}$$

where $\triangle d = d_{\varphi+1}^{n+1} - d_{\varphi}^{n+1}$. Equation (5.53) is the linearised model of the nonlinear equations. The matrix $\frac{\partial r(d_{\varphi}^{n+1}, t^{n+1})}{\partial d_{\varphi}}$ is called the system Jacobian matrix or tangent stiffness modulus. Figure 5.7 shows the linearisation and iterative procedure using Newton's method for a single degree of freedom system.

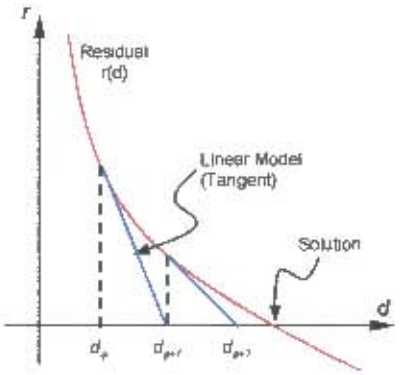

Figure 5.7: Newton-Raphson method for nonlinear iterative procedures

Nonlinear iterative methods also include the Modified Newton-Raphson and the Quasi Newton's method. The Newton-Raphson method described above recalculates the tangent stiffness modulus at each iteration as shown in Figure 5.7. The Modified Newton-Raphson method calculates the tangent stiffness modulus at the start and subsequently uses this in the following iterations, thus the tangent stiffness modulus is not updated at each iteration. The Quasi Newton's method starts an increment by iterating twice using the Modified Newton-Raphson method, it then forms a secant through these two iteration residual solutions to obtain a solution to a third iteration. Successive iteration solutions are then obtained by forming secants through the previous two iteration residual solutions.

With large systems of nonlinear equations the time for a particular method to converge on a solution becomes important. It has been found that the Newton's method has a better convergence rate for highly nonlinear problems [94].

Chapter 6

Optimisation and Genetic Algorithms

6.1 Introduction

Optimisation techniques refer to those methods directed toward finding the parameters of a problem which maximise or minimise a certain function, such as weight, strength and dimension. These techniques require a measure of grading the effectiveness of a solution to a problem; this is commonly in the form of a mathematical expression known as a fitness function. This mathematical model takes the form of a parametric description and gives a measure of the effectiveness of the solution based on the parameters.

Traditional optimisation techniques, known as hill climbing techniques, require relations between the variables and the quantity to be optimised. If these relations are linear then these problems can be solved directly. However, iterative searches have to be used to find the solutions where they are nonlinear. One such iterative scheme is nonlinear regression. However, these nonlinear traditional hill climbing techniques have been found to be problematic when three or more nonlinearly-related variables are solved for, or when the relations between the variables cannot be explicitly defined [127]. This has led to new methods of optimisation such as genetic algorithms (GA), which do not require explicit differential relations between the variables. Instead they require a single objective function which describes whether a set of parameters is converging to an optimal solution. This therefore makes GA a powerful and useful optimisation tool where relations between the variables cannot be defined.

The chapter starts by briefly reviewing traditional optimisation techniques, this is followed by a review of the GA method, implementation, theory and constraints. The chapter ends by comparing traditional methods with GAs. Details of the GAs used in this work and their implementation with the finite element approximation are given in Chapter 9.

6.2 Traditional optimisation techniques

The analogy of a blind man climbing a mountain is useful when explaining traditional optimisation methods. By feeling the gradient of his surroundings, he takes a step in the direction of the steepest slope. If he continues in this manner he shall reach a point where he can no longer proceed, thus reaching a point where all around him the slope tends downward. This point could be considered by the blind man as the top of the mountain.

In a similar manner traditional optimisation or hill climbing techniques start at a single point

and use local information (local gradients) to look for the best direction in which to move (i.e. they take a step at a time). Having taken a step in a particular direction, new local information is collected and the process continued until a maximum is found. Thus these methods require derivatives of all the variables in order to be used. They are also path dependent and rely on a good starting position.

Probably the most famous of all the traditional optimisation techniques is Newton's method, which starts off at a position and then utilises the gradient and a linear-extrapolation to find its next solution and continues until a desired minimum/maximum is obtained. Other methods include those of Runga-Katta and Gauss [128]. A major problem with these techniques is stability. Some hill climbing techniques do not converge upon a solution, instead they bounce back and forth. More advanced methods such as the Levenburg and Marquard method [126], have tried to circumvent these problems by adjusting their step size or distance of travel taken along their path by relating this to the slope of the surface.

6.3 Genetic algorithms

6.3.1 Introduction

Genetic algorithms were invented by Holland in the 1960s with the aim of formally using adaptation as it occurs in nature and applying it to computer systems [129]. A GA is a method of moving from one population of chromosomes (a string of genes, or bits) to a new population by using a kind of natural selection, or selection, together with genetic operators such as crossover, mutate and inversion. Each gene has a particular allele (one or zero). Selection is the process of deciding which of the chromosomes in a population are to be used to produce a new generation. This is usually decided by ranking the population of chromosomes according to a fitness function and choosing the best candidates. Crossover is where a new chromosome is created by exchanging subparts of two chromosomes, similar to biological recombination. Mutations are spurious changes to the allele values of genes in a chromosome, and inversion reverses the order of a gene subset in a chromosome. As can be seen from the terminology, GAs are based on genetics and the principles of reproduction, hence biological terms such as generation, population, chromosome, crossover and mutation are used.

When used in optimisation, a GA manipulates a population of chromosomes using the genetic operators to produce a new generation with the intent of generating chromosomes which produce better solutions, based on previous generations. The members, or chromosomes of a population act as a memory for the GA, and selection is used to bias new generations toward optimal solutions. An objective function $\phi(x)$ defines whether a solution obtained from a generation member is effective, while a penalty function $p(x)$ defines whether a generation member violates any constraints that may be imposed in the problem. The fitness function $f(x)$ is generally a function of the penalty and objective functions, i.e. $f(x) = f(p(x), \phi(x))$. The value obtained from the

fitness function, or fitness value provides a measure of the solution's performance, where the closer the solution gets to the desired outcome without violating any constraints, the greater the fitness value. Many methods of terminating GAs have been proposed [130, 131]; however, two methods are preferred: 1) when a predetermined number of generations is reached or 2) when no improvement is seen over a certain number of iterations.

6.3.2 Implementation of a simple genetic algorithm

The principal data object of a GA is the chromosome. This is a binary encoding of a set of parameters. For example, a problem may depend on three parameters for which an optimal solution is desired. Each parameter will be encoded into a binary number and placed together in sequence to form a single binary encoded chromosome, which represents a population member and contains all the parameters. Consider the following parameters, 6, 5 and 9; in 4-bit binary form these numbers are represented as follows: 0110, 0101 and 1001. Placing them together in sequence gives 011001011001 which is the chromosome representing the parameter group 6, 5 and 9 in 4-bit binary form. These chromosomes are then operated on by either the crossover, mutation or inversion operators to produce new population members.

For example, assume that one would like to maximise the real-valued function $f(x, y, z) = \sin x - \cos 2y - \cos z$. One could then encode candidate solutions of x, y and z as bit strings or chromosomes, similar to that described above. The fitness value for a particular chromosome can be obtained by translating the chromosome into real numbers x, y and z and evaluating the function $f(x, y, z)$ at this point. For example, using the chromosome 011001011001 which represents the parameter group 6, 5 and 9, and assuming that these are ordered; i.e. $x = 6$, $y = 5$ and $z = 9$, one can substitute these into $f(x, y, z)$ and yield a fitness value of 1.471.

Using the method of encoding and decoding the parameters in a chromosomes, as well as the genetic operators, one can now formulate a simple GA to maximise the function $f(x, y, z)$. Figure 6.1 shows a flow chart for this.

6.3.3 The Schema Theorem and how genetic algorithms work

Although GAs are simple to describe and program, their behaviour can be complicated. Many questions still exist about how they work and for what types of problems they are best suited [129]. Much work has been done on the theoretical foundations of GAs [132–134], the basis of which was formulated by Holland [132], where GAs work by discovering, emphasising and recombining good building blocks, or schema (schemata) of solutions in a highly parallel fashion.

A schema is a set of bit strings whose template can be described by ones, zeros and asterisks, where the asterisks represent wild cards. For example, the schema $H = 1 * * * 1$ represents the set of all 5-bit strings that begin and end with one. Instances are those strings which fit this schema, for example 10101 and 11001. The order of a schema is the number of defined bits (non-asterisks), thus H is of order 2. The defining length of a schema is the distance between the outermost defined bits, which is four for H. It should be noted that not all possible subsets of a

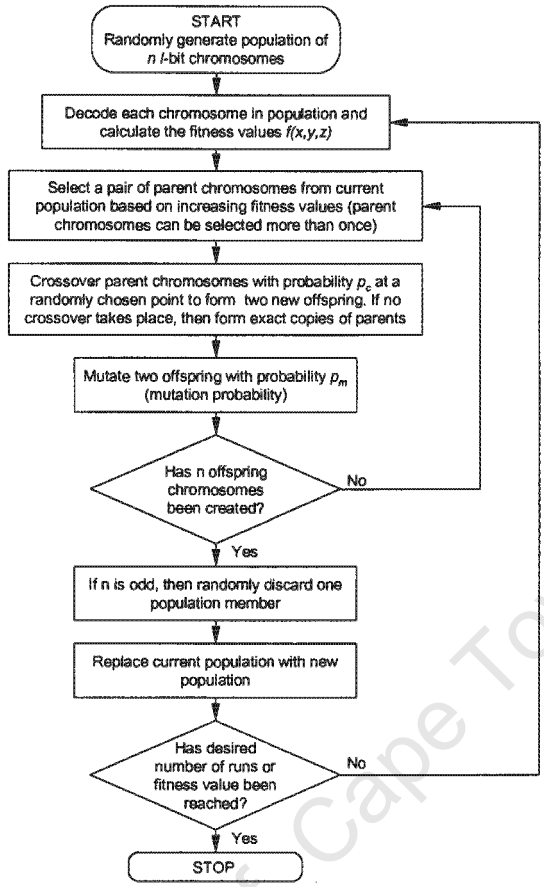

Figure 6.1: Flow chart of genetic algorithm for maximising $f(x, y, z)$

set of l-length bit strings can be described as schemata. There are 2^l possible bit strings of length l, and thus 2^{2^l} possible subsets of strings, but there are only 3^l possible schemas.

Any given length l bit string is an instance of 2^l difference schema, thus, any given population of n strings (chromosomes) contains instances of between 2^l and $n \times 2^l$ different schemas. This means that, at a given generation, while explicitly evaluating the fitness of n strings in the population, it is implicitly estimating the average fitness of a much larger number of schemas, where the average fitness of a schema is the average fitness of all possible instances of that schema.

The approximate increase or decrease of these good schema instances from generation to generation is described as follows. Let H be a schema with at least one instance present in the population at time t. Let $m(H, t)$ be the number of instances of H at time t, and let $\hat{u}(H, t)$ be the observed average fitness of instances of H in the population at time t. We want to calculate $E(m(H, t + 1))$, the expected number of instances of H at time $t + 1$. Through selection, the expected number of offspring of a string x is equal to $f(x)/\bar{f}(t)$, where $f(x)$ is the fitness of x and $\bar{f}(t)$ is the average fitness of the population at time t. Assuming that x is in the population at time t, and $x \in H$ (an instance of H) and ignoring crossover and mutation, we have

$$E(m(H,t+1)) = \sum_{x \in H} \frac{f(x)}{\bar{f}(x)} \tag{6.1a}$$

$$= \frac{\hat{u}(H,t) \times m(H,t)}{\bar{f}(x)} \ . \tag{b}$$

Crossover and mutation can both create and destroy instances of H. Looking at the destructive effects of these operators and including them in (6.1a) will give a lower bound on $E(m(H,t+1))$.

Let p_c be the probability that crossover will be applied to a string, and suppose an instance of H is selected to be a parent. The lower bound on the probability $S_c(H)$ that H will survive crossover can be given by

$$S_c(H) \geq 1 - p_c(\frac{d(H)}{l-1}) \ , \tag{6.2}$$

where $d(H)$ is the defining length of H, and l is the length of bit strings in the search space.

Let p_m be the probability of any bit being mutated, then $S_m(H)$; the probability that schema H will survive under mutation of an instance H, is

$$S_m(H) = (1 - p_m)^{o(H)} \ , \tag{6.3}$$

where $o(H)$ is the order of H. Including these in (6.1a) gives

$$E(m(H,t+1)) \geq \frac{\hat{u}(H,t) \times m(H,t)}{\bar{f}(x)} \left(1 - p_c \left[\frac{d(H)}{l-1}\right]\right) \left[(1-p_m)^{o(H)}\right] \ . \tag{6.4}$$

This is known as the schema theorem [134, 135], and it describes the growth of a schema, or building blocks from one generation to the next. Equation (6.4) is a lower bound, as it only deals with the destructive effects of the crossover and mutation operators.

In evaluating a population of n strings the GA implicitly estimates the average fitness of all the schemas that are present in the population, and increases or decreases their representation according to (6.4). This and the effect of selection is to gradually bias future generations toward instances of good schemas.

6.3.4 Constraints and feasibility in genetic algorithms

GAs are widely used for unconstrained optimisation problems. However, many engineering problems are highly constrained and nonlinear, which results in a complex search space with regions of feasibility and infeasibility [137–142].

Constraints can be classified into two categories, viz. explicit and implicit. Explicit constraints are those which can be checked without finding a solution. An example is the value of a design variable which has a maximum value constraint. Implicit constraints are those that can only be checked once a solution is found. An example of this would be where the result of the solution affects a parameter.

Many approaches have been proposed to check for constraints in GAs, but none has shown to be superior [142]. The most efficient and direct method of handling constraints is to embed them in the coding of the individual members, which is possible with explicit constraints. However, when this approach is not possible, penalty functions can be used to describe the feasibility of a solution, by penalising those members which violate the constraints, thus excluding them further or giving them a low ranking. In this way penalty functions create an unconstrained problem [140].

The exclusion of infeasible solutions has been found to be very effective in specialised problems [140, 141, 143]. If the number of infeasible solutions is small compared to the generation size, then discarding them is a good idea. If this number is large then the algorithm may waste time looking for solutions that are not feasible. Another problem with eliminating solutions could mean possible generations are lost where members violate constraints by small amounts. Thus, penalties which are too harsh may cause those members which do not violate the constraints to quickly dominate future generations and limit the ability of the algorithm to search for the optimal solution. Similarly, if the penalties are too lenient then infeasible solutions could flourish [138,140]. Richardson *et al.* [140] tried several different approaches to assigning penalty functions, using the derivatives of the problem function to give an indication of how far a feasible solution is from the constraint boundary. But this meant derivatives would need to be formulated which is not always possible. He suggested that approximations could be used where derivative functions were not possible.

Powell and Skolnick [144] proposed a method that can cope with linear and nonlinear constraints. Feasible solutions are mapped into an interval from 1 to ∞ and the infeasible solutions from 1 to $-\infty$. If a constraint is violated then the infeasible solution is given a value of 1 minus the solution's deviation from the constraint boundary.

A difficulty with GAs in applying penalty functions is that they tend to be problem dependent. Skalak *et al.* [145], however, presented a method of applying penalty functions which are problem independent. A variable penalty function is used which is related to the length of time the algorithm has run, where the penalty is initially very lenient and becomes progressively harsher as the algorithm runs. They show that convergence to the global optimal solution is guaranteed. This method helps to "bridge" across isolated clusters of feasible solutions initially. They also use a "Russian roulette" method of eliminating population members [138,146] where a weighted coin is tossed for each member of the population to decide if it is eliminated. This is done starting at the bottom of the rank-ordered population list and continues until the population size is reduced, so that those members at the top of the rank-ordered population list are favoured.

6.3.5 Genetic algorithms vs. traditional approach to optimisation

Consider an example of an objective function $\phi(x, y)$ defined by a surface S, whose value we wish to maximise (Figure 6.2).

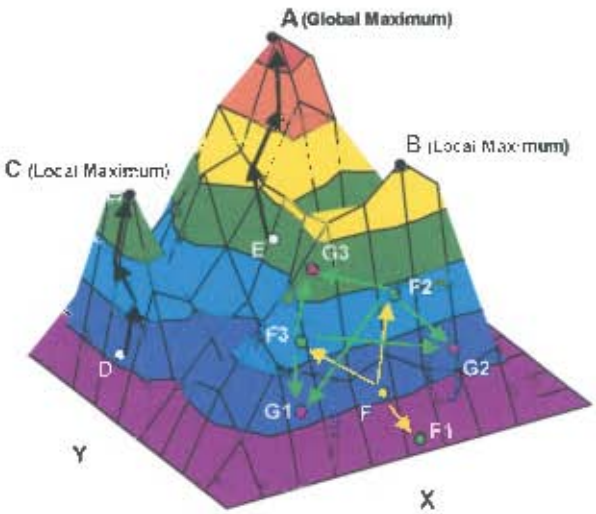

Figure 6.2: Surface S of objective function ϕ illustrating traditional and genetic algorithm methods

The global maximum is denoted by point A, and local maxima by points B and C (point A is also considered a local maximum).

As stated earlier, traditional hill climbing methods rely heavily on their starting point; a bad starting point could lead to a local maximum. For example, if point D is chosen as the starting point, the local solution of C will be found by the optimisation algorithm. However, if a starting point E is chosen the global maximum is found by the optimisation algorithm.

GAs work in a different way and are not path dependent. The only criterion for starting is that the function should be a solution to the problem (it is on the surface S). The GA forms several offspring (population) which are similar in form. These offspring are then tested and ranked according to the objective value $\phi(x, y)$ obtained. From this ranked population a number of the good members are paired (crossover) to form a new generation and the process is continued until a global solution is found. For example, if a starting point F is chosen (refer to Figure 6.2), and a generation formed, where three members incorporate a generation (F_1, F_2 and F_3), then from the two best members of the generation found, i.e. F_2 and F_3, a new generation is formed (G_1, G_2 and G_3). This process is repeated until the global solution is found.

Table 6.1 summarises some of the differences between GAs and traditional optimisation methods [147].

	Genetic algorithm	Traditional optimisation methods
Variables	Work with a coded set of variables	Work with the variables
Searching Method	A population of solutions	A single solution
Possibility of being trapped	Low	High
Type of information	Objective function information	Gradient information
Types of rules	Probabilistic transition rules	Deterministic rules

Table 6.1: Differences between GAs and other optimisation methods

6.3.6 The benefits of genetic algorithms

The distributed evolutionary approach means that GAs are unlikely to become trapped at a local maximum. Since GAs do not need derivative information, the relations between the variables and the objective function are not required. A GA is not path dependent and therefore does not rely on its initial starting point. GAs are able to work in domains that are discontinuous, ill-defined, or which have many local maxima.

GAs are particularly suited to searching large, complicated and unpredictable search spaces. The parallel nature (ability of GA to search a number of solutions at one time) is also an advantage. Another advantage of GAs over traditional methods is their ability to maximise their search space capabilities by introducing mutations into certain generations.

Although the GA seems robust, it does have the drawback of being computationally expensive in that it generally takes longer to converge on a solution. However, its advantages as a general purpose optimisation tool capable of solving many variables that are multidimensional, discontinuous and nonlinear, far outweigh its drawback of computational expense. Thus, a GA has potential in nonlinear problems having a large number of variables, where the problem is not well-defined and difficult to describe by way of differential relations.

Chapter 7

Compliance Testing

7.1 Introduction

In this chapter we describe the various methods and techniques used by researchers to measure compliance. We then describe the two methods used in the work to measure compliance. Subsequently, we look at the manufacture, preparation and structure of the composite graft samples for testing, and present the results of a comparative study on the compliance testing methods used.

7.2 Compliance testing of grafts and natural vessels

As described in Chapter 2, two forms of compliance are defined: diameter compliance (C_d) and volume compliance (C_v), where $C_v \approx 2C_d$, assuming there is no change in vessel length and that second order changes in diameter are negligible (refer to Appendix G). Henceforth we use diameter compliance (C_d) only, and thus compliance will imply diameter compliance, unless otherwise mentioned.

7.2.1 Measuring compliance in vitro

A number of methods have been used to simulate in vivo (physiological) blood pressure and flow conditions [66, 67, 148–152]. The difficulty with in vitro testing is the need to be able to create specific pressure and flow characteristics, depending on the position of the vessel in the body (refer to Figure 2.3). Further complexity is added when considering the testing of natural vessels in vitro, where tissue degradation (desiccation) due to the lack of oxygen and nourishment supplied by the blood, causes changes in the vessel's mechanical properties. Thus, depending on the complexity and the functionality of the equipment, vessels may need to be tested soon after removal from the body (< 2 hrs). Some equipment can cater for this, by the use of culture media or by circulating blood with oxygenators and carbon dioxide (CO_2) scrubbers [67, 149]. Invariably in vitro equipment can simulate either flow or pressure characteristics, but not both. Pressure and flow waves are always correlated; however, the pressure waveform of a system is produced by the imposed flow rate and the elasticity (compliance) of the system, including the graft sample. Consequently the reproduction of both physiological pressure and flow under simulation conditions is impossible [148].

Thus, the requirements of an in vitro compliance rig need to be tailored specifically to the desired application. An ideal in vitro compliance rig would cater for the following:

- full range, adjustable pressure wave characteristics mimicking those observed in vasculature

- full range, adjustable flow wave characteristics for shear forces and variation in flow characteristics in vasculature
- oxygenation, CO_2 scrubbers, blood and/or cultivation media for extended testing of natural tissue/blood vessels and/or the testing of a graft's self healing capabilities
- real time flow, pressure, diameter, volume and longitudinal displacement readings at proximal, central and distal positions of test sample
- ability to cater for the testing of porous grafts, either through natural clotting with blood or with a luminal liner
- physiological temperature control
- graft attachment; fixed strain vs. free moving vs. constant axial load
- compliant vs. noncompliant proximal and distal anastomotic graft attachment.

Figure 7.1 highlights the variables that are relevant in the design of an in vitro compliance test rig.

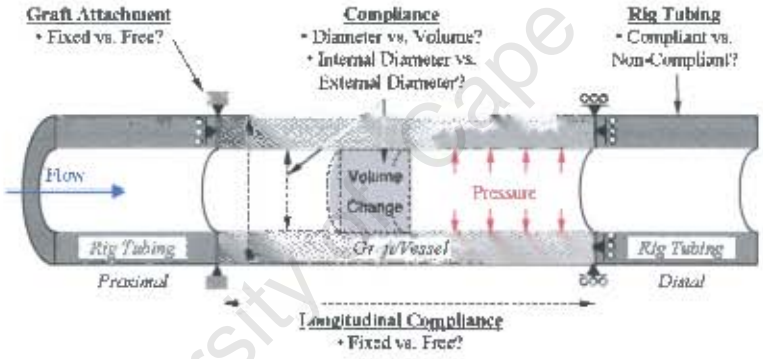

Figure 7.1: Schematic of sectioned graft showing relevant design parameters

7.2.1.1 Reproduction of physiological pressure and flow

A number of methods have been used to simulate the physiological hemodynamics of the vasculature. Law *et al.* [153] made use of a modified peristaltic pump to create the desired flow waveforms; however the system was only able to mimic the flow and not the pressure wave. Output flow rates were only adjusted by changing the diameter of the compression tubing used in the pump. A needle valve was used to adjust the flow in the circuit and the pump was controlled by a stepper motor, which was linked to a computer; thus various waveforms could be produced by computer control of the stepper motor. Feedback was provided by monitoring the ultrasonic flow probe. Insert profiles were used to smooth out the flow characteristics of the roller pump. Figure 7.2 (a) below shows the modified peristaltic pump used by Law *et al.* [153].

Schima *et al.* [151] made use of a ventricle pumping system to pump fluid through a circulation loop and test the shear stress on endothelialised grafts. Compressed air was used to drive the membrane in an artificial ventricle, two one-way mechanical valves were used to ensure flow

direction was consistent (Figure 7.2 (b)). Two windkessel chambers were used to smooth out the flow characteristics produced from the pumping chamber, and to create the necessary back pressure (Figure 7.2 (c)). Although good flow characteristics were produced, the system did not produce the correct corresponding pressure waveforms.

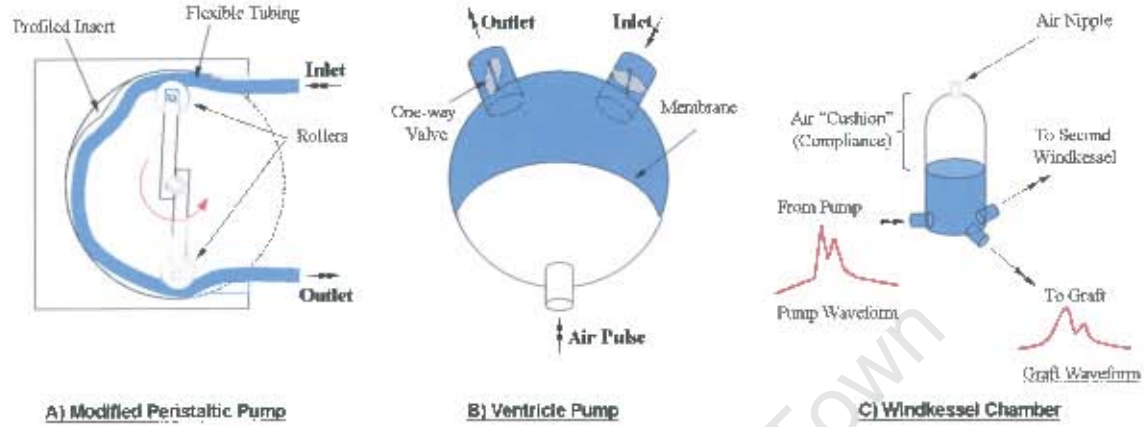

Figure 7.2: Schematics of; (a) modified peristaltic pump used by Law et al. [153], *(b) ventricle pump and (c) windkessel chamber used to smooth out pressure waveforms by Schima et al.* [151]

Holdsworth *et al.* [154] made use of opposing stepper controlled positive displacement pumps, where a valve was used to direct flow between strokes. Thus negative pressure and flow could be produced, which is difficult to produce in a peristaltic pumping system such as that used by Law *et al.*. Since the amount of fluid displaced with each step of the motor is constant, waveforms are easily programmed. No feedback controls or correction factors were required for the system since there was negligible attenuation and the system was stable over long periods.

Labadie *et al.* [155] built a perfusion system and tested canine carotid arteries as well as human saphenous vein portions, using a fluid filled testing chamber maintained at physiological temperature and a tissue culture medium. A pulsatile waveform was produced with use of a centrifugal pump and a computer controlled gate valve, which allowed for accurate recreation of the pressure pulse. Brant *et al.* [156] utilised a similar system to test canine vessels. Both groups used noninvasive methods to measure diameter change, namely a laser micrometer. This method only determined external diameter changes of the vessels.

Charara *et al.* [148] produced good physiological flow conditions using a computer controlled flow simulator, which used a programmable positive displacement piston pump, controlled by means of a stepper motor, similar to that used by Holdsworth *et al.*. This is reported to produce physiological flow, however, the response of the pump to high frequency commands showed frequency dependent phase lags. Thus, for complex flow simulations a correction input command had to be predetermined to produce a desired flow pattern. To ensure that laminar flow was observed through the sample, a straight tube of length 25 times the internal diameter (ID) of the vessel was placed on the proximal side, although complications with laminar flow are observed

for small diameter vessels ($\leqslant$ 6 mm).

Giudiceandrea *et al.* [67, 149] developed a flow circuit which utilised a variable speed electromagnetic centrifugal pump, in series with a governable flow waveform conditioner. In order to test porous graft structures the structures were pre-clotted, by forcing freshly obtained human blood through the graft. This process was repeated until no transluminal leaking was observed. They also tested human arterial segments, which were stored in Ringer's lactate solution at 4 °C and studied within 24 hrs of harvest. The measurement of pressure was done at discrete points with a Miller micro-tip transducer. The perfusion solution was made of a mixture of Dextran, M199 (minimum essential medium), bovine solution and L-glutamine, the viscosity of which approached that of human blood. A gas mixture of O_2 and CO_2 was bubbled through the fluid, and was maintained at 37 °C by a heat exchanger. Ultrasound techniques were used to measure internal diameter changes noninvasively.

7.2.1.2 Diameter measurements

Noninvasive methods. Ultrasound [67, 71, 80, 157–162], laser micrometer [148], imaging, volume change [78, 163], Magnetic Resonance Imaging (MRI) and X-ray techniques [164] are some of the noninvasive methods used. Ultrasound techniques are the most popular, followed by volume change and the laser micrometer. Since no restrictive effects are placed on the vessel during testing, this makes noninvasive methods advantageous. Both internal and external diameters (OD) can be measured using ultrasound and MRI techniques, while X-rays and volume change can only measure ID, and imaging and laser micrometers, only OD. An advantage of ultrasound, MRI and X-ray over other methods is that they can be used to make in vivo measurements, without exposing the vessel, unlike imaging and the laser micrometer, which would require vessel exposure. Volume change techniques cannot be used in vivo. Only instantaneous measurements can be made using the MRI technique, which limits its application.

With ultrasound, the higher the frequency probe used the better the resolution (7.5 MHz gives a resolution of around 1 μm, depending on the signal strength, position, depth, and material being assessed). However, the type of equipment used is of importance. Kawasaki *et al.* [80] used a phase locked echo tracking system equipped with a real time linear array scanner to obtain the in situ data. Various frequency ultrasound probes were used, depending on the location and acoustic condition of the vessel.

A number of methods have been used to translate the ultrasound data into meaningful information. Kawasaki *et al.* and Tai *et al.* [67, 80] used phase locked echo tracking systems to interpret this data (Figures 7.3 (a), (b) and (c)), while Stok *et al.* [165] used image analysis on M-mode captured images.

Charara *et al.* [148] used a laser micrometer (Benchmike model 183B, LaserMike Inc., Dayton, OH, USA) to measure the distension of a vessel , with a resolution of 0.5 μm. Sonoda *et al.* [164] used X-ray techniques to measure the internal diameter of a vessel under static conditions

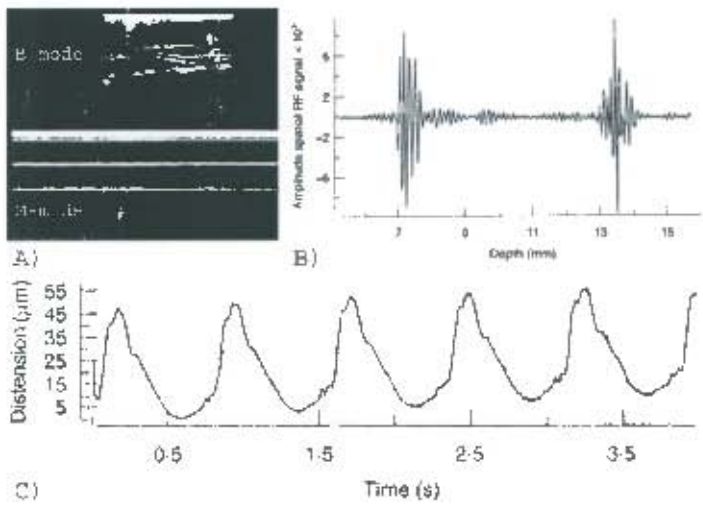

Figure 7.3: (a) B and M-mode images of saphenous vein: (b) resultant radio-frequency signal generated by anterior and posterior walls; (c) distension-time curve generated by wall tracking system [67]

at various predefined pressure points. Figure 7.4 shows a) the schematic of the X-ray set up and b) captured images with increasing pressure.

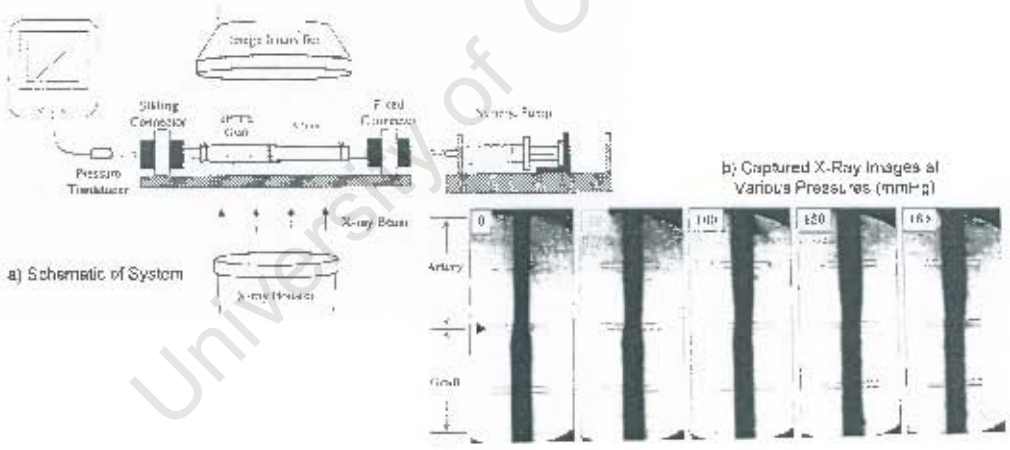

Figure 7.4: Schematic of X-ray imaging equipment used by Sonoda et al. [164] *and series of captured images at various pressures (mmHg)*

Igo *et al.* [163] used fluid volume change in the vessel to measure volume compliance. Figure 7.5 shows a schematic of their equipment.

Invasive methods. These include cantilevers [21, 66], strain gauges [13, 58, 166] and linear displacement transducers (LDT). Murgo *et al.* [166] made use of a cantilever strain gauge method to calculate and measure diameter change in vivo, where they measured diameter changes of natural vessels. A number of other researchers have used the same method [13, 58]. Simultaneous pressure and diameter readings were taken in situ at two weeks and three months to assess the change in compliance with implant time. A drawback of this method is the amount of inva-

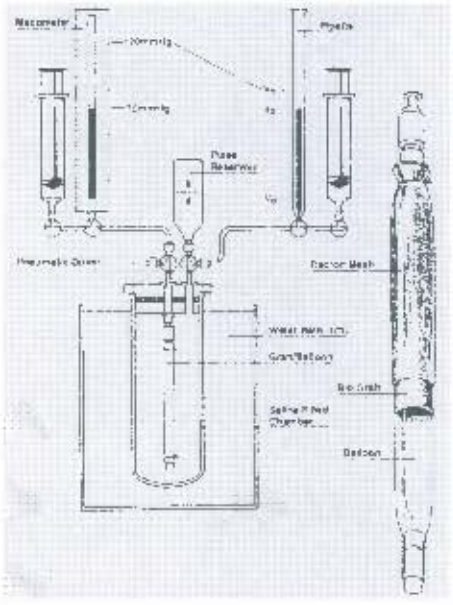

Figure 7.5: Schematic of equipment used by Igo et al. [163] *to measure dynamic volume compliance*

sive surgery required to expose the vessel and to measure diameter change. MacKellar [21] used small lever arms which rested on the graft's external surface; the arms had a displacement sonomicrometer attached to the ends of the arms. Figure 7.6 shows the errors involved in using this technique.

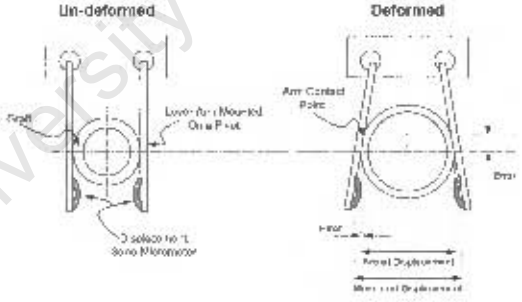

Figure 7.6: Errors caused by cantilevers used by MacKellar [21]

Millam [66] used a weight suspended cantilever system attached to calibrated LDTs to measure the diameter changes of grafts in vitro. However due to the forces required to move the weights, the readings were highly invasive.

7.2.1.3 Graft anastomotic attachment and sample length

Various methods of graft attachment are used. Commonly graft samples are either fully fixed at the anastomosis, free, pre-strained by a certain axial strain, or a constant load is applied axially. The two most commonly used are predefined axial strain or load. Millam [66] and Tai *et al.* [67] used a predefined axial strain of 10%, while Charara *et al.* [148] and Igo *et al.* [163] used a axial pre-load. Charara *et al.* used a longitudinal tension of 4 N (400 g). Igo *et al.* allowed the

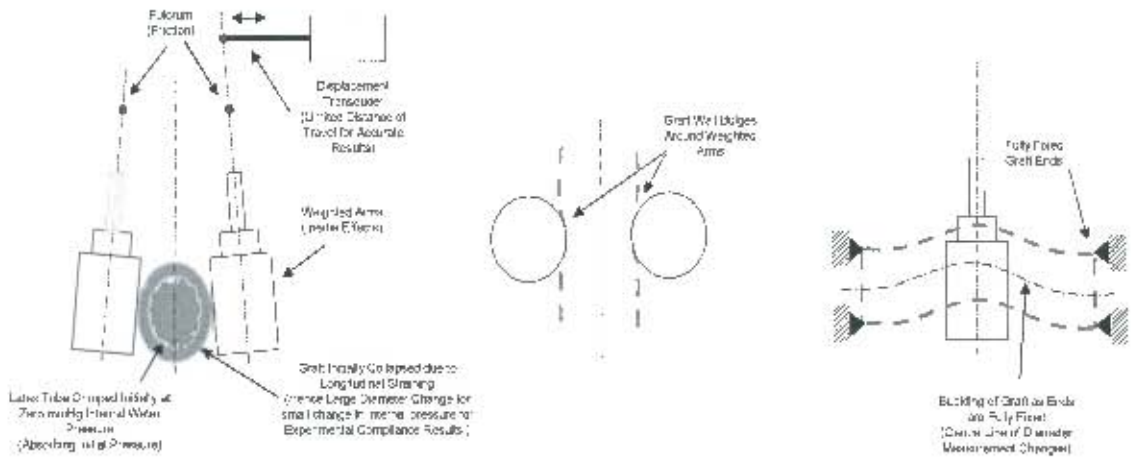

a) Sectional View of Mechanical Method of Measuring Real Time Diameter Change of Graft

b) Plan View Showing Bulging Of Graft Around Weighted Arms

c) Side View Showing Buckling Of Graft as Ends are Fully Fixed

Figure 7.7: Weighted cantilever and LDT problems used by Millam [66]

graft sample to hang vertically and had a small mass attached to the distal end (see Figure 7.5). MacKellar [21] on the other hand did not apply any axial load but rather fixed both anastomoses. Problems encountered in trying to apply a constant axial load include the presence of friction. This was not an issue in the work of Igo *et al.* as their graft sample is suspended vertically (Figure 7.5). However, this rig does not allow for fluid flow through the vessel sample. Charara *et al.* attached a pulley system to the distal anastomosis of the graft sample and reduced friction with the use of an air bed runner. Sonoda *et al.* [164] allowed the graft to move freely in the longitudinal direction (see Figure 7.4). In the physical case, the graft would be exposed to an axial load which would be dynamic. Thus a better method than simply applying a constant load or axial strain would be to apply a dynamic load; this could be achieved with the use of a spring which is axially loaded, where the spring load will vary with longitudinal strain observed by the graft sample.

It should be noted that international standards such as the AAMI require that an axial pre-load of 0.3-0.6 N (30-60 g) be applied to the graft sample prior to testing.

Apart from the method of anastomosis attachment, the type of tubing used at the anastomoses is of importance. The use of highly rigid (noncompliant) tubing would affect the compliance of the vessel sample; however, this is heavily dependent on the sample length used. Other researchers have used arteries or commercially available grafts (Dacron®, e-PTFE) to allow for some compliance. Freshly harvested arteries would be best as these would be similar to the vessel application, while most commercially available grafts are noncompliant ($\leqslant$1-2 %/100 mmHg) and are thus no different to rigid tubing.

It is also important to consider the length of the sample to be used, to ensure that edge effects are minimised. Igo *et al.* used vessel segments of roughly 160 mm in length for testing, while Millam used sample lengths of 80-100 mm, Charara *et al.* used segments lengths of 100 mm.

7.2.1.4 Porous grafts and pressure loss

Most of the testing thus far has been on nonporous graft structures; problems arise in the case of in vitro testing of porous grafts. Two methods are possible to test porous structures in vitro: pre-clotting the structure with blood until no transmural leakage is observed [67, 149], and the use of thin luminal inserts [78, 163].

Problems are encountered when luminal liners play too great a mechanical role. Thus an important consideration is the type of liner used. Igo *et al.* used polyurethane balloons which had diameters 50 % greater than the vessel diameters, with an average wall thickness of 0.005 mm. Conti *et al.* [78] used latex liners of minimum wall thickness of 0.38 mm.

7.2.2 The compliance rig

A compliance testing rig was designed and built, initially by MacKellar [21], and then developed further by Millam [66]. Major adjustments have been made to the rig developed by Millam to ensure consistent, stable pressure curves and noninvasive diameter measurements. A closed loop system was introduced with an adjustable non-return valve, allowing for further flow and pressure control in the system. Diameter measurement techniques were changed from the invasive weighted cantilever and LDT (see Figure 7.7) to noninvasive methods, which include ultrasound and image capturing techniques. The compliance rig is able to perform static and dynamic testing and simulate a range of both blood flow and pressure waves. A short description of the compliance rig is presented.

Figure 7.8 shows a schematic of the compliance rig. The system consists of a closed fluid channel simulating the blood systemic tree. A reservoir (WSV) which is pressurised to achieve the physiological pressure range, and a roller pump (RP) are used to induce a cyclic pressure pulse similar to that of the heart. A adjustable non-return value (1WV) is used to control the back flow/pressure during a cycle. A graft sample (GS) is placed within the system and its temperature controlled by a water bath (WB) in connection with a heat exchanger (HE) and heating unit (HU). Syringes S1 and S2 are used to control the fluid air ratio in the windkessels W1 and W2, which are used to smooth out the pressure curves. Additionally W2 and a needle valve (T3) are used to control the back pressure and flow characteristics. Real time data for pressure are recorded at the proximal (PT1) and distal (PT2) positions as well as diameter measurements collected through either a CCD Digital Camera (Sony CCD-IRIS) connected to a digital capturing card (Digitiser, Apple Macintosh) and a computer (Apple Macintosh G3), or with ultrasound techniques using an ultrasound probe (7 MHz, Acuson) and ultra sound machine (Acuson 128XB/10).

For static compliance testing, needle valves, T1 and T2 are fully closed and an internal pressure is applied to the graft sample from a water reservoir via syringe (S1). Graft samples are placed in a saline or phosphate buffered saline (PBS) solution, with the water bath kept at 37°C via the heat exchanger (HE), where diameter and pressure are recorded. Two methods of diameter measurement were used: digital imaging technique and the ultrasound technique.

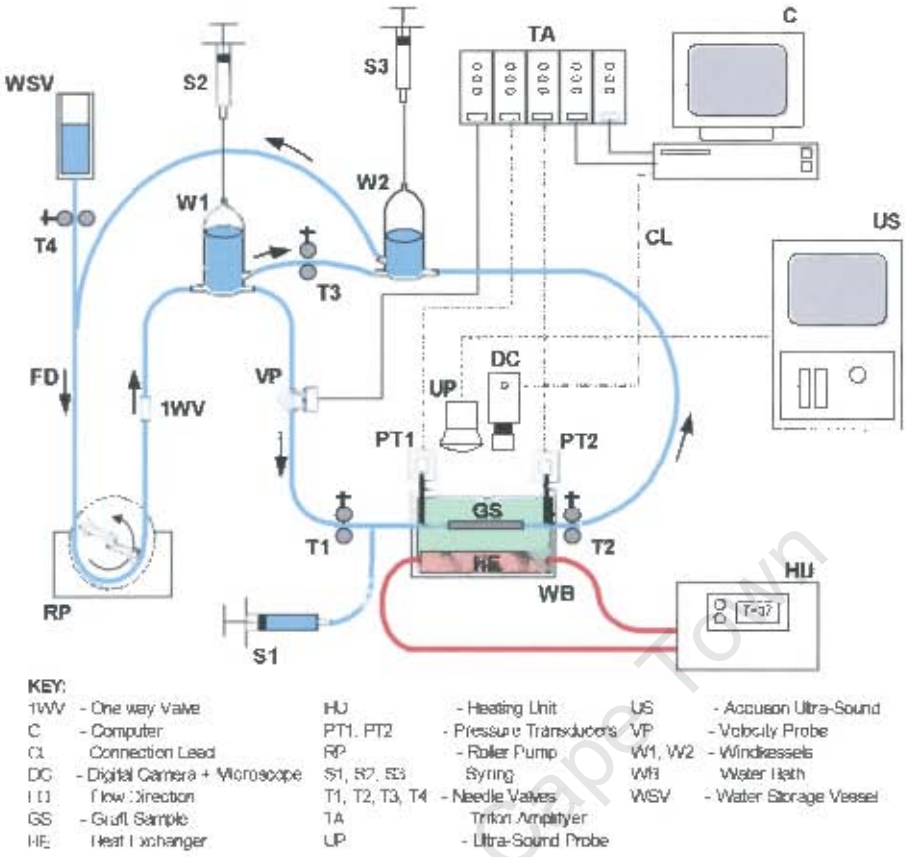

Figure 7.8: Compliance test equipment

Digital imaging technique. A digital camera (Sony CCD-IRIS) connected to a PC (Apple Macintosh G3) with frame grabbing hardware and software (Strata Videoshop© version 3.0.4) was used to capture a series of digital images over a period of time. The digital camera was attached to a microscope (Leica MS 5) for magnification. This microscope was placed above the graft sample (Figure 7.9) and the focal plane was adjusted until the edge of the graft was in focus (Figure 7.10). A submerged reference rule was placed alongside the graft and adjusted until it was brought into the same focal plane. This reference rule was used to ensure that minimal distortion in measurement was incurred due to refracted light through the water surface.

The video sequence was recorded over four pressure cycles (3.32 s) at 25 frames per second (0.04 s/frame) into phase alternating line (PAL) format at high resolution (768×576 pixels). Thus, 83 frames were collected over the recording period. Due to the recording time lag of 0.01 s between the first, second, third and fourth pressure cycles, diameter changes are recorded at intervals of 0.01 s for a pressure pulse period of 0.83 s over the 3.32 s. The recorded images were then converted into a series of *.pct images (768×576 pixels) using Strata Videoshop© (Macintosh Version 3.0.4) and analysed using Scion Image® for Windows V: Beta 4.0.2 (Scion Corporation). Using the reference rule and Scion Image®, pixel measurements across the image are converted to millimeters. Using this frame resolution, reliable measurements down to 9.26 μm

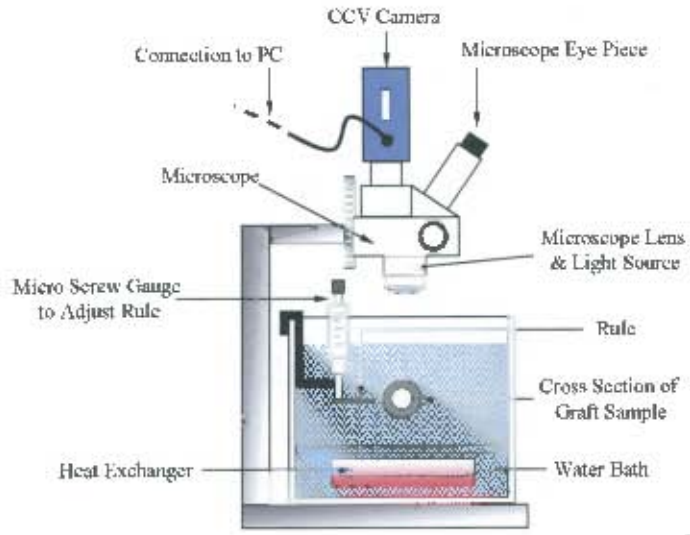

Figure 7.9: Schematic of camera and microscope setup for digital imaging purposes

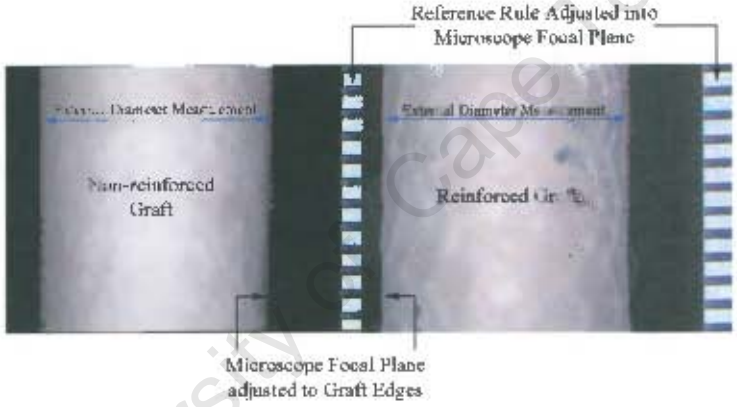

Figure 7.10: Digital frames captured from non-reinforced and reinforced grafts during compliance testing

could be made.

Given the need to record compliance values greater than 2 %/100 mmHg and using equation (2.1), where $\Delta P = 40$ mmHg (80 to 120 mmHg) and $d = 4$ mm, gives $\Delta d = 32\ \mu$m. Thus, measurements of 9.26 μm were considered sufficient.

Due to the use of digital imaging techniques to measure compliance, and the measurement of OD, it is important to quote results either in terms of OD or to adjust these to cater for the wall thickness in the results obtained. In order to cater for wall thickness, each porous graft structure had a section cut from each end and placed under a microscope for image analysis of ID and OD, as well as wall thickness. Again, Scion Image® for Windows V: Beta 4.0.2 was used to analyse the cross sectional images. Figure 7.11 below shows the cross section of a porous graft end and the points used to analyse the internal and external diameters from which wall thickness (w) is calculated.

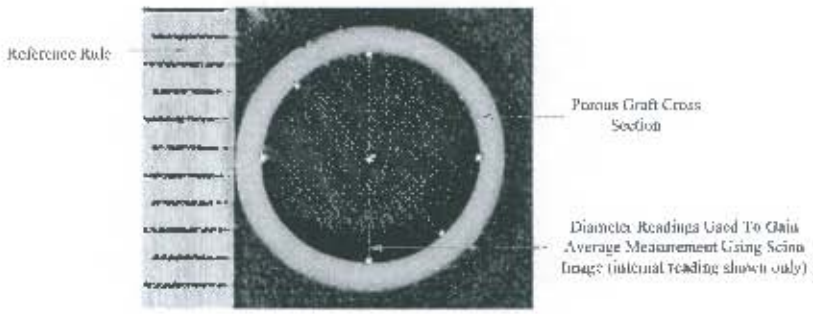

Figure 7.11: Digital image of graft cross-section used in image analysis

Readings from these are used directly to calculate ID for graft compliance (assuming no wall compression); however for reinforced grafts, the fabric reinforcing thickness was added into the calculation.

Ultrasound technique. Ultrasound techniques were also used to measure internal diameters noninvasively. An ultrasound machine (Acuson 128XB/10), with a 7 MHz probe, gave image resolutions of up to 10 μm; however, image resolution and recordings were difficult to use due to the scattering of the reflected ultrasound caused by the porous PU structure. For vessels made of solid PU or silicone, images were very good; however, before using the porous grafts it was necessary to soak them in ethanol and water to ensure that all air was expelled from the porous structure prior to testing. Following this procedure, a lower scattering effect was seen from the graft surfaces due to the micro pores of the graft structure. Figure 7.12 shows the scattered ultrasound image of a cross section of the porous graft.

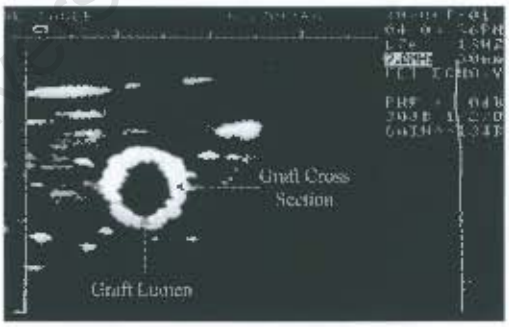

Figure 7.12: Ultra-sound image of porous graft cross-section showing distorted image due to trapped air in micro-porous structure

7.2.3 The reinforced and non-reinforced graft samples

Manufacture of the porous graft structures. The porous grafts were manufactured from a proprietary PU developed by Medtronic Inc. (Code M48) by vacuum/pressure casting the PU solution (20 % M48 by mass dissolved in NMP) with extractable porogens (particles responsible for producing pores), followed by phase precipitation (solidification of PU) and porogen

extraction. Highly regular spherical porogens (Gelatin microspheres, Thies Technologies, St. Louis, USA) were used to produce well defined pores and pore sizes. The porogen are pre-packed in an annular mould prior to infiltration of the openings with the polymer solution . The PU/microsphere moulds are then placed in ethanol where the PU is allowed to solidify. Ethanol is used to reduce PU and microsphere swelling, which may cause pre-stressing and damage to the PU porous structure. The gelatin microspheres are then extracted with water once the PU had cured completely. The process is illustrated in Figure 7.13.

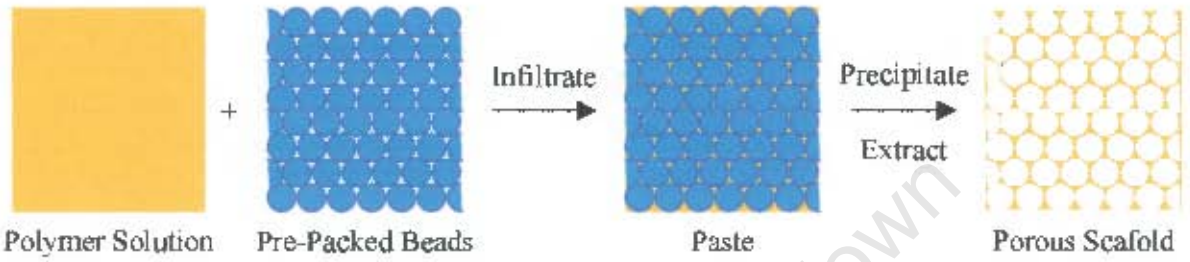

Figure 7.13: Pre-packed spherical porogens and phase inversion and extraction process to produce pores

Porogen particles are packed into an annular column consisting of a glass tube (ID = 5.4 mm) and central stainless steel mandrel (OD = 4.0 mm) with an upper and lower reservoir. The upper reservoir is filled with the PU solution and a pressure (750 kPa) applied. A vacuum is drawn (100 kPa) from the lower reservoir, forcing the PU solution through the packed column.

Upon complete infiltration of the PU/solvent solution into the packed gelatin microspheres the grafts were demoulded on the stainless steel mandrels and the PU precipitated by phase inversion. Subsequent extraction of the porogen beads was done by extensive washing. Figure 7.14, shows the sequential steps of the vacuum/pressure cast graft production after; (b) removal of column from mould with upper reservoir; (c) column with upper reservoir removed; (d) the graft on mandrel removed from glass cylinder and phase inversion; (e) porogen extraction in suitable solvent and washing; and (f) the graft once dried and removed from mandrel.

The porogen particles were sorted by sieving techniques into three size groups: 90-106, 106-125 and 125-150 μm. These different porogen sizes were used to produce different graft pore sizes. On average the pores created were 1.21 ± 0.07 μm times the diameter of the porogens used, and the interconnecting pore windows were approximately half the size of the pores (window:pore 0.52 ± 0.04) [9]. Figure 7.15 shows SEM images of a) the gelatin microspheres ($\times$350); b) graft cross section ($\times$44); c) graft wall ($\times$225); and d) pore showing pore windows ($\times$3500).

Further details on the manufacture and differentiation of the porogen sizes and analysis of the porous structure as a self healing graft can be found in the work by Bezuidenhout [9].

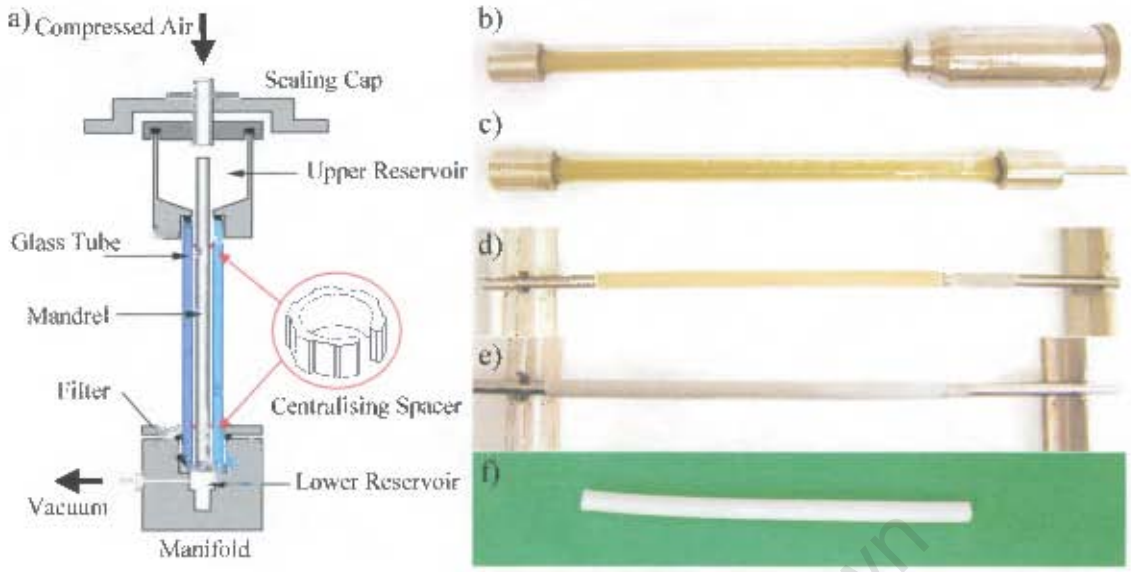

Figure 7.14: Graft rig and manufacturing process

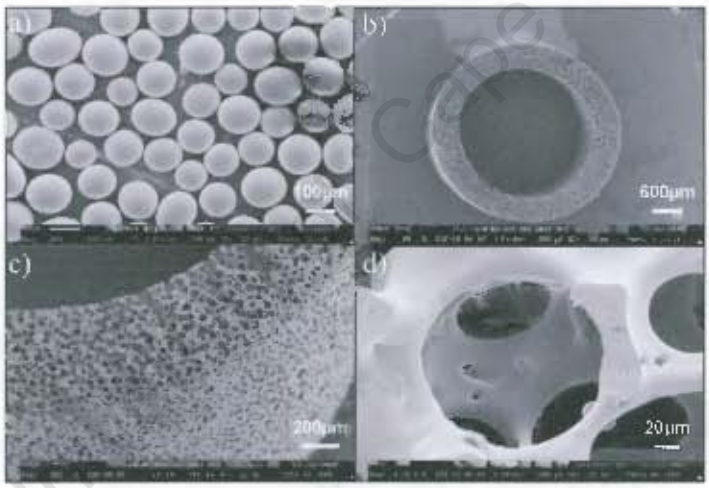

Figure 7.15: SEM images of (a) porogens gelatin microspheres, (b) porous graft cross-section, (c) porous graft wall and (d) porous structure

Manufacture of the non-reinforced and reinforced graft samples. The manufacture of the non-reinforced graft samples used for compliance testing utilise a 50 mm porous graft core with two 20 mm e-PTFE graft anastomoses (Atrium, 4 mm, 30 μm ID) (refer to Figure 7.17). These e-PTFE graft ends were anastomosed to the porous graft section by repeated application and drying of a polyurethane solution (5 % M48 by mass in Chloroform, $CHCl_3$) while the segments were constrained on a central mandrel. These e-PTFE graft ends ensure that graft samples are not damaged during testing and can be reused. They also ensure consistent longitudinal strains during testing. Reinforced samples utilise non-reinforced porous graft samples where fabric socks are applied gently and gradually over the porous grafts ensuring uniformity. At one of the anastomosis regions of the porous graft the fabric was anastomosed to the structure by additional

application of a polyurethane solution (10% M48 by mass in Chloroform). A higher concentrated polyurethane solution was used to reduce the absorption into the porous structure. Once this anastomotic region was cured, the fabric sock was strained, by uniformly and evenly stretching the fabric over the graft sample to the required amount, and then constrained by clamping and then applying repeated layers of polyurethane solution. This process is demonstrated in Figure 7.16.

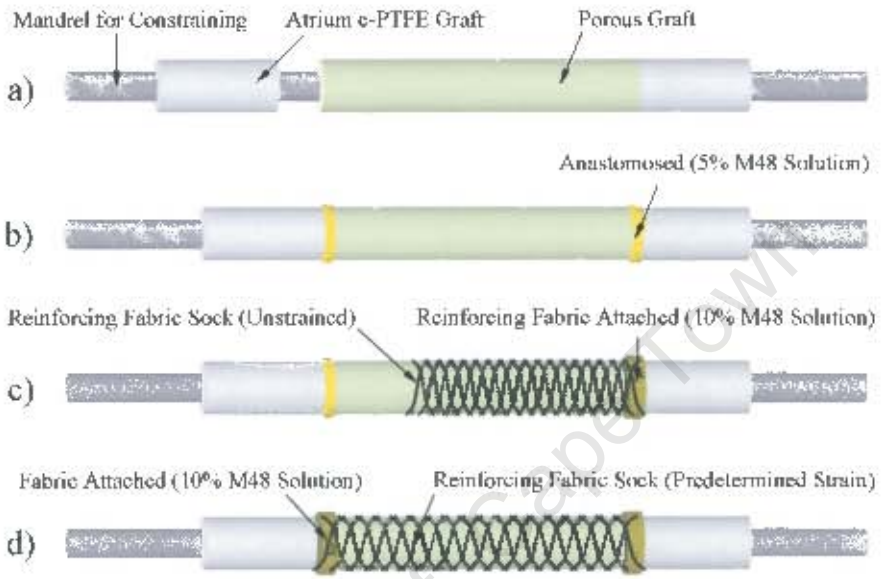

Figure 7.16: Processes to manufacture non-reinforced graft and reinforced graft samples

Pressure loss liners are inserted with the use of an application rod through the luminal section of the graft samples prior to testing. Figure 7.17 shows a schematic of composite graft, while Figure 7.18 shows images of the latex liner, and non-reinforced and reinforced porous grafts.

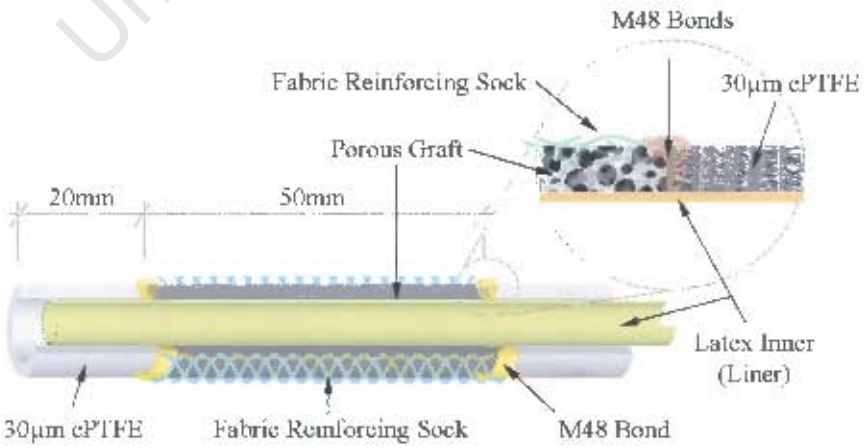

Figure 7.17: Schematic of composite test graft sample showing fabric reinforcing and e-PTFE ends

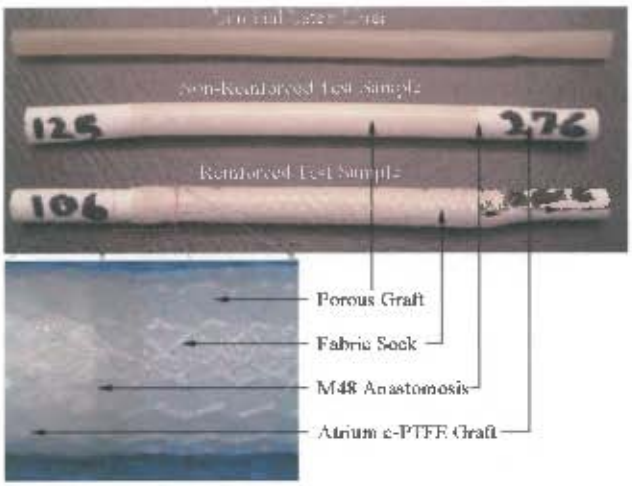

Figure 7.18: Luminal latex liner, reinforced and non-reinforced graft test samples

7.3 Comparative compliance study of standard silicon graft samples

To ensure that the various techniques used to measure compliance yield comparable results to that observed in literature, standard compliant silicon tubes were ordered from a commercial supply company[1]. These were initially tested using both the ultrasound and visual techniques described in Section 7.2.2, however, due to the consistently low results obtained, a research group[2] was also employed to test the standard samples. The variation in compliance results observed by the various groups are illustrated in Figure 7.19.

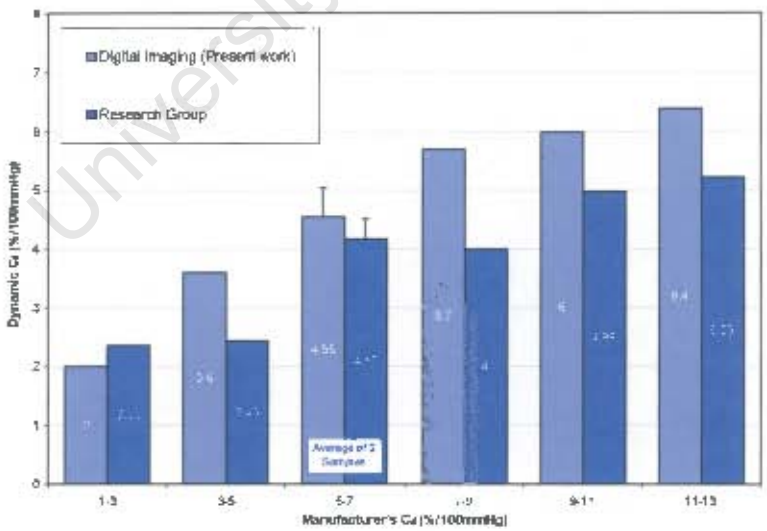

Figure 7.19: Variation in compliance values obtained from standard silicon compliant grafts

[1]Dynatek-Dalta Scientific Instruments, 105 E. Fourth Street, Galena, MO 65656, USA, Tele # : 417-357-6155, Fax #: 417-357-6327.

[2]Vascular Hemodynamic Laboratory, University Department of Surgery, Royal Free and University College Medical School, UCL, The Royal Free Hospital, London, NW3 2QG, UK, Tele # : +44 207 830 2901, Fax #: +44 207 431 4528.

The compliance values obtained in the present study and from the research group are consistently lower than those stipulated by the manufacturer. However, the present study and the research groups results are consistent with each other. This raises the question of the calibration and calculation of compliance by each group. It was established that the manufacturer uses a volume technique [78] similar to that of Igo *et al.* [163] described in Section 7.2.1.2, where no axial load or strain is applied to the graft prior to testing. While, the research group applies a 10% axial strain to the graft and measures diameter change using the ultrasound phase locked echo tracking system described in [67] and illustrated in Figure 7.3.

New compliance values were obtained for some of the silicon graft samples with no axial load applied. Table 7.1 details the new compliance values obtained.

Manufacturer's Result %/100 mmHg	**In House Result** %/100 mmHg
2.0 ± 1.0	2.1
6.0 ± 1.0	5.4 ± 0.3
12.0 ± 1.0	9.2

Table 7.1: Variation in compliance results with no axial strain

Again, the compliance results are lower than those stipulated by the manufacturer, however the difference observed is reduced. This is once more, attributed to the different measurement techniques used to test the samples.

Chapter 8

Modelling with ABAQUS

8.1 Introduction

A porous polymer graft with fabric reinforcing is required to be modelled mathematically and computationally using a general purpose finite element (FE) package. ABAQUS© version 5.8-8 is one such commercial package which has the capacity to accommodate a wide range of material models. ABAQUS© is used to model the graft structure for various types of fabric reinforcing described by the fabric constitutive model. Using a genetic algorithm (GA), the fabric model coefficients are adjusted until a solution giving the required dynamic diameter compliance (C_d) for the various porous structures is found. The solutions are then utilised in circumferential and longitudinal finite element simulations to obtain the stress-strain characteristics of the fabric reinforcing in accordance to the AAMI and ISO standards for cardiovascular graft implants [167, 168].

The type of elements, material constitutive equations and approximations used to describe the physical graft and tensile tests by finite element methods are discussed in this chapter. Section 8.2 discusses the material models used and the implementation of the fabric constitutive relation in ABAQUS©. It then describes the finite element models, elements, the applicable boundary and load conditions, and the assumptions used to simplify the analyses.

8.2 The material models

ABAQUS© accommodates a range of material models, including the hyperelastic and hyperfoam models described in Chapter 4. It does not have an intrinsic anisotropic fabric material model, but provision is made for the implementation of special constitutive relations through a user material subroutine (UMAT) [94, 169–171]. If intrinsic material models are used, ABAQUS© allows users to input material coefficients according to the material model or physical test data, where in the latter case a least squares method is used to fit coefficients [94].

The porous polymer material model (hyperfoam). The intrinsic ABAQUS© isotropic hyperfoam material model is based on Ogden's strain energy function [94] as described by equation (4.82). The physical test data from tensile, compressive and simple shear tests are used to obtain the material coefficients. This material model is then utilised in single element patch tests to compare the model results to the physical test data. No viscoelastic effects are incorporated for the porous structures.

The latex material model (hyperelastic). ABAQUS© has two intrinsic isotropic hyperelastic material models which can be used to describe the latex material behaviour. These are the Ogden and polynomial hyperelastic material models described by equations (4.81) and (4.79). Typical order values for the strain energy functions are $N = 1$ or 2 for the polynomial function and $N = 1$ to 6 for the Ogden function. The higher the order, the better the model fit for the material typically, however this is conditionally true as the system can become unstable. Physical test data from tensile, compressive and simple shear tests were utilised for these materials. This material model is utilised in a single element patch test to compare the model results to the physical test data. No viscoelastic effects are modelled.

The fabric material model. As mentioned earlier (Section 4.11) a new constitutive relation is proposed for coarse knit fabrics under tensile behaviour as described by equation (4.122). This material model is to be implemented in the finite element package using the UMAT. The finite element models for which this fabric material model will be used include a graft model (tensile and compressive deformation), a uniaxial tensile model (tensile, compressive and shear deformation), and circumferential and longitudinal tensile models (tensile, compressive and shear deformation). From these various deformation modes, bending can be disregarded. Since the fabric thickness is small in comparison to its other dimensions it can be considered a membrane, and subject to plane stress conditions. Coarse knitted fabrics are also highly compressible, and so incompressibility is not enforced. Thus, the implementation of the fabric constitutive model in the UMAT will reflect these relations.

It is assumed that the fabrics used are highly elastic, and viscoelastic effects are neglected.

8.3 Implementation of the fabric material model in ABAQUS©

ABAQUS© provides a user interface for users develop their own constitutive material models through the UMAT subroutine. This subroutine performs two functions: it updates the stresses and the solution dependent state variables to their values at the end of each increment, and it provides the material elasticity tensor for the constitutive model. The discrete elasticity tensor is defined by

$$K^{\sigma\varepsilon}_{ijkl} = \frac{\partial \triangle \sigma_{ij}}{\partial \triangle \varepsilon_{kl}}, \tag{8.1}$$

where $\triangle\sigma$ and $\triangle\varepsilon$ are the stress and strain increments. For large strain computations an appropriate conjugate stress-strain measure is needed (see Section 4.5.4). Since the proposed strain energy function is already defined in terms of Green strain E an appropriate conjugate pair would be Green strain and the second Piola-Kirchhoff stress S. The second Piola-Kirchhoff stress and elasticity tensor are defined in terms of the strain energy by

$$S_{ij} = \frac{\partial w}{\partial E_{ij}}, \tag{8.2}$$

and

$$K^{SE}_{ijkl} = \frac{\partial S_{ij}}{\partial E_{kl}} = \frac{\partial^2 w}{\partial E_{ij} \partial E_{kl}} \,. \tag{8.3}$$

Objective rates and corotational framework form. It is necessary in a large strain framework to describe rates of change of stress using corotational or objective rates. We use the Jaumann rate as an appropriate corotational rate; this is given by

$$\sigma^{\nabla J}_{ij} = \frac{D\sigma_{ij}}{Dt} - W_{ik}\sigma_{kj} - \sigma_{ik}W_{kj} \tag{8.4}$$

where W is the spin tensor. The Jaumann rate is designated by the superscript J. Next we need to relate $\sigma^{\nabla J}$ to D, through a relation of the form

$$\sigma^{\nabla J}_{ij} = K^{\sigma J}_{ijkl} D_{kl} \,, \tag{8.5}$$

where $K^{\sigma J}$ is found in terms of K^{SE}. Using the fourth elasticity tensor

$$\Psi^{(4)}_{ijkl} = K^{\tau}_{ijkl} = F_{im}F_{jn}F_{kp}F_{lq}K^{SE}_{mnpq} \,, \tag{8.6}$$

this relation can be expressed in the Truesdell rate of Cauchy stress, designated by the superscript T, according to

$$\sigma^{\nabla T} = J^{-1}\tau^{\nabla c} = J^{-1}K^{\tau}{:}D = K^{\sigma T}{:}D \,, \tag{8.7}$$

where

$$K^{\sigma T} = J^{-1}K^{\tau} \,. \tag{8.8}$$

Using the relations between tangent moduli, and specifically the relation between the Jaumann and Truesdell moduli of equation (4.103a), we have in index notation,

$$K^{\sigma T}_{ijkl} = K^{\sigma J}_{ijkl} - K'_{ijkl} + \sigma_{ij}\delta_{kl} = K^{\sigma J}_{ijkl} - K^{*}_{ijkl} \,, \tag{8.9}$$

where

$$K^{*}_{ijkl} = \frac{1}{2}\left(\delta_{ik}\sigma_{jl} + \delta_{il}\sigma_{jk} + \delta_{jk}\sigma_{il} + \delta_{jl}\sigma_{ik}\right) - \sigma_{ij}\delta_{kl} \,. \tag{8.10}$$

ABAQUS© requires that the stress be explicitly defined as Cauchy 'true' stress for large strain applications [94,172]. Thus we need the relation between the Cauchy and second Piola-Kirchhoff stress defined by (4.36) in the form

$$\sigma_{ij} = J^{-1}F_{ik}S_{kl}F_{jl} \,. \tag{8.11}$$

From equations (8.8), (8.9) and (8.10) one can obtain $K^{\sigma J}$ from K^{SE}. It should be noted that, unlike the Fung model (equation (4.118)), incompressibility is not enforced.

Special operators implemented in the ABAQUS© numerical models. For the ABAQUS© numerical models, special operators are used for the fabric material model. These are as follows:

- *Orientation:* The orientation parameter [169] is used to define the transverse directions of the fabric model. This ensures that material properties remain orientated as the elements rotate and deform.

- *Membrane element thickness:* A thickness of 100 μm was used for the membrane elements or fabric.
- *Poisson's ratios v_{13} and v_{31}:* Membrane elements used to model the fabric ensure a plane stress state. Deformation through the thickness is also assumed to remain constrained.

Details of these operators and their implementation in the numerical models can be found in the ABAQUS© manuals [169, 171].

8.4 Single element and multi-element patch test models

Single element model patch tests were set up to test and assess the material model behaviour under certain forms of deformation. The fabric patch test is utilised to assess the implications for each of the fabric model coefficients, namely C, a_1, a_2, a_3, a_4, a_5, a_6, a_7, a_8 and a_9, while the porous and latex patch tests are utilised to assess the accuracy of the material models against their physical tensile, compressive and shear test counterparts.

8.4.1 Single element models

Single element models were set up with boundary and load conditions set to describe uniaxial tensile, compression and simple shear tests.

The uniaxial tensile and shear models give the general stress-strain characteristics of the fabric model, while a uniaxial tensile model is used to compare the fitted material data to model solutions for the latex liner. The single element model used for the latex and fabric is a simple four-noded bilinear membrane element.

For the porous structures a single eight-noded plane stress cubic element is used with the hyperfoam material model ($n = 6$). The eight-noded cubic element also uses a linear interpolation function to describe the approximate field variables. Figure 8.1 shows the single element models used and the various load and boundary conditions.

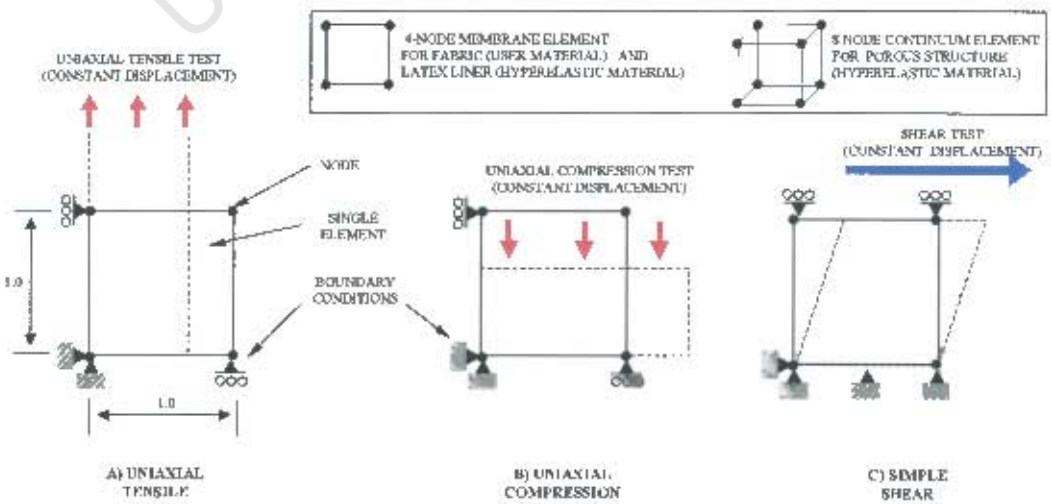

Figure 8.1: Single element uniaxial tensile, compressive and simple shear patch test models

8.4.2 Multi-element mesh models for the fabric material constitutive equation

A multi-element patch test was also utilised to ensure that element orientation and type did not affect the results. Two mesh models were used: one a uniform mesh, with consistently ordered four-noded membrane elements, and the other, a non-uniform mesh with three and four-noded membrane elements (Figure 8.2). These two meshes were used in uniaxial tension and simple shear tests. The stress and strain behaviour are not only compared between the two mesh types, but also with the single element models at 40 % uniaxial and shear strain.

Figure 8.2: Uniform and non-uniform meshes

8.5 The finite element models

Four distinct computational models were considered: the graft model, the uniaxial tensile model, and circumferential and longitudinal tensile models. The graft model is used to find the static and dynamic compliance values and curves for the coefficients C, a_1, a_2, a_3, a_4, a_5, a_6, a_7, a_8 and a_9 corresponding to a fabric reinforcing. The uniaxial tensile model is utilised in a GA to assess the ability of the fabric model to model physical fabric samples in tension, and to assess the optimisation capabilities of the GA. The circumferential and longitudinal tensile models are used to provide stress-strain characteristics of the fabric solutions found from the optimised graft models. This circumferential and longitudinal model stress-strain characteristics are used to provide a textile manufacturer with the requirements for the fabric reinforcing.

8.5.1 The graft model

This model simulates the behaviour of the porous graft structures, which are reinforced externally with a fabric sock. Due to the symmetry of the problem, only one half of the longitudinal section of the graft and a quarter of the graft in the circumferential direction need be modelled.

Eight-noded continuum elements without twist are used to model the porous polymer structure, while four-noded linear membrane elements without twist are used for the fabric reinforcing sock.

The load conditions include an internal pressure on the inner surface of the porous structure. The load applied depends on whether a static or dynamic compliance test is being analysed.

The boundary conditions are as follows: the end nodes are fully fixed, while the central nodes are fixed in the axial direction and are allowed no angular twist, yet are free to move radially. The element mesh is refined longitudinally toward the fixed end, but remains uniform in the radial and circumferential directions. Figure 8.3 shows a schematic of the element, boundary and load conditions used for the graft section modelled.

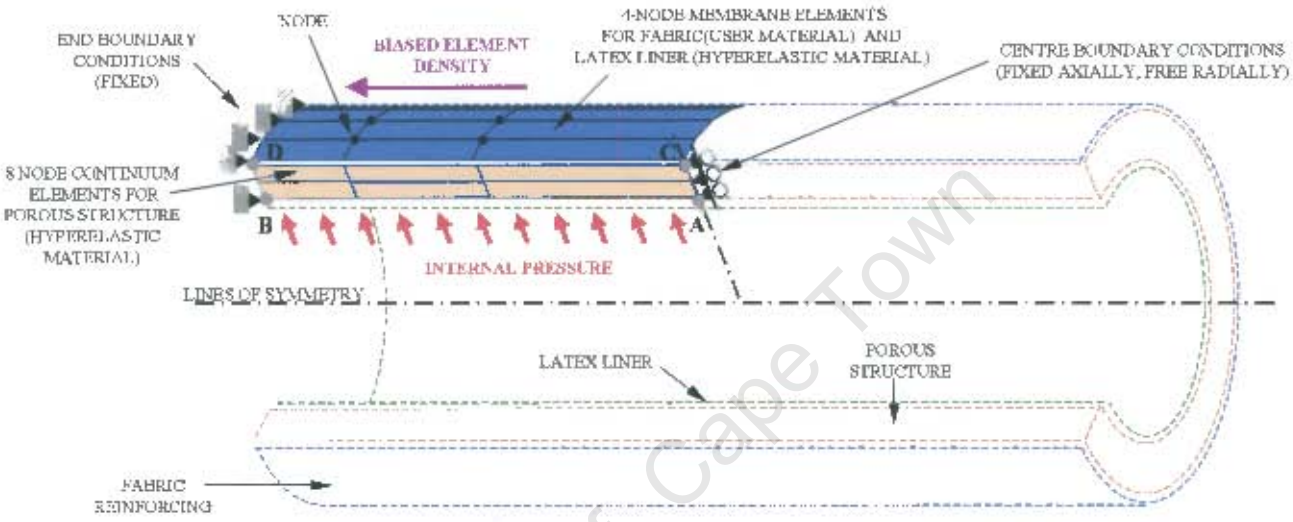

Figure 8.3: Graft finite element model

Both the dynamic and static graft models have a common first step of a pre-defined longitudinal (axial) strain of 10 %, as seen in the physical tests. The subsequent steps define the difference between the dynamic and static models.

Dynamic compliance model. The dynamic compliance model utilises one displacement step and two load steps. The displacement step produces a 10 % axial strain on the graft structure while the second is a static step which brings the internal pressure on the graft lumen wall to 100 mmHg (13332 Pa); the third step represents pulsatile blood pressure by a dynamic pressure wave. The second step ramps the internal pressure linearly over a period of four seconds. The third step uses the six-term Fourier series

$$\alpha = A_o + \sum_{1}^{n} (B_n \sin n\varpi(t - t_o)) \quad \text{for } t \geq t_o \tag{8.12a}$$

$$\alpha = A_o \text{ for } t \leq t_o\,, \tag{b}$$

to mimic the pressure pulse. Here n is the number of terms ($n = 6$), ϖ is the frequency (period $T = 0.83s$, $\varpi = 15.14$ rad/s), t_o the time at which cyclic load starts ($t_o = 0$), A_o the initial amplitude ($A_o = 13332$ Pa), and B_n are the Fourier series constants ($B_1 = 2418.5$, $B_2 = 691.0$, $B_3 = 230.33$, $B_4 = 115.17$, $B_5 = 114.7$, $B_6 = 114.7$). Figure 8.4 below shows the dynamic

applied pressure compared to the average of the proximal and distal pressure curves obtained from the compliance rig (Section 7.2.2).

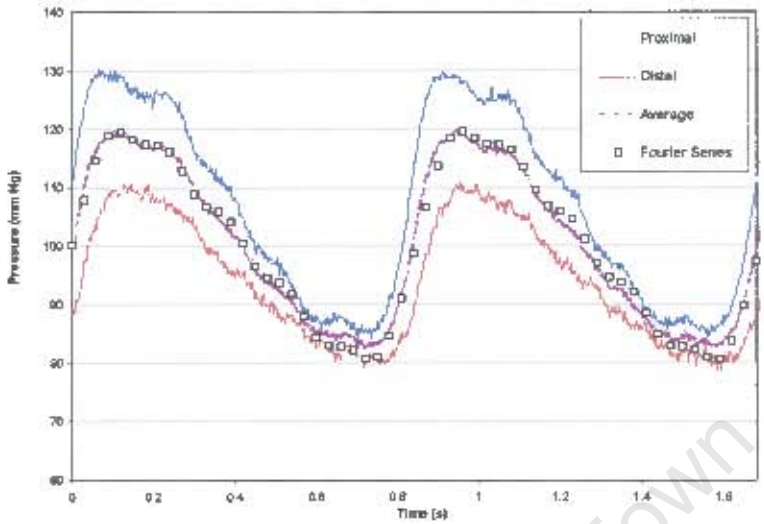

Figure 8.4: Comparison of the Fourier model with physical pressure curves

Static compliance model. The static compliance model has an initial axial strain step, followed by a second and final step which linearly ramps the internal pressure of the graft statically to 300 mmHg. This mimics the physical static compliance test carried out on a graft.

The luminal latex liner. A luminal latex liner is utilised in the physical testing of graft compliance to prevent pressure loss through the graft wall due to its inherent porosity. Thus in some of the graft models a luminal latex liner is modelled using four-noded membrane elements, as indicated in Figure 8.3. The luminal latex liner is only included in the graft model for the purpose of comparison with experimental results. However, when the GA is utilised to find optimal solutions to the fabric reinforcing, the luminal latex liner is not modelled.

8.5.2 The circumferential and longitudinal tensile test models

The AAMI Standard, (Sections 8.3.1 [167], "Method for determination of circumferential tensile strength" and 8.3.2 [167, 168], "Method for determination of longitudinal tensile strength") (the ISO standard [168] is the same in this regard), provides guidelines for the tensile test procedures of vascular prosthetic grafts in the circumferential and longitudinal directions. Following these guidelines, circumferential and longitudinal tensile test apparatus and procedures were developed with slight modifications to allow for the testing of small diameter fabric reinforcing socks. The tensile models simulate these physical situations. Mechanical solutions gained from the physical and finite element models are in the form of force per unit length vs. displacement curves for the fabric reinforcing samples, according to textile manufacturer test procedures and the ISO/AAMI Standards [167, 168].

The circumferential tensile test model. Figure 8.5 shows the physical circumferential tensile test done on fabrics at 37 °C.

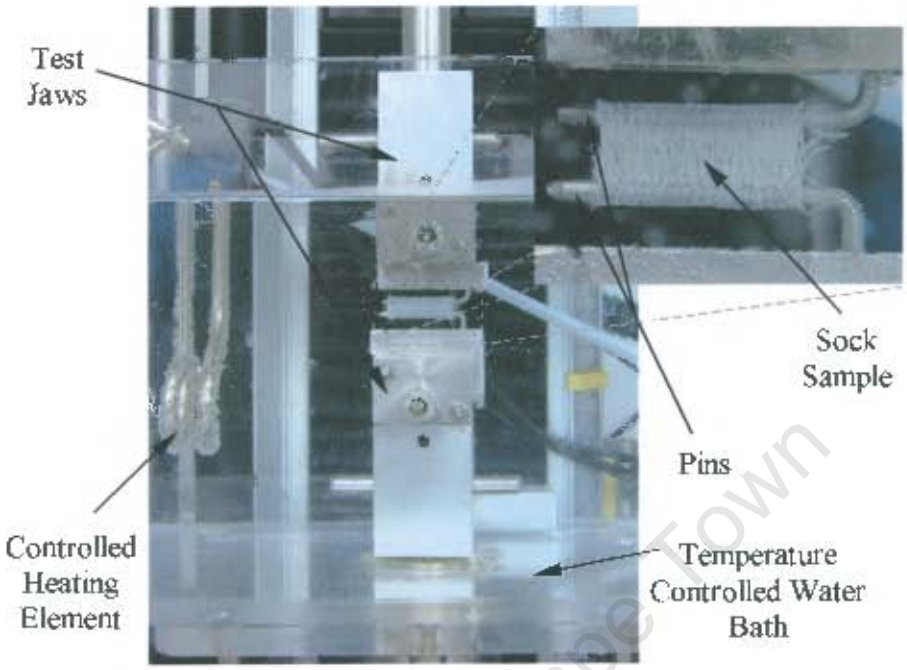

Figure 8.5: Circumferential tensile test equipment used with Instron™ tensile tester

Due to the geometry of the problem and loading conditions a quarter of the model is analysed. Figure 8.6 shows the corresponding finite element mesh.

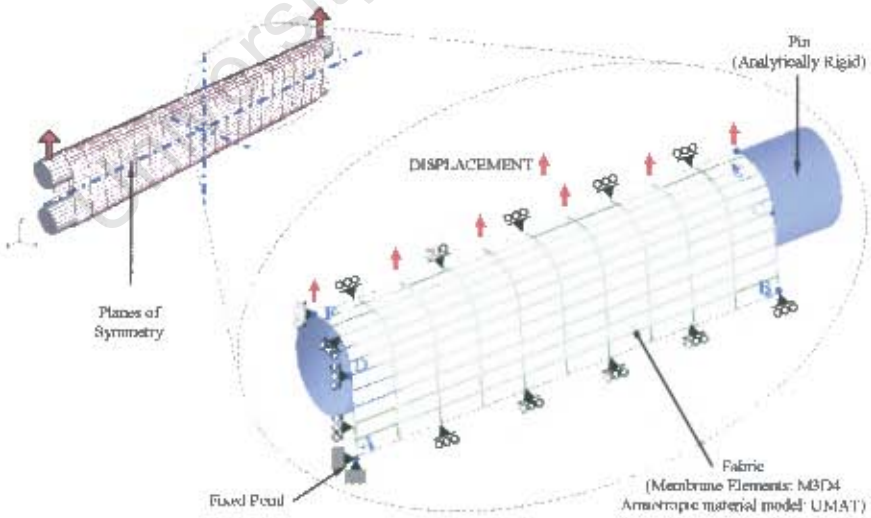

Figure 8.6: Quarter symmetric finite element mesh of circumferential tensile test

Two steps are used in the circumferential tensile model: an initial contact step, which establishes contact between the analytically rigid pin and the fabric, and a second, which displaces the top pin at 200 mm/min (Cardiovascular Implants Standards [167, 168]), until 50% circumferen-

tial strain is obtained.

The fabric UMAT model assumes that the fabric has zero bending stiffness; thus, no force is required to bend the fabric (idealistic, however the fabrics we are looking at are extremely thin and display negligible bending stiffness properties with respect to tensile characteristics). Thus, for a fabric reinforcing tube with an internal diameter of 5 mm, an initial displacement of 1.712 mm is observed without any reaction force on the pin. This is demonstrated in Figure 8.7.

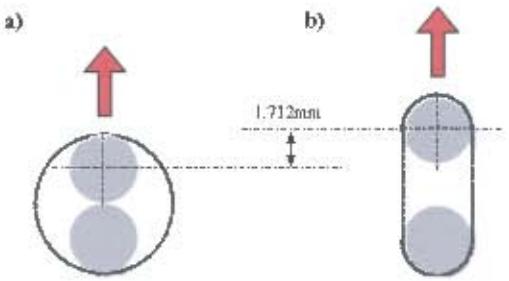

Figure 8.7: (a) Initial zero-stress state and (b) position at which total observed bending is reduced to zero in fabric reinforcing

Force per unit length in the circumferential tensile model was calculated according to:

$$\text{Force per unit length} = \frac{F}{2L}, \tag{8.13}$$

where L is the initial sample length (36.0 mm) and F the force experienced by the displaced pin. A "soft" contact model is used; this takes the form of an exponential function for the pressure-clearance relation. This allows the gradual transfer of load from the pin to fabric. The pin is assumed to be smooth and frictionless. The orientations of the material properties were mapped onto the membrane elements, ensuring that the fabric principal directions were in-plane with the membrane surface.

The longitudinal tensile test. Longitudinal fabric sample lengths of 48.0 mm were clamped flat at the ends and subjected to uniaxial tension. Figure 8.8 shows the full and quarter symmetric finite element model used to obtain the force per unit length vs. displacement curves for the fabric reinforcing in the longitudinal direction. The longitudinal tensile model uses a single step, which displaces the end of the fabric tube at a strain rate of 200 mm/min (Cardiovascular Implants Standards [167, 168]) to 100 % axial strain.

Force per unit length in the longitudinal tensile model is calculated according to

$$\text{Force Per Unit Length} = \frac{2F}{\pi\phi_i}, \tag{8.14}$$

where ϕ_i is the initial diameter and F the force.

8.5.3 The uniaxial tensile model

This model simulates uniaxial tensile tests, undertaken on an Instron™ test rig. The model is used to obtain the stress-strain curves for a fabric with a particular set of material coefficients.

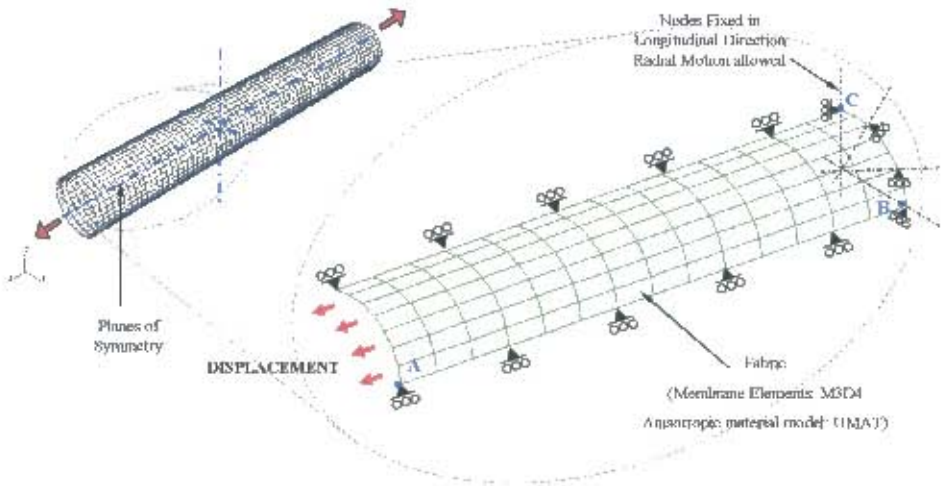

Figure 8.8: Quarter symmetric finite element model of longitudinal tensile test

The model makes full use of symmetry to simplify the analysis. A single quasi-static step is used where a fixed displacement of 9.0 mm is ramped over a period of 5.4 s. This represents a strain rate of 200 mm/min (Cardiovascular Implants Standards [167, 168]) when only half of the axial model is represented. Four-noded membrane elements are utilised in this model, where the element mesh is refined toward the free edge and displaced end. The common boundary conditions for the uniaxial tensile test can be seen in Figure 8.9 which shows the uniaxial model and its boundary and displacement conditions.

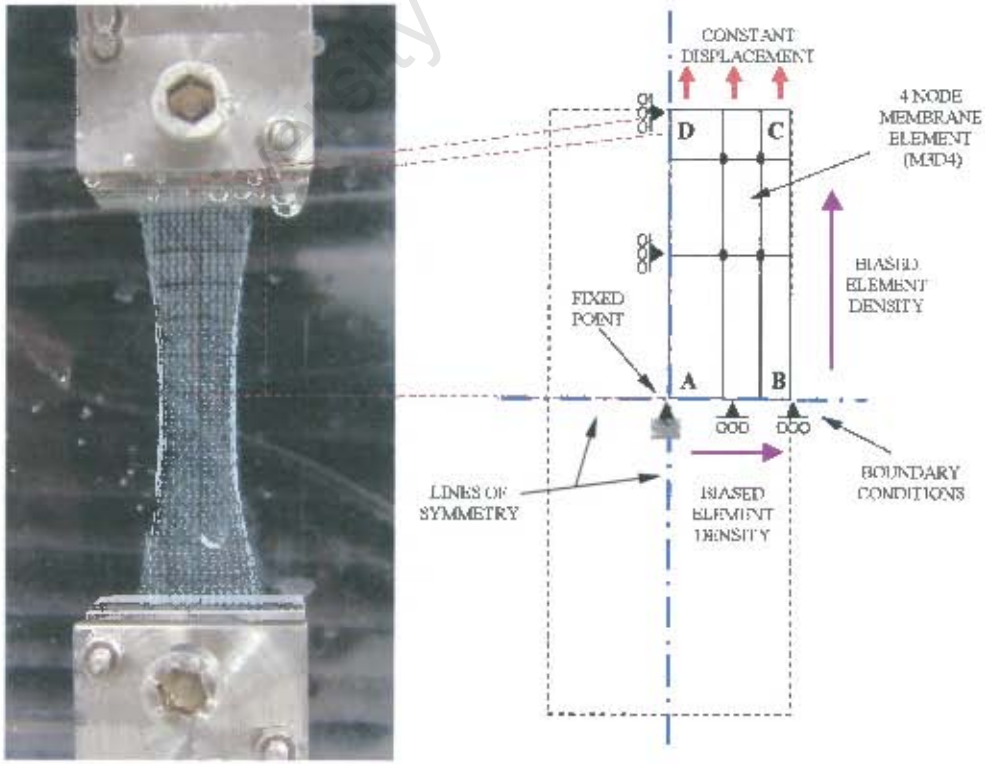

Figure 8.9: Quarter symmetric finite element model of uniaxial tensile test

Edge AB is free to move horizontally but is fixed vertically, while edges AD and DC are free to move vertically but not horizontally. For this computational model, the loaded boundary DC and the edge BC were expected to have a greater variation in stresses and deformation and therefore the element mesh is refined toward these edges.

8.6 Mesh sensitivity studies (element density)

In order to ensure acceptable accuracy, mesh sensitivity studies were performed on each of the models until a sufficient level of refinement was obtained.

To carry out a consistent mesh sensitivity study, critical points across each model were chosen for observation, where it was assumed that there would be sensitivity to mesh refinement. The number of elements were then increased and the stress and deformation states monitored to obtain stress, strain, and displacement profiles across the models. Element and density refinement was stopped when the change in stress at the critical points was considered negligible from one element number/density to the next.

Details of the mesh sensitivity analysis can be viewed in Appendix A, which shows tabular results of the critical points for the various models assessed in the mesh sensitivity analysis. It also shows graphically the variation in stress, displacement and other fields at these relevant points. Below is a brief summary of the results of Appendix A.

Graft model. For the one-eighth symmetric graft model, points A^G, B^G, C^G, D^G, C^F and D^F (refer to Figure 8.3) were chosen as critical points on the graft model. To differentiate between the porous polymer material and fabric reinforcing, superscripts G and F are used respectively. A^G and B^G lie on the lumen surface of the porous graft. Points C^G, D^G, C^F and D^F lie parallel to A^G and B^G on the external surface of the graft and fabric reinforcing. Points B^G, D^G and D^F are the end points of the graft which represent the point of graft attachment, while points A^G, C^G and C^F represent the center of the graft. These points were chosen because stress variation and deformation are expected to be greatest at these extremities. Point A^G is of most concern, as the values of displacement and pressure are used in the calculation of diastolic diameter and compliance (C_d) for the GA. CPU time is another important factor, as the GA needs not only to be effective but also efficient. All computational work was implemented on a Pentium 4, 1.7 GHz processor with 265 MBytes of memory.

A single static load step was introduced placing an internal pressure of 100 mmHg (13332 Pa) on the graft lumen wall. This pressure was ramped over a period of time, where at the end of the step the stress and deformation states for each of the critical points were assessed for increasing model element numbers. Models containing 130 ($r = 4$, $c = 4$ and $l = 6$), 210 ($r = 5$, $c = 5$ and $l = 8$), 300 ($r = 5$, $c = 6$ and $l = 10$), 414 ($r = 6$, $c = 7$ and $l = 10$), 520 ($r = 6$, $c = 8$ and $l = 10$), 616 ($r = 7$, $c = 8$ and $l = 11$), 720 ($r = 7$, $c = 9$ and $l = 11$) and 2000 ($r = 12$, $c = 18$ and $l = 35$) elements, were assessed, where r, c and l represent the number of elements

model solutions. This point was chosen to be a distance of 5 mm horizontally and vertically in from point A^U. The model mesh was adjusted to ensure that this point was represented by a node. A quasi-static displacement step was introduced displacing edge DC^U by 9.0 mm ramped over a period of 5.4 s, where at the end of the step the stress states at the critical points were assessed for models containing 50 ($x = 5$ and $y = 10$), 98 ($x = 7$ and $y = 14$), 153 ($x = 9$ and $y = 17$), 200 ($x = 10$ and $y = 20$), 253 ($x = 11$ and $y = 23$), 300 ($x = 12$ and $y = 25$), 351 ($x = 13$ and $y = 27$) and 1200 ($x = 24$ and $y = 50$) elements, where the numbers for x and y represent the number of elements in the horizontal and vertical directions respectively. Figure 8.15 shows the critical values of force/length, local axial ($E22$), transverse ($E11$) strains and CPU time obtained for the various number of elements used in the uniaxial tensile model.

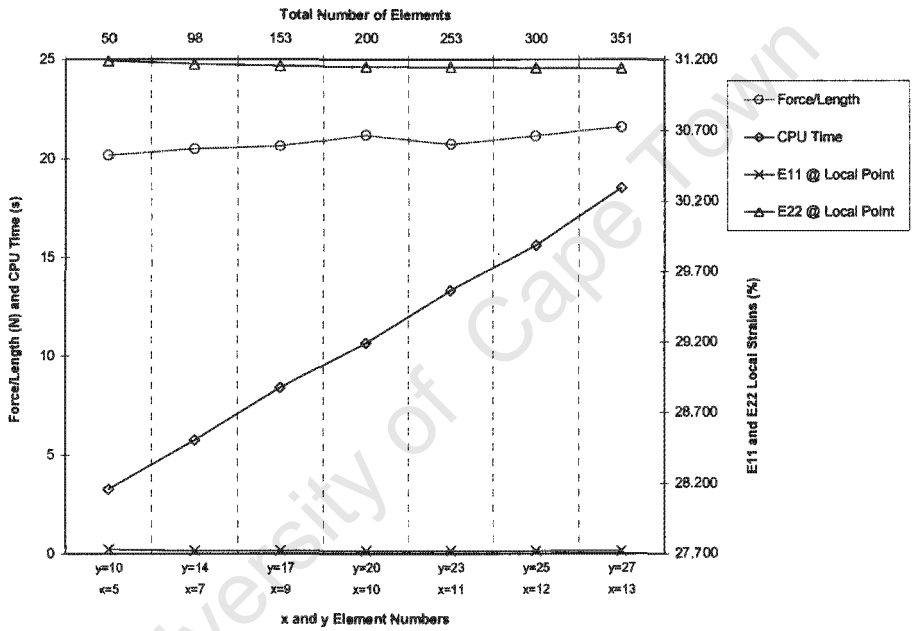

Figure 8.15: CPU time, force per unit length and local axial ($E22$) and transverse ($E11$) strains vs. element number for uniaxial tensile finite element model

As before, percentage differences to the very refined mesh model (1200 elements) were calculated for increasing mesh refinement and from this an optimal model chosen based on minimal CPU time requirements and percentage differences, the results of which can be seen in Table A.2 in Appendix A. From these differences the 200 element model was chosen as this gave percentage differences of 1.82, 0.01 and 0.06 % for force per unit length, local transverse ($E11$) and axial ($E22$) strains which are used in GA2. Stress variations at the critical points were all under 4.00 %, except at point C^U, where values are around 65 % lower than the refined mesh model. This is to be expected at point C^U, where maximum stress and strain fields are going to occur. Since this model is only used in GA2, which uses objective functions in terms of force per unit length, local transverse and axial strains this large variation in stress values at point C^U was not considered a problem. The CPU time required to run this model was 10.6 s.

edge by 10.0 mm ramped over a period of 10 s, where at the end of the step the stress states at the critical points were assessed for models containing 98 ($c = 7$ and $l = 14$), 200 ($c = 10$ and $l = 20$), 300 ($c = 12$ and $l = 25$), 392 ($c = 14$ and $l = 28$), 480 ($c = 16$ and $l = 30$), 595 ($c = 17$ and $l = 35$), 684 ($c = 18$ and $l = 38$) and 3200 ($c = 40$ and $l = 80$) elements, where c and l represent the number of elements in the circumferential and longitudinal directions respectively. Figure 8.14 shows the critical values of force/length, circumferential strain and CPU time obtained for the various number of elements used in the longitudinal tensile model.

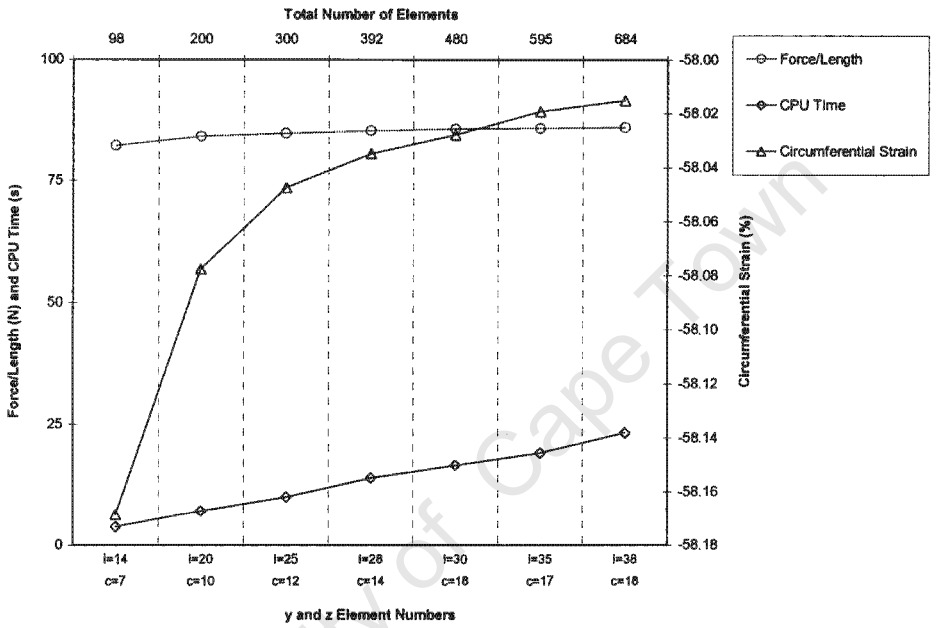

Figure 8.14: CPU time, force per unit length and circumferential strain vs. element number for longitudinal tensile finite element model

From Figure 8.14 convergence is obtained with increasing elements. As before the percentage difference to the very refined mesh model (3200 elements) was calculated and an optimal model chosen based on CPU time requirements and minimal percentage differences, the results of which can be seen in Table A.4 in Appendix A. The 480 element model was chosen for both the GA and final model runs, as differences of 1.85 and 0.01 % were seen between this and the 3200 element model for force per unit length and circumferential strain respectively, while stress variations were all under 12.9 % at all critical points. The CPU time required to run this model was 16.6 s, which is low compared to the circumferential tensile model, which it is used with in GA3.

Uniaxial tensile model. Similarly for the uniaxial tensile model, points A^U, B^U, C^U and D^U (refer to Figure 8.9) were chosen as critical points. These points lie at the corners of the FE model and represent the centre of the fabric (A^U), the edge of the fabric (B^U) the centre of the displaced edge (C^U) and the corner of the displaced edge (D^U). Points A^U, C^U and D^U were chosen, because the stress variation is expected to be great while point B was chosen for displacement variation. Another point, E^U is used to analyse localised experimental strains to

quasi-static displacement step was introduced, displacing the rigid pin by 9.0 mm ramped over a period of 10 s, where at the end of the step the stress states at these critical points were assessed for models containing 20 ($y = 2$, $c = 2$ and $l = 5$), 110 ($y = 5$, $c = 6$ and $l = 10$), 200 ($y = 10$, $c = 10$ and $l = 10$), 520 ($y = 10$, $c = 16$ and $l = 20$), 600 ($y = 14$, $c = 16$ and $l = 20$), 800 ($y = 20$, $c = 20$ and $l = 20$) and 1856 ($y = 28$, $c = 30$ and $l = 32$) elements, where y, c and l represent the number of elements in the vertical, circumferential and longitudinal directions respectively. Figure 8.13 shows the critical values of force/length, axial strain and CPU time obtained for the various number of elements used in the circumferential tensile model.

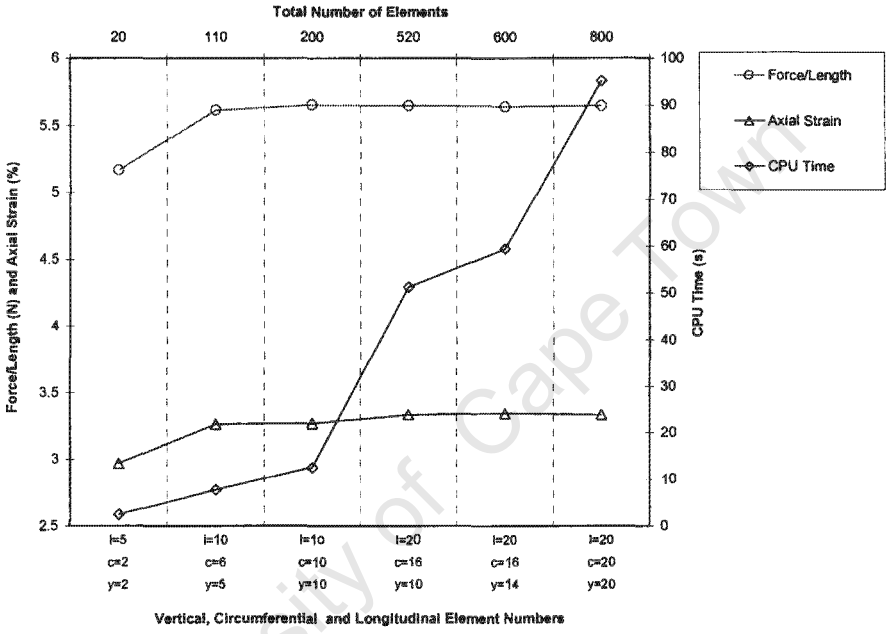

Figure 8.13: CPU time, force per unit length and axial strain vs. element number for circumferential tensile finite element model

Again, convergence is seen with an increase in number of elements. In a similar manner the percentage difference to the converged solution of the very refined mesh model (1056 elements) was calculated and an optimal model chosen based on CPU time requirements and minimal percentage differences (refer to Table A.3 in Appendix A). From this it was found that the 520 element model gave the desired results where a difference of 0.03 % was observed in force per unit length and 0.45 % in axial strain while no difference was observed in the circumferential strain. Stress variation was less than 1.5 % between this 520 element model and the fine mesh model, only major differences were observed for axial stresses ($S11$) at points A, B and F, with variations of 38.0, 27.2 and 69.9 %. The CPU time required to run this model was 51.2 s, which is considered sufficiently low for the GA.

Longitudinal tensile model. For the longitudinal tensile model, points A^L and B^L (refer to Figure 8.8) were chosen as critical points. Points A^L and B^L lie at the end of the fabric tube and the center, respectively. A quasi-static displacement step was introduced displacing the clamped

its efficiency. However, once GA1 had obtained a good solution the 520 element model would be used to obtain the final results. [Further details of the element model field values at these points and percentage errors can be viewed in Table A.1 of Appendix A.]

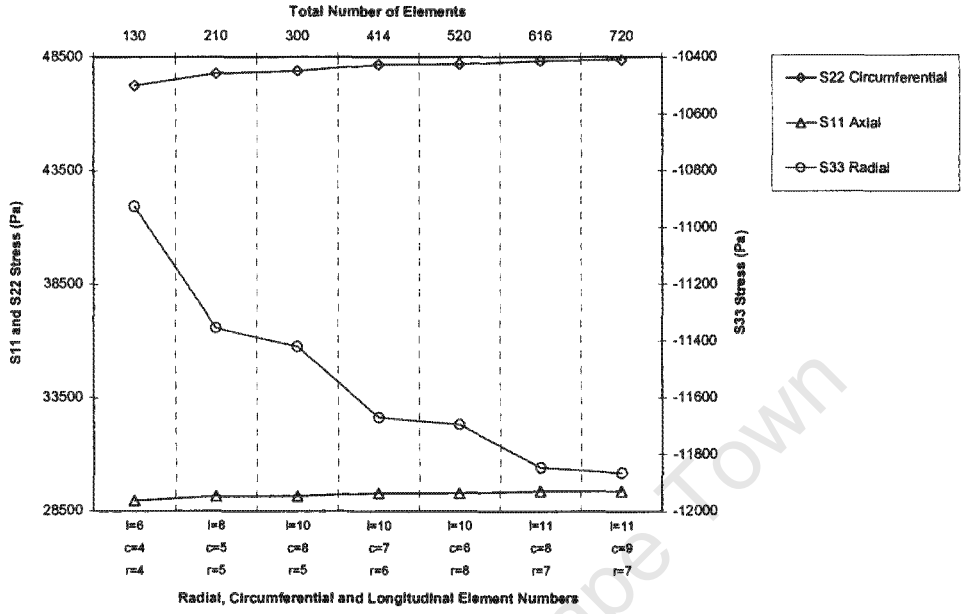

Figure 8.11: Stress values at point A^G vs. element number

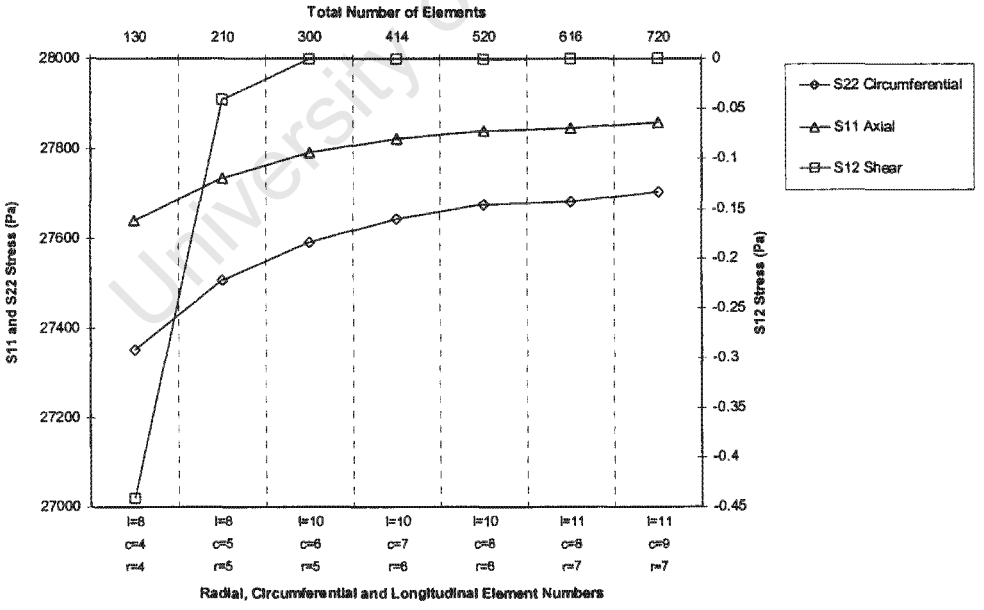

Figure 8.12: Stress values at Point C^F vs. element number

Circumferential tensile model. Similarly for the circumferential tensile model, points A^C, C^C, D^C and E^C (refer to Figure 8.6) were chosen as critical points, as they were expected to have the greatest stress variation, while points B^C and F^C were chosen for displacement variation. A

in the radial, circumferential and longitudinal directions respectively.

Figures 8.10, 8.11 and 8.12 show the critical values of internal diameter and stresses at points A^G and C^F also the CPU time and compression seen by the wall between points A^G and C^G used in the graft finite element model. From these figures it can be seen that with increased element number there is convergence on consistent stress and strain values, while CPU time increases. From the 2000 element graft finite element model it took a total of 3185 s to run, and obtain the following results: ID = 3.879 mm, graft wall compression=4.962 %, $S22 = 48800$ Pa, $S11 = 29640$ Pa and $S33 = -12290$ Pa for Point A^G and $S22 = 27780$ Pa and $S11 = 27910$ Pa for point C^F (where $S22$, $S11$ and $S33$ are circumferential, axial and radial stresses respectively). Setting this as our reference finite element model, the lower element model percentage differences were calculated for the various field variables at the critical points.

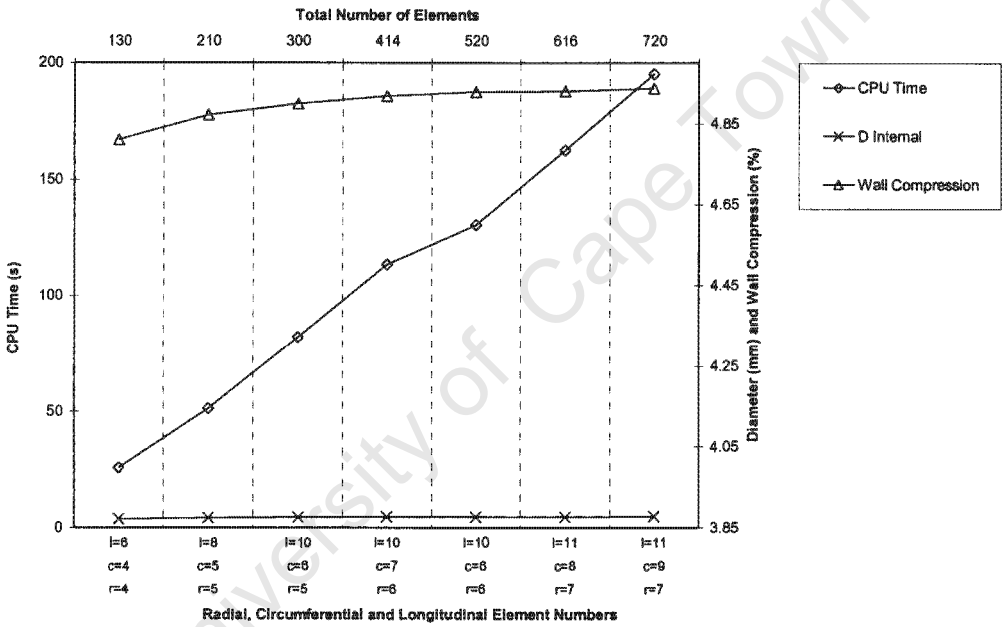

Figure 8.10: CPU time, internal diameter at point A^G and wall compression between A^G and C^G vs. element number for graft finite element model

The 130 element model took 25.7 s to run and gave percentage differences of 11.13 % for $S33$ at point A^G and 0.18 % for internal diameter. From the results it was observed that the 520 element model gave a maximum difference of 4.88 % for $S33$ at point A^G and 0.04 % for internal diameter and ran to completion in 130 s, which was considered sufficient for the requirements of GA1. However, when utilising this in GA1 and including the dynamic pulse pressure step in the analysis the time for completion was increased 10 fold to 1240 s which was considered inefficient. Thus it was decided that since the objective function was dependent on the internal diameter and also the stress-strain characteristics of the fabric, the 210 element model which gave a maximum difference of 0.13 % for internal diameter and 0.98 % for circumferential stress while only taking 51 s to run to completion was considered a better model to use in GA1 to maximise

Chapter 9

The Genetic Algorithms and Implemented Process

9.1 Introduction

This chapter proceeds with a description of GA1 and its implementation with the graft finite element model to find the fabric coefficients which optimise the compliance of the fabric reinforced grafts. The objective, penalty and fitness functions of GA1 are also presented. Objective, penalty and fitness functions for a second and third genetic algorithm, known as GA2 and GA3, are given. GA2 is used to find the fabric coefficients which best describe the uniaxial tensile test data of physical fabric samples; this is used to validate the fabric constitutive material model. GA3 is used to find the fabric coefficients which best describe the circumferential and longitudinal tensile properties of physical fabric tubes.

9.2 The genetic algorithms and the optimisation process

The basis of this work is to find the requirements of a fabric reinforcing so that a porous graft structure has a specific compliance, displays nonlinear stiffening, and has a preferred diastolic internal diameter, while maintaining its structural integrity. Optimisation and modelling techniques are utilised to enhance the search for the best fabric reinforcing, with a view to finding successful solutions to small to medium diameter prosthetic grafts. Figure 9.1 shows a schematic approach to finding the optimal fabric reinforcing by using finite element modelling and optimisation techniques.

Perl® a free ware scripting computer language is used to code the GA. This implements and analyses the finite element models in ABAQUS®, the results of which are then read and utilised in the objective, penalty and fitness functions of the GA. The process is repeated until desired results are obtained or a pre-defined number of generations is reached.

Three GAs are utilised in the work, namely GA1, GA2 and GA3. The first, GA1, optimises the fabric model coefficients C, a_1, a_2, a_3, a_4, a_5, a_6, a_7, a_8 and a_9 (see equation (4.121)) to obtain a dynamic compliance (C_d) of 6 %/100 mmHg, a diastolic diameter (d_{dia}) of 4.00 mm, and to display nonlinear stiffening from a dynamic graft finite element model. A number of "good" solutions are kept over the generations, and are then utilised in tensile test models to obtain a range of circumferential and longitudinal tensile stress-strain requirements for the adventitial fabric reinforcing.

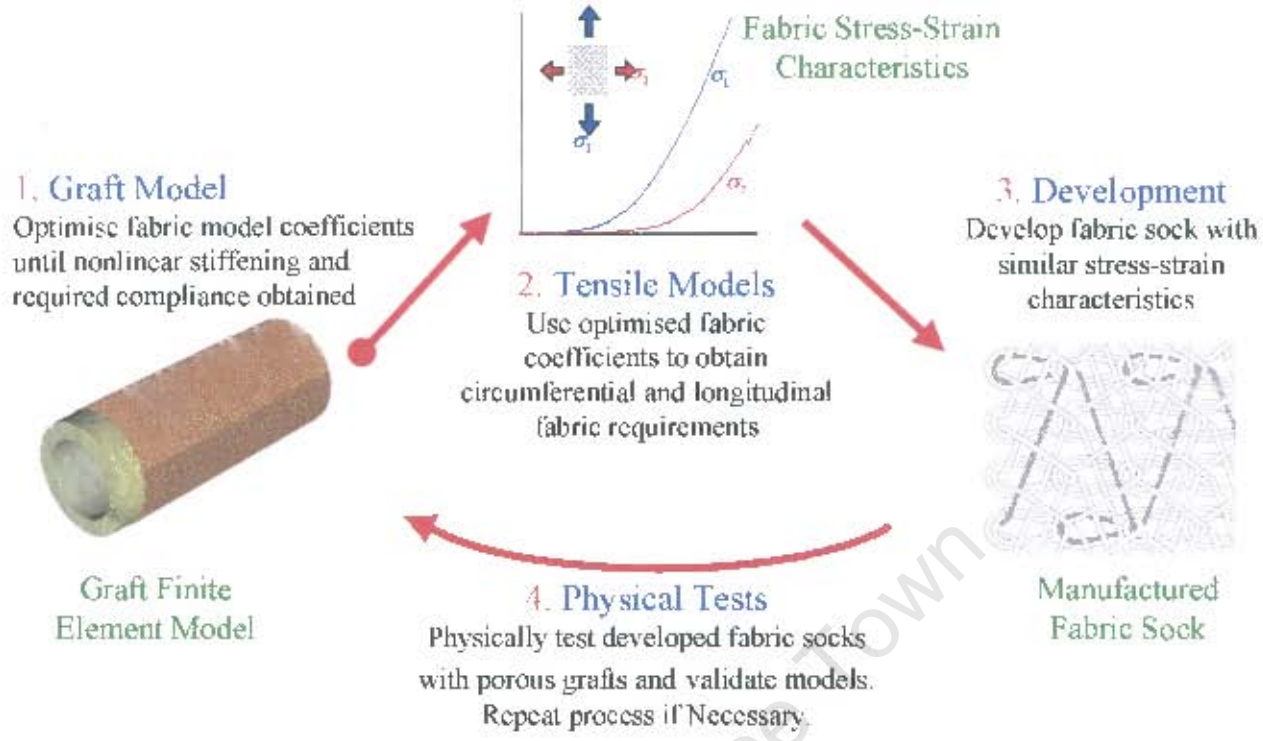

Figure 9.1: Process of finding the fabric reinforcing requirements

The second, GA2, optimises the fabric model coefficients to obtain mutually orthogonal uniaxial stress-strain curves for a number of physically tested fabrics. This GA runs mutually orthogonal uniaxial tensile test finite element models for a single set of fabric coefficients, to obtain stress-strain characteristics in the warp and weft directions. These coefficients are then optimised until they resemble physically tested data. GA2 is used to obtain comparative data for the modelling process and to identify the ability of the fabric constitutive model to describe fabric uniaxial tensile behaviour.

GA3 is similar to GA2, except that circumferential and longitudinal tensile models are implemented. Figure 9.2 shows a flow chart of the Perl® script for the three GAs.

9.2.1 GA dynamic search space

Range: The search space of the GAs is dynamically adjusted over the generations; an initial range is set for each coefficient and thereafter the range is biased between the first and second ranked solutions of the previous generation. The range is biased 3 : 2 toward the first ranked solution. The search space range is also reduced linearly, by 2.5 % over each generation, confining and refining the search area after each generation. The initial search space coefficient ranges are: $0.0 < C \leqslant 20000.0$ and $0.0 \leqslant a_i \leqslant 20.0$, with the initial values $C = 10000.0$ and $a_i = 10.0$.

An explicit constraint is made on the search space range of coefficient C over the generations, which ensures that this value remains positive. Thus

$$\{C | C \geq 0.0\} \tag{9.1}$$

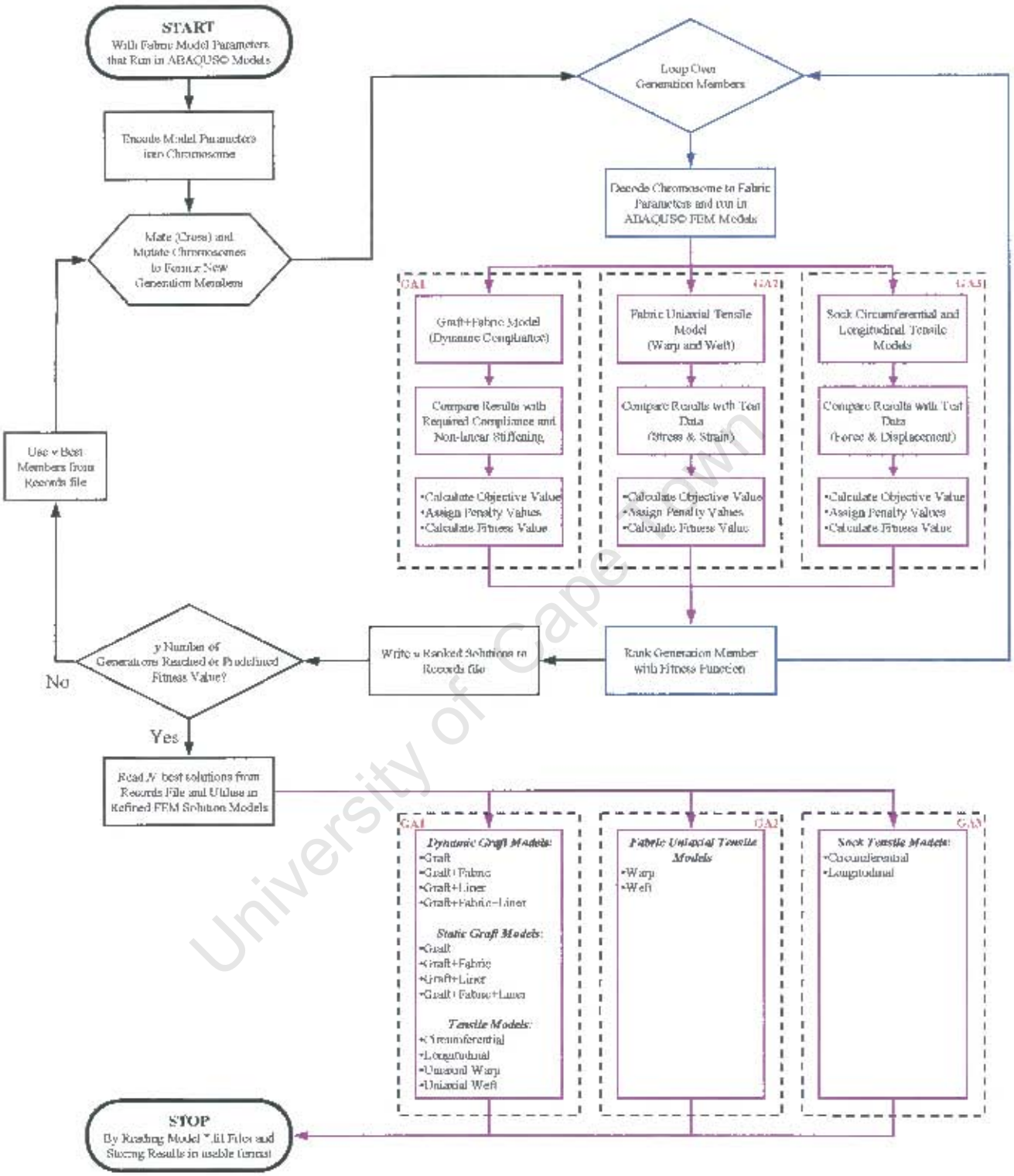

Figure 9.2: Flow chart of Perl® Script used to implement GAs

Due to the mathematical material model for the fabric described by equation (4.121), allowing the coefficient C to be negative would allow fabric compressive or zero stress solutions under tensile strain, which is not realistic. Thus, by constraining C to be positive the number of useful population members in a generation is maximised. With the dynamic range being biased 3 : 2

toward the first ranked solution, if the first ranked solution coefficient C tends to zero then the range would be reduced more than 2.5 % per generation. To prevent this, if C tends to zero the range is reduced by 2.5 % and then shifted so that it is always greater than zero.

Resolution: To increase the chances of finding "good" solutions efficiently while maximising the search capabilities of the GA, the accuracy or resolution of the search space after each generation was increased. Initially the resolution is low, giving a large yet sparse search space. This allows the GA to maximise its search initially over a wide range. Later, as the resolution increases and the search space is reduced, the GA is constrained to refining the "good" solutions obtained.

Initially an n bit binary number is used to encode each scaled coefficient into the chromosome; this gives a resolution of $\{R\}/2^n$, where $\{R\}$ represents the coefficient range and n the bit size. Thus initially a 5 bite binary number is used giving resolutions of $a_i : \frac{20}{2^5} = 0.625$ and $C : \frac{20000}{2^5} = 625.0$. The resolution or bit size is increased every 10^{th} generation. Thus by the 50^{th} generation the bit size would be 10, and bearing in mind that the range $\{R\}$ would be reduced by 50%, the final resolution used would be $a_i : \frac{10}{2^{10}} = 9.7656 \times 10^{-3}$ and $C : \frac{10000}{2^{10}} = 9.7656$.

Figure 9.3 shows graphically how a two dimensional parameter search space is reduced from $(x^{G1}_{\max} - x^{G1}_{\min})$ to $(x^{G2}_{\max} - x^{G2}_{\min})$, biased 3 : 2 between the first and second ranked solutions of generation 1 ($1st^{G1}$, $2nd^{G1}$) and the resolution of the search increased from n^{G1}_x to n^{G1}_x for parameter x and n^{G1}_y to n^{G1}_y for parameter y.

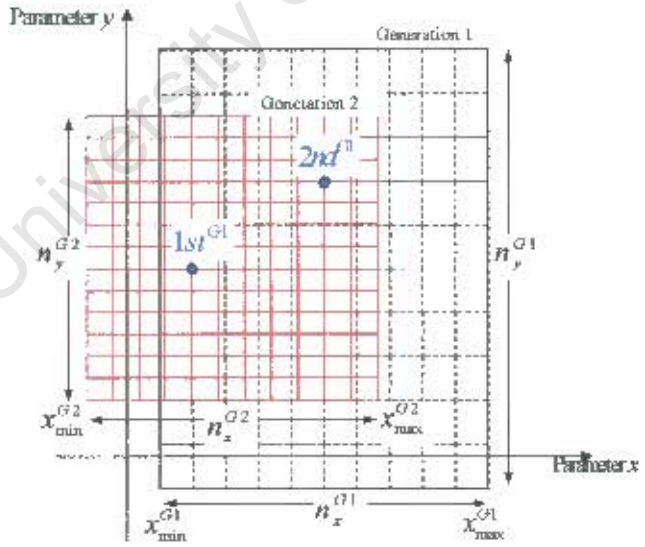

Figure 9.3: Schematic illustrating change in parameter range and resolution from one generation to another

9.2.2 GA termination

The termination of the GAs is set when a certain fitness value $f(C, a_i)$ is achieved, or when 50 generations has been reached. Typically, good solutions were found within 35 generations

for GA1, 40 generations for GA2, while GA3 obtained reasonable solutions but not the desired fitness value.

9.2.3 The objective, penalty and fitness functions for GA1

The solution sought by GA1 requires a specified compliance value (C_d), a certain diastolic diameter (d_{dia}), and needs to display a nonlinear stiffening characteristic by optimising the fabric coefficients C, a_1, a_2, a_3, a_4, a_5, a_6, a_7, a_8 and a_9. Thus, the objective function is a weighted summation of the partial objective functions, where the partial objective functions depend on the normalised difference between the finite element model solution and the target solution for each of these desired graft characteristics. The fitness function is a penalty weighted function of the objective function. The following section describes the various partial objective functions, penalty functions and finally the fitness function of GA1.

Figure 9.4 shows two pressure-diameter curves, one obtained from the numerical model and the other the desired solution.

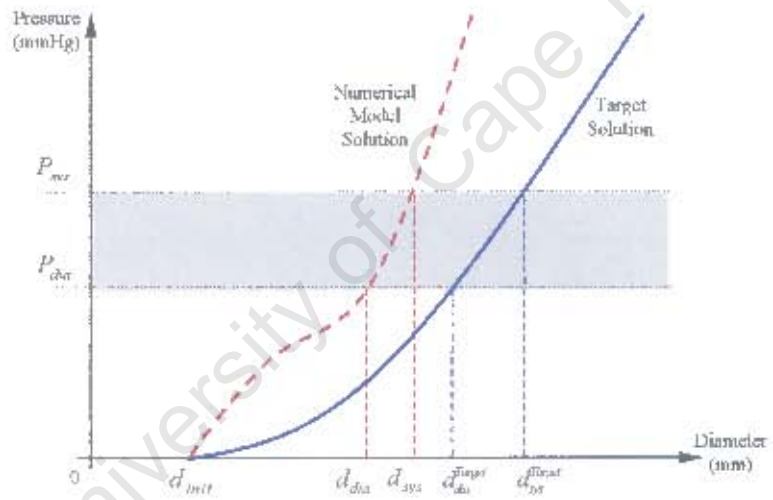

Figure 9.4: Pressure vs. diameter curves showing numerical solution and target solution

Values indicated on Figure 9.4 are initial internal diameter (d_{init}), diastolic and systolic internal model diameters (d_{dia}, d_{sys}), diastolic and systolic pressures (P_{dia}, P_{sys}), target internal diastolic diameter (d_{dia}^{Target}), and target compliance (C_d^{Target}). Values of d_{dia}, d_{sys}, P_{dia} and P_{sys} are obtained from the dynamic graft finite element model analysis, from which model compliance (C_d) and a nonlinear stiffening characteristic (J) are calculated according to

$$C_d = \frac{d_{sys} - d_{dia}}{d_{dia}} \times \frac{100}{P_{sys} - P_{dia}} \times 100\,, \tag{9.2}$$

$$J = \frac{(d_{dia} - d_{init})(P_{sys} - P_{dia}) - P_{dia}(d_{sys} - d_{dia})}{P_{dia}}\,. \tag{9.3}$$

The nonlinear stiffening characteristic J is simply the difference in diameter change per unit

pressure from zero to P_{dia} and from P_{dia} to P_{sys}. C_d and d_{dia} are used to calculate the partial objective values for the model, while j is used as a penalty function.

Objective and partial objective functions. From equation (9.2) a partial objective function formulated for compliance, is given by

$$\phi^{\triangle C_d} = \left[1 - \left\{\left|\triangle C_d^{normalised}\right| \left(\frac{1}{(m^{\wedge C_d} - 1)}\right)\right\}\right], \tag{9.4}$$

where

$$\triangle C_d^{normalised} = \frac{C_d - C_d^{target}}{C_d^{target}}, \tag{9.5}$$

$$m^{\wedge C_d} = \begin{Bmatrix} 1 + \left|\frac{C_d^{max} - C_d^{target}}{C_d^{target}}\right| & \text{for: } C_d > C_d^{target} \\ 1 + \left|\frac{C_d^{min} - C_d^{target}}{C_d^{target}}\right| & \text{for: } C_d \leq C_d^{target} \end{Bmatrix}. \tag{9.6}$$

From (9.4), $\phi^{\triangle C_d}$ tends to unity as C_d approaches C_d^{target}. This is graphically represented in Figure 9.5.

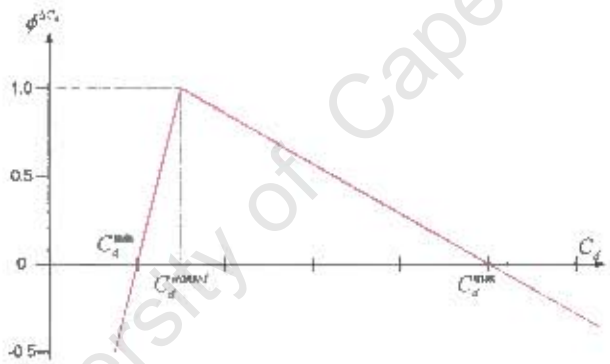

Figure 9.5: Graphical representation of partial objective function $\phi^{\wedge C_d}$

From the obtained d_{dia}, a partial objective function is formulated for the diastolic diameter, this is given by

$$\phi^{\wedge d_{dia}} = \left[1 - \left\{\left|\triangle d_{dia}^{Normalised}\right| \left(\frac{1}{(m^{\triangle d_{dia}} - 1)}\right)\right\}\right], \tag{9.7}$$

where

$$\triangle d_{dia}^{normalised} = \frac{d_{dia} - d_{dia}^{target}}{d_{dia}^{target}}, \tag{9.8}$$

$$m^{\wedge d_{dia}} = \begin{Bmatrix} 1 + \left|\frac{d_{dia}^{max} - d_{dia}^{target}}{d_{dia}^{target}}\right| & \text{for: } d_{dia} > d_{dia}^{target} \\ 1 + \left|\frac{d_{dia}^{min} - d_{dia}^{target}}{d_{dia}^{target}}\right| & \text{for: } d_{dia} \leq d_{dia}^{target} \end{Bmatrix}. \tag{9.9}$$

Like equation (9.4), (9.7) tends to unity as the model diastolic diameter d_{dia} tends to the target diastolic diameter d_{dia}^{target}.

The parameters $m^{\Delta C_d}$ and $m^{\Delta d_{dia}}$ are multiples used to bias future generations from a certain side and partially to penalise $\phi^{\Delta C_d}$ and $\phi^{\Delta d_{dia}}$, respectively. For example, due to tissue ingrowth in the porous grafts, compliance will be reduced after implantation; thus higher compliance values are preferred. From Figure 9.5 it can be seen that the partial objective value $\phi^{\Delta C_d}$ is biased towards model C_d values which are greater than C_d^{target}. These parameters are also used to partially penalise $\phi^{\Delta C_d}$ and $\phi^{\Delta d_{dia}}$ by making them negative if model C_d or d_{dia} go above or below pre-defined boundary values $C_d^{\max}$and $C_d^{\min}$. Thus,

$$\text{if } \left\{C_d | C_d \leq C_d^{\min} \text{ and } C_d \geq C_d^{\max}\right\} \text{ then } \phi^{\Delta C_d} \text{ is negatively weighted}, \tag{9.10}$$

$$\text{if } \left\{d_{dia} | d_{dia} \leq d_{dia}^{\min} \text{ and } d_{dia} \geq d_{dia}^{\max}\right\} \text{ then } \phi^{\Delta d_{dia}} \text{ is negatively weighted}. \tag{9.11}$$

From these partial objective functions an objective function

$$\phi^{GA1} = \frac{\left(w^{C_d} \times \phi^{\Delta C_d^{dyn}}\right) + \left(w^{d_{dia}} \times \phi^{\Delta d_{dia}}\right)}{\left(w^{C_d} + w^{d_{dia}}\right)} \tag{9.12}$$

is used to calculate the objective value, where w^{C_d} and $w^{d_{dia}}$ are pre-defined weightings used to bias the objective value to either the compliance or diastolic diameter. From (9.12), ϕ^{GA1} will tend to unity as $\phi^{\Delta C_d^{dyn}}$ and $\phi^{\Delta d_{dia}}$ tend to unity.

Global penalties. The following are the global penalties for GA1:

$$\text{if } C_d \leqslant 0.0\%/100mmHg \text{ then } p^{GA1} = -\infty \text{, else } p^{GA1} = 1, \tag{9.13}$$

$$\text{if } C_d = C_d^{target} \text{ then } p^{GA1} = -\infty \text{, else } p^{GA1} = 1, \tag{9.14}$$

$$\text{if } d_{dia} = d_{dia}^{target} \text{ then } p^{GA1} = -\infty \text{, else } p^{GA1} = 1, \tag{9.15}$$

$$\text{if } j \leqslant 0.0 \text{ then } p^{GA1} = -\infty \text{, else } p^{GA1} = 1. \tag{9.16}$$

Equation (9.13) ensures that the finite element results give an expected positive compliance. With equations (9.14) and (9.15), although we are optimising for C_d^{target} and d_{dia}^{target}, due to numerical errors, such as round-off, these exact solutions will never be achieved. Equation (9.16) ensures that those solutions which do not display nonlinear stiffening are dismissed. Thus these penalties ensure that models which do not converge or show no nonlinear stiffening are eliminated from future generations. While the partial penalties described by (9.10) and (9.11) only weight a solution negatively, but do not necessarily expel the solution from future generations.

Fitness function. The following fitness function is used to compare the finite element solution to the required solution in GA1:

$$\text{Fitness Function } f^{GA1} = p^{GA1} \times \phi^{GA1}. \tag{9.17}$$

9.2.4 The objective, penalty and fitness functions for GA2

The solution sought by GA2 is a set of fabric material model coefficients (C, a_1, a_2, a_3, a_4, a_5, a_6, a_7, a_8 and a_9) which best describe a physical fabric under uniaxial tension in mutually orthogonal directions (warp and weft). The same fabric material model coefficients are utilised in two fabric uniaxial tensile models, one describing uniaxial tension in the warp and the other in the weft direction. This is implemented in the finite element model input deck by swapping the material model terms a_1 with a_2, a_5 with a_6, and a_8 with a_9. The fabric material model is optimised to the warp and weft uniaxial stress-strain characteristics of a physically tested fabric, as well as localised axial and transverse strains. The numerical results for axial stress (σ), localised axial strain (ε_A), and localised transverse strain (ε_T) are collected from both the warp and weft models and are compared with physical data.

Figure 9.6 shows a physical test fabric sample (tested in the warp direction), from which localised axial and transverse strains are obtained at corresponding pre-defined axial strains. The representative quarter symmetric numerical solution is also illustrated. Field variable superscripts represent either model or physical data, n represents material orientation (warp or weft), while subscripts represent axial, A or transverse, T strains or stress and i represents the pre-defined axial strain at which the field variables are obtained (10, 20 or 30 %).

For the same fabric material coefficients, the numerical warp and weft model solutions of stress, localised axial and transverse strains at pre-defined axial strains of 10, 20 and 30 % are compared to physical data from which partial objective values are calculated. These partial objective functions are formulated from the normalised differences between the model and data solutions. The corresponding model and data curves are illustrated in Figure 9.7 for a particular fabric orientation (warp or weft).

From physical data, the following are collected for pre-defined axial strains of 10, 20 and 30 %: axial stress (σ_{Ai}^{Data}), localised axial strain (ε_{Ai}^{Data}) and localised transverse strain (ε_{Ti}^{Data}), while from the model the equivalent model solutions are collected: σ_{Ai}^{Model}, ε_{Ai}^{Model} and ε_{Ti}^{Model}. From these the partial objective values are calculated.

Objective and partial objective functions. The stress partial objective functions for GA2 are

$$\phi^{\sigma_A^n} = \frac{\sum_{i=10\%,10\%}^{30\%} w_{\sigma_{Ai}}^n \left[1 - \left\{ |\triangle \sigma_{Ai}^n| \left(\frac{1}{\left(m_{\sigma_{Ai}}^n - 1\right)} \right) \right\} \right]}{\sum_{i=10\%,10\%}^{30\%} w_{\sigma_{Ai}}^n}, \tag{9.18}$$

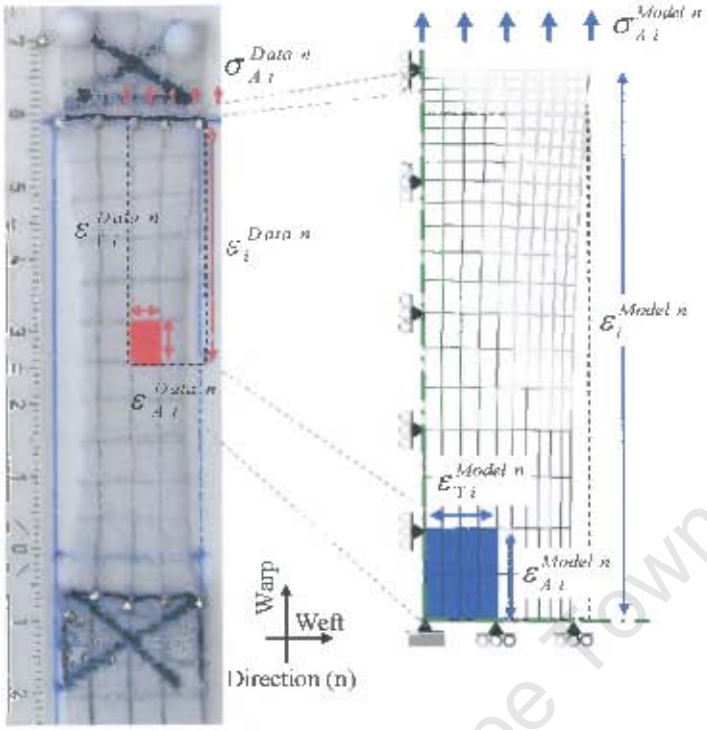

Figure 9.6: Uniaxial tensile fabric test and numerical solution illustrating GA2 parameters used

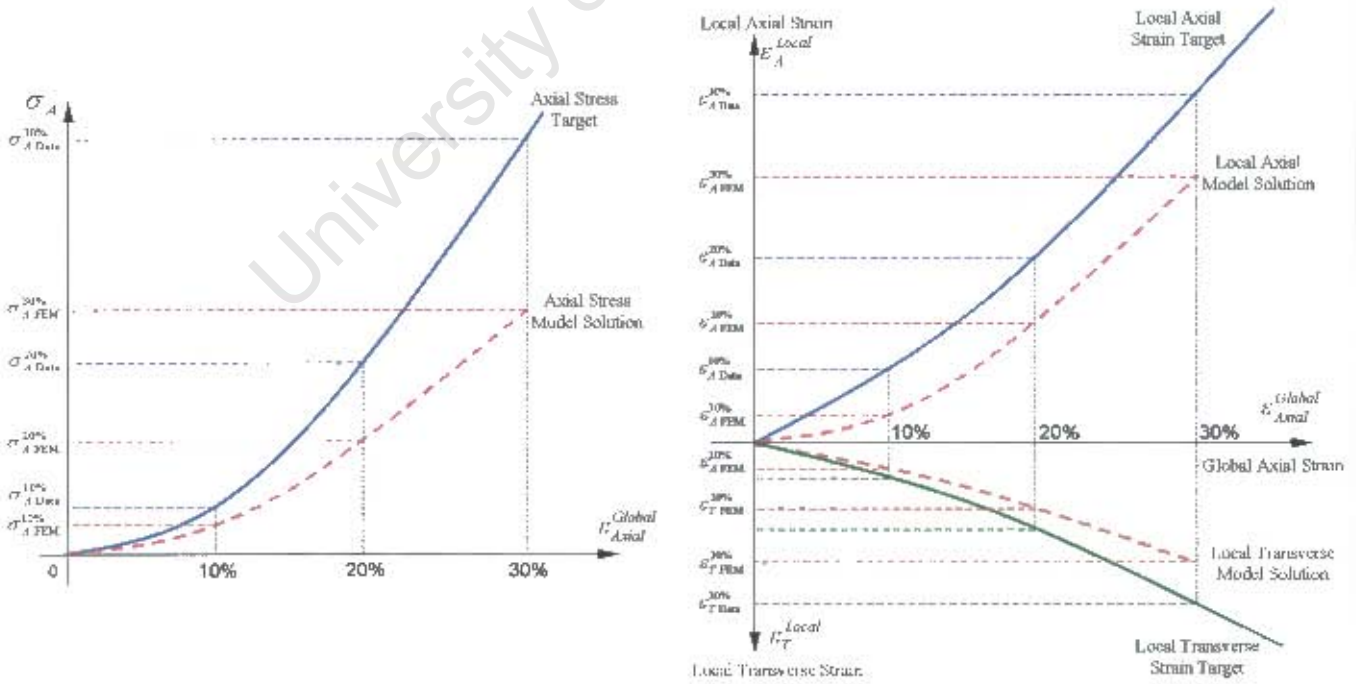

Figure 9.7: Uniaxial tensile numerical solution vs. target solution

where n is the direction of the uniaxial tensile test (warp or weft), i the pre-defined axial strains of 10, 20 and 30%, $w^n_{\sigma_A}$ are the weightings for the pre-defined axial strain field values,

$$\triangle\sigma^n_{Ai} = \frac{\sigma^{Model\,n}_{Ai} - \sigma^{Data\,n}_{Ai}}{\sigma^{Data\,n}_{Ai}}, \tag{9.19}$$

and

$$m^n_{\sigma_{Ai}} = \begin{cases} 1 + \left|\frac{\sigma^{\max\,n}_{Ai} - \sigma^{Data\,n}_{Ai}}{\sigma^{Data\,n}_{Ai}}\right| & \text{for: } \sigma^{Model\,n}_{Ai} > \sigma^{Data\,n}_{Ai} \\ 1 + \left|\frac{\sigma^{\min\,n}_{Ai} - \sigma^{Data\,n}_{Ai}}{\sigma^{Data\,n}_{Ai}}\right| & \text{for: } \sigma^{Model\,n}_{Ai} \leq \sigma^{Data\,n}_{Ai} \end{cases}. \tag{9.20}$$

Similarly, the partial objective functions for localised axial strains are

$$\phi^{\varepsilon^n_A} = \frac{\sum_{i=10\%,10\%}^{30\%} w^n_{\varepsilon_{Ai}} \left[1 - \left\{|\triangle\varepsilon^n_{Ai}| \left(\frac{1}{(m^n_{\varepsilon_{Ai}} - 1)}\right)\right\}\right]}{\sum_{i=10\%,10\%}^{30\%} w^n_{\varepsilon_{Ai}}} \tag{9.21}$$

where

$$\triangle\varepsilon^n_{Ai} = \frac{\varepsilon^{Model\,n}_{Ai} - \varepsilon^{Data\,n}_{Ai}}{\varepsilon^{Data\,n}_{Ai}}, \tag{9.22}$$

$$m^n_{\varepsilon_{Ai}} = \begin{cases} 1 + \left|\frac{\varepsilon^{\max\,n}_{Ai} - \varepsilon^{Data\,n}_{Ai}}{\varepsilon^{Data\,n}_{Ai}}\right| & \text{for: } \varepsilon^{Model\,n}_{Ai} > \varepsilon^{Data\,n}_{Ai} \\ 1 + \left|\frac{\varepsilon^{\min\,n}_{Ai} - \varepsilon^{Data\,n}_{Ai}}{\varepsilon^{Data\,n}_{Ai}}\right| & \text{for: } \varepsilon^{Model\,n}_{Ai} \leq \varepsilon^{Data\,n}_{Ai} \end{cases}. \tag{9.23}$$

The local transverse strains partial objective functions are

$$\phi^{\varepsilon^n_T} = \frac{\sum_{i=10\%,10\%}^{30\%} w^n_{\varepsilon_{Ti}} \left[1 - \left\{|\triangle\varepsilon^n_{Ti}| \left(\frac{1}{(m^n_{\varepsilon_{Ti}} - 1)}\right)\right\}\right]}{\sum_{i=10\%,10\%}^{30\%} w^n_{\varepsilon_{Ti}}}, \tag{9.24}$$

where

$$\triangle\varepsilon^n_{Ti} = \frac{\varepsilon^{Model\,n}_{Ti} - \varepsilon^{Data\,n}_{Ti}}{\varepsilon^{Data\,n}_{Ti}}, \tag{9.25}$$

$$m^n_{\varepsilon_{Ti}} = \begin{cases} 1 + \left|\frac{\varepsilon^{\max\,n}_{Ti} - \varepsilon^{Data\,n}_{Ti}}{\varepsilon^{Data\,n}_{Ti}}\right| & \text{for: } \varepsilon^{Model\,n}_{Ti} > \varepsilon^{Data\,n}_{Ti} \\ 1 + \left|\frac{\varepsilon^{\min\,n}_{Ti} - \varepsilon^{Data\,n}_{Ti}}{\varepsilon^{Data\,n}_{Ti}}\right| & \text{for: } \varepsilon^{Model\,n}_{Ti} \leq \varepsilon^{Data\,n}_{Ti} \end{cases}. \tag{9.26}$$

The difference in stress and localised axial and transverse strain values from model and test results are taken at 10, 20 and 30 % axial strain in the warp and weft directions. This difference is normalised and then weighted to ensure that those solutions which model the test results accurately at lower strains are retained for further generations. As with GA1, the partial objective values tend to unity as model stresses, localised axial and transverse strains tend toward physical data. Similarly, parameters $m^n_{\sigma_{Ai}}$, $m^n_{\varepsilon_{Ai}}$ and $m^n_{\varepsilon_{Ti}}$ are multiples used to bias future generations from a certain side and partially penalise their respective partial objective functions.

The partial penalties and weightings for GA2 are as follows:

$$\text{if } \left\{\sigma_{Ai}^{n} | \sigma_{Ai} \leq \sigma_{Ai}^{\min\, n} \text{ and } \sigma_{Ai} \geq \sigma_{Ai}^{\max\, n}\right\} \text{ then } \phi^{\sigma_A^n} \text{ are negatively weighted ;} \tag{9.27}$$

$$\text{if } \left\{\varepsilon_{Ai}^{n} | \varepsilon_{Ai}^{n} \leq \varepsilon_{Ai}^{\min\, n} \text{ and } \varepsilon_{Ai}^{n} \geq \varepsilon_{Ai}^{\max\, n}\right\} \text{ then } \phi^{\varepsilon_A^n} \text{ are negatively weighted ;} \tag{9.28}$$

$$\text{if } \left\{\varepsilon_{Ti}^{n} | \varepsilon_{Ti}^{n} \leq \varepsilon_{Ti}^{\min\, n} \text{ and } \varepsilon_{Ti}^{n} \geq \varepsilon_{Ti}^{\max\, n}\right\} \text{ then } \phi^{\varepsilon_T^n} \text{ are negatively weighted ;} \tag{9.29}$$

$$w_{x\,10\%}^{n} > w_{x\,20\%}^{n} > w_{x\,30\%}^{n}. \tag{9.30}$$

For equation (9.30), x represents either axial stress σ_A, localised axial strain ε_A, or localised transverse strain ε_T. This ensures that numerical models which do not run to completion are weighted accordingly. Tests which fail to reach 10 % axial strain are given a lower ranking to those which reach an axial strain of 20 %, similarly for 20 and 30 %, thus favouring those models which run to completion.

The objective function for GA2 is represented in terms of the partial objective functions by

$$\phi^{GA2} = \frac{w_{obj}^{\sigma_A^{Warp}} \phi^{\sigma_A^{Warp}} + w_{obj}^{\sigma_A^{Weft}} \phi^{\sigma_A^{Weft}} + w_{obj}^{\varepsilon_A^{Warp}} \phi^{\varepsilon_A^{Warp}} + w_{obj}^{\varepsilon_A^{Weft}} \phi^{\varepsilon_A^{Weft}} + w_{obj}^{\varepsilon_T^{Warp}} \phi^{\varepsilon_T^{Warp}} + w_{obj}^{\varepsilon_T^{Weft}} \phi^{\varepsilon_T^{Weft}}}{w_{obj}^{\sigma_A^{Warp}} + w_{obj}^{\sigma_A^{Weft}} + w_{obj}^{\varepsilon_A^{Warp}} + w_{obj}^{\varepsilon_A^{Weft}} + w_{obj}^{\varepsilon_T^{Warp}} + w_{obj}^{\varepsilon_T^{Weft}}}, \tag{9.31}$$

where w_{obj}^{i} are pre-defined weightings and i represents the partial objective function to which the weightings apply. These weightings are used to bias the objective value to either the warp or weft direction, to stresses, to localised axial and or transverse strains. From equation (9.31), ϕ^{GA2} will tend to unity as $\phi^{\sigma_A^{Warp}}$, $\phi^{\sigma_A^{Weft}}$, $\phi^{\varepsilon_A^{Warp}}$, $\phi^{\varepsilon_A^{Weft}}$, $\phi^{\varepsilon_T^{Warp}}$ and $\phi^{\varepsilon_T^{Weft}}$ tend to unity.

Global penalties. The penalty functions for GA2 are given by the following:

$$\text{if } \sigma_{A\,10\%}^{n} \leqslant 0.0 \text{ then } p^{GA2} = -\infty \text{ else } p^{GA2} = 1\,, \tag{9.32a}$$

$$\text{if } \sigma_{T\,10\%}^{n} \leqslant 0.0 \text{ then } p^{GA2} = -\infty \text{ else } p^{GA2} = 1\,, \tag{b}$$

$$\text{if } \varepsilon_{T\,10\%}^{n} \geqslant 0.0 \text{ then } p^{GA2} = -\infty \text{ else } p^{GA2} = 1\,. \tag{c}$$

For the same reasons as given for GA1, the penalty functions described by equations (9.32a-c) ensure that the models run and the results obtained are reasonable.

Fitness function. The following is the fitness function for GA2s and the warp and weft uniaxial tensile finite element model solutions compared to physical data:

$$\text{Fitness Function } f^{GA2} = p^{GA2} \times \phi^{GA2}\,. \tag{9.33}$$

9.2.5 The objective, penalty and fitness functions for GA3

An additional GA, denoted by GA3, is used to find the fabric coefficients of two manufactured

sock structures which were used in reinforcing the porous grafts for physical compliance tests. These sock structures are tested in the longitudinal and circumferential directions in an Instron tensile test rig as described earlier in Chapter 8. Similar partial objective, objective and penalty functions as described for GA2 are used for GA3; however warp and weft uniaxial tensile finite element models are replaced by circumferential and longitudinal finite element models, respectively. Stresses are replaced with force per unit length (F/L), while the partial objective functions for localised axial and transverse strains are not incorporated into the objective and penalty functions, as no physical data for these field variables was collected. Force per unit length is used rather than stress, as this is the standard for the circumferential and longitudinal tensile tests [165, 166].

Objective and partial objective functions. The following equation describes the two partial objective functions for GA3:

$$\phi^{F/L^n} = \frac{\sum_{i=\varepsilon 1,\Delta\varepsilon}^{\varepsilon 3} w^n_{F/L_i}\left[1-\left\{|\triangle F/L^n_i|\left(\frac{1}{\left(m^n_{F/L_i}-1\right)}\right)\right\}\right]}{\sum_{i=\varepsilon 1,\Delta\varepsilon}^{\varepsilon 3} w^n_{F/L_i}} \tag{9.34}$$

where

$$\triangle F/L^n_i = \frac{F/L^{Model\,n}_i - F/L^{Data\,n}_i}{F/L^{Data\,n}_i}\,, \tag{9.35}$$

$$m^n_{F/L_i} = \left\{\begin{matrix} 1+\left|\frac{F/L^{\max\,n}_i - F/L^{Data\,n}_{Ai}}{F/L^{Data\,n}_i}\right| & \text{for: } F/L^{Model\,n}_i > F/L^{Data\,n}_i \\ 1+\left|\frac{F/L^{\min\,n}_i - F/L^{Data\,n}_i}{F/L^{Data\,n}_i}\right| & \text{for: } F/L^{Model\,n}_i \leq F/L^{Data\,n}_i \end{matrix}\right\}, \tag{9.36}$$

and n is the direction (circumferential or longitudinal), i the pre-defined strains in these two directions and w^n_{F/L_i} weightings for pre-defined strains. Again parameters m^n_{F/L_i} are multiples used to bias future generations from a certain side and partially penalise their respective partial objective functions. Similarly, the closer the model force per unit length solutions in the circumferential and longitudinal directions come to the physical data, the closer the partial objective functions tend to unity. The partial penalties and weightings for GA3 are as follows:

$$\text{if } \left\{F/L^n_i | F/L^n_i \leq F/L^{\min\,n}_i \text{ and } F/L^n_i \geq F/L^{\max\,n}_i\right\} \text{ then } \phi^{F/L^n} \text{ are negatively weighted}\,, \tag{9.37}$$

$$w^n_{F/L_{\varepsilon 1}} > w^n_{F/L_{\varepsilon 2}} > w^n_{F/L_{\varepsilon 3}}\,. \tag{9.38}$$

For equation (9.38), $\varepsilon 1$, $\varepsilon 2$ and $\varepsilon 3$ are the pre-defined strains and $\varepsilon 1 < \varepsilon 2 < \varepsilon 3$.

The objective function for GA3 is described by

$$\phi^{GA3} = \frac{w^{F/L^{Circ}}_{obj}\phi^{F/L^{Circ}} + w^{F/L^{Long}}_{obj}\phi^{F/L^{Long}}}{w^{F/L^{Circ}}_{obj} + w^{F/L^{Long}}_{obj}} \tag{9.39}$$

where w^i_{obj} are the weighting factors, where i represents the partial objective function to which the weighting applies. Thus these weightings can be used to bias the GA toward either finding the best circumferential or longitudinal solutions.

Global penalties. The global penalty functions for GA3 are described by the following:

$$\text{if } F/L^n_i \leqslant 0.0 \text{ then } p^{GA3} = -\infty \text{ else } p^{GA3} = 1\,. \tag{9.40}$$

Fitness function. The fitness function for GA3 is represented in terms of the penalty and objective functions and is described by:

$$\text{Fitness Function } f^{GA3} = p^{GA3}\phi^{GA3}\,. \tag{9.41}$$

Chapter 10

Validation of the Fabric, Porous and Latex Models

10.1 Introduction

The latex and porous material models need to be validated against experimental data and the fabric material model needs to be assessed to ensure that it can characterise fabrics under tension to a satisfactory degree.

In this chapter, single element patch tests are utilised to validate the porous and latex material models against relevant experimental data. These single element tests are also used to assess the influence of each coefficient (C, a_i) on the fabric material model. The chapter confirms that the fabric material model and GA2 can be used to optimise the fabric material coefficients to reasonably describe fabric under tensile forces. All physical tests were carried out under or close to physiological conditions.

10.2 Validation of the hyperfoam and hyperelastic material models

The modelling and optimisation at this stage are solely conceptual. Physical comparisons need to be made before optimised solutions can be used and fabric reinforcing produced for the various porous graft structures, with some degree of confidence. Tensile, compressive and shear tests were performed on unit samples of the currently available porous structures (90-106, 106-125 and 125-150 μm bead grafts), and tensile tests were performed on the latex balloons that are used to line the porous grafts to prevent pressure loss during testing. The test results obtained from the physical tests were then used in the hyperfoam and hyperelastic models used to describe the mechanical characteristics of the porous and latex structures respectively.

10.2.1 The porous hyperfoam model and patch tests

An Instron™ test rig was utilised to obtain simple shear, uniaxial tensile, and compressive test data for the various porous graft structures. To obtain decent sized test samples on the Instron™, 8 mm diameter cast bead rods were manufactured for the various porogen sizes, as described by Bezuidenhout [9]. The Instron™ test jaws were modified to allow for a heated water bath. Figure 10.1 below shows the test rig as well as an 8 mm porous rod being placed under tension, utilising the modified tensile jaws.

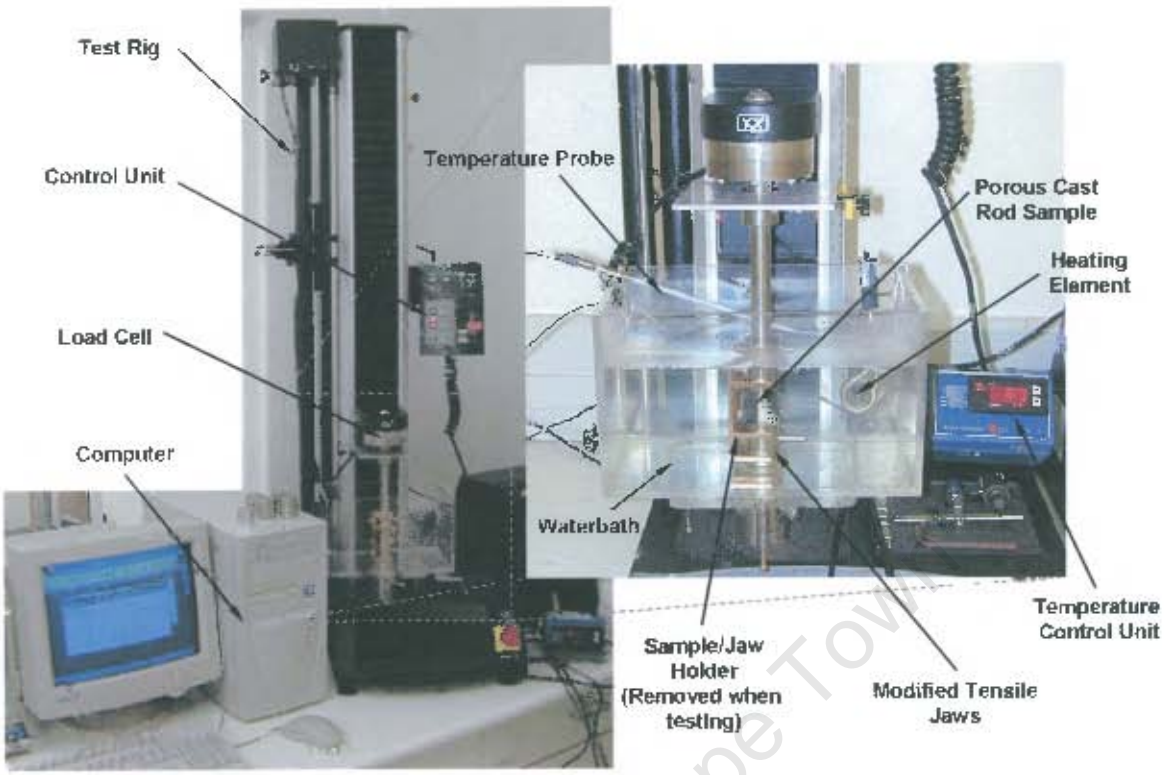

Figure 10.1: Instron™ test rig, with custom built tensile test jaws and water bath

Due to the difficulty of working with the fine porous structures without inducing prior stresses, specialised jaws were manufactured to assist in reducing the handling and pre-stressing of the samples. The specialised jaws consisted of a jaw holder which had arms of predefined lengths into which the respective jaws fitted, with the assistance of grooves. The arms allowed the jaws to be rotated around the longitudinal axis, while being fixed in the axial direction. The bead cast rods were cut into sample lengths of 30 mm and 5 mm for the tensile and compressive specimens respectively, while shear samples of $5 \times 5 \times 10$ mm were cut from the bead cast rods. A cutting block with set blade slot positions was utilised to minimise the crushing of the porous structure while preparing these test specimens. Figure 10.2 shows the jaws in their respective test positions as well as the various components used, and a schematic of the cutting block.

The tensile and shear specimens were glued to their respective jaws using a highly viscous gel type cyanoacrylate super glue. The rapid setting and high viscosity of the glue prevented it from soaking into the porous structure through capillary action, while providing a firm attachment. To ensure that these samples were located centrally, a spacer was utilised to centrally position the shear sample, while the tensile jaws had central locating bores of 2 mm depth which allowed for the samples to be glued into place.

As mentioned earlier, a jaw holder was utilised to ensure that no pre-stressing was induced in the tensile and shear specimens. The two respective tensile or shear jaws were fixed relative to each other before the samples were positioned and glued into place. The jaws, specimen and

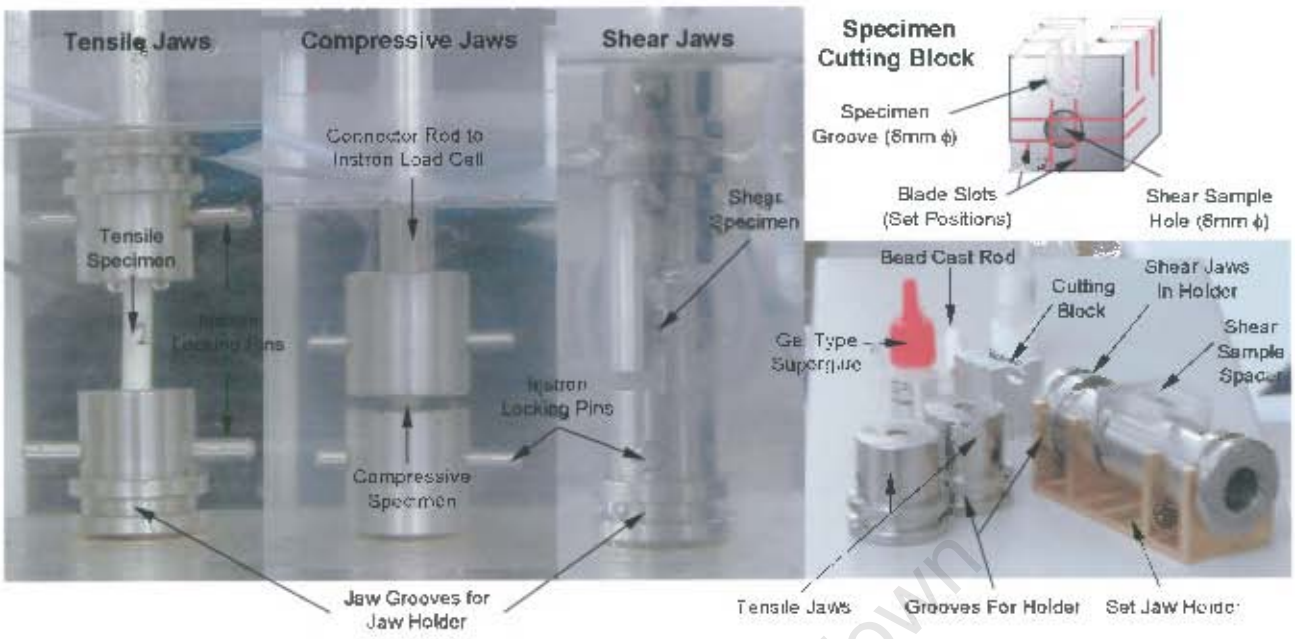

Figure 10.2: Specially built tensile test jaws showing various components to ensure minimal stresses are placed on porous samples prior to testing

holder were then positioned in the water bath and attached to the tensile tester with the use of locking pins. Before testing, the jaw holder was removed. The use of the jaw holder was not necessary for the compressive tests; however, care was taken to ensure that the compressive test specimen was located centrally prior to testing. These compressive jaws were also lined with a glycerol oil film to ensure that during compression the samples were minimally constrained radially [94]. Experimental test data was obtained for a sample size of $n = 3$ for bead cast porous structures with the following porogen particle sizes; 90-106, 106-125, and 125-150 μm.

Using a single plane stress ($\sigma_{33} = 0$), eight-noded unit square continuum element as described in Section 8.4, model tensile, compressive and shear tests (see Figure 8.1) were analysed and compared to experimental data. The comparative curves for the various porogen/porous structure experimental data vs. single element models for tensile, compression and shear can be seen in Figures 10.3 and 10.4.

From Figures 10.3 and 10.4 it can be seen that the model solutions follow the physical solutions reasonably to 30% strain in compression and 55% in tension. This experimental data was utilised in ABAQUS® and a hyperfoam model (order $n = 4$) was used to fit the data. The Poisson effect was adjusted to allow for the minimal difference in the least squares fit between the physical and model data. The least squares error for maximum tensile, compressive and shear strains before the model deviates from the experimental data for each porogen size is shown in Table 10.1. The root mean square (rms) error for the mathematical expressions fitting the physical test data for the 90-106, 106-125 and 125-150 μm bead porous structures were 6.13, 5.56 and 4.99% respectively.

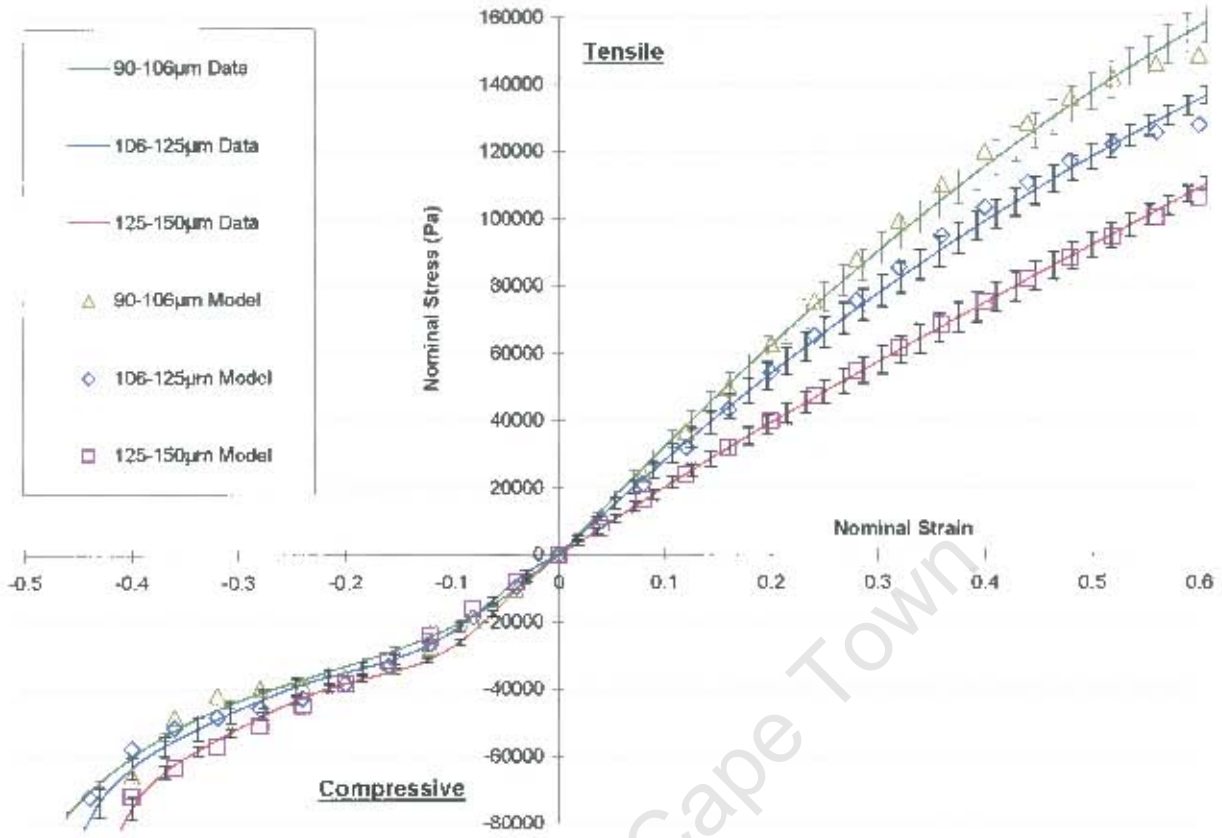

Figure 10.3: Physical vs. model tensile and compressive stress-strain curves for porous specimens and single element models

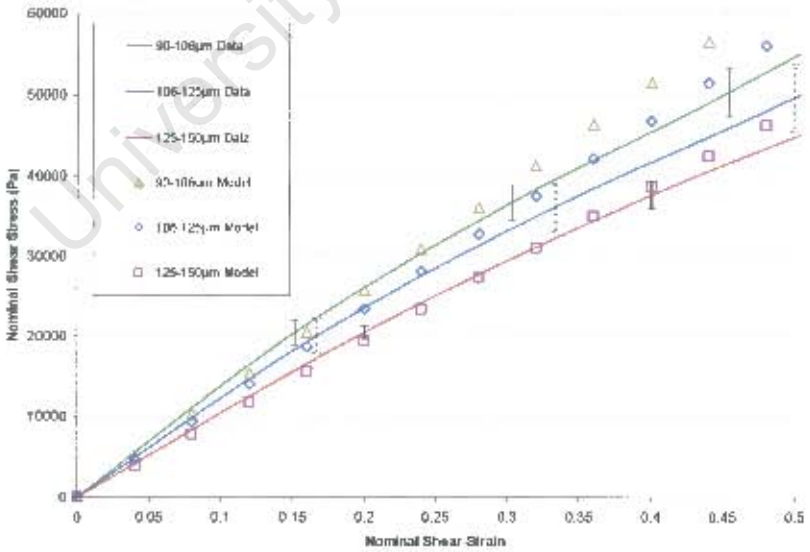

Figure 10.4: Physical vs. model simple shear stress-strain curves for porous specimens and single element models

These single element patch tests show that the numerical tests are valid to strains of 35% for shear and 55% for uniaxial tension and were sufficiently accurate within this physical range.

Description	90-106 μm	106-125 μm	125-150 μm
Order (n)	4	4	4
Effective Poisson's Ratio (υ)	0.08	0.075	0.035
Root Mean Square Error (rms %)	6.13	5.56	4.99
Max Tensile Strain	0.57	0.56	0.62
Max Compressive Strain	0.3	0.36	0.4
Max Shear Strain	0.32	0.33	0.48
Max Stability Strain (Tensile, Compressive and Shear)	0.7	0.7	1.0
Hyperfoam Model coefficients			
μ_1	0.5411×10^6	0.3501×10^6	1.9262×10^5
μ_2	0.1528×10^6	-0.8453×10^5	-0.3373×10^5
μ_3	-0.3936×10^6	-0.2128×10^6	-0.8682×10^5
μ_4	0.1337×10^6	0.6388×10^5	0.2566×10^5
α_1	2.449	2.771	1.2571
α_2	4.694	5.358	1.2655
α_3	-1.575	-1.271	-2.6509
α_4	-3.571	-3.282	-4.6589

Table 10.1: Least squares fit of hyperfoam model to porous test data

Since the material is used with a maximum tensile strain of about 30 % under physiological conditions, these limits were not considered problematic. The patch tests also show that results at higher strains diverge from the physical tests and therefore are unreliable for failure analysis. From these simple unit model analyses, the mathematical expressions for the material behaviour, namely porous structures, were viewed as substantially usable in a wide range of strains (less than 30 % for compression and 55 % for tensile).

10.2.2 The latex hyperelastic model and patch test

Similar tensile material tests were carried out on the latex liner. Specimens were obtained from liner samples by utilising a standard 5×25 mm dog bone cutter to cut samples along the axis of the liner samples. These were then set up in the water bath using a set of standard tensile jaws for uniaxial tensile testing (see Figure 8.9).

Single element models vs. experimental data. Using a single plane stress ($\sigma_{33} = 0$), four-noded unit square membrane element as described in Section 8.4, model tensile tests (see Figure 8.1) were analysed and the results compared to experimental data. The comparative curves for the latex experimental data vs. the single element model are shown in Figure 10.5, where it can be seen that the model solution has a very satisfactory fit, and follows the experimental data exactly. This experimental data was utilised in the computational model and a Ogden hyperelastic model (order $n = 6$) was used to fit the data. The least squares errors for the latex material model to experimental data are shown in Table 10.2. The root mean square (rms) error for the mathematical expressions fitting the physical test data is zero.

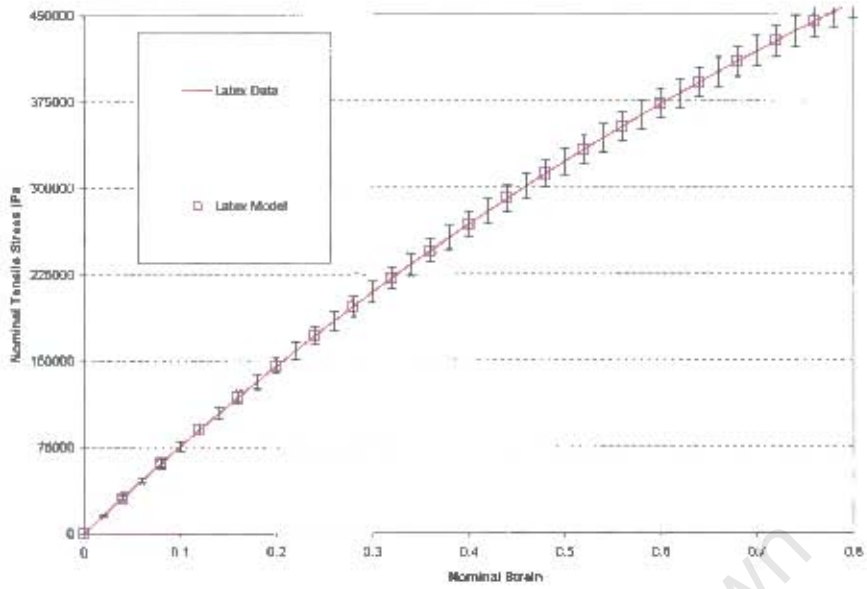

Figure 10.5: Physical vs. model uniaxial tensile stress-strain curves for latex specimen and single element model

Description	Latex
Order (n)	6
Effective Poisson's Ratio (ν)	0.0
Root Mean Square Error (rms %)	0.0
Max Tensile Strain	0.7
Hyperelastic Model coefficients	
μ_1	0.6023×10^6
μ_2	-0.9005×10^5
μ_3	7102.0
μ_4	-0.2971×10^6
μ_5	0.5788×10^5
μ_6	2513.0
α_1	2.0
α_2	4.0
α_3	6.0
α_4	−2.0
α_5	4.0
α_6	−6.0

Table 10.2: Least squares fit of hyperelastic model to latex test data

10.3 Fabric material coefficients

The validation of the porous and latex material models has been shown above, using intrinsic hyperfoam and hyperelastic material models. However, due to the use of a modified Fung model with compressibility to model the fabric material which has not been shown to model fabrics before, one needs to show that the material model does display fabric mechanical properties, as well as validate it against experimental data. This section looks at the single element models and the effect of each fabric material coefficient (C, a_i) on the material mechanics.

10.3.1 The fabric single element models

Arbitrary fabric coefficients were employed in the single element tensile and shear patch tests and varied slightly to observe their influence on stress and strain behaviour. Figures 10.6 and 10.7 display the stress-strain results, while Figures 10.8 and 10.9 plot the normalised stress values, which are obtained from dividing the stress values obtained at 20% tensile strain and 10% shear strain by the $C = 10000.0$ and $a_i = 10.0$ model solutions.

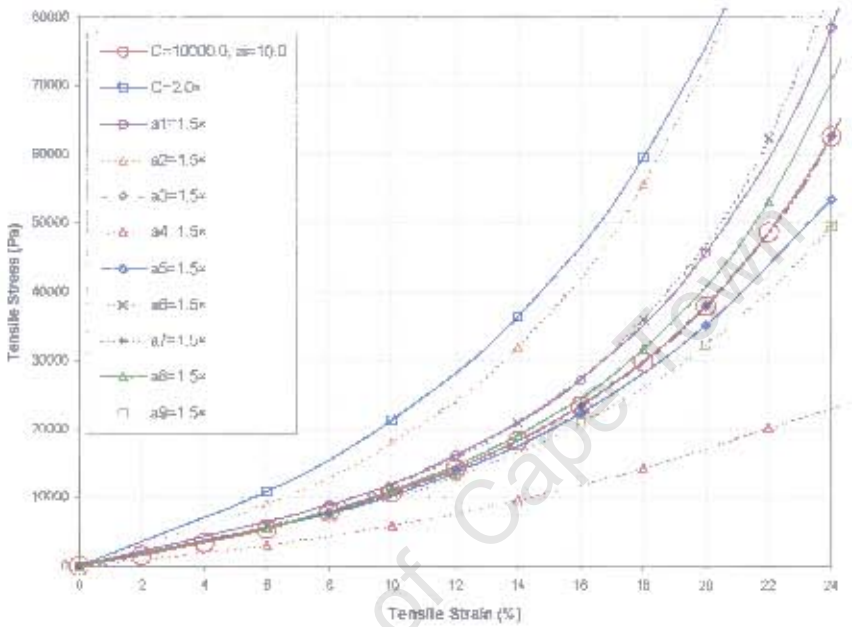

Figure 10.6: Effect of coefficients C and a_i on uniaxial tensile stress-strain curves

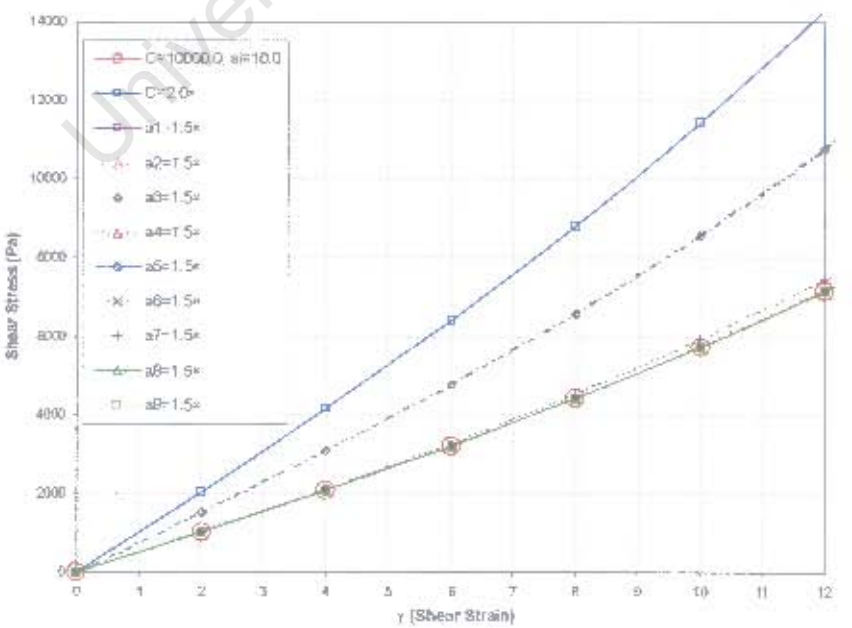

Figure 10.7: Effect of coefficients C and a_i on simple shear stress-strain curves

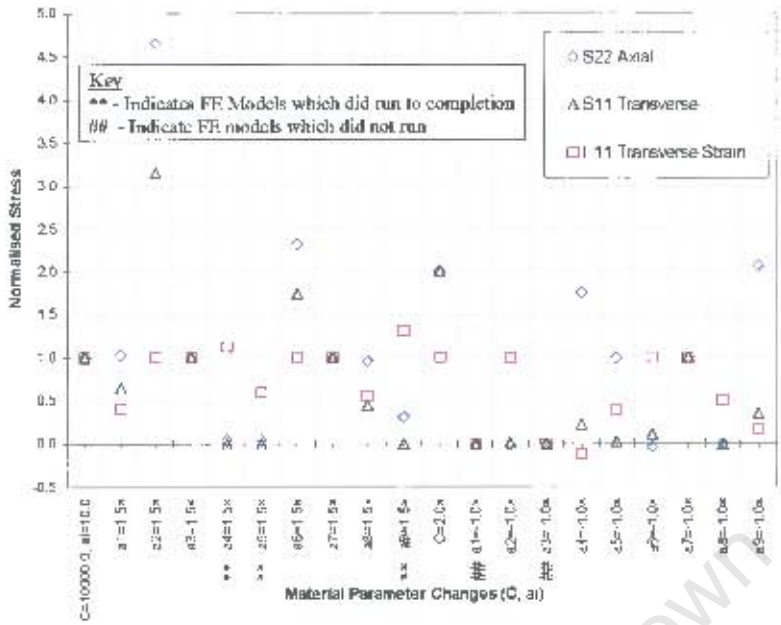

Figure 10.8: Normalised stress and transverse strain values from tensile patch tests due to fabric model coefficient changes

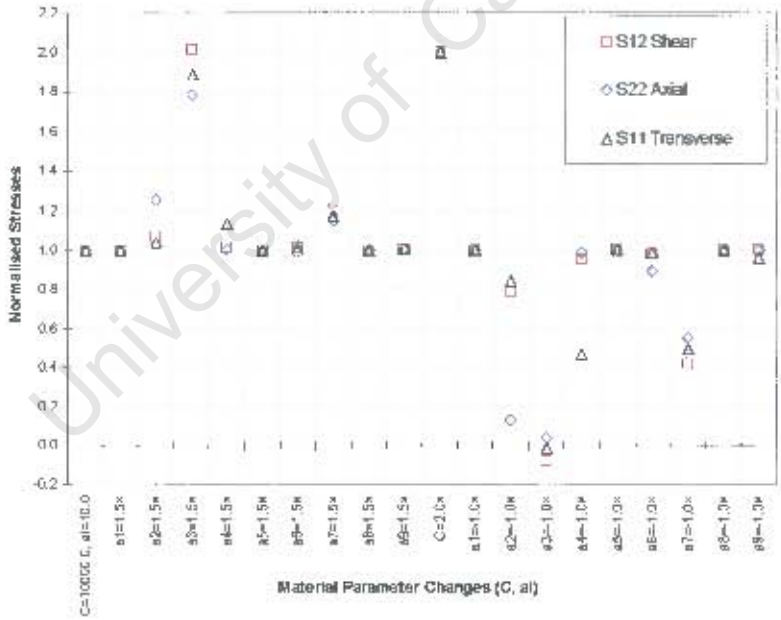

Figure 10.9: Normalised stress and transverse strain values from shear patch tests due to fabric model coefficient changes

From Figure 10.6 the typical uniaxial tensile stress-strain curve for the material model displays the characteristic nonlinear stiffening effect seen in fabrics. If we define the subscripts i and j to denote the direction of uniaxial tension and the transverse direction, respectively, the following can be observed (note: that results above are for $i = 2$):

- The magnitude of stress increases proportionately to the coefficient C.
- The nonlinear stiffening effect is greatly increased by increasing coefficients which affect terms containing E_{ii}^2, i.e. a_1 and a_2.
- No change in tensile stiffening is observed by increasing coefficients which affect terms containing E_{ij}, i.e. a_3 and a_7.
- The nonlinear stiffening effect is greatly reduced by increasing coefficient a_4 which affects the $E_{ii}E_{jj}$ term. It is slightly reduced by increasing coefficients which affect E_{jj}^3 terms, and moderately increased by increasing coefficients which affect E_{ii}^3 terms, i.e. a_5 and a_6.
- The nonlinear stiffening effect is slightly increased by increasing a_8 which affects the $E_{jj}^3E_{ii}$ term, and it is slightly reduced by increasing a_9 which affects the $E_{jj}E_{ii}^3$ term.
- The effect of changing the coefficients a_1 to a_9 is dependent on the power of the strain terms to which they contribute. Those that affect lower order terms have a larger influence.

More information regarding coefficient change is gained from Figure 10.8, which plots the normalised stresses and transverse strain values for each modified coefficient. The following is observed:

- The magnitude of both axial and transverse stresses is proportional to coefficient C; however, transverse strain is not affected by its change.
- The transverse strain or Poisson's effect is dependent on terms containing both E_{ii} and E_{jj}, i.e. a_4, a_8 and a_9, where increasing terms a_4 and a_9 increases the transverse strain (note: both these models did not run to completion, a_4 is 65 % and a_9 is 87.5 % complete), while increasing a_8 greatly reduces the transverse strain.
- The transverse strain is heavily dependent on the terms E_{jj} and E_{jj}^3, i.e. increasing terms a_1 and a_5 greatly reduces the transverse strain (note: model $a_5 = 1.5\times\ a_9$ is only 66 % complete).
- An increase in a_1, which affects term E_{jj}^2, greatly reduces the transverse stress S_{jj} while only slightly increasing the axial stress S_{ii}.
- An increase in a_2, which affects term E_{ii}^2 increases both axial and transverse stress, where the change in axial stress is dominant.
- An increase in a_4, a_5, a_8 and a_9, reduces both axial and transverse stress values. Terms a_4, a_5, and a_9 greatly reduce both stress values, while a_8 greatly reduces the transverse stress and moderately reduces axial stress.
- An increase in a_6 greatly increases the axial and transverse stress values, however, this increase is not as pronounced as that observed by increasing a_2.
- Negative coefficients typically reduce transverse strain. A negative a_4 produces a negative normalised transverse strain, indicating that positive strains are observed in this direction, which is unrealistic. For a_7 no change is observed in stress values or transverse strain, while a negative a_2 and a_6 reduce the stress values but do not affect the transverse strain. (note: the

finite element models could not converge upon a solution when a_1 and a_3 were negative).

- Negative values of a_4 and a_9 increase the axial stress while reducing the transverse stress. Coefficient a_5 does not change the axial stress but reduces the transverse stress. Terms a_2 and a_6 both make the axial stress compressive whilst in tension, which is unrealistic. Coefficient a_8 reduces both the axial and transverse stress values considerably.

It is apparent from the strain energy function described by (4.122) that the magnitude and ratio of the coefficients contribute to the change in stress and strain. Thus, the above observations are only made for specific changes in coefficient magnitude, namely, $1.5\times$ and $-1\times$.

Figure 10.7 shows typical shear stress-shear angle curves obtained from the simple shear model. It can be seen that the model does not match the initial high modulus which is a characteristic of fabrics under shear as observed in Figure 3.8; however, this initially high modulus is only seen between $0 - 0.8\,°$, after which the relation is predominantly linear. Although not clearly observed in Figure 10.7, the shear stress-strain relation becomes slightly curved by increasing coefficients a_3 and a_7.

Although the coefficients used were arbitrary, a number of combinations were tried. The stress-strain relations above show that it is possible to describe a fabric's tensile and shear properties with the anisotropic strain energy function used by Fung [32] to describe soft tissue.

Curvature. Using sixth order polynomial curve fitting and Figure 10.6, the maximum curvature ($\kappa_{\max}$), its corresponding radius of curvature ($\rho_{\min}$) and the tensile strain values at which these occur can be used to obtained a better understanding of the nonlinear stiffening effect with coefficient variation, by using the formula

$$\frac{1}{\rho} = \kappa = \frac{\ddot{y}}{\left(1 + (\dot{y})^2\right)^{\frac{3}{2}}} \tag{10.1}$$

for curvature [173], where $\dot{y}$ and $\ddot{y}$ are the first and second derivatives of the curve fitted function $y(\varepsilon)$. Table 10.3 lists the obtained maximum curvature values, and their corresponding strains and ratios.

Fabric Coefficients/Ratios	$\kappa_{\max}$	$\rho_{\min}$	Strain (ε)	Ratio of $\kappa_{\max}$	Ratio of ε
$C = 10000.0, a_i = 10.0$	0.108	9.270	10.2	1.000	1.000
$C = 2\times$	0.252	3.965	9.6	2.338	0.941
$a_1 = 1.5\times$	0.124	8.065	9.0	1.149	0.882
$a_2 = 1.5\times$	0.471	2.123	8.7	4.366	0.853
$a_3 = 1.5\times$	0.108	9.270	10.2	1.000	1.000
$a_4 = 1.5\times$	0.078	12.751	16.7	0.727	1.637
$a_5 = 1.5\times$	0.095	10.523	10.8	0.881	1.059
$a_6 = 1.5\times$	0.126	7.907	8.8	1.172	0.863
$a_7 = 1.5\times$	0.108	9.270	10.2	1.000	1.000
$a_8 = 1.5\times$	0.138	7.264	10.1	1.276	0.990
$a_9 = 1.5\times$	0.146	6.836	13.4	1.356	1.314

Table 10.3: Curvature values for tensile stress-strain curves

As indicated in Table 10.3, increases in coefficients C, a_1, a_2, a_6, a_8 and a_9 all increase the maximum curvature values and thus have a substantial nonlinear stiffening effect. As expected, by increasing a_2 there is a significant increase in curvature (4.466×). The strain value at which maximum curvature occurs is reduced by increasing C, a_1, a_2, a_6 and a_8, most notably for a_2 and a_6 while only slightly for a_8. Increasing a_9 greatly increases the position at which maximum curvature occurs. No change in curvature or position is observed by increasing coefficients a_3 and a_7, while increasing coefficients a_4 and a_5 reduce the curvature. An interesting result observed in Figure 10.6, by increasing a_9 there appears to be a reduction in nonlinear stiffening, yet from Table 10.3 curvature is seen to increase. This may be explained by the observed higher strain value at which this maximum curvature occurs.

Uniform and non-uniform multi-element fabric meshes. The uniform four-noded and non-uniform three and four-noded multi-element fabric patch test meshes in Figure 8.2 were also analysed and compared with the single element models presented in Figure 8.1. Table 10.4 below shows the results of the comparative tests and Figure 10.10 shows the results of the corresponding tensile and shear tests.

Description		**Multi Element**		**Single Element**
		Uniform	*Non-uniform*	
Tensile	$S11$	6.776	6.776	6.776
	$S22$	0.168×10^7	0.168×10^7	0.168×10^7
	$S12$	0.0	0.0	0.0
	$U1$	-0.581	-0.581	-0.581
Shear	$S11$	$-0.24 \times 10^5 \rightarrow 1.75 \times 10^5$	$-0.23 \times 10^5 \rightarrow 1.73 \times 10^5$	0.41×10^5
(Range)	$S22$	$-0.188 \times 10^5 \rightarrow 4.92 \times 10^5$	$-0.193 \times 10^5 \rightarrow 4.82 \times 10^5$	0.59×10^5
	$S12$	$0.072 \times 10^5 \rightarrow 2.86 \times 10^5$	$0.097 \times 10^5 \rightarrow 2.81 \times 10^5$	0.86×10^5

Table 10.4: Comparison of uniform and non-uniform multi-element patch test results

As can be seen no differences were observed between the various models, and the observed stress values (11 and 22 directions) at 40% strain were equal and uniform throughout the elements, indicating that the material model is implemented correctly in the commercial finite element package.

10.4 Validation of the fabric constitutive equation and UMAT subroutine

Before the fabric model can be implemented, it needs to be validated against experimental data. Four random fabrics with potential use as a reinforcing were chosen to assess the GA and the ability of the fabric constitutive model to simulate the physical fabric mechanics to a reasonable degree. These four fabrics were physically tested to obtain transverse uniaxial stress-strain data as well as local and global strain effects. The data obtained was utilised in GA2 to obtain the exponential model coefficients C, a_1, a_2, a_3, a_4, a_5, a_6, a_7, a_8 and a_9 which best described the mutually orthogonal tensile behaviour of these fabrics. GA2 is also used to measure the

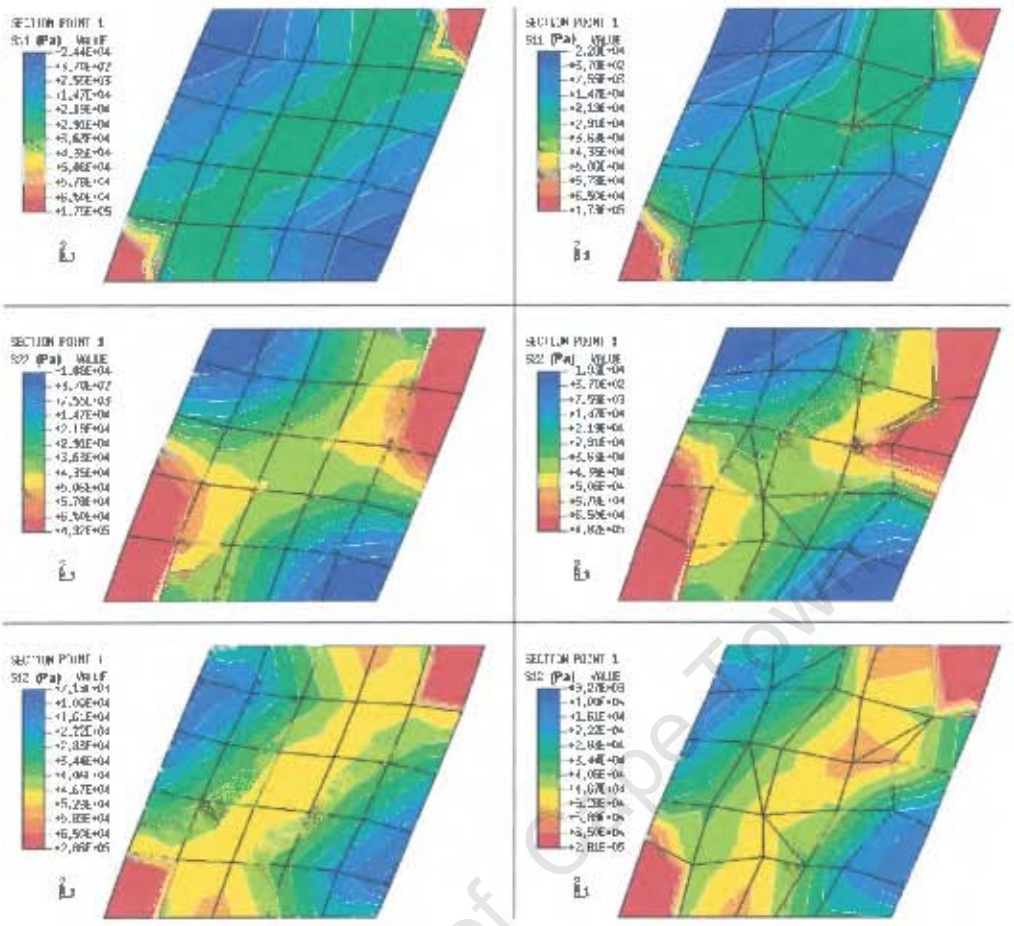

Figure 10.10: Comparison of stress fields across uniform and non-uniform multi-element shear patch tests

effectiveness of the GA as well as the typical objective and penalty functions implemented.

10.4.1 Tensile experimental data for fabric samples

The Instron™ tensile test rig was again utilised to obtain uniaxial stress-strain curves in the warp and weft directions of fabric samples. Samples of dimensions 60.0×20.0 mm were initially pre-loaded to 1 % nominal strain at a strain rate of 50 mm/min to ensure that material inconsistencies were reduced before data collection. The samples were then strained to 50 % nominal strain at a strain rate of 200 mm/min, the strain rate stipulated by medical implant authorities [167, 168]. Tests were performed in a water bath maintained at 37 °C. Figure 10.11 shows the Instron™ tensile rig and a fabric sample being tested.

10.4.2 Transverse strain tests

Due to the difficulty in monitoring lateral strain effects with the Instron™ tensile tester as a result of the curling effects at the edges during the tensile tests, fabric samples were strained in steps of 10, 20 and 30 % on a flat bed in a water bath maintained at 37 °C. Digital images were then taken to view lateral strain effects. A uniform square grid (5×5 mm) was marked on each sample to visually determine the localised strain effects (refer to Figure 10.12). Strengthening stitch lines

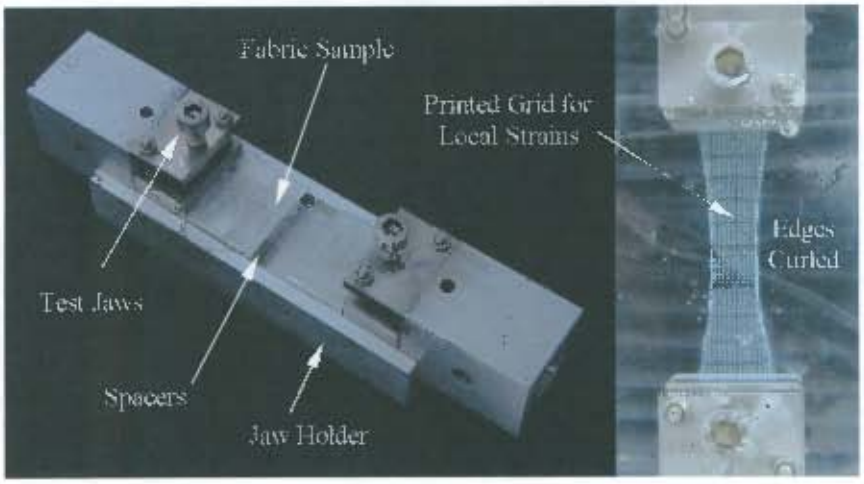

Figure 10.11: Fabric uniaxial tensile test jaws and holder

were also sewn at both ends of the samples to minimise localised stress concentrations.

Figure 10.12 shows a collection of the digital images collected for a fabric sample, where a single grid at the fabrics centre is highlighted. A central grid was chosen as it was found during tests that edge effects such as curling affected the strain measurements close to the edges.

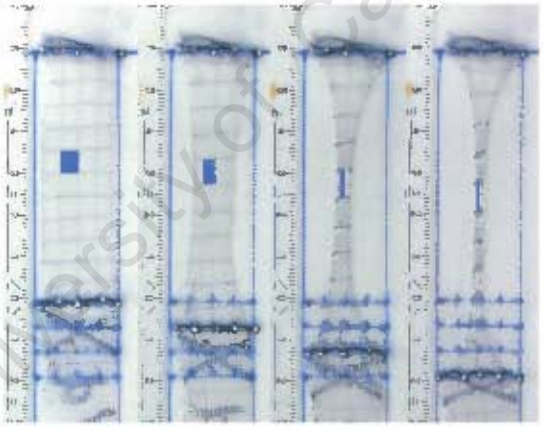

Figure 10.12: Uniaxial tensile test images collected at 0, 10, 20 and 30 % axial strain (central grid used to obtain local strains is highlighted)

The transverse (warp and weft) stress-strain data collected for each fabric sample can be viewed in Figures C.4, C.5 and Table C.1 of Appendix C.

10.4.3 Optimised model solutions for fabric samples

Implementing GA2 for each of the four fabric samples from a single starting point (namely $C = 10000$, $a_i = 1.0$), a total of 47, 42, 39 and 45 generations were reached before convergence on a set of single solutions was found. Table 10.5 shows the model coefficients for each fabric sample obtained from GA2, including the fitness values and the generation number. Table 10.6 shows the stress-strain data compared to model solutions found by GA2. Figure C.3 and C.6 of

Appendix C show the axial stress and transverse strain vs. axial strain curves obtained from GA2 compared to test data.

Fabric Sample	1	2	3	4
Coefficients				
C	26444.0	9766.2	12401.0	10299.0
a_1	9.6714	12.77	38.689	81.086
a_2	15.815	15.414	5.2838	35.152
a_3	86.94	12.895	25.122	39.747
a_4	15.742	12.322	19.878	84.289
a_5	−3.8816	2.3294	−9.9038	−22.657
a_6	21.377	−5.3519	0.92224	20.526
a_7	−39.528	−13.246	28.778	43.484
a_8	−5.0215	5.1202	10.485	94.932
a_9	8.5257	−1.9179	12.086	124.26
Fitness Value $f(C, a_i)$	0.999854	0.99962	0.99968	0.99970
Objective Value $\phi(C, a_i)$	0.99985	0.99962	0.99968	0.99970
Partial Objective Values				
$\phi^{\sigma_A^{warp}}$	0.99980	0.99957	0.99998	0.99998
$\phi^{\sigma_A^{weft}}$	0.99993	0.99938	0.99947	0.99971
$\phi^{\varepsilon_A^{warp}}$	0.99972	0.99981	0.99989	0.99987
$\phi^{\varepsilon_A^{weft}}$	0.99938	0.99967	0.99991	0.9998
$\phi^{\varepsilon_T^{warp}}$	0.99991	0.99987	0.99935	0.99934
$\phi^{\varepsilon_T^{weft}}$	0.99981	0.99993	0.99979	0.99935
Generation	47	42	39	45

Table 10.5: Model coefficients for fabric samples obtained from GA2

10.4.4 Model solutions vs. experimental data

Axial stress with axial strain. Fabric samples 1, 3 and 4 show high degrees of anisotropy and nonlinear stress-strain relations in both the warp and weft directions, while fabric sample 2 shows a comparatively lower degree of anisotropy and an almost linear stress-strain relation in the weft direction (Figure C.3 of Appendix C). Figure 10.13 illustrates the difference between model and physical stress-strain curves obtained for fabric sample 1.

The model solution found for fabric sample 1 follows the weft stress-strain curve accurately up to 28 % strain, and thereafter diverges, giving higher stress values. In the warp direction, there is marked difference between the model solution and physical data after 13 % strain. This, and the model solutions found for fabric samples 3 and 4 show excellent model fits to test data in one of either warp or weft directions, and a reasonable solution in the transverse direction. Since the normalised difference between model solutions and test data is not biased towards one direction or the other (i.e. it treats warp and weft equally), the GA tends to bias itself in either one direction or another once a possible solution is found.

Fabric Sample	1		2		3		4	
	Data	Model	Data	Model	Data	Model	Data	Model
σ_A^{warp}								
10% ε_A^{warp}	53350	55436	39427	19704	4828	4887	20625	20177
20% ε_A^{warp}	487022	275388	113327	66708	11163	11235	52128	52196
30% ε_A^{warp}	2627791	2109254	217058	234610	22344	20054	91164	88428
ε_A^{Local}								
10% ε_A^{warp}	7.90	10.95	7.692	10.23	12.5	10.47	13.51	10.84
20% ε_A^{warp}	18.42	21.68	20.51	20.41	22.5	21.05	21.62	22.11
30% ε_A^{warp}	31.58	32.26	28.21	30.56	32.5	31.79	40.54	34.87
ε_T^{Local}								
10% ε_A^{warp}	−13.16	-11.12	−5.26	-5.16	−9.52	-2.94	−19.44	-6.17
20% ε_A^{warp}	−26.32	-25.91	−7.895	-10.53	−16.67	-6.47	−36.11	-13.92
30% ε_A^{warp}	−44.74	-42.78	−15.79	-15.94	−23.81	-10.72	−77.78	-24.84
σ_A^{weft}								
10% ε_A^{weft}	24995	23731	67401	16851	124041	56879	83924	74167
20% ε_A^{weft}	69272	63709	135218	58352	722478	332393	780401	524116
30% ε_A^{weft}	134503	148320	197992	217081	2064245	3048111	2835539	5135705
ε_A^{Local}								
10% ε_A^{weft}	5.26	10.63	7.69	10.22	12.82	11.25	9.76	11.09
20% ε_A^{weft}	18.42	21.34	15.38	20.46	23.08	21.97	31.71	21.97
30% ε_A^{weft}	31.58	32.11	23.08	30.71	33.33	32.66	39.02	33.18
ε_T^{Local}								
10% ε_A^{weft}	−5.56	-5.93	−5.13	-4.60	−26.47	-22.13	−39.39	-13.36
20% ε_A^{weft}	−22.22	-13.64	−10.26	-10.31	−55.88	-39.95	−78.79	-26.19
30% ε_A^{weft}	−30.56	-24.94	−15.38	-17.28	−64.71	-53.98	−87.88	-40.36

Table 10.6: Model solutions compared to test data for fabric samples

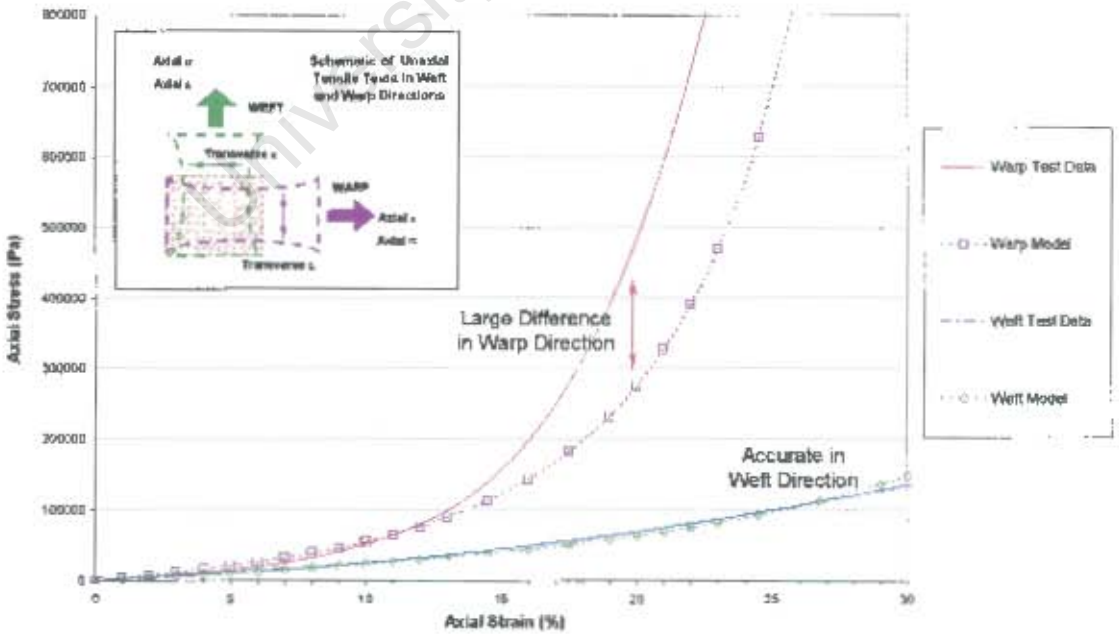

Figure 10.13: Comparison of physical and model axial stress-axial strain curves for fabric sample 1

The GA or the fabric model, however, failed to find a good solution for fabric sample 2, which has an almost linear stress-strain relation in the weft direction. Since the objective and fitness functions used were the same for all fabric samples the GA may be regarded as stable, and does converge upon good solutions. Thus, failure is due to the fabric model's inability to model almost linear uniaxial tensile stress-strain behaviour.

Transverse with axial strain. Curves of transverse strain vs. axial strain in the warp and weft directions for the fabric samples can be observed in Figure C.6 of Appendix C. Figure 10.14 shows the solution obtained for fabric sample 1. A close correlation is obtained, with a small difference seen in the warp direction (< 1 % transverse strain), while in the weft direction, differences are roughly 1.5 % the transverse strain.

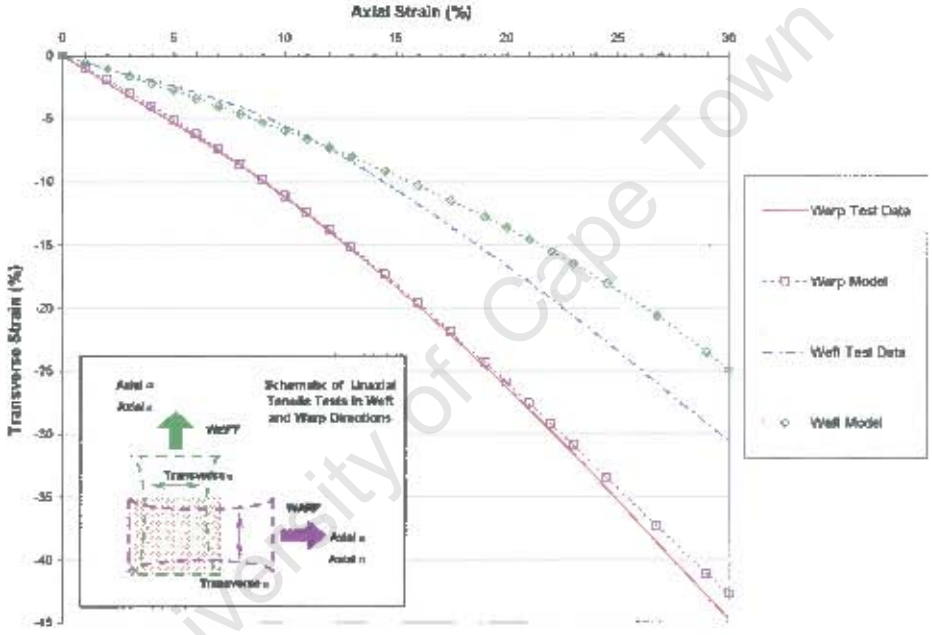

Figure 10.14: Comparison of physical and model transverse strain-axial strain curves for fabric sample 1

The warp transverse strain curves obtained for fabric sample 2 give a difference less than 1.2 % in transverse strain, and for axial strains less than 20 %. However, the solution obtained for fabric sample 2 is largely linear, while fabric sample 1 shows an increase in the Poisson's effect with an increase in axial strain. Large differences are seen for fabric samples 3 and 4 , however the weft model solution for fabric sample 3 compares well, where a difference of less than 2 % in transverse strain are observed.

From the preceding discussion and the data presented in Appendix C, the solutions obtained from GA2 are satisfactory, where the fabric material model is capable of modelling large variations in transverse anisotropy. However, in the case of fabric sample 2, where a linear stress-strain relation is observed the fabric model fails to provide a good solution.

The uniaxial stress fields and the deformation states for fabric model 1 in both the warp and

weft directions are shown in Figures 10.15, 10.17 and 10.18. Figure 10.15 and 10.17 show the increase in principal stress and deformation at 10, 20 and 30% axial strain respectively. Figure 10.18 compares the principal stress states and deformations at 30% axial strain for both the warp and weft solutions.

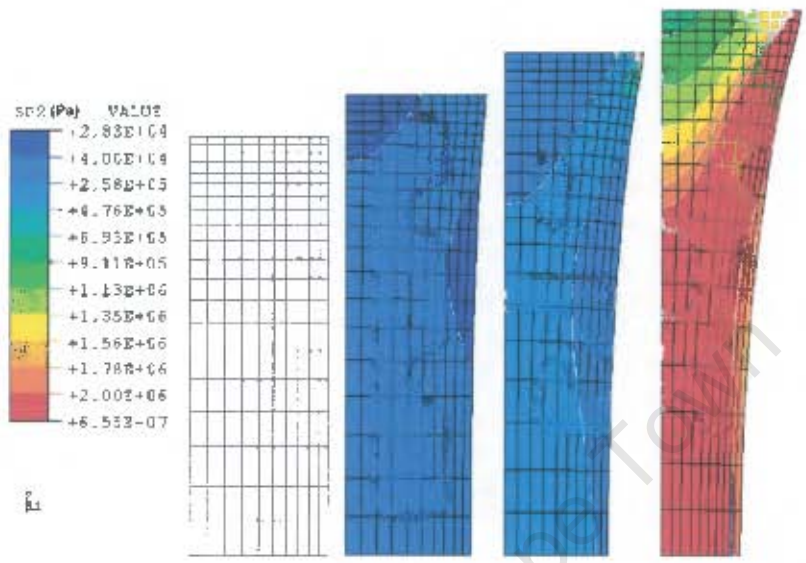

Figure 10.15: Maximum principal stress and deformation at 0, 10, 20 and 30% axial strain for fabric sample 1 model in warp direction

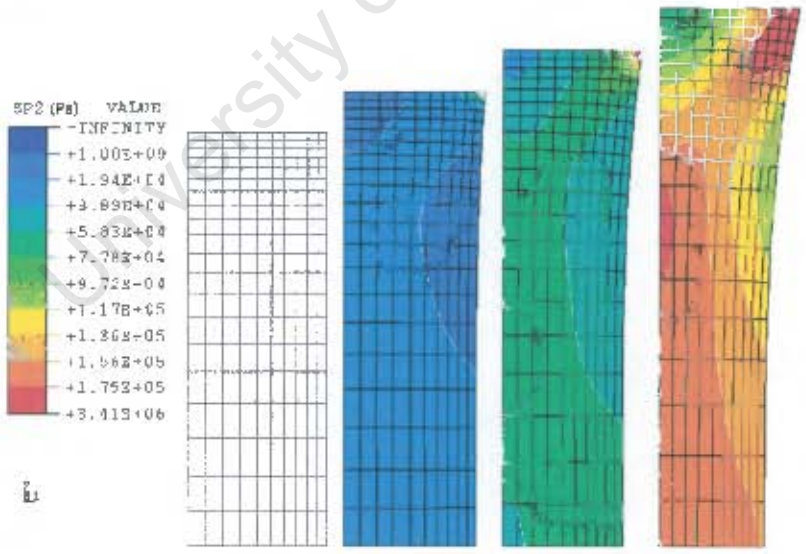

Figure 10.16: Maximum principal stress and deformation at 0, 10, 20 and 30% axial strain for fabric sample 1 model in weft direction

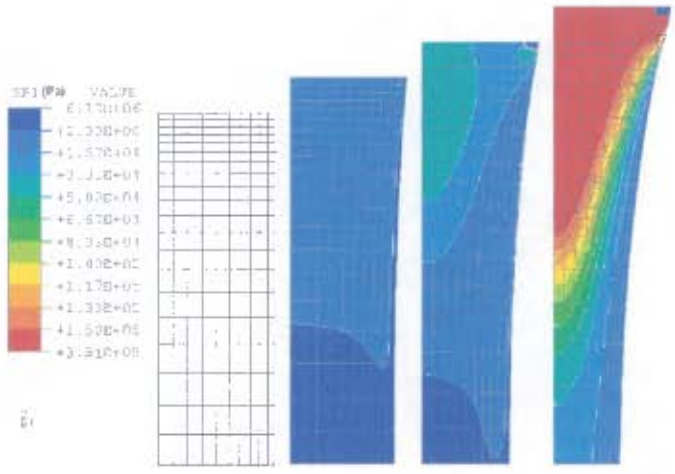

Figure 10.17: Minimum principal stress and deformation at 0, 10, 20 and 30% axial strain for fabric sample 1 model in warp direction

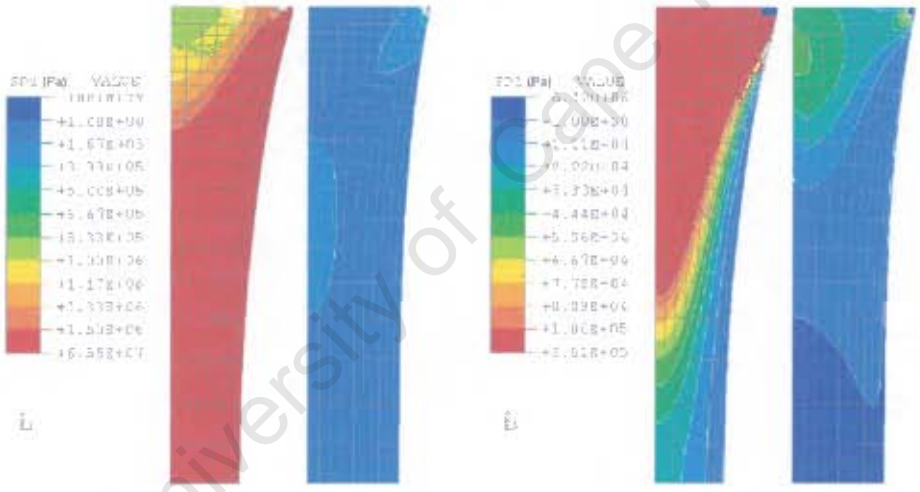

Figure 10.18: Comparison of principal stresses and deformation at 30% axial strain in both warp and weft directions for fabric sample 1

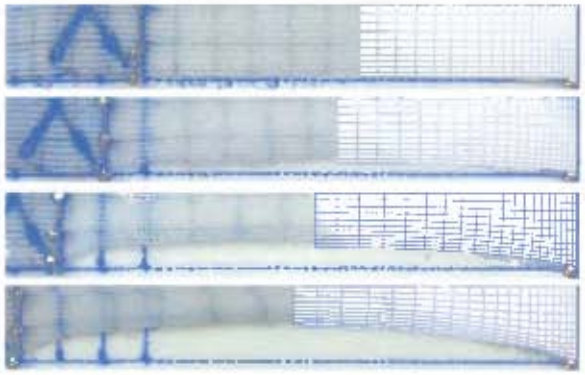

Figure 10.19: Comparison of test vs. model deformation at 0, 10, 20 and 30% axial strain in warp direction

In Figures 10.16 and 10.17 the stress fields observed across the fabric at various axial strains are consistent. As expected, stress concentrations tend toward point C (the displaced corner). For the transverse stress or minimum principal stress SP_1(as these coincide), a reduction is seen toward edge AB (the horizontal centre line). For axial stress or maximum principal stress SP_2 (as these coincide), stress concentrations tend toward point A (the centre). These were to be expected, although for SP_2 this is seen to increase half way down the free edge BC and toward the midpoint of edge AD as seen in Figure 10.16. This increase can be accounted for by viewing the fabric as a system of cables, as shown in Figure 10.20, where the maximum axial stresses would be observed along the cable ties.

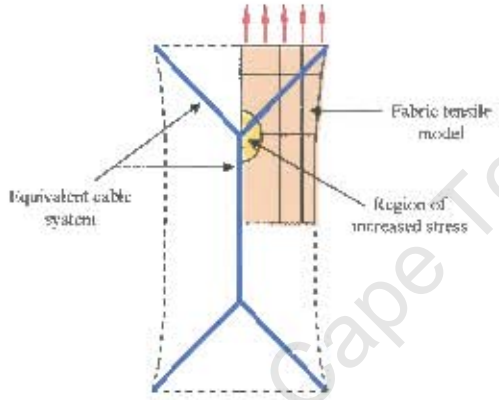

Figure 10.20: Equivalent cable system for fabric in uniaxial tension

The region of increased axial stress along the free edge at point B can be accounted for by the observation that the further away from the displaced edge, the more evenly distributed the axial stress will be across the fabric.

10.5 Concluding comments

From the patch tests and experimental results it can be seen that the latex and porous structures are acceptably modeled, and thus validated, using the procedures detailed in earlier chapters. With the single element patch tests on the fabric material model, the effect of coefficient change on material characteristics was observed and assessed. The viability of the fabric model was done using GA2 and a range of fabric samples tested under uniaxial tension, where a variety of fabric behaviour is capable of being modeled by the strain energy function. However, linear stress-strain relations are not capable of being modelled.

Chapter 11

GA1 and Optimisation on Compliance

11.1 Introduction

The chapter describes the static and dynamic numerical graft model solutions for the various pore sized grafts without adventitial fabric reinforcing. GA1 is utilised to find optimal fabric reinforcing solutions to each of these graft types. The solutions found by GA1 are discussed. These fabric reinforcing solutions are then implemented in the circumferential and longitudinal tensile finite element models to obtain the fabric requirements in terms of force per unit length vs. displacement, as stipulated in international standards for vascular implants [167, 168].

11.2 Non-reinforced porous finite element graft models

11.2.1 Dynamic compliance and wall compression

Table 11.1 gives the dynamic and static compliance values obtained for each porous graft type, from the graft numerical models. Other values displayed include wall compression (%) and diastolic and systolic internal diameters (mm).

Graft Pore Size (μm)	90-106		106-125		125-150	
	Static	*Dynamic*	*Static*	*Dynamic*	*Static*	*Dynamic*
d (%/100mmHg)	16.9	16.0	20.3	19.2	33.9	31.5
Internal Diameter ϕ_i (mm)						
Diastolic	4.088	4.064	4.160	4.133	4.378	4.342
Systolic	4.377	4.319	4.516	4.445	5.002	4.879
Wall Compression (%)						
Diastolic	5.46	1.91	6.25	1.97	8.31	1.28
Systolic	7.72	5.68	8.99	6.51	13.06	8.77

Table 11.1: Dynamic compliance values for non-reinforced graft models

As expected compliance increases with increased pore size, as the larger the pores the weaker the structure. There is little difference between the dynamic and static compliance values; however, as pore size increases, a slight increase is seen in the static compliance. Diastolic and systolic internal diameters reflect similar characteristics with respective static and dynamic compliance. However, there is a large difference between the static and dynamic wall compression values obtained; for dynamic values the compression observed is much lower, this is due to the lagging wall response with pressure pulse observed in the dynamic numerical models. On average, the pores created in the graft structures were $1.21 = 0.07$ times the diameter of the porogens from which they were formed, while the interconnecting windows were 0.52 ± 0.04 times the

diameter [9]. Thus for the lower diameter porogen group of 90-106 μm, the minimum pore size window produced is approximately 47 μm in diameter; after a maximum wall compression of 5.68 % during the pressure cycle, a minimum window pore size of 44 μm is obtained for cellular in-growth. The average diameter of a capillary is 8-10 μm, while the diameter of a functional arteriole, endothelium and a single layer of smooth muscles is roughly 30 μm [32, 174]. Thus, all the pore sized graft groups with maximum wall compression allow for arteriole, endothelium and smooth muscle cell activity and in-growth based on the results observed.

Stress fields in the non-reinforced graft walls. Figure 11.1 displays the dynamic hoop (circumferential), radial and axial stress fields through the various pore size non-reinforced graft structures at mean internal pressure (100 mmHg). The stress fields and sizes are displayed to the same scale to highlight the difference in field and diameters.

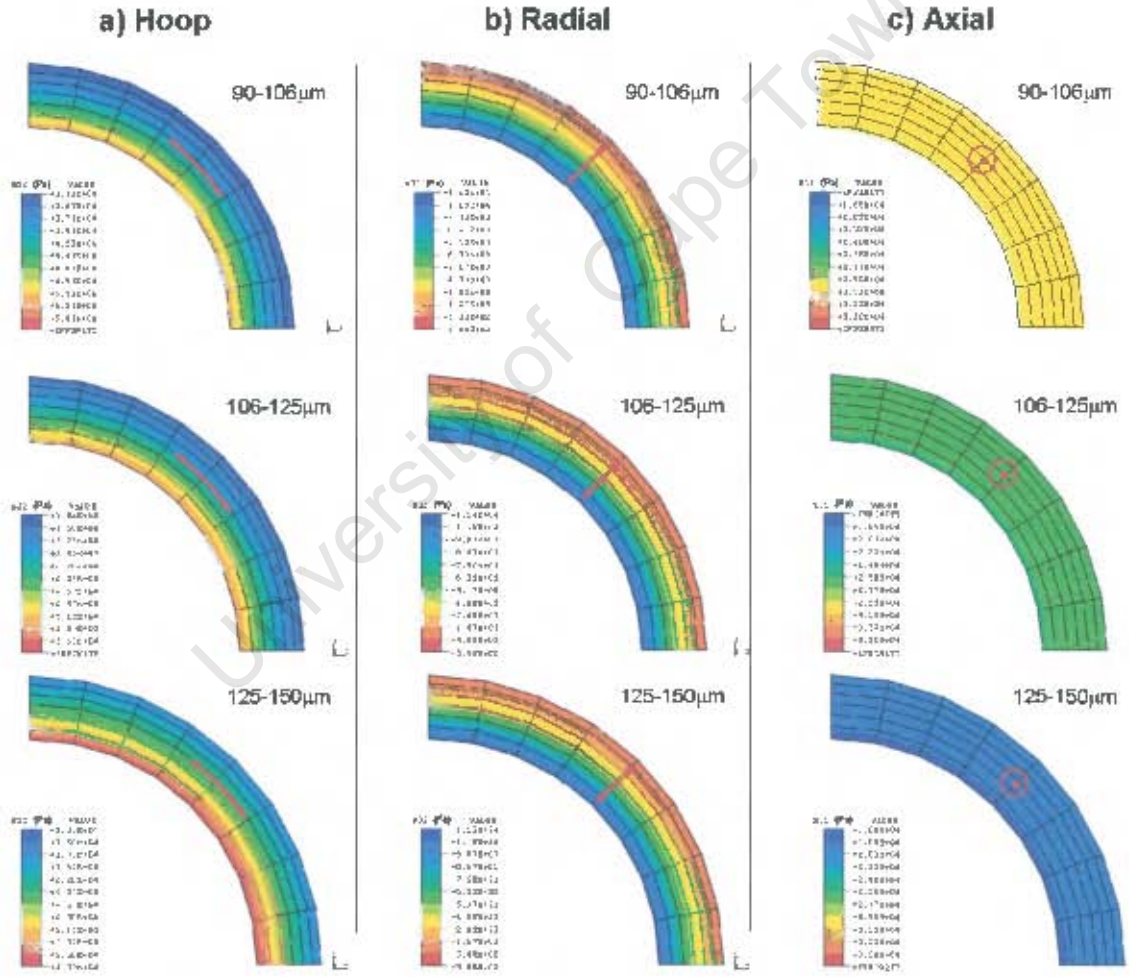

Figure 11.1: Hoop, radial and axial stress variation through 90-106, 106-125 and 125-150 μm porous grafts obtained at 100 mmHg

Figure 11.2 plots the hoop, radial and axial stress profiles for the various pore sized non-reinforced graft structures.

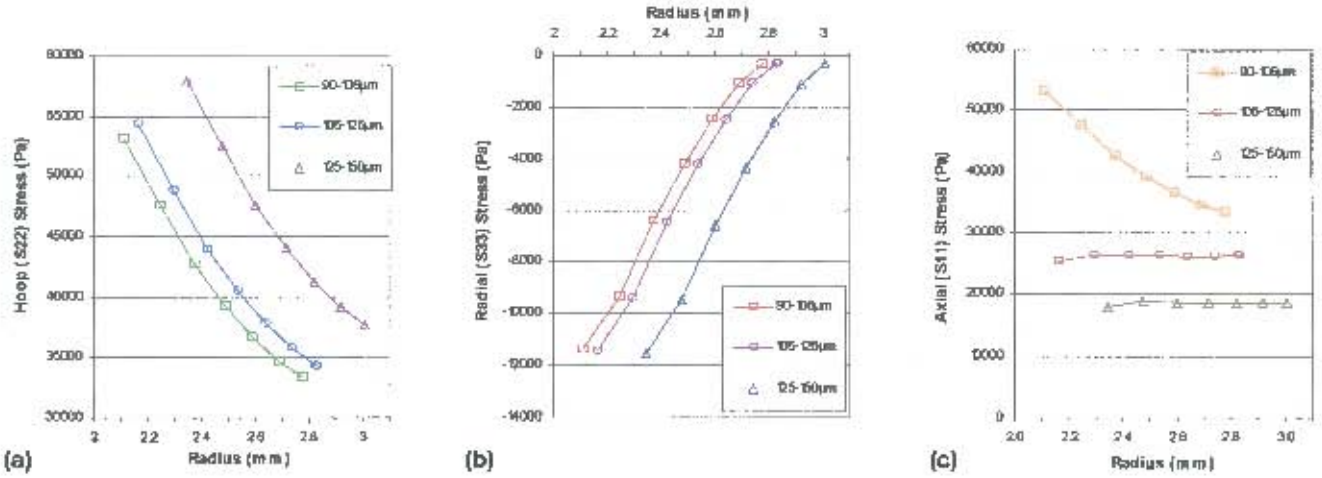

Figure 11.2: Comparison of (a) hoop, (b) radial and (c) axial stress through various porous graft wall structures at 100 mmHg

From the contour plots and graphs in Figures 11.1 and 11.2, the hoop stress fields increase with increased pore size, with the difference between the 90-106 and 106-125 μm being less than that observed between the 106-125 and 125-150 μm. The magnitude of the radial stress for each pore sized group is equal through the wall thickness, as expected.

It is also observed that the axial stress fields decrease considerably in magnitude with increased pore size. The shape of the hoop and radial stress profiles through the graft wall are similar for increasing pore size. However, a variation in axial stress profiles is observed between the pore sized grafts. The stronger 90-106 μm pore sized graft has a higher axial stress at the luminal surface which decays as it tends toward the adventitial surface, while the axial stress profiles through the wall are almost constant for the weaker 106-125 and 125-150 μm. Thus, the weaker large pore sized grafts tend to distribute the axial load evenly through the wall.

11.2.2 Static pressure-diameter curves for non-reinforced grafts

Figure 11.3 gives the static pressure vs. normalised change in internal diameter (P vs. $\Delta d/d_o$) curves for the individual pore size grafts. Typically, increasing the pore size weakens the graft structure and thus over-inflation occurs at lower pressures, causing higher compliance values. As observed, these non-reinforced porous grafts display no stiffening characteristics; in fact, they become weaker at higher pressures, and thus ballooning (aneurysms) may occur if the structure fails while in vivo, hence the need for an external support.

11.3 GA1 optimised fabric reinforced graft model solutions

11.3.1 Reinforcing fabric model solutions

Implementing GA1, a total of 38, 31 and 29 generations were required before reasonable solutions were obtained for increasing pore sized grafts, respectively. A further 8 and 5 generations were required to attain the desired 0.95 fitness value for the 106-125 and 125-150 μm graft types;

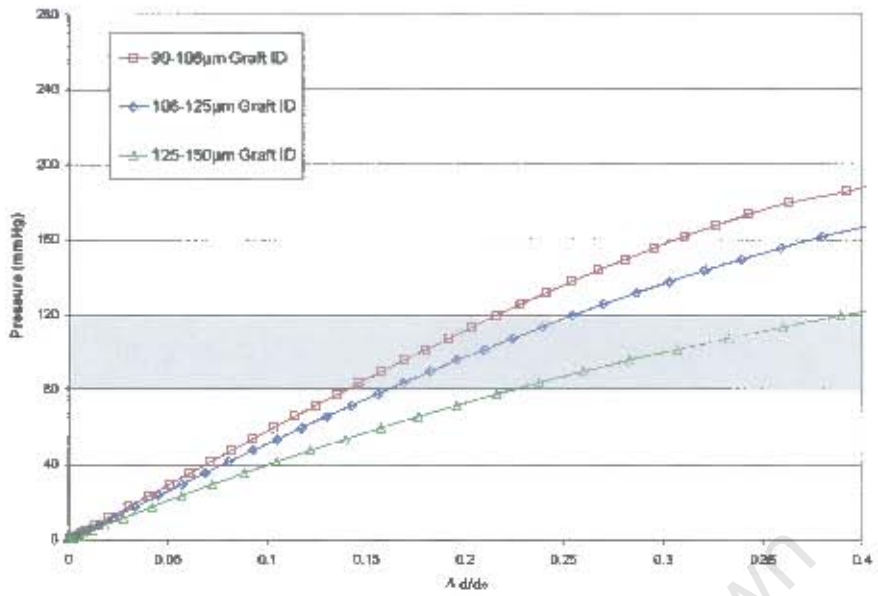

Figure 11.3: Numerical model static P vs. internal $\Delta d/d_o$ curves for the pore sized grafts

however, the full 50 generations were needed before the 90-106 μm graft type obtained a 0.948 fitness value. Table 11.2 displays the optimal fabric model solutions obtained from GA1 for each of the pore sized grafts. The table includes compliance values, compression, internal diameter, fabric circumferential strain, model coefficients, and fitness and objective values obtained.

11.3.2 Dynamic compliance and wall compression

The results obtained from GA1 gave dynamic diameter compliance values of 6.4, 6.9 and 7.1 %/100 mmHg and diastolic diameters of 3.965, 3.998 and 4.000 mm for the 90-106, 106-125 and 125-150 μm pore sized fabric reinforced grafts, respectively. The results demonstrate that GA1 does converge to good solutions. Wall compression values at diastolic and systolic pressures are presented in Table 11.2, where a maximum compression of 6.20 % is obtained by the 125-150 μm pore sized graft. The circumferential strain observed in the fabric solution is greatest for the 106-125 μm pore size fabric reinforced graft, with a value of 8.85 %, while values of 8.13 % and 8.70 % were observed for the 90-106 and 125-150 μm reinforced pore size grafts, respectively. In contrast, the internal diameters at the systolic pressure for the 90-106 and 106-125 μm are less than the 125-150 μm reinforced pore size graft, implying that the adventitial reinforcing fabric plays a larger role in the weaker structures, or increased pore size.

Figure 11.4 displays internal diameter and wall compression with time curves for the 125-150 μm non-reinforced vs. the reinforced pore size graft types. The internal diameter is in phase with the pressure pulse. However, the external diameter change is lagging, as expected. Radial or wall compression for the non-reinforced graft leads the pressure by 0.04 s, while the reinforced graft lags by 0.02 s. The non-reinforced graft's wall compression varies considerably over the pressure cycle, which is an undesirable characteristic for a self-healing porous graft, where it is essential that the pores remain open, and varying little in dimension over the cycle.

Graft Pore Size	(μm)	*90-106*	*106-125*	*125-150*
Dynamic C_d	(%/100mmHg)	6.4	6.9	7.1
Internal Diameter ϕ_i	(mm)			
	Diastolic	3.965	3.998	4.000
	Systolic	4.067	4.109	4.113
Wall Compression	(%)			
	Diastolic	2.93	3.24	3.82
	Systolic	4.82	5.31	6.20
Fabric Circumferential Strain (%)				
	Diastolic	6.61	7.19	7.08
	Systolic	8.13	8.85	8.70
Fabric Model Coefficients				
	C	607.969	977.145	3881.518
	a_1	0.028	15.885	17.748
	a_2	270.643	204.607	133.838
	a_3	1.719	21.012	6.662
	a_4	24.310	16.631	25.734
	a_5	2.745	−28.013	13.785
	a_6	64.376	50.642	66.498
	a_7	8.014	−24.693	−18.083
	a_8	−8.797	−13.284	2.018
	a_9	−9.155	14.190	20.619
Fitness Value	$f(C, a_i)$	0.9484	0.9552	0.9509
Objective Value	$\phi(C, a_i)$	0.9484	0.9552	0.9509
Partial Objective Values				
	$\phi^{\wedge C_d^{dyn}}$	0.9693	0.9329	0.9230
	$\phi^{\wedge d_{dia}}$	0.9119	0.9943	0.9996
Generation Number		50	39	34
Total Time	(hh:mm:ss)	41 : 48 : 12	30 : 13 : 31	22 : 37 : 13

Table 11.2: Solutions obtained from GA1 for reinforced porous grafts

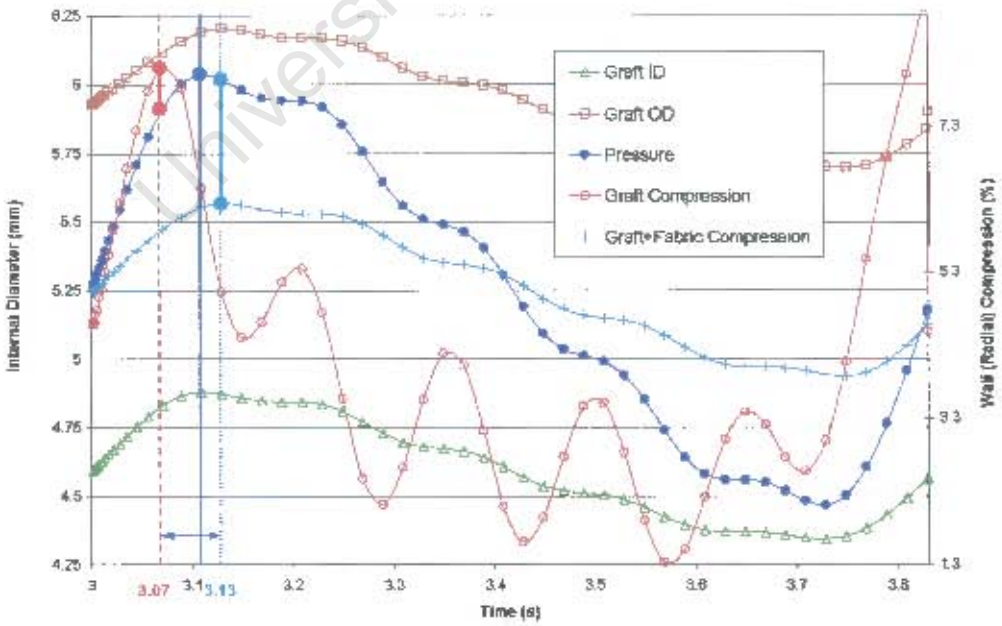

Figure 11.4: Internal (ID), external diameter (OD) and wall compression vs. time curves for non-reinforced and reinforced 125-150 μm pore sized grafts

Dynamic stress fields through graft wall and fabric reinforcing. Figure 11.5 displays the dynamic hoop (circumferential), radial and axial stress contour plots, while Figure 11.6 plots the hoop, radial and axial stress profiles for the various pore size adventitial fabric reinforced grafts at mean pressure (100 mmHg)

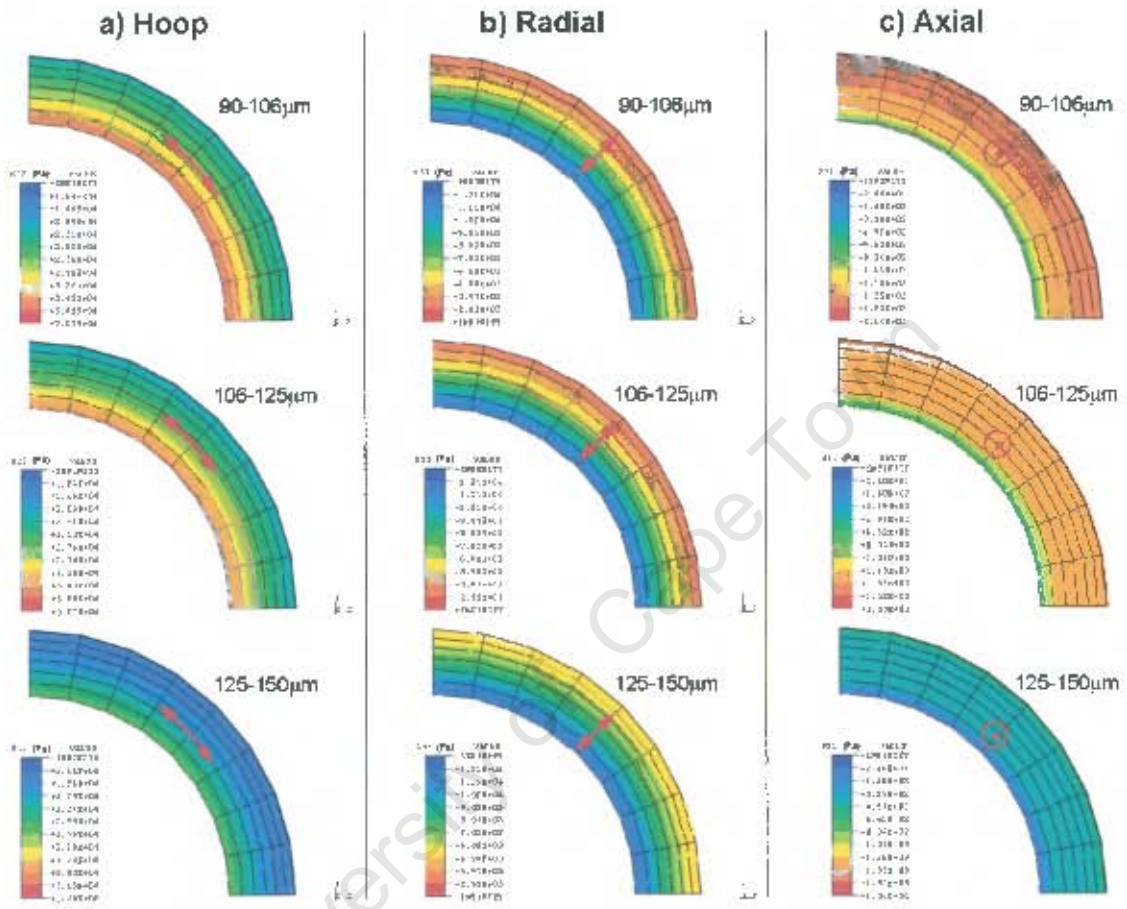

Figure 11.5: Hoop, radial and axial stress variation through 90-106, 106-125 and 125-150 μm optimal fabric reinforced porous grafts obtained at 100 mmHg

The high fabric stress values, indicated by the sharp change in stress profile in Figures 11.6(a) and (c), obtained for the 125-150 μm reinforced graft compared to the 106-125 and 90-125 μm structures, illustrate that the fabric reinforcing used for the weaker 125-150 μm graft plays a dominate role, while this role is reduced for the 106-125 and 90-125 μm structures.

Comparing Figure 11.6 with 11.2, the fabric reinforcings reduce and level out the circumferential stresses observed. They also reduce and level out the axial stress in the 125-150 μm graft, while only a reduction is observed in the 106-125 and 90-125 μm structures. With the addition of the reinforcing, the compressive radial stress is observed to increase toward the outer (adventitial) surface, while relatively small changes are observed at the lumen for all graft types.

The stress contour plots and profiles observed in Figures 11.5 and 11.6 indicate that the fabric reinforcing plays a dominate role in providing the correct compliance, and reducing circumfer-

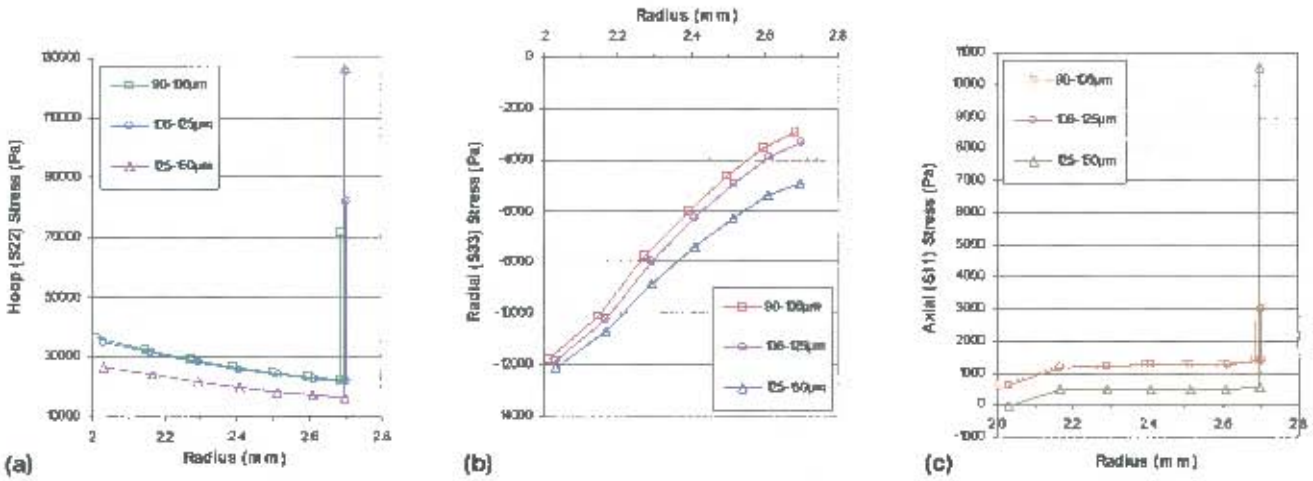

Figure 11.6: Comparison of (a) hoop, (b) radial and (c) axial stress through optimal fabric reinforced porous wall structures at 100 mmHg

ential and axial stresses observed in the porous graft structures.

11.3.3 Static pressure-diameter curves for fabric reinforced grafts

The fabric model solutions obtained from GA1 were utilised in static numerical graft models to obtain static pressure vs. normalised change in diameter curves for the reinforced 90-106, 106-125 and 125-150 μm pore sized grafts. Figure 11.7 displays the internal and external diameter curves obtained for the various structures. The region where nonlinear stiffening starts to occur is indicated on the figure.

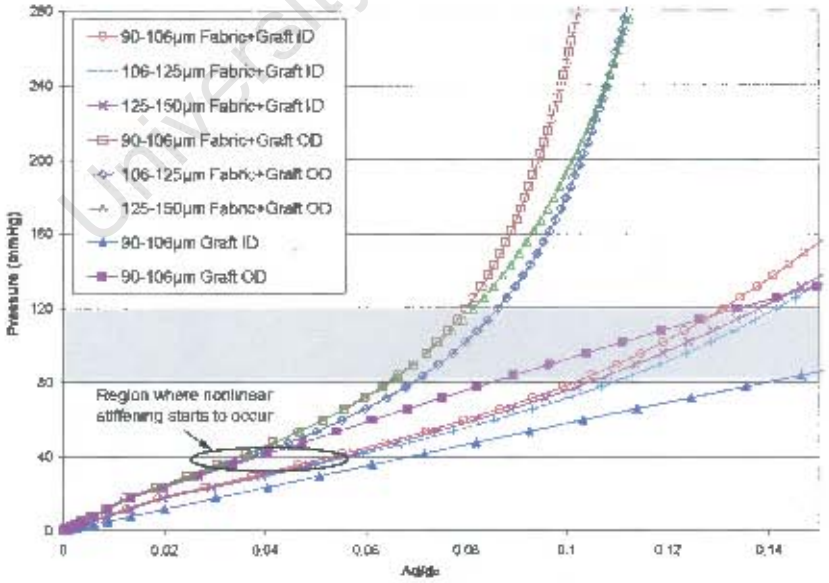

Figure 11.7: Numerical model static P vs. internal and external $\Delta d/d_o$ curves for the optimal fabric reinforced porous grafts obtained from GA1

From Figure 11.7, the grafts exhibit nonlinear stiffening characteristics when the fabric re-

inforcing is utilised. The region where nonlinear stiffening starts to occur is below the physiological range, and occurs at 35 mmHg for the 125-150 μm and 36. mmHg for the 90-106 μm reinforced pore size grafts. In natural blood vessels this nonlinear stiffening is observed throughout the vessels' loading history (see Figure 2.9). The difference in nonlinear stiffening between the internal and external diameter curves is apparent, where the internal stiffening is not as pronounced due to compression of the graft wall. However, after tissue ingrowth the porous structures' compression characteristics will be reduced giving a pronounced internal diameter nonlinear stiffening effect.

If one views the pressure-diameter relations of the external porous graft wall (without the reinforcing) and the reinforcing fabric separately one obtains two characteristic curves. By the addition of these two pressure-diameter relations, one can obtain an estimate for the pressure-diameter relation of the combined structure. This is demonstrated in Figure 11.8 for the 125-150 μm pore size graft, where the addition of the external diameter non-reinforced graft curve (Graft OD) with the fabric's pressure-diameter relation (Fabric) one obtains an estimate for pressure-diameter relation of the combined structure (Addition of Graft and Fabric OD curve) which is similar to the fabric reinforced graft solution (Fabric+Graft OD).

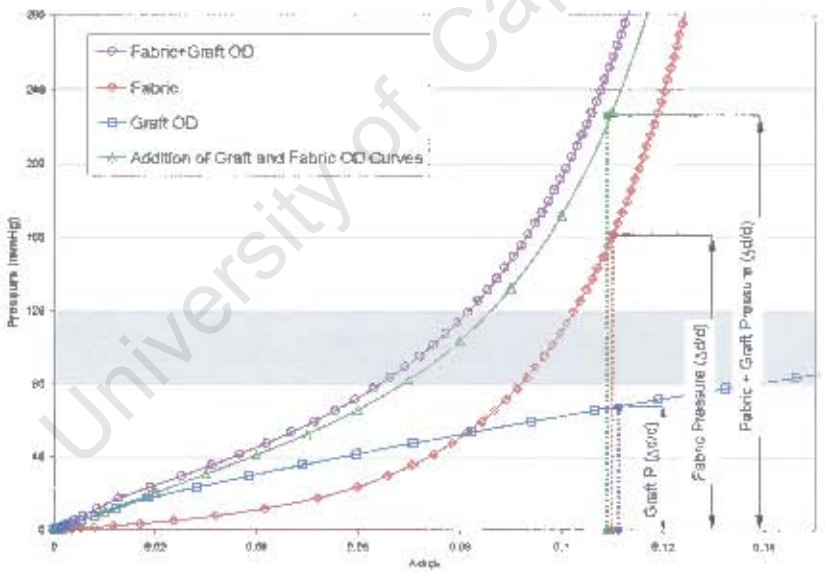

Figure 11.8: Static P vs. external $\triangle d/d_o$ for 125-150 μm pore sized graft, the reinforcing sock and the combined structure

11.4 Circumferential and longitudinal model solutions

The fabric model solutions obtained from GA1 are also implemented in the circumferential and longitudinal tensile numerical models to obtain the fabric requirements in terms of force per unit length vs. displacement. These force per unit length vs. displacement curves will be used to develop physical fabric reinforcing samples.

11.4.1 Circumferential stress-strain curves

Figures 11.9 and 11.10 display plots of force per unit length vs. displacement for the first three fabric reinforcing solutions obtained from GA1 for the 125-150 μm graft in the circumferential and longitudinal directions, respectively.

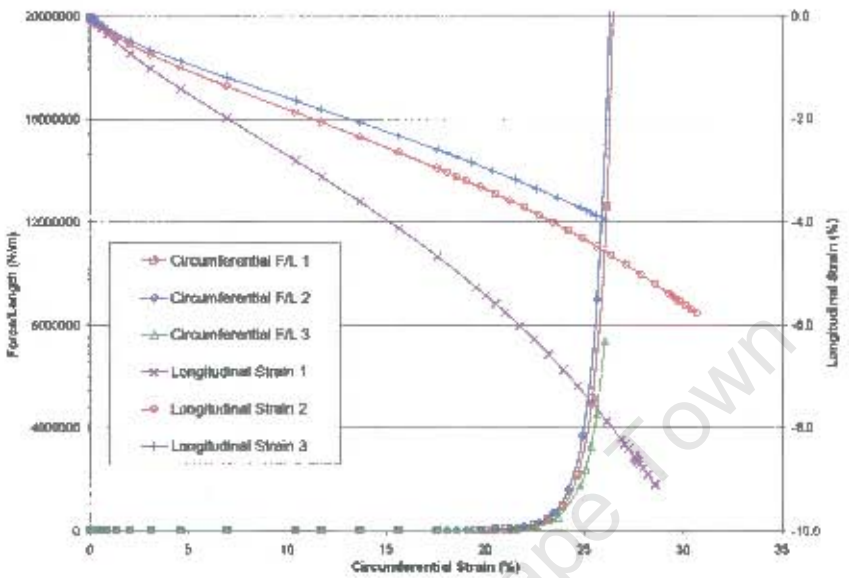

Figure 11.9: Three fabric reinforcing solutions for 125-150 μm pore sized grafts obtained from GA1; circumferential tensile numerical simulation results

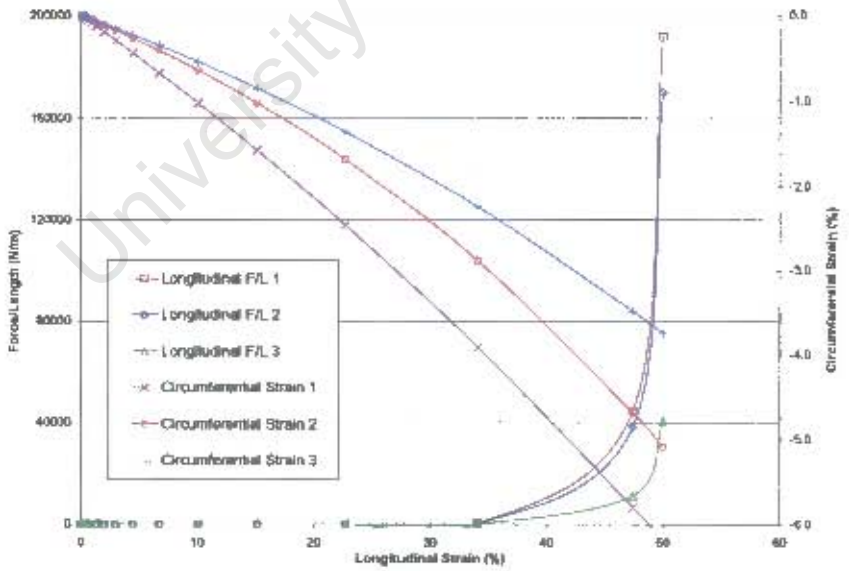

Figure 11.10: Three fabric reinforcing solutions for 125-150 μm pore sized grafts obtained from GA1; longitudinal tensile numerical simulation results

The circumferential force-displacement curves for the first three solutions are similar, however, a large difference is observed in the longitudinal force-displacement curves. Table 11.3 exhibits the variation in compliance, wall compression, internal diameter, fabric circumferential

strain and the fitness values for the first three fabric reinforcing solutions to the 125-150 μm graft. As can be seen, a number of reinforcing solutions are possible to obtain the desired compliance, diastolic diameter and nonlinear stiffening characteristics for a particular porous structure.

Solution Number		*1*	*2*	*3*
Dynamic C_d	(%/100mmHg)	7.1	7.0	7.2
Internal Diameter ϕ_i	(mm)			
	Diastolic	4.000	3.992	4.000
	Systolic	4.113	4.104	4.115
Wall Compression	(%)			
	Diastolic	3.82	3.82	3.82
	Systolic	6.20	6.20	6.20
Fabric Circumferential Strain (%)				
	Diastolic	7.08	7.03	7.07
	Systolic	8.70	8.68	8.74
Fabric Model Coefficients				
	C	3881.518	4282.589	4282.589
	a_1	17.748	13.737	12.918
	a_2	133.838	133.236	126.283
	a_3	6.662	2.250	2.554
	a_4	25.734	15.106	12.542
	a_5	13.785	18.598	14.050
	a_6	66.498	68.905	66.776
	a_7	−18.083	−11.465	−21.364
	a_8	2.018	11.242	4.791
	a_9	20.619	18.212	14.993
Fitness Value	$f(C, a_i)$	0.9509	0.9451	0.9448
Objective Value	$\phi(C, a_i)$	0.9509	0.9451	0.9448
Partial Objective Values				
	$\phi^{\Delta C_d^{dyn}}$	0.9230	0.9257	0.9134
	$\phi^{\Delta d_{dia}}$	0.9996	0.9791	0.9997
Obtained from Generation		34	32	30

Table 11.3: Three best solutions obtained from the generations of GA1 for 125-150μm fabric reinforced grafts

Figure 11.11 illustrates the different pressure-diameter relations obtained from the first three reinforcing solutions for the 125-150 μm graft. Slight variations are observed in the curvature, however the compliance and diastolic diameter requirements are consistent for each solution as indicated in Table 11.3.

Figures 11.12 and 11.13 compare the circumferential and longitudinal tensile fabric reinforcing solutions obtained from GA1 for the different pore sized graft types. From these figures, pronounced differences are observed in the required fabric reinforcing for each pore sized graft.

In the circumferential direction, there is a large change in force per unit length at 16, 18 and 20 % circumferential strain for increasing pore size, respectively. The circumferential transverse strains are high in the 90-106 and low for the 106-125 μm graft types reinforcing solutions. In the longitudinal direction, the fabric reinforcing requirement for the 125-150 μm graft stiffens much earlier than the 90-106 and 106-125 μm reinforcing solutions, and the longitudinal transverse strains are high for the 125-150 μm fabric reinforcing.

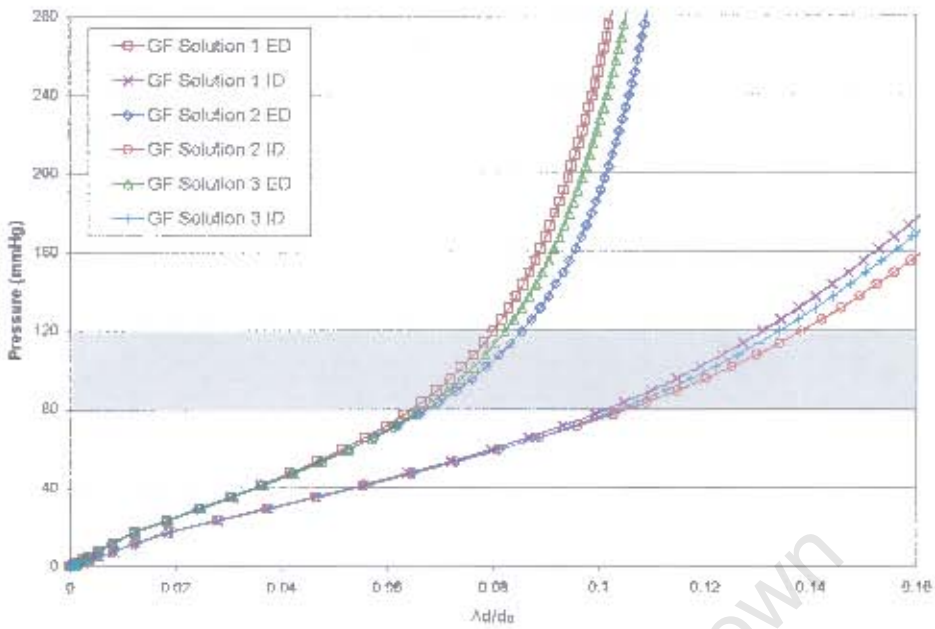

Figure 11.11: Numerical simulation of static P vs. internal and external $\Delta d/d_o$ for the first three fabric reinforced solutions obtained from GA1 for the 125-150 μm graft

It is apparent that the fabric reinforcing solutions for the various pore sized grafts display significantly different behaviour, yet they achieve the goal of reducing the stress fields in the porous structures while obtaining the correct compliance and diastolic diameters indicated in Table 11.2.

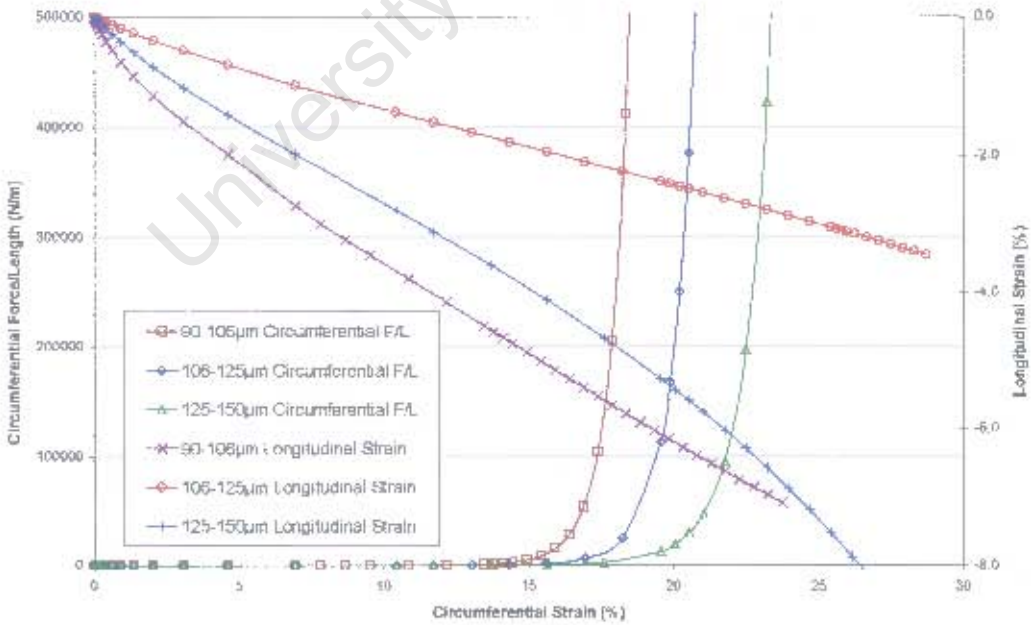

Figure 11.12: Optimal fabric reinforcing circumferential tensile model solutions for porous grafts obtained using GA1

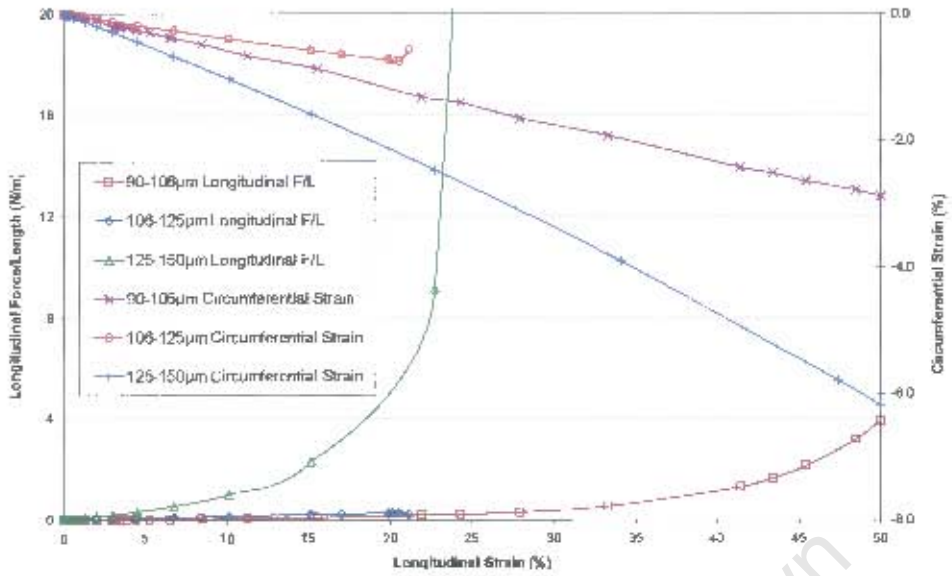

Figure 11.13: Optimal fabric reinforcing longitudinal tensile model solutions for porous grafts obtained using GA1

11.4.2 Circumferential stress fields for reinforcing fabrics

Figure 11.14 displays the deformed and undeformed fabric circumferential tensile model solution for the 125-150 μm graft obtained from GA1. As expected, the fabric contracts transversely during circumferential tensioning, indicating that GA1 found realistic model solutions.

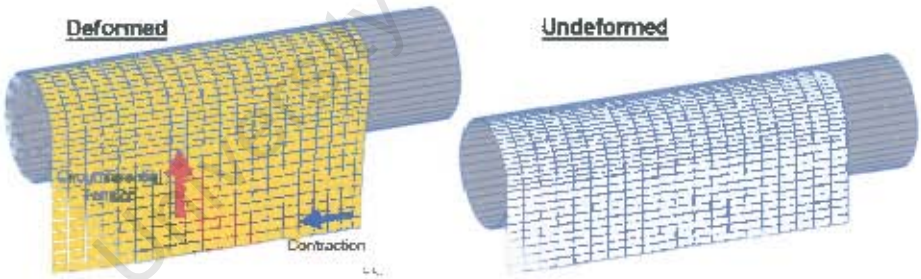

Figure 11.14: Deformed and undeformed optimal circumferential tensile solution for 125-150 µm porous graft type

Figure 11.15 depicts the circumferential ($S22$), axial ($S11$) and shear ($S12$) stress fields for the fabric circumferential tensile model solution above. The stress fields are reasonable, where the maximum stress values observed are in the circumferential direction. This circumferential stress is a maximum at the centre and reduces toward the edge of the fabric reinforcing tube. The distribution of longitudinal stress is similar, where a maximum is observed at the centre. It should be noted that both the circumferential and longitudinal stress fields are in tension and the circumferential stress is roughly 25 times higher than the longitudinal stress.

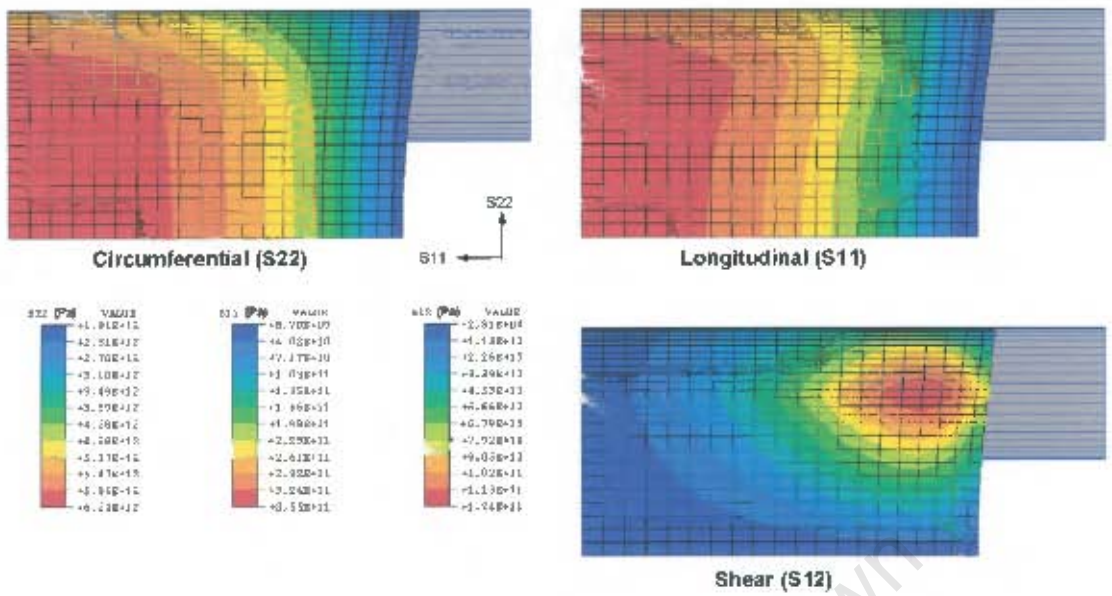

Figure 11.15: Circumferential (S22), axial (S11) and shear (S12) stress fields for optimal circumferential tensile solution for 125-150 μm porous graft type

11.4.3 Longitudinal stress fields for reinforcing fabrics

Figure 11.16 displays the axial ($S11$) and circumferential ($S22$) stress fields and the deformed and undeformed configurations of the fabric longitudinal tensile model solution for the 125-150 μm graft obtained from GA1. Again, realistic deformation in the circumferential direction is observed due to longitudinal tension.

The axial stress field observed is a maximum at the centre of the fabric reinforcing tube (if one ignores edge effects due to model constraints), while circumferential stress is observed to be a maximum at the clamped end, as expected. The maximum longitudinal stress is 3×10^6 times higher than the maximum circumferential stress.

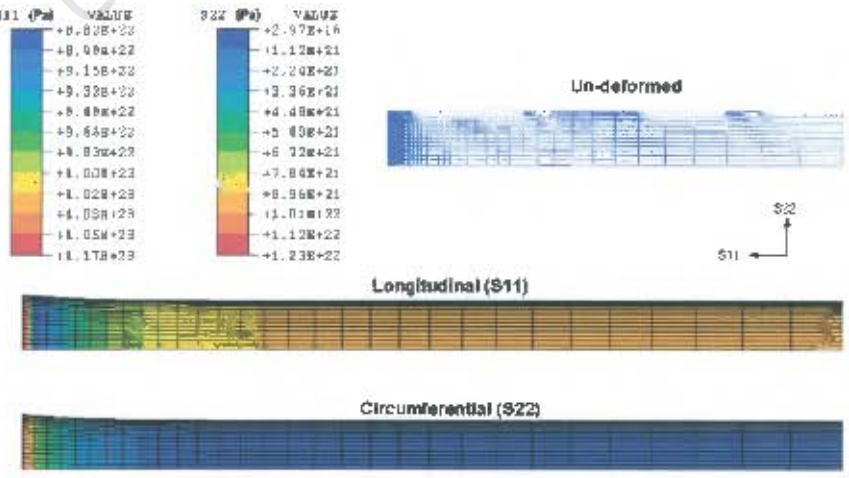

Figure 11.16: Circumferential (S22) and axial (S11) stress fields for optimal longitudinal tensile solution for 125-150 μm porous graft type

11.4.4 Physiological circumferential strains of reinforcing fabric solutions

Figure 11.17 displays the physiological operating region of the reinforcing fabric solutions in the circumferential tensile models based on the circumferential strain values specified in Table 11.2. From this, the force-displacement region in which the reinforcing solutions operate can be obtained. Corresponding circumferential force per unit length values of 3 and 22.5 N/m were obtained from circumferential strains of 6.61 and 8.85 % as indicated in Figure 11.17.

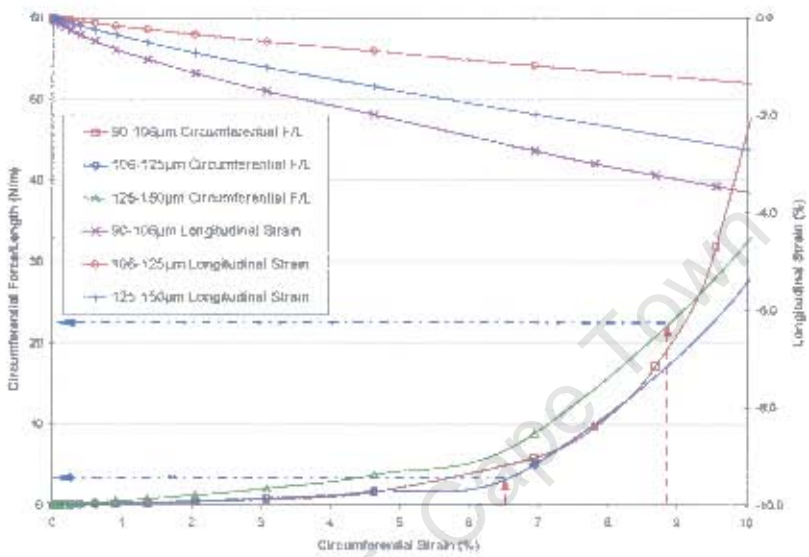

Figure 11.17: Physiological operating region of the reinforcing fabric solutions in the circumferential tensile models

Chapter 12

The Development of the Fabric Reinforcing Samples

12.1 Introduction

The previous chapters have focused on the use of computational approaches to simulate the behaviour of three fabric reinforced porous graft types. The simulations have been used in conjunction with a genetic algorithm to optimise the fabric model coefficients to ensure that these reinforced grafts have a desired compliance, diastolic diameter and a nonlinear stiffening response. These optimal fabric model coefficients were used to find the transverse force-displacement requirements of the fabric reinforcing in the circumferential and longitudinal directions.

This chapter discusses the development of two prototype fabric reinforcing tubes and the differences between the prototypes produced and the solutions obtained by GA1. The chapter then considers the fabric solutions obtained from GA3 to model the prototypes produced. Finally, finite element simulations and compliance values are re-established using the fabric model solutions obtained from GA3. These new numerical solutions are used in the following chapter to validate the numerical solutions.

12.2 Development of sample fabric reinforcing socks

A specialist manufacturer of medical grade fabric prostheses[1] was approached to produce prototype reinforcing structures which displayed the required longitudinal and circumferential force-displacement numerical solutions obtained from GA1 as described in Figures 11.12 and 11.13. Other fabric characteristics, such as fabric porosity, texture and yarn thickness were specified; as detailed in Table 12.1.

Description	*Units*	**Ideal**	**Maximum**	**Minimum**
Sock Internal Diameter	mm	5.0	5.5	5.0
Fabric Wall Thickness	μm	50	250	50
Fibre Thickness	μm	20	50	20
Pore Size Diameter	mm	1.0	1.0	0.3
Surface Area Coverage	%	30	75	30

Table 12.1: Desired characteristic of fabric reinforcing

A number of initial fabric reinforcing samples with a large variation in characteristics were

[1] Secant Medical LLC, 700 Park Avenue, Perkasie, PA 18944, USA, Tele # : 215-257-8680, Fax #: 215-257-8875.

manufactured for review, a subset of which are shown in Figure 12.1.

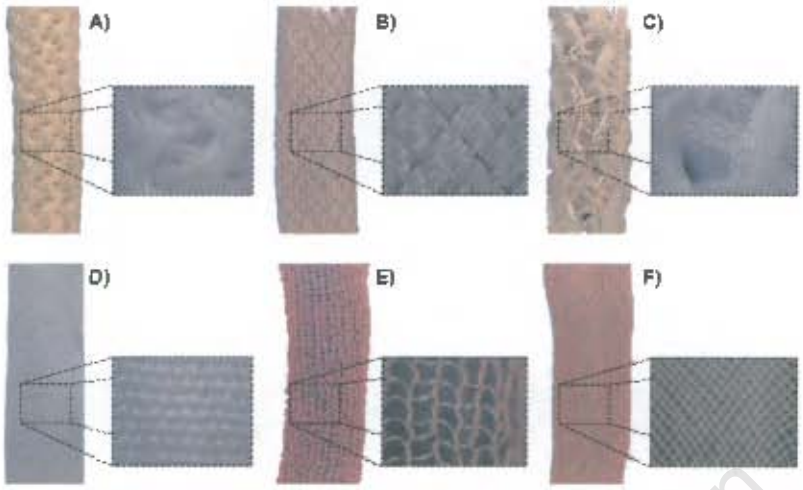

Figure 12.1: Initial fabric reinforcing samples provided by manufacturer

Samples C, E and F were identified as being preferential, as they satisfied the requirements of Table 12.1. The ideal solution would be sample F, as this has a fine mesh structure which will not adversely affect the grafts' healing properties by preventing cellular ingrowth. However, it is a straight braid structure which is unlikely to produce the required nonlinear stiffening characteristics, unlike the knitted samples C and E.

From these candidates, a number of sample iterations were carried out to obtain the required circumferential and longitudinal force-displacement characteristics obtained from the solutions in GA1. Figure 12.2 shows a sequence of iterative reinforcing socks developed from initial candidates C, E and F.

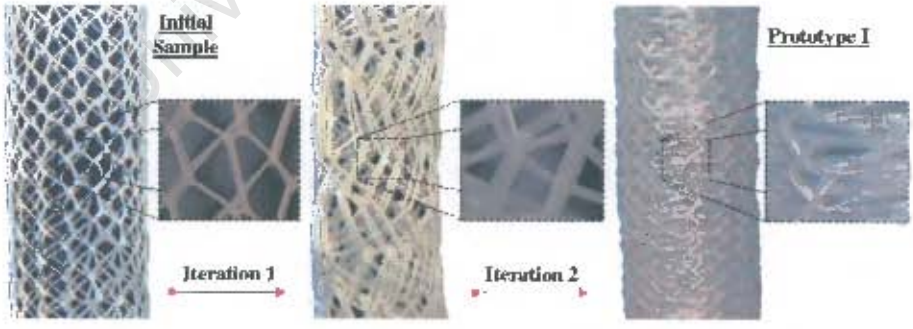

Figure 12.2: Iterative development of reinforcing prototype I

It was not, however, possible to develop and manufacture final fabric reinforcing socks with the desired characteristics obtained from GA1 due to time and cost constraints. Instead, two of the iterative reinforcing samples which displayed similar circumferential and longitudinal force-displacement characteristics described in Chapter 11 are used to obtain physical results. The two samples chosen are referred to as prototypes I and II. Both prototypes were produced from 50 μm

Dacron fibre threads with a 0.35 mm pore size diameter and a surface coverage of between 70 and 75%.

Apart from not matching the transverse force-displacement requirements of GA1, the prototype samples were produced with a 6 mm internal diameter, which is larger than the external diameter of the porous grafts (5 mm). This was to allow the graft sample to be inserted into the reinforcing sock. To ensure, that the adventitial reinforcing socks fitted the outer wall of the porous grafts, the fabric reinforcing had to be pre-strained in the longitudinal direction over the graft samples. Figure 12.3 illustrates the difference in reinforcing sock and graft diameter and the required longitudinal straining of the fabrics over the graft samples, in order for the reinforcing to fit to the external wall of the graft.

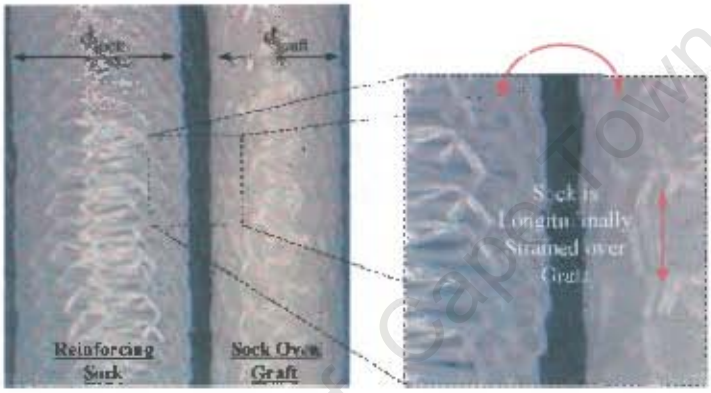

Figure 12.3: Required longitudinal straining of prototype reinforcing samples to fit the porous graft samples

To ensure that consistent reinforced graft test samples were produced, each prototype sock sample was longitudinally strained over the graft by the same amount. Table 12.2 shows the longitudinal strains applied to the adventitial reinforcing sock prototypes I and II, to ensure that they conformed to the external surfaces of the porous grafts.

Reinforcing *Prototype*	**Longitudinal Strain** (%)
I	59 ± 1.9
II	91 ± 1.7

Table 12.2: Longitudinal strains applied to fabric prototypes to fit porous graft samples

The longitudinal straining induces a pre-stress in the reinforcing structure. This change in stress and deformation states will need to be accounted for when comparing finite element model solutions and experimental results.

Fabric reinforcing tensile tests adjusted for longitudinal strain. Due to the longitudinal straining, new circumferential and longitudinal force-displacement curves had to be obtained. In order to obtain the new curves, the fabric socks were pre-strained longitudinally as specified in Table 12.2, and then placed in a tensile tester. Figure 12.4 shows prototype II in the circumfer-

ential tensile tester, where the sample is longitudinally strained prior to testing.

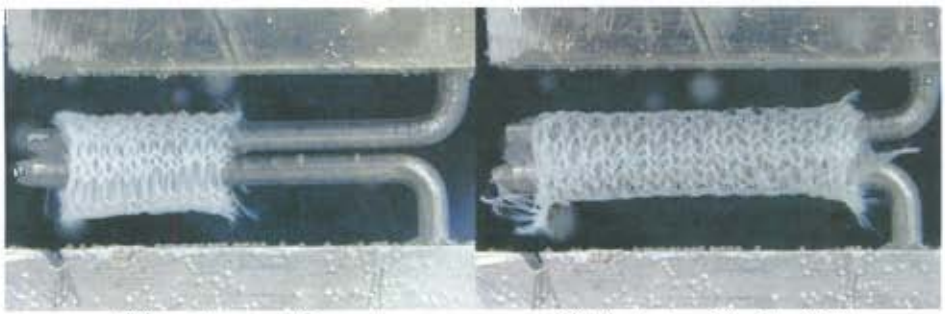

a) Manufactured 6mm ϕ Reinforcing Prototype *II*

b) Prototype *II* with 91% longitudinal Pre-Strain (5mm ϕ)

Figure 12.4: Prototype II before and after longitudinal strain in circumferential tensile test

Variation between GA1 model solutions and prototype fabric reinforcing samples. *(a) Circumferential:* Figure 12.5 shows the circumferential force-displacement curves for prototypes I and II, with and without longitudinal stain. The optimal fabric reinforcing model solution for the 90-106 μm pore sized graft obtained from GA1 is also displayed.

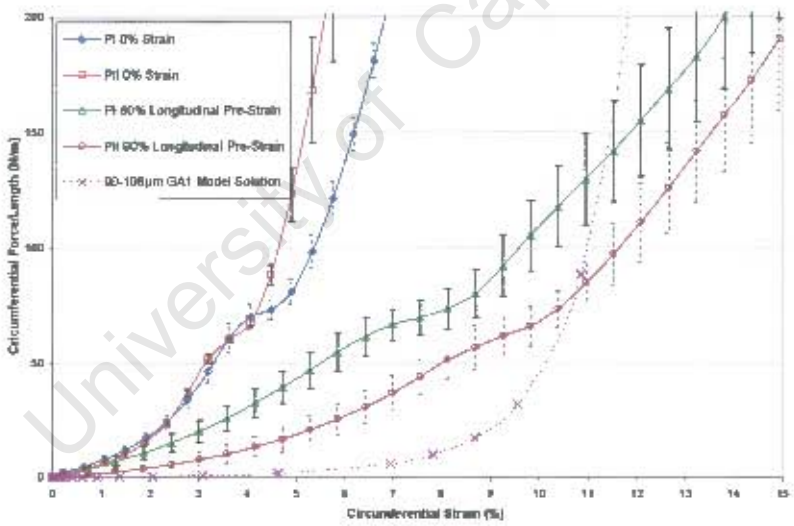

Figure 12.5: Circumferential tensile test results of reinforcing prototypes I and II, with and without longitudinal strain applied

The prototype characteristic curves are considerably different to those required by the numerical solution for the 90-106 μm pore sized graft. Both prototypes stiffen in the circumferential direction earlier than required. The position of maximum curvature for the solutions obtained from GA1 occur at around 9.1% strain (refer to Section 10.3.1), for prototypes I and II this occurs at 2.2 and 1.9% respectively, and 2.8 and 1.9% for the longitudinally strained prototype samples. Little difference is observed between prototypes I and II without longitudinal straining, only when the samples are longitudinally strained is a large difference observed. The difference

in the circumferential force-displacement curves for the longitudinal strained prototypes vs. the model solution will give lower compliance values for the prototype samples, as gradients are larger and stiffening occurs earlier than the numerical solution.

When reviewing Table 11.2 it can be seen that the physiological circumferential strains at which the 90-106 μm fabric reinforcings will possibly operate according to the computational solutions of GA1 occur between 6.61 and 8.13 %. If one looks at this region in Figure 12.5, it can be seen that the circumferential force per unit length of the longitudinally strained prototype samples is 6-12 times greater in magnitude.

Using the circumferential numerical solutions obtained from GA1 at the physiological operating strains for a particular graft type, one can obtain the diastolic and systolic circumferential force per unit length requirements of the adventitial reinforcing as described in Section 11.4.4. These diastolic and systolic force per unit length values can then be used to gain estimate physiological circumferential strains which would occur if other reinforcing types are used. This is illustrated in Figure 12.6 for the 90-106 μm GA1 solution and prototype I.

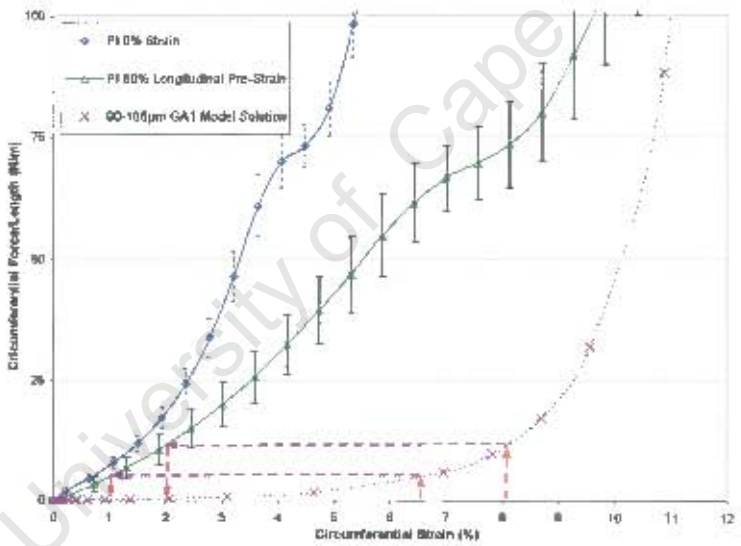

Figure 12.6: Estimate physiological circumferential strains for prototype I based on force per unit length requirements from 90-106 μm GA1 solution

From Figure 12.6, the physiological strains of 6.6 and 8.9 % give diastolic and systolic force per unit length values of 5.1 and 11.5 N/m from the GA1 solution. Using these force per unit length values and the circumferential curve obtained from prototype I, one can obtain estimate physiological circumferential strains which would be observed if prototype I were used to reinforce the 90-106 μm graft type. Estimate circumferential strains of 1 and 2 % are obtained which are substantially lower than 6.6 and 8.9 %. For prototype I, the circumferential curve between the diastolic and systolic force per unit length values is approximately linear compared to the GA1 solution.

GA1 optimises on a 6 %/100 mmHg compliance, a 4.00 mm diastolic internal diameter, and

nonlinear stiffening. Thus, given that compliance is proportional to the difference in the diastolic and systolic circumferential strains, it can be seen that the compliance of the graft using the estimate circumferential strains of prototype I will be reduced considerably (roughly two thirds assuming that little or no wall compression is observed). A circumferential strain of 6.6% from the GA1 solution which gives a 4.088mm diastolic internal diameter (Table 11.2), thus, the estimate circumferential strain value of 1% will give a considerably lower diastolic diameter. This and the fact that the circumferential curve between the diastolic and systolic force per unit length values is approximately linear for prototype I, means that prototype I used as a reinforcing for the 90-106 μm graft will not produce the required 6 %/100 mmHg compliance, 4.00 mm diastolic diameter and nonlinear stiffening.

(b) Longitudinal: Figure 12.7 shows the longitudinal force-displacement curves of both reinforcing prototypes, with and without longitudinal staining. These are also compared to one of the optimal reinforcing solutions for 90-106 μm pore sized grafts obtained from GA1.

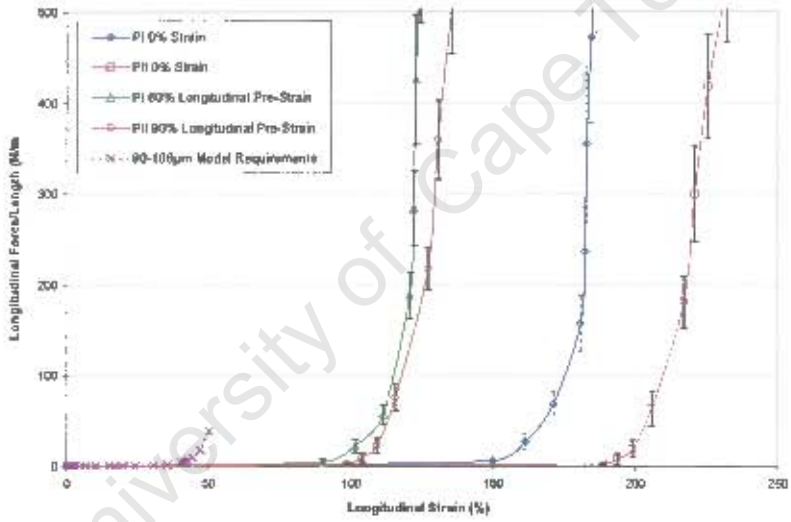

Figure 12.7: Longitudinal tensile test results of reinforcing prototypes I and II, with and without longitudinal strain applied

From the longitudinal curves of Figure 12.7, the manufactured prototypes do not match the optimal requirements obtained from GA1. The maximum curvature of the unstrained prototypes occurs at 163% and 198% longitudinal strain. However, with the longitudinal straining this is reduced to 111 and 109% respectively. Thus the model compliance and diastolic diameter predictions from GA1 will not be achieved.

General reinforcing characteristics of prototypes. Other required characteristics of the adventitial reinforcing were assessed for prototypes I and II, with and without longitudinal straining. Table 12.3 shows the other required prototype characteristics.

From Figures 12.5 and 12.7 and Table 12.3 it can be seen that the prototype reinforcing samples are far from ideal as an optimal reinforcing sock based on the results of GA1. However due

Description	*Units*	Not Strained		Strained	
		I	II	I	II
Sock Internal Diameter	mm	$5.8 - 0.5$	6.0 ± 0.6	$5.0 + 0.3$	$5 \div 0.3$
Fabric Wall Thickness	μm	$600 \perp 100$	$450 \perp 150$	$600 \perp 100$	$450 \perp 150$
Fiber Thickness	μm	$50 = 10$	50 ± 10	$50 = 10$	50 ± 10
Pore Size Diameter	mm	$0.8 = 0.6$	0.8 ± 0.5	3.2 ± 0.1	$3.1 + 0.5$
Surface Area Coverage	%	83 ± 8	$79 - 6$	70 ± 7	$68 \perp 5$

Table 12.3: Fabric prototype characteristics with and without applied longitudinal strain

to time constraints and cost factors it was not possible to produce the required samples for direct correlations.

12.3 GA3 and prototype fabric model solutions

To validate the numerical solutions, a reverse procedure of obtaining the fabric models which describe the prototypes' circumferential and longitudinal tensile stress-strain characteristics are required for implementation in the numerical graft model. The genetic algorithm GA3 is used to optimise the fabric material model coefficients to the circumferential and longitudinal tensile experimental results for prototypes I and II. As described in Chapter 9, this GA utilises the same fitness and objective functions as GA2; however, the partial objective and fitness functions for local axial and transverse strains are excluded, as transverse strain data was not collected.

12.3.1 GA3 solutions to prototypes

Implementing GA3 for both the longitudinally strained prototypes, the full 50 generations were needed in order to obtain a set of solutions for prototypes I and II. Table 12.4 shows the model parameters for the longitudinally strained reinforcing prototypes obtained from GA3, including the fitness values and the generation number.

Pre-strained prototype		*I*	*II*
Fabric model coefficients			
	C	165856.0	131290.1
	a_1	0.165	0.846
	a_2	38.989	26.041
	a_3	19.378	22.779
	a_4	0.933	1.1694
	a_5	0.057	-0.105
	a_6	-29.794	-18.299
	a_7	7.999	1.313
	a_8	7.512	4.031
	a_9	1.483	-0.670
Fitness value	$f(C, a_i)$	0.8132	0.7623
Objective value	$\phi(C, a_i)$	0.8132	0.7623
Partial objective values			
	$\phi^{F/L^{Circ}}$	0.9633	0.9615
	$\phi^{F/L^{Long}}$	0.6631	0.5601
Generation number		50	50
Total time	(hh:mm:ss)	64 : 48 : 36	72 : 31 : 52

Table 12.4: Model coefficients for fabric prototypes obtained from GA3

As observed the fitness values obtained are low, namely, 0.81 and 0.76 for prototypes I and II respectively. If one views the partial objective values from which the fitness values are calculated, namely $\phi^{F/L^{Circ}}$ and $\phi^{F/L^{Long}}$ the circumferential force-displacement models fit the experimental data well ($\phi^{F/L^{Circ}} > 0.96$), while the longitudinal force-displacement model do not ($\phi^{F/L^{Circ}} < 0.66$).

Figures 12.8 and 12.9 show respectively the circumferential and longitudinal force-displacement solutions obtained from GA3 compared to test data. The fabric models obtained from GA3 give good solutions in the circumferential direction while correlations in the longitudinal direction are reasonable at lower strains (< 60 %), hence the low $\phi^{F/L^{Long}}$ partial objective value in Table 12.4. However, with the longitudinal force per unit length vs. strain curves, the fabric reinforcings are not likely to operate at longitudinal strains greater than 25 %, thus, the model solution is acceptable.

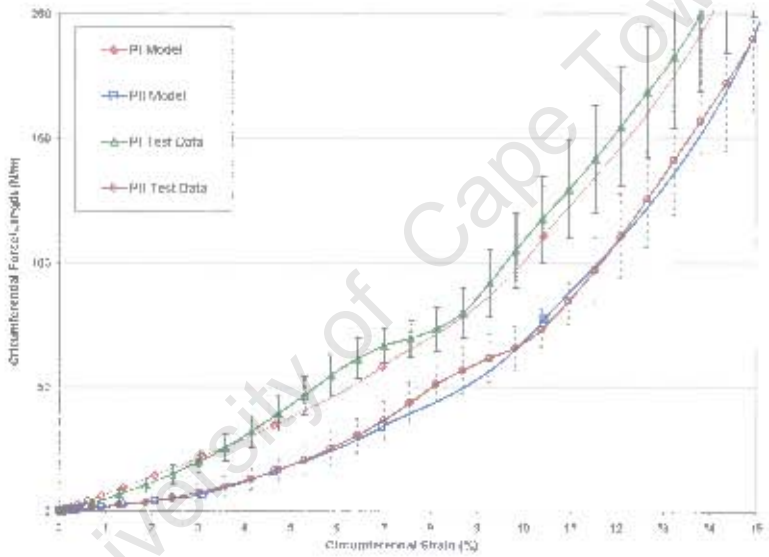

Figure 12.8: GA3 circumferential force-displacement solutions vs. experimental data for longitudinally strained prototypes

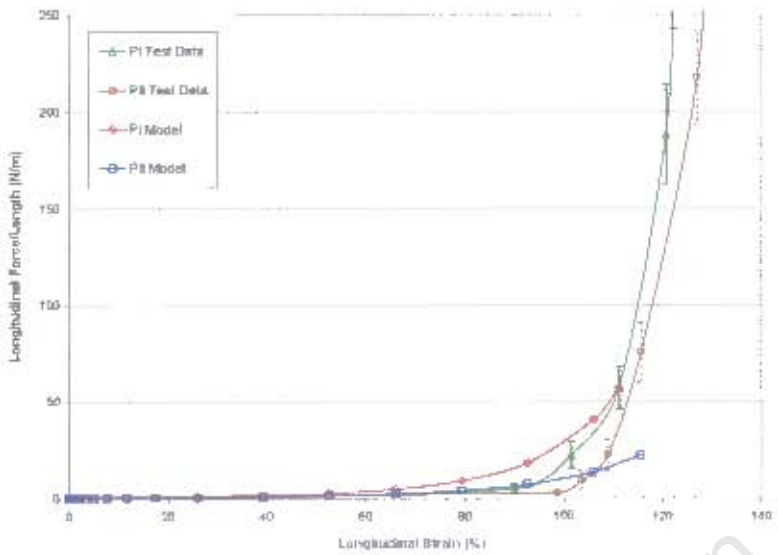

Figure 12.9: GA3 longitudinal force-displacement solutions vs. experimental data for longitudinally strained prototypes

12.3.2 Numerical graft simulations with GA3 model solutions

Using the fabric models solutions obtained from GA3 which describe the pre-strained prototypes I and II in circumferential and longitudinal tensile tests, computational graft simulations were run and new static and dynamic compliance curves and values obtained. Table 12.5 gives the various compliance, diastolic and systolic diameters, radial (wall) compression and fabric circumferential strain values obtained from these simulations for prototype I.

Graft Pore Size (μm)	90-106		106-125		125-150	
	Static	*Dynamic*	*Static*	*Dynamic*	*Static*	*Dynamic*
C_d (%/100mmHg)	5.54	5.31	5.78	5.54	6.21	5.98
Internal Diameter ϕ_i (mm)						
Diastolic	3.75	3.75	3.76	3.76	3.77	3.78
Systolic	3.84	3.83	3.85	3.84	3.87	3.86
Wall Compression (%)						
Diastolic	3.17	3.33	3.47	3.68	4.07	4.24
Systolic	5.23	5.09	5.69	5.55	6.58	6.49
Fabric Circumferential Strain (%)						
Diastolic	2.08	2.17	2.14	2.23	2.23	2.34
Systolic	3.24	3.22	3.34	3.31	3.49	3.47

Table 12.5: Graft numerical solutions using prototype I model obtained from GA3

From Table 12.5, the fabric circumferential strains observed are low; between 2 and 3.5%. However, these are higher than the expected 1 and 2% for the 90-106 μm pore sized graft solutions (refer to Section 12.2)

Figures 12.10 and 12.11 show the stress fields through the various pore sized grafts, for the prototype I reinforcing fabric model.

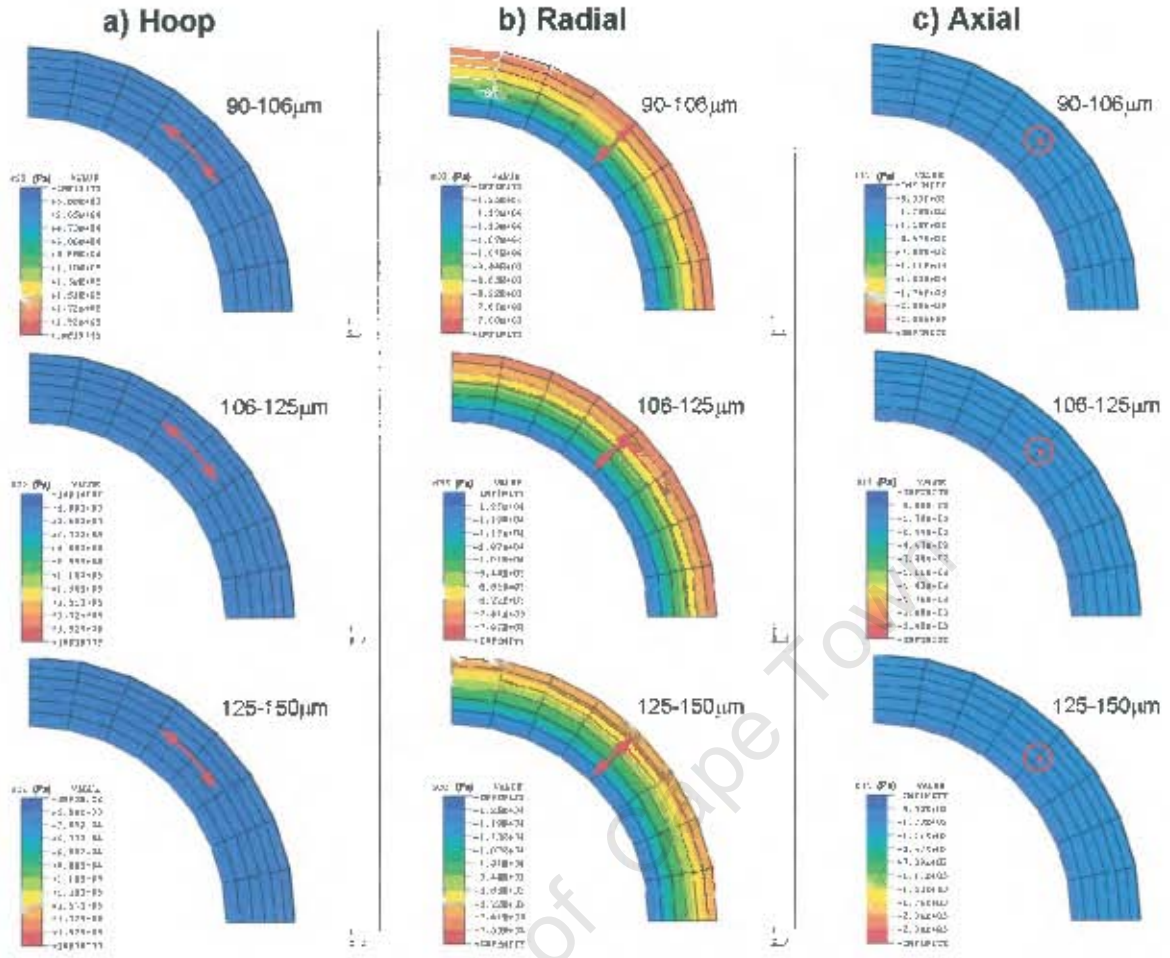

Figure 12.10: Hoop, radial and axial stress variation through 90-106, 106-125 and 125-150μm prototype I reinforced porous grafts obtained from the dynamic graft finite element model at 100 mmHg

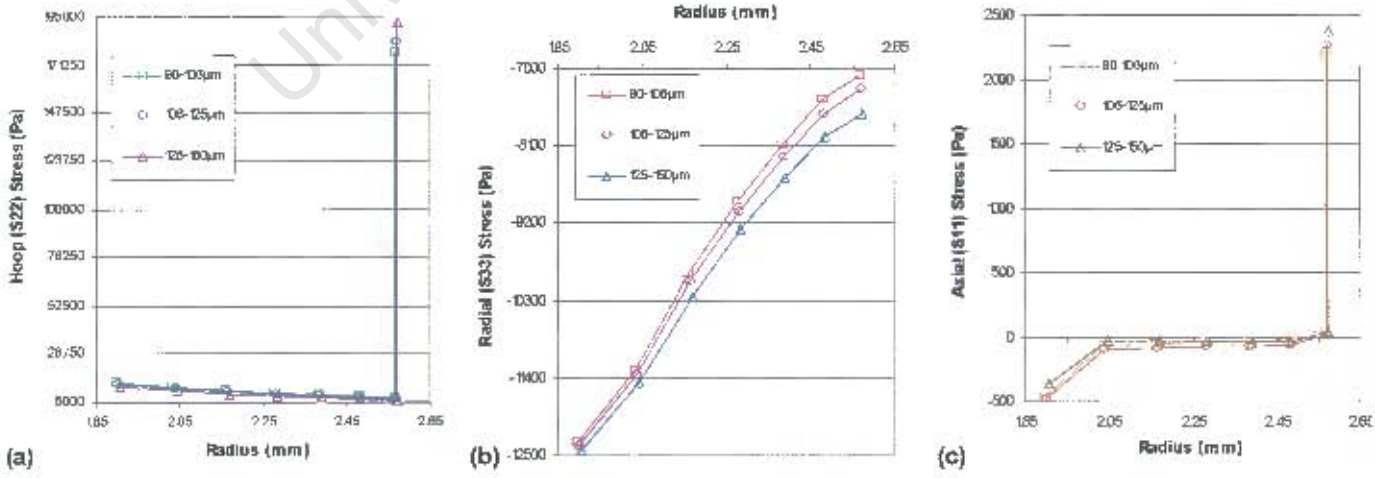

Figure 12.11: Comparison of (a) hoop, (b) radial and (c) axial stress through prototype I reinforced porous wall structures at 100 mmHg

There is little difference between the hoop and axial stress values for the various graft types

due to the stiff reinforcing, while only a slight difference is observed in the radial stress values. This is considerably different to what was observed for the non-reinforced grafts in Figure 11.2. As can be seen, the prototype model solutions play a dominant role in the mechanics of the graft structures, due to their non-compliant characteristics.

Figure 12.12 shows the predicted pressure-diameter (internal and external) relations of the various prototype I reinforced pore sized grafts utilising the fabric solution obtained from GA3. An approximately linear relation is observed (a straight line is highlighted on the graph to display the slight nonlinear stiffening characteristics).

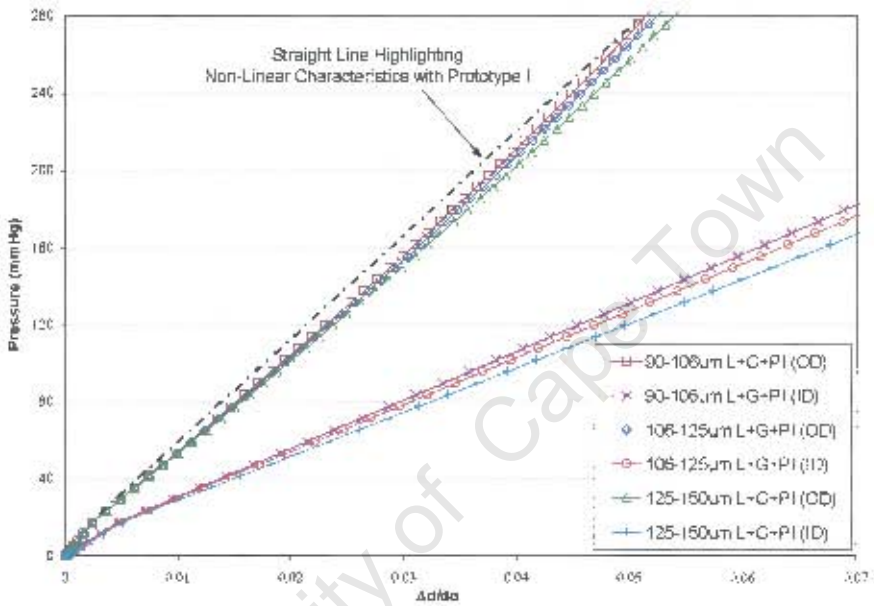

Figure 12.12: Model static P vs. internal and external $\Delta d/d_o$ curves for the prototype I reinforced porous grafts

Chapter 13

Compliance Experimental Results and Implant Studies

13.1 Introduction

In this chapter experimental compliance results are obtained for the various reinforced and non-reinforced pore sized grafts using the visual technique discussed in Chapter 7. Unfortunately, the supply of prototype II reinforcing was limited and no samples were left after tensile testing to obtain compliance data, thus, in this chapter reinforced grafts refer to those grafts reinforced with prototype I only.

The experimental compliance results obtained are used to correlate the graft numerical models solutions which include the latex liner. The chapter concludes with a single baboon implant study, where the effect of the fabric reinforcing in vivo is observed using a 125-150 μm pore size prototype I reinforced graft.

13.2 Luminal latex liners and pressure loss

With in vitro testing of porous graft structures, to prevent pressure loss through the graft lumen a luminal latex liner is employed. A local manufacturer of latex products[1] was asked to develop these luminal latex liners. The liners were manufactured by dipping various sized mandrels in latex solutions and then allowing them to dry, before removing them. To ensure that the liner wall thickness was uniform along its length, the mandrels were rotated continuously in a horizontal plane. Details of the latex solution used, the number of latex coats (dipping) and the speed at which the mandrel was rotated while the latex was allowed to dry could not be obtained from the manufacturer due to protection of manufacturing methods.

It was found that latex liners made on a 3.7 mm diameter mandrel gave the required 3.62 ± 0.15 mm external diameter after drying. The liner wall thickness varied from sample to sample; however, after visual inspections and the removal of bad samples a wall thickness of 192 ± 22 μm was obtained. The method used to take measurements and visually inspect the liners was done from digital images under a microscope, as described in Chapter 7.

13.2.1 Static compliance curves for luminal liners and numerical solutions

Static pressure vs. diameter curves for a number of latex liners (sample size: $n = 6$) were

[1] Roynhardt Pvt. Ltd., Johannesburg, Republic of South Africa, Tel #: 127 11 474 3488.

collected using the digital imaging method and the compliance rig described in Chapter 7. An equivalent finite element model was used to gain numerical solutions, where the hyperelastic constitutive model obtained in Chapter 10 was implemented for the latex material. Figure 13.1 shows the experimental and numerical curves of pressure against diameter change obtained.

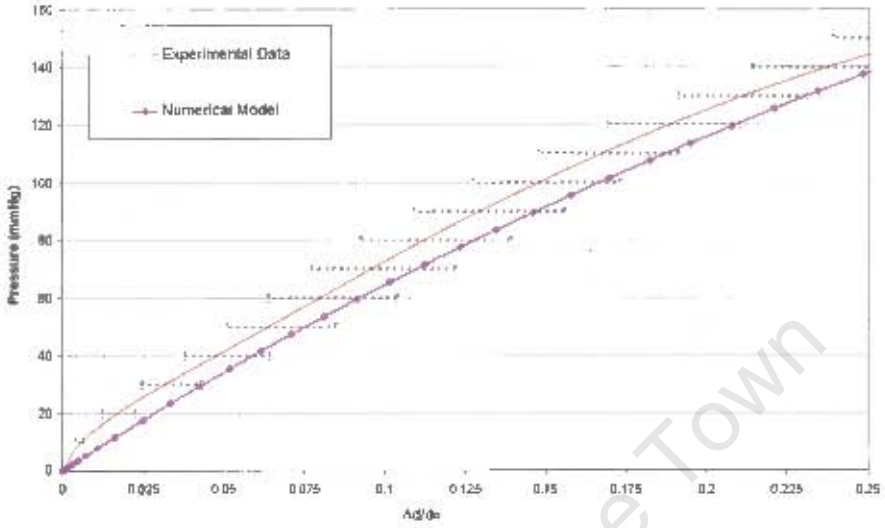

Figure 13.1: Experimental and numerical model static P vs. external $\triangle d/d_o$ curves for luminal latex liners

From Figure 13.1, a good numerical solution is obtained. Even though the numerical model fits within the boundaries of the experimental results and follows the shape of the curve, it does over predict the diameter change with pressure. This is due to the initial small diameter change observed in the experimental data as the pressure is increased from 0 to 20 mmHg. Although every care is taken to ensure that the experimental data collected is consistent and accurate, this initial small increase in diameter with pressure may be attributed to the axial pre-strain applied to the samples prior to testing. This axial pre-strain would cause a pressure drop in the latex liner due to the compliance rig being a closed flow circuit; thus, the initial increase in pressure is used to bring the internal pressure back to zero, while a small increase in diameter is observed. Inspite of the difference in computational and experimental results the numerical model was deemed satisfactory.

13.3 Static compliance curves for reinforced and non-reinforced grafts

13.3.1 Static compliance curves including the latex liner

Static external diameter P vs. $\triangle d/d_o$ curves were obtained for both the reinforced and non-reinforced pore size grafts of 90-106, 106-125 and 125-150 μm, incorporating the latex liner. Figures 13.2 and 13.3 display the curves obtained from the various reinforced and non-reinforced grafts (sample size: $n = 3$). The latex liners and non-reinforced pore sized grafts show a balloon-

ing effect as pressure is increased. However, with the addition of prototype I, nonlinear stiffening is observed.

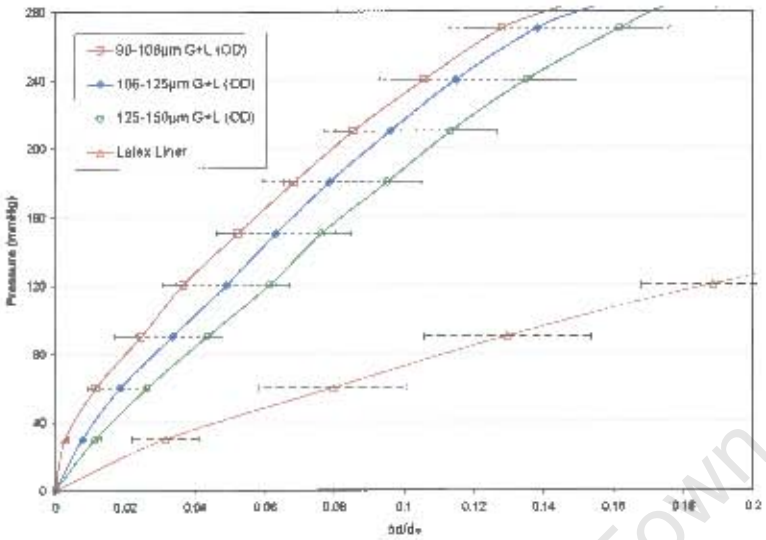

Figure 13.2: Static P vs. external $\Delta d/d_o$ curves obtained for the porous grafts without reinforcing (latex curve included for comparison)

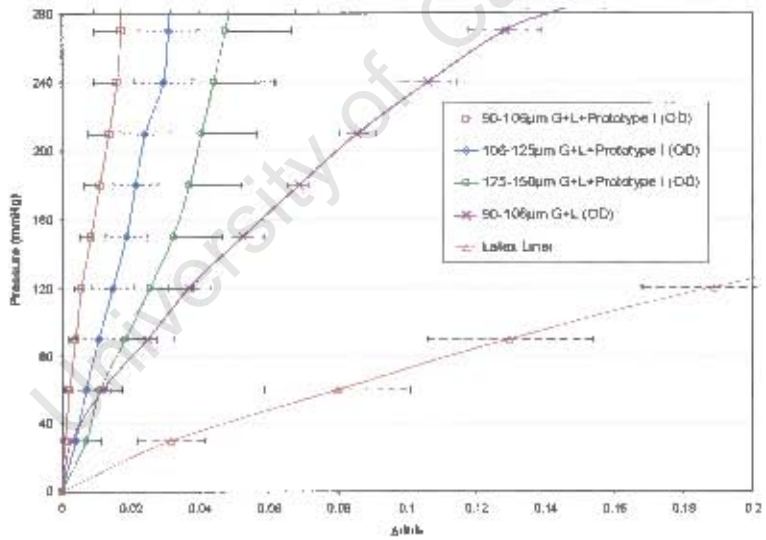

Figure 13.3: Static P vs. external $\Delta d/d_o$ curves obtained for prototype I reinforced porous grafts (90-106 µm non-reinforced porous graft and latex curves included for comparison)

13.3.2 Static compliance curves after analytically removing effect of luminal liner

Before dynamic compliance tests can be done on the grafts, equivalent physiological pressures need to be found; these are the elevated pressures at which the grafts are physically tested in the compliance rig, and at which the mechanical effects of the luminal liners are eliminated. Internal diameter curves are obtained from the external diameter curves by subtracting the individual sam-

ple graft wall thicknesses, as described in Section 7.2.2. It should be noted that this does not take into account compression through the graft wall. The equivalent pressures and diameter changes are obtained by finding where pressure differences of 80 and 120 mmHg occur between the internal diameter graft and the luminal liner curves. Figure 13.4 illustrates the process employed to obtain equivalent diastolic and systolic pressures of 126.0 and 202.5 mmHg, and internal and external diameter changes of 0.056 ± 0.008 and 0.111 ± 0.004 for the 90-106 μm non-reinforced pore size graft.

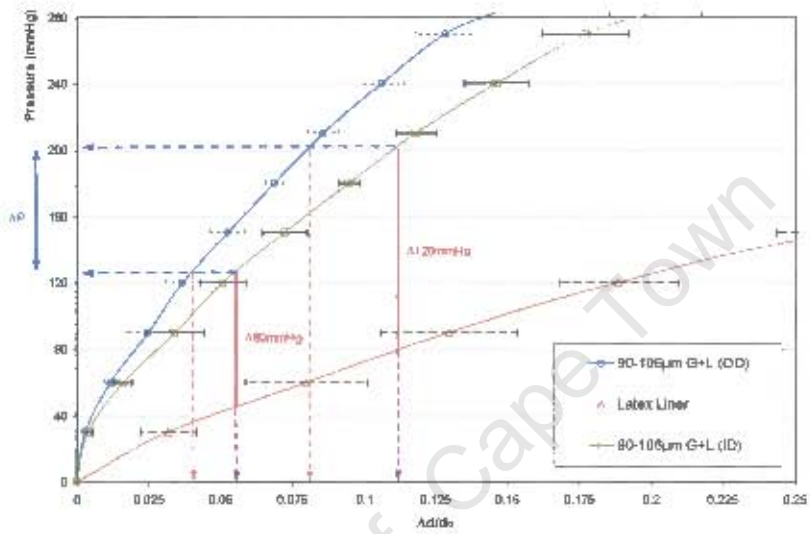

Figure 13.4: Calculation of internal diameter and equivalent 80 and 120 mmHg pressure differences between porous graft internal diameter and latex

Table 13.1 gives the equivalent physiological data values obtained for the various reinforced and non-reinforced pore size grafts after analytically subtracting the effects of the latex liner. This table also gives the static compliance values calculated from the equivalent diameter changes (uncertainty values for Static C_d were calculated by using the weighted method proposed by Kline and McClintock [175]).

Graft Type		**Non-Reinforced**			**Reinforced**		
Pore Size	(μm)	*90-106*	*106-125*	*125-150*	*90-106*	*106-125*	*125-150*
Sample Size	(n)	3	3	3	3	2	3
Equivalent Pressure							
(mmHg)	*Diastolic*	126.0	144.0	163.2	83.2	102.1	116.4
	Systolic	202.5	218.3	243.0	127.6	149.7	167.8
Equivalent Internal							
$\Delta d/d_0$	*Diastolic*	0.056±0.008	0.083±0.021	0.116±0.011	0.006±0.003	0.019±0.010	0.039±0.011
	Systolic	0.111±0.004	0.139±0.025	0.189±0.018	0.011±0.004	0.029±0.009	0.056±0.017
Static C_d							
(%/100mmHg)		13.0±2.4	12.9±7.8	16.4±4.6	1.3±1.2	2.5±3.3	4.1±4.9

Table 13.1: Equivalent physiological data for reinforced and non-reinforced grafts after latex subtraction

13.4 Dynamic compliance tests after adjusting for luminal liner

The compliance rig was set up to produce pressure pulses similar to those used in the dynamic graft numerical model (Figure 8.4) with equivalent diastolic and systolic pressure values taken from Table 13.1. However, it proved difficult to produce similar pressure waveforms for samples which needed equivalent diastolic-systolic pressure differences greater than 70 mmHg; thus, new numerical dynamic graft models were implemented using pressure functions which described these pressure waveforms.

Figure 13.5 shows curves of pressure and internal diameter vs. time, for a 125-150 μm non-reinforced graft sample. The actual equivalent diastolic and systolic pressures obtained were 169.6 and 238.5 mmHg, against the required values of 163.2 and 243.0 mmHg from Table 13.1.

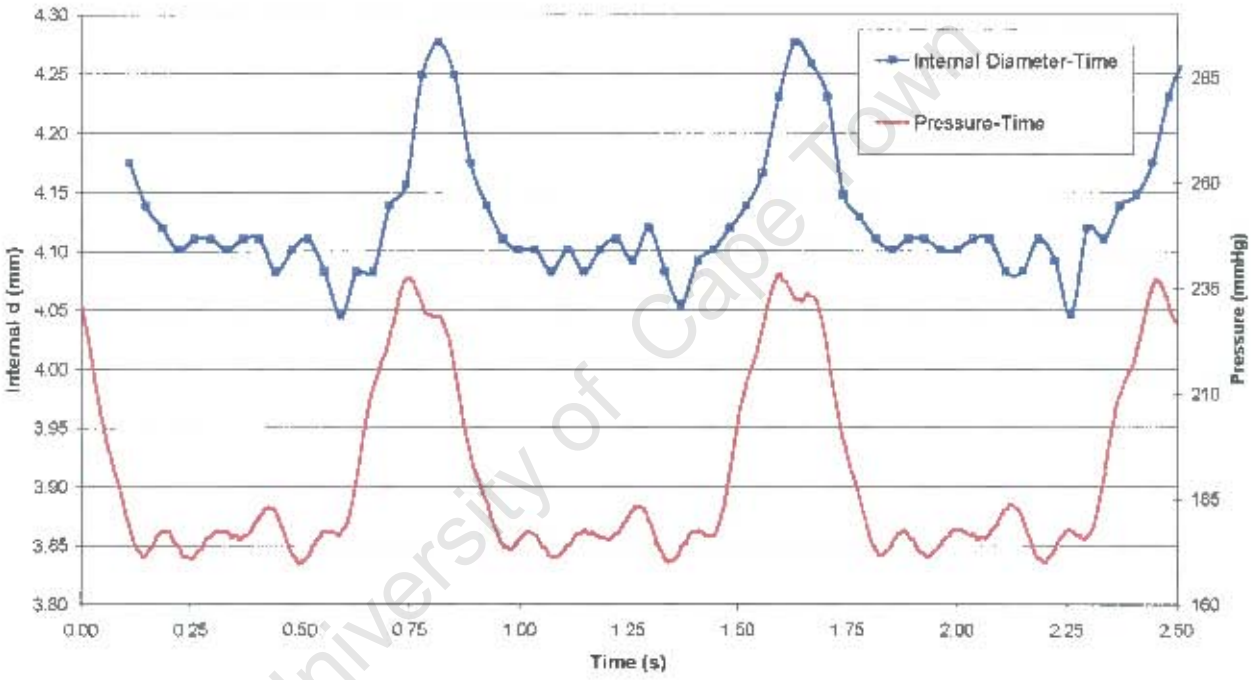

Figure 13.5: Pressure and internal diameter vs. time curves obtained from compliance rig for 125-150 μm porous graft sample

From the pressure-time and internal diameter-time curves, values of diastolic and systolic diameters were collected and used to calculate the dynamic compliance. Table 13.2 presents the actual equivalent pressures used, the external and internal diameter values obtained, and also gives the calculated dynamic compliance based on the collected data.

13.4.1 Dynamic compliance values

Figure 13.6 displays a bar chart of the dynamic compliance values obtained for non-reinforced vs. reinforced pore sized grafts. Included on the chart are the probability values associated with a Student's t-test using a one-tailed distribution between the groups.

Graft Type		Non-Reinforced			Reinforced		
Pore Size	(μm)	*90-106*	*106-125*	*125-150*	*90-106*	*106-125*	*125-150*
Sample Size	(n)	3	3	3	3	2	3
Pressure	(mmHg)						
	Diastolic	123.9	149.3	169.6	80.7	98.4	110.9
	Systolic	201.4	216.7	238.5	125.4	150.8	165.1
External d	(mm)						
	Diastolic	5.265±0.061	5.218±0.064	5.327±0.107	5.39±0.059	5.256±0.105	5.348±0.130
	Systolic	5.472±0.082	5.416±0.031	5.577±0.098	5.416±0.055	5.297±0.072	5.403±0.139
Internal d	(mm)						
	Diastolic	3.878±0.075	3.894±0.043	4.042±0.059	3.256±0.085	3.513±0.031	3.457±0.107
	Systolic	4.085±0.098	4.092±0.010	4.292±0.052	3.283±0.079	3.555±0.002	3.513±0.104
Dynamic C_d (%/100mmHg)		13.3±1.2	12.7±2.9	15.5±1.3	2.1±0.8	3.0±2.4	4.0±0.7

Table 13.2: Dynamic data for reinforced and non-reinforced grafts using equivalent pressures from static curves

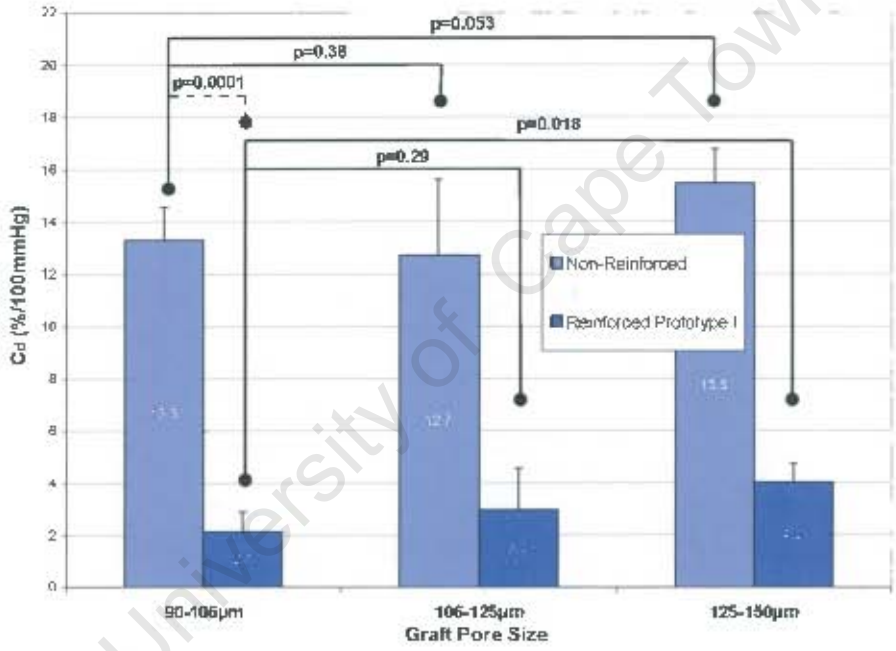

Figure 13.6: Bar chart of dynamic compliance values for reinforced and non-reinforced porous grafts (p values obtained from 1-tailed t-test)

With the addition of the adventitial reinforcing prototype I (described in Chapter 12), it was observed that there is a significant reduction in compliance (1-tailed t-test, $n = 3$: $p < 0.0015$ for all pore size graft groups). Between the various pore size graft group, significant differences were observed between the 90-106 and 125-150 μm grafts, both reinforced and non-reinforced ($p = 0.018$ and 0.053 respectively).

13.4.2 Static and dynamic compliance values

Figure 13.7 presents the static and dynamic compliance values obtained in a bar chart for the non-reinforced pore sized graft groups. No significant difference was observed between the static and dynamic compliance values.

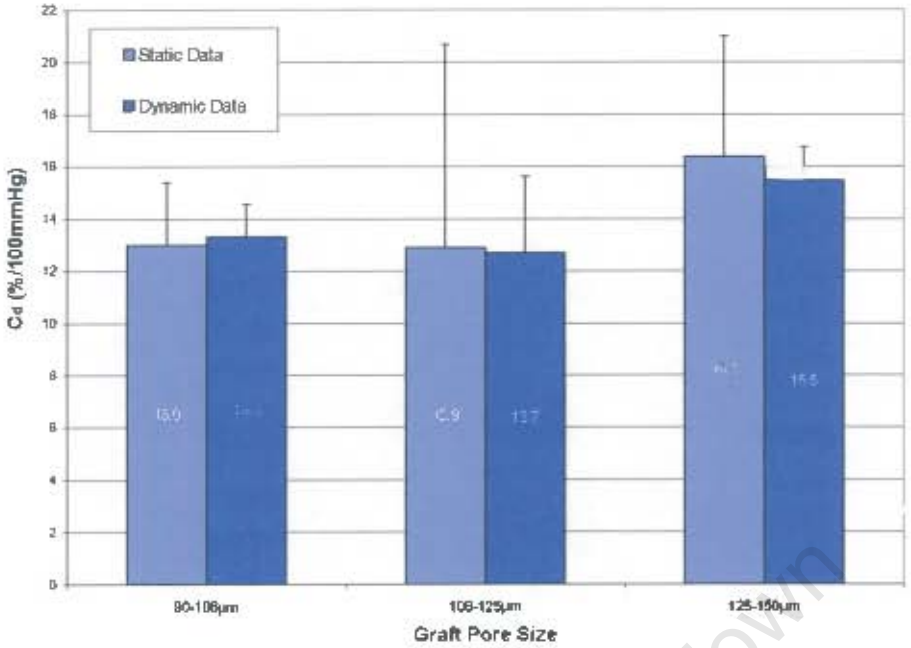

Figure 13.7: Comparison of dynamic and static compliance values for porous grafts

13.5 Comparison of numerical and experimental data

Table 13.3 presents numerical and experimental static and dynamic compliance values. Experimental data was obtained from internal diameter P vs. $\Delta d/d_o$ curves after latex subtraction, while the numerical solutions were obtained from Chapters 11 and 12 without modelling the latex liner.

Graft Type		**Non-Reinforced**			**Reinforced**		
Pore Size	(μm)	*90-106*	*106-125*	*125-150*	*90-106*	*106-125*	*125-150*
Static C_d	(%/100mmHg)						
	Experimental	13.0±2.4	12.9±7.8	16.4±4.6	1.3±1.2	2.5±3.3	4.1±4.9
	Numerical Model	16.9	20.3	33.9	5.54	5.78	6.21
Dynamic C_d	(%/100mmHg)						
	Experimental	13.3±1.2	12.7±2.9	15.5±1.3	2.1±0.8	3.0±2.4	4.0±0.7
	Numerical Model	16.0	19.2	31.5	5.3	5.5	6.0

Table 13.3: Numerical vs. experimental dynamic compliance values

The numerical solutions obtained over estimate compliance by 2.7, 6.5 and 16.0 %/100 mmHg for the non-reinforced grafts with increasing pore size, respectively. These differences are large; however, if one considers external diameter data, thus eliminating any errors caused by subtracting the graft wall thickness and wall compression to obtain internal diameter data, and recomputing the numerical solutions with the latex liner, one can obtain comparable numerical pressure vs. external diameter solutions for the non-reinforced and reinforced graft types.

Figures 13.8 and 13.9 show comparisons of static P vs. external $\Delta d/d_o$ model solutions including the latex liner vs. experimental data for the 90-106 and 125-150 μm non-reinforced

and reinforced pore size grafts.

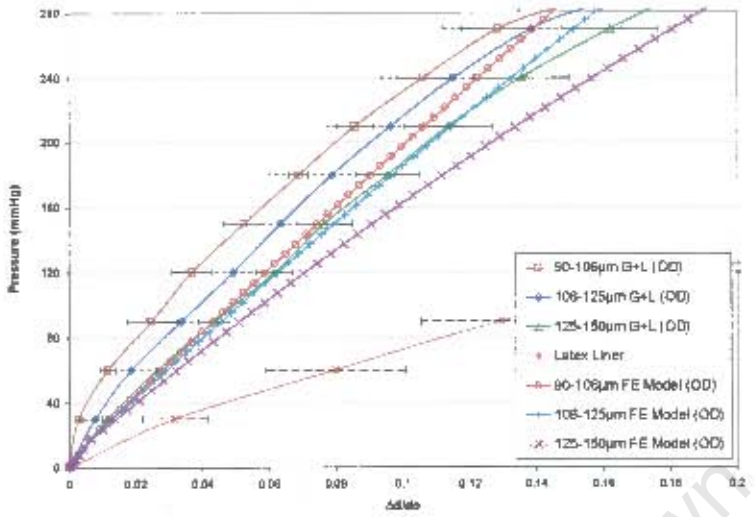

Figure 13.8: Experimental and numerical results of static P vs. external $\triangle d/d_o$ for non-reinforced grafts

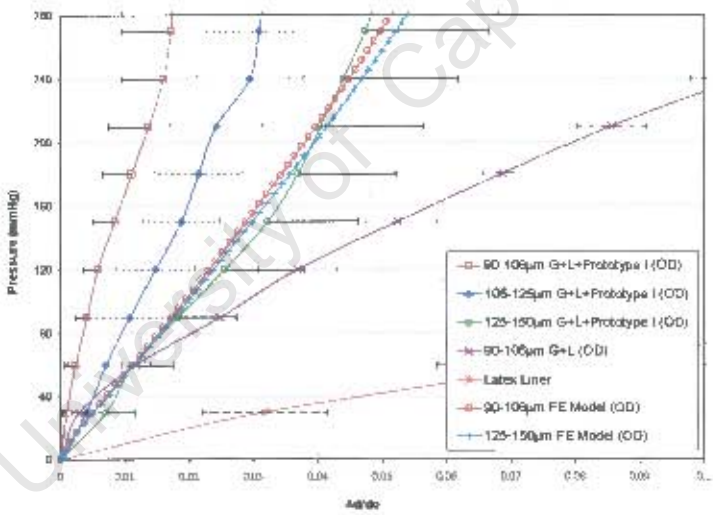

Figure 13.9: Experimental and numerical results of static P vs. external $\triangle d/d_o$ for reinforced grafts

From Figure 13.8, the numerical solutions are more compliant and display a reduced nonlinear P vs. $\triangle d/d_0$ response than physically observed. From Figure 13.9 the numerical solutions are again more compliant with the addition of prototype I, and little difference is observed in the numerical solutions between the various reinforced porous graft types. However, the effect of the reinforcing on the numerical solutions does follow the experimental data, where a 3.6% reduction in diameter change is observed in the numerical solution and a 3.1% reduction for the physical data for the 90-106 μm graft at 120 mmHg. The same is observed for the 125-150 μm graft where a reduction in diameter change of 4.5% is observed in numerical data and 3.8% for

the physical data at 120 mmHg. Despite the more compliant numerical results, close numerical correlations based P vs. external $\triangle d/d_0$ are obtained for both the non-reinforced and reinforced 125-150 μm graft types.

Table 13.4, compares the numerical and experimental static compliance data obtained using external diameter data. Better numerical and experimental correlations are obtained for compliance from the external diameters, illustrating that the method used to calculate the compliance by subtracting the wall thickness and latex liner is not ideal. The numerical compliance values obtained fit the physical results, however, the reinforced 90-106 μm grafts numerical solution does not.

Graft Type	**Non-Reinforced**			**Reinforced**		
Pore Size (μm)	*90-106*	*106-125*	*125-150*	*90-106*	*106-125*	*125-150*
Sample Size (n)	3	3	3	3	2	3
Pressure (mmHg)						
Diastolic	126.0	144.0	163.2	83.2	102.1	116.4
Systolic	202.5	218.3	243.0	127.6	149.7	167.8
External $\triangle d/d_0$						
Experimental						
Diastolic	0.040±0.006	0.061±0.017	0.085±0.009	0.004±0.002	0.012±0.007	0.025±0.012
Systolic	0.082±0.005	0.102±0.020	0.138±0.014	0.006±0.003	0.019±0.006	0.035±0.015
Numerical Model						
Diastolic	0.062	0.076	0.099	0.014	0.021	0.015
Systolic	0.103	0.118	0.161	0.023	0.033	0.024
Static[2] C_d (%/100mmHg)						
Experimental	10.1±1.9	9.7±5.9	12.2±3.9	0.5±0.7	1.7±2.1	2.4±4.5
Numerical Model	9.7	9.8	14.2	2.0	2.8	2.0

Table 13.4: Numerical vs. experimental static compliance values based on external diameter

13.6 Comparative compliance study on reinforced and non-reinforced graft samples

Two randomly chosen graft samples, one reinforced and the other not, were sent to a commercial compliance test company[3] and a research group[4] for a comparative compliance study. Table 13.5 shows the dynamic compliance results obtained from each group.

Group	*Commercial Tester*[3]	*Research Group*[4]	*In-House*
Dynamic C_d	(%/100mmHg)	(%/100mmHg)	(%/100mmHg)
Non-Reinforced (*Sample code: 150-212*)	4.4	10.7	9.6
Reinforced (*Sample code: 125-201*)	2.9	2.6	2.5
Latex Liner Utilised	9.7	20.2	20.6

Table 13.5: Comparison of complaince values obtained by various groups

[2]Static compliance calculated from the external diameter without analytically subtracting the latex liner.

[3]Dynatek-Dalta Scientific Instruments, 105 E. Fourth Street, Galena, MO 65656, USA, Tele # : 417-357-6155, Fax #: 417-357-6327.

[4]Vascular Hemodynamic Laboratory, University Department of Surgery, Royal Free and University College Medical School, UCL, The Royal Free Hospital, London, NW3 2QG, UK, Tele # : +44 207 830 2901, Fax #: +44 207 431 4528.

From Table 13.5 the commercial company obtains a significantly different result for the non-reinforced graft sample, while consistent results are observed by all for the reinforced graft sample. The deviation in the commercial companies result for the non-reinforced sample may be due to the different testing method used as discussed in Section 7.3. However, from Section 7.3, when a number of standard silicon samples which do not require latex liners were tested, the in-house results were consistently lower for the compliant silicone samples (> 4 %/100 mmHg), while for those lower than 4 %/100 mmHg the results were consistent with the commercial company. From this, and noting the variation in the compliance values for the latex liners used by each group it is believed that this difference is due to the variation in liner used. Where the commercial company used a non-compliant liner which when used with the relatively weak non-reinforced porous graft sample the liner plays the dominant mechanical role. With the stiff reinforced sample, the latex liner does not play a dominant mechanical role, thus, the variation in compliance is low. This illustrates the need for highly compliant liners when testing weak porous graft samples and the variation in obtained compliance results using different liners.

13.7 Primate implant study

To see the effect of the fabric reinforcing, a four week in vivo primate study[5] was done using prototype I on a 125-150 μm pore size graft. An isolated chacma-baboon femoral model was used, which differentiates between transanastomotic and transluminal healing (details of this model, implant and explant procedures, histological processing and image analysis can be obtained from the work by Bezuidenhout [9]). The graft samples are prepared in a similar manner to those used in the in vitro compliance testing (refer to Figure 7.17); however, this isolated chacma-baboon femoral model does not allow for the study of compliance effects on healing due to the use of shorter graft segments (20 mm) and longer stiff e-PTFE (30 mm) segments.

13.7.1 Explant histology

Histological staining and analysis were done on cross-sectional slices of the graft explant from the center of the vessel. Figure 13.10 shows an Hematoxylin and Eosin (H&E) stain. A cross-section plane is indicated on the pre-implant graft sample to show the relevant position of the H&E stained slide. An H&E stain gives a general overview of what is happening on a cellular level. More specifically, it stains cell nuclei and highlights foreign body giant cell (FBGC) activity and thus cellular inflammatory response.

From Figure 13.10 there is a large body of FBGC activity around the fabric reinforcing fiber, indicating an inflammatory response around the fabric reinforcing. This response could be heightened due to the shearing and frictional forces between the individual yarns as they respond mechanically to pulsating pressure loads. In order for a knitted fabric to display nonlinear

[5] All animal experiments described in this dissertation were performed after approval by the Animal Ethics Committee at the University of Cape Town and in compliance with the "Principles of Laboratory Care" and the guidelines for the care and use of laboratory animals [176].

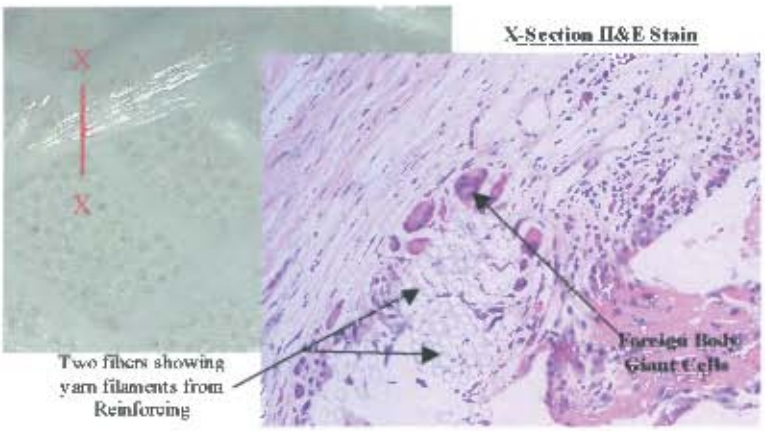

Figure 13.10: Circumferential cross-section X-X of implanted sample showing H&E stain and FBGC inflammatory response

stiffening, individual yarns are required to slide over each other as they straighten and lock as the load is increased, thus under pulsatile conditions this interaction between the yarns is heightened causing high cellular activity in this region and thus inflammation. From this initial in vivo study of prototype I it is too premature to totally exclude the use of fabrics due to the localised inflammatory response, but rather an optimal fabric type and material solution should be sought which reduces the inflammatory response such as mono-filament which will reduce the yarn interaction to single points and inert materials.

Chapter 14

Discussion of Results

14.1 Introduction

The design characteristics of a small diameter prosthetic graft have been the subject of this study. Using a combination of mathematical and computational models for the mechanical characteristics of fabrics and the porous graft structures, optimal reinforcing fabric models were found using a genetic algorithm (GA1). The reinforcing fabric models combined with a particular porous graft structure were required to achieve a specific compliance, diastolic internal diameter, and to display nonlinear stiffening characteristics. The mathematical models, numerical methods and optimisation techniques have produced satisfactory results and have been shown to converge on a number of solutions to the problem. Physical correlations were made with the numerical solutions. This chapter discusses the results of the preceding chapters.

14.2 The fabric constitutive material model

The fabric constitutive relation is a nonlinear, anisotropic elastic material model, and does not incorporate all the complex aspects of fabric behaviour. It does however, give an indication for the requirements of an ideal fabric reinforcing for a compliant, adventitial-styled graft. The exponential strain energy model does not include anisotropic viscoelastic and plastic components which are complex to model and implement [177], and which falls outside the scope of this study. The model does, however, describe the nonlinear stiffening characteristics of a fabric under tensile loading and a linear characteristic under shear, as observed in Chapter 8. These characteristics are heavily dependent on the fabric model coefficients used to describe the material properties.

It was found from the fabric patch tests and the solutions obtained from GA2 that a number of the coefficients namely; C, a_1, a_2, a_3 and a_4 should remain positive to ensure realistic fabric uniaxial tensile solutions. Negative coefficients would produce unrealistic compressive stresses and negative Poisson's effects under tension. GA2 validated the fabric model against warp and weft uniaxial tensile test data for a number of fabric samples, where good correlations were observed (Figure C.2 of Appendix C). However, the fabric model fails to model fabrics with linear stress-strain relations, as seen with fabric sample 2. To possibly overcome this, a combined polynomial and exponential function was used by Tong and Fung [32] to model the large variation in anisotropic nature of a rabbit's abdominal skin, where the function took the following form:

$$W = P + \frac{C}{2}e^{Q}, \tag{14.1}$$

where

$$P = \frac{1}{2}(\alpha_1 E_{11}^2 + \alpha_2 E_{22}^2 + \alpha_3(E_{12}^2 + E_{21}^2) + \alpha_4 E_{11} E_{22}) \,, \tag{14.2}$$

and

$$Q = (a_1 E_{11}^2 + a_2 E_{22}^2 + a_3(E_{12}^2 + E_{21}^2) + a_4 E_{11} E_{22} + \gamma_1 E_{11}^3 + \gamma_2 E_{22}^3 + + \gamma_3 E_{11}^2 E_{22} + \gamma_5 E_{11} E_{22}^2) \,. \tag{14.3}$$

This strain energy function was shown to give greater anisotropic behaviour and variation in relations in the transverse directions, thus, a similar function could be utilised to cater for the linear stress-strain components. Thirteen coefficients however would need to be solved for when using this function. The P term in (14.1) may cause "polynomial wiggling", giving unrealistic fabric behaviour [130]. However, it is observed that small amounts of "polynomial wiggle" are seen in the circumferential tensile test data in Figure 12.5.

Another possible fabric material model which would be convex for all possible sets of material parameters, thus avoiding material instabilities could be adapted from the constitutive model for artery layers proposed by Holzapfel *et al.* [178] which takes the following form:

$$\bar{\psi}(\bar{I}_4, \bar{I}_6) = \frac{k_1}{2k_2} \sum_{i=4,6} \left\{ \exp\left[\bar{I}_i - 1\right]^2 - 1 \right\} \,, \tag{14.4}$$

where, $\bar{I}_4 = \bar{C} : A_1$ and $\bar{I}_6 = \bar{C}^2 : A_1$, A_i is defined as the tensor product of $a_{0i} \otimes a_{0i}$, where a_{0i} is a material reference direction vector. This particular anisotropic material model uses only two coefficients, k_1 and k_2 for two dimensional problems making it easier to implement and utilise. $k_1 > 0$ is a stress-like material parameter and $k_2 > 0$ is a dimensionless parameter.

Other methods which could be implemented are discrete models and a function similar to that proposed by Alsawaf [112] (refer to Section 4.10). Discrete models could be used to simulate individual fibre structures, however, present findings strongly suggest that this is not a realistic possibility without better and faster modelling techniques used to describe each individual fibre in the fabric construction. Another case against discrete modelling would be its implementation in the genetic algorithm, where the fabric design will take on several parameters, such as, fibre yarn and fabric construction, frictional play between yarns and methods of penalising discrete models which are not possible to manufacture. Estimates of friction and the ideal approach of modelling yarns as cylindrical rods would compound the error in approximating the fabric structure.

Alsawaf [112] proposed a two stage linear function to describe uniaxial deformation of a weave, however instead of linear functions, two exponential functions could be used, one with an initially low stiffness and curvature and a second, which is only implemented when a critical point is reached which has a higher stiffness and curvature. This method may however be difficult to implement, where continuity along the function would need to be enforced and transverse interplay would be difficult to define.

Although time and effort may be spent on the modelling of the fabric and its behaviour outside the body, its physical application in the human body must be assessed. When implanted in the body, the physical behaviour of the fabric will change considerably over time, where cells will seed themselves to the fabric, changing its mechanical nature. Thus, a time dependent model for tissue in-growth should be incorporated in the constitutive relation, where with time, an increase in stiffness can be included by increasing C, while, the orthogonal anisotropic nature and orientation may be adjusted by varying the a_i coefficients, i.e.:

$$\begin{aligned} C \text{ and } a_i &= f(t) \\ \text{where } C, a_i &\rightarrow \textit{Limit} \text{ when } t \rightarrow \infty \end{aligned} \tag{14.5}$$

The nature of this change with time will require extensive experimental data to obtain realistic relations, with variation in material type and fabric construction. The use of growth factors in the porous structure to enhance cellular healing would also need to be included.

14.3 Finite element modelling

A number of finite element models were implemented, namely; the graft, uniaxial tensile, circumferential and longitudinal tensile models. In addition the single element, uniform and non-uniform multi-element patch test models were also implemented. In these models a number of simplifications and assumptions were made, namely:

- The fabric is modelled as a continuum.
- Bending stiffness is not accounted for by modelling the fabric with membrane elements.
- The fabric reinforcing remains in a stress-free state after longitudinal straining over the porous graft.
- No relative motion is allowed in the contact between the fabric, latex liner and the porous graft.
- The latex liner and the fabric remain continuously in contact with the porous graft.
- Initial stress-free state of the fabric in the circumferential tensile model after pure bending has been reduced to zero
- A soft contact model is assumed between the fabric and the pin in the circumferential tensile model.
- The fabric sample remains circular in cross-section in the longitudinal tensile analysis.

A number of these can be considered poor assumptions, such as the initial stress-free state of the fabric in the circumferential tensile model and the fabric sample remains circular in cross-section in the longitudinal tensile analysis. The initial stress-free state of the fabric in the circumferential tensile test is unrealistic as bending of the fabric prior to this initial starting point would produce stress fields before pure circumferential straining took place (refer to Figure 8.7). However, membrane elements were used which do not account for bending stiffness, thus it would be

better to model the fabric with shell elements which do incorporate bending stiffness.

The assumption that the pulled end of the longitudinal tensile model remains circular in cross-section is not valid. In the physical test the sample ends are clamped flat prior to testing. This would produce a stress to the sample end. Again, modelling the fabric with shell elements and clamping the sample in the analysis would reduce the error in the assumption.

Other assumptions could be improved to give better approximations to the physical application, such as allowing for the relative motion and dislocation of contact between the fabric, the latex liner and the porous graft structure. With knitted fabrics a large amount of relative fibre motion is observed in the fabricated structure which is not necessarily uniform or evenly distributed, thus, a contact model which allows for this relative motion should be implemented.

14.3.1 Mesh sensitivity studies

Element mesh refinement is an important factor in finite element modelling, typically the finer the mesh, the better the approximation of the piecewise functions to a consistent solution. Mesh sensitivity studies were conducted on all finite element models. In these mesh sensitivity studies, the element density and number were varied across the model until consistent stress-strain results were seen at a number of critical point. The meshed models were compared to a considerably refined model and the percentage difference in results evaluated, a summary of which can be reviewed in Section 8.6 and detailed results examined in Appendix A. From these studies the lowest element number model which gave consistently equivalent stress-strain fields were utilised. To reduce GA simulation times, a compromise was reached between mesh refinement and analysis time, where only field variables used in the GA objective functions were considered in the mesh sensitivity studies, thus, coarser models were used to speed up the GA simulation times.

To reduce the error in the finite element approximation further and obtain better descriptions to the field variables across the elements, higher order piecewise functions, or elements such as eight-noded membrane and twenty-noded continuum elements could be used. Using higher order elements will however increase analysis and GA simulation times.

14.3.2 Fabric constitutive model implementation in ABAQUS

The constitutive fabric model uses the conjugate Second Piola-Kirchhoff stress S, and Green Strain E. Further UMAT subroutines were developed although not described in the work using the same exponential function, however, other strain measures and their respective conjugate stresses replacing E and S. These included stretch ratio λ, the Right Cauchy deformation tensor C, logarithmic strain $\ln \varepsilon$ and pure stretch U, some of these proved difficult to implement while others displayed convergence problems when more than one element was implemented in an analysis.

Membrane elements are used to model the fabric as a continuum, thus bending stiffness is not included in the finite element models. The exclusion of bending and the use of membrane

elements is reasonable, not only from the aspect of coarse knit fabrics having a very low bending stiffness, but under the physical applications the fabric is used to reinforce the graft, little bending is observed. However, as stated earlier in the case of the circumferential and longitudinal models this assumption is far from ideal and further steps should be taken to implement shell elements which incorporate bending stiffness.

Patch tests were done on the implementation of the material model using single linear, uniform and non-uniform multi-linear element models where small relative variations in fabric coefficients were assessed. The single and multi-element patch tests show that the material model is functional in ABAQUS©, however, no sensitivity or stability analyses were performed. Good correlations were observed between the uniform and non-uniform multi-element models, while the study of small adjustments in coefficient magnitude gave an indication of their mechanical contribution to the material model.

14.3.3 The graft finite element model

The graft model makes full use of symmetry, thus only one half of the graft and a 90 degree sector in the circumferential direction is modelled. Although an axisymmetric model would be computationally efficient, it is not possible to implement the anisotropic fabric constitutive material model in an axisymmetric membrane element. One could have modelled a smaller sector, reducing analysis times or allowing for an increased mesh while keeping analyses times constant.

The element density was biased toward the fixed end, where stress field gradients were expected to be high, while remaining constant through the graft wall thickness. The graft model uses a pressure load on the inner surface and fixes the latex liner and fabric reinforcing to the porous graft walls by fixing common element nodes. As discussed previously, this fixed contact is not ideal.

Instead of implementing the longitudinal straining of the adventitial fabric reinforcing over the graft in the numerical model, new axial strained circumferential and longitudinal tensile test data were obtained for the reinforcing prototypes. By implementing the longitudinal straining of the adventitial fabric reinforcing over the graft one would include the initial stress state of the fabric in the numerical graft model, giving a better approximation to the physical situation. However, the contact model between the fabric and the graft would need to be adjusted to take into account large relative motion and friction in order to achieve this.

14.3.4 The tensile finite element models

The tensile models (uniaxial, circumferential and longitudinal) also make full use of symmetry, where quarter symmetric models are implemented. Element density is biased toward certain critical edges or points, where stress field gradients again were expected to be high.

Circumferential model: The circumferential tensile model starts at a position where pure bending in the sample has in theory been reduced to zero (see Figure 8.7), as mentioned earlier this is a poor approximation as bending stiffness is not incorporated. Again implementing shell elements will allow for bending stiffness to be incorporated. The soft contact model used between the fabric and the analytically rigid pin, was not validated and could be a source of error.

Longitudinal model: The longitudinal tensile model assumes that the clamped end remains circular in cross-section while being strained in the axial direction. This is not a representation of the physical test employed and thus, a source of error. The implementation of shell rather than membrane elements will allow the numerical model to simulate the ends being clamped prior to longitudinal tension.

Uniaxial model: With the good approximations and boundary conditions used in the uniaxial tensile model, combined with the element density being biased both in the horizontal and vertical directions toward the displaced point C (see Figure 8.9), this model was considered reasonable.

14.4 The genetic algorithms and optimisation

The search features of the GA were; dynamic search space, a step-wise increase in search space resolution after n generations and a linear reduction in search space range after each generation. The dynamic search space allows the genetic algorithm to adjust the search boundaries after each generation, where boundaries are redefined between the first and second ranked solutions, biased two thirds toward the first ranked solution after each generation. Implicit constraints are imposed on these boundaries, ensuring that certain coefficients remain positive, such as coefficient C. This dynamic search space is seen as a major advantage as model coefficients diverged considerably from the initial starting values (see Tables 10.5, 11.2 and 12.4). The step wise increase in search space resolution was implemented to search a coarse grid over n generations before being refined. With the linear reduction of search space range after each generation it was found that step-wise increasing resolution after n generations was not necessarily effective, as this limited the widespread searching capabilities of the GA. The implementation and magnitude of these GA features can easily be adjusted, two distinct techniques were used, namely; 1. using an initially large search space with a linear reduction in range and step-wise increase in resolution and 2. using a small, fixed search range and resolution. Both techniques use the dynamic search space feature. These techniques are illustrated graphically in the Figure 14.1.

Technique 1, is the general method, while 2 is a special case. There are advantages and disadvantages of both methods, however technique 2 has the same disadvantage as traditional "hill climbing" techniques in that a local maximum might be found limiting the GAs search capabilities and fixing it on a single local solution which may not be the global maximum. This technique was found to be a good for GA3 where a large number of finite element models did not

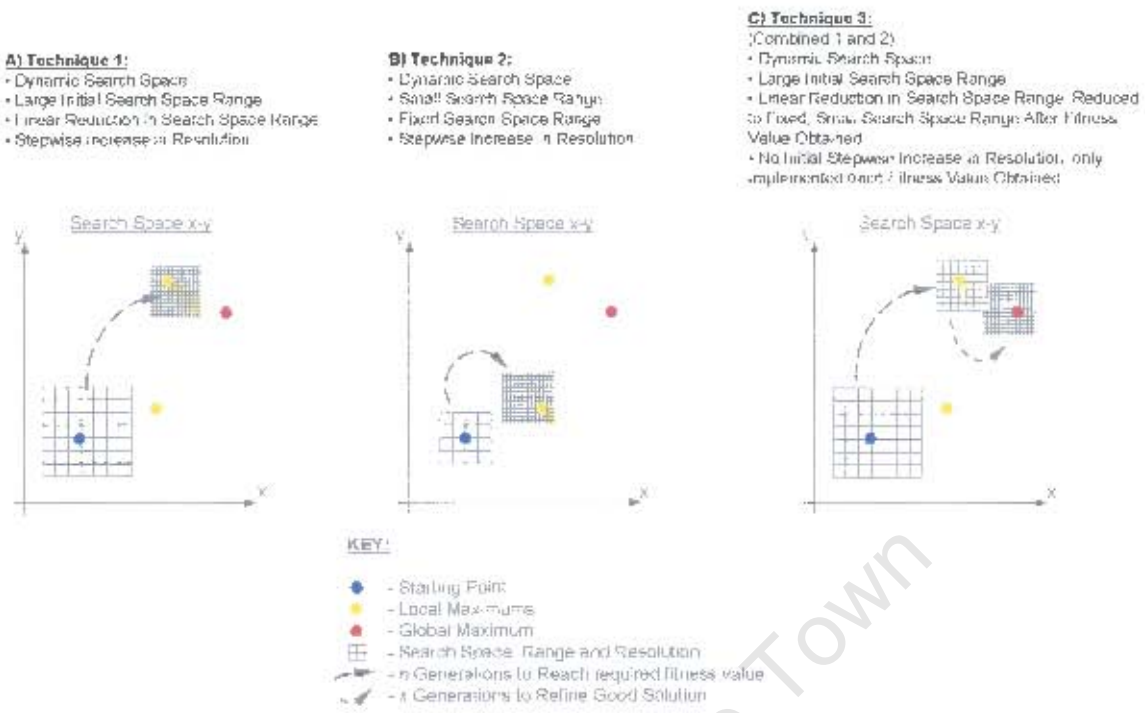

Figure 14.1: Schematic of various dynamic search space techniques for GA

run or failed due to heavy penalties. Using technique 1, only a small percentage of the population ($< 12\,\%$) gave usable models, limiting the GAs capabilities, however, using technique 2 this percentage increased to roughly $32\,\%$. In the case of GA2 it was found that technique 2 was time intensive.

Although no extensive study was performed on the adjustment of these parameters, a qualitative study revealed that, utilising the dynamic search space was beneficial, where an initial low resolution and linear reduction in range gave better results. The step-wise increase of resolution and a fixed small search range should only be implemented when a reasonable solution is found, thus, increasing the resolution is used to refine the obtained solution, this is referred to as technique 3. If further studies are implemented, it is recommended that technique 3 be utilised.

The magnitudes of the parameters used to control the GAs can easily be adjusted. Thus, weightings for the partial objective functions can be adjusted accordingly, allowing the GA to optimise on certain criteria first or in a biased fashion, for example, in GA1 the partial objective functions for C_d and d_{dia} were weighted toward C_d allowing the GA to optimise on C_d first and then refine for d_{dia} later. It was found that adjusting the partial objective weightings changed the solutions found.

Each GA was automated to save a number of ranked solutions in each generation and grade them into a global solutions array. Once a pre-defined fitness value was achieved (typically 0.95) or a number of generations reached, the GA would analyse the global solutions in a number of numerical models (see Figure 9.2). GA1 not only utilised a dynamic graft model, it also generated circumferential and longitudinal tensile simulations and a number of static and dynamic

graft models using the global solutions. Not all the global solutions would solve in the circumferential and longitudinal tensile simulations, or the static and dynamic graft models. Thus, a number of the global solutions were annulled, due to their in-ability to converge in other finite element models, reducing the number of possible solutions. However, this is not observed in GA2 and GA3 as the same numerical models are analysed after optimisation.

14.4.1 GA1 and the fabric reinforced graft compliance

GA1 optimises for an objective function in terms of dynamic diameter compliance C_d, diastolic diameter and an overall nonlinear stiffening characteristic in a dynamic graft model and is thus, directly dependent on the graft's internal diameter with pressure and is indirectly dependent on the compression seen through the graft wall and longitudinal changes. This has areas of weakness in terms of the graft's physical application and the test results obtained from the compliance rig. For example, the appropriateness of fixing both ends when longitudinal constraints affect diameter change, in essence a grafts anastomoses will never be fixed but will allow longitudinal strain physically in the human body. Thus, if data is available on the longitudinal changes seen by natural blood vessels and on the minimum amount of compression allowable in the porous structure to promote tissue ingrowth, these requirements can be implemented into the objective function and weighted accordingly to find those solutions which give a required compliance, optimal wall compression and axial strain. Another possibility is optimising on the nonlinear stiffening index β defined by Hayashi *et al.* [79] (Section 2.6), rather than compliance. A benefit to this, is the nonlinear stiffening requirements would be incorporated in the objective function rather than as a penalty, as is currently implement in GA1.

Although the optimal solutions are intended to describe a fabric reinforcing, the solutions obtained from GA1 can be used to find materials and structures which behave in a similar fashion. Thus, the adventitial reinforcing solutions do not need to be restricted to fabrics, but can be used for other structures as long as their application does not limit other features, such as the allowance of cellular ingrowth through the reinforcing structure and into the porous graft.

14.4.2 GA2 and the uniaxial tensile tests

The results obtained from GA2, which tries to find the fabric model coefficients of four physical fabric specimens and their uniaxial stress-strain behaviour in the warp and weft directions, gave reasonable solutions for fabric samples 1, 3 and 4. However, a poor solution was found for sample 2, which showed a linear stress-strain relation in the weft direction.

Variation in the optimised solutions and the physical tensile test data collected could have arisen due to the following:

- The strain-energy function used to describe the fabrics behaviour does not allow for both linear and nonlinear stress-strain relations.
- The fitness function utilised in GA2 was not effective, allowing the GA to converge on a

solution which is not optimal.

- The penalty function and constraint criteria were harsh, causing potential generations to be lost if they slightly violated the constraints.

The strain-energy function has already been discussed in Section 14.2. The fitness function in GA2 utilised a normalised difference method between the model axial stress and transverse strain with test results at 10, 20 and 30% axial strain. These normalised differences were weighted accordingly to give a higher ranking to those generation members which modelled the lower strains better. Since good solutions were obtained for fabric samples 1, 3 and 4, the objective and fitness functions are seen to be functional. Again, the same penalty functions and constraint criteria were used to find good solutions to fabric samples 1, 3 and 4. From log files produced by GA2 the number of potential generations lost due to these penalty functions and constraints was no different for fabric sample 2 to those which produced good solutions. Thus, it is seen to be the fabric constitutive relation which is the cause of the GAs inability to converge upon reasonable solutions for the linear stress-strain fabric relation.

14.4.3 GA3 and the fabric circumferential and longitudinal tensile tests

GA3 used similar partial objective, objective and fitness functions as GA2, however instead of warp and weft uniaxial tensile models, circumferential and longitudinal models were implemented. No experimental transverse strain behaviour was utilised, as no physical data was collected. Thus, the model solutions obtained from GA3 might not model some of the fabric's physical characteristics.

14.5 Uniaxial tensile test data of fabric samples

Uniaxial tensile tests. The use of custom built tensile jaws for the uniaxial tensile tests (Figure 10.11), ensured minimal deformation of the fabric samples prior to testing. During the tensile testing of the fabrics it was observed that edge effects, such as fraying and curling, prevented the evaluation of localised deformation, thus local transverse and axial deformation was analysed using a flat bed with pre-set deformation points. Every effort was made to ensure that tensile test procedures were consistent, however the following could have affected the data collected:

- The method of attaching the sample ends between the tensile jaws allowed for some lateral slipping and thus the fabric was seen to contract at points along the displaced edge.
- Due to the highly deformable fabrics used, small amounts of deformation may have occurred during sample preparation.
- Test samples were cut from fabric sheets, this caused the edges to fray. This highlights the error in assuming the fabric is a continuum.
- Test sample edges started to curl due to bending,. thus, it was difficult to evaluate local

deformation.

Transverse and axial strain tests. The simple use of a flat bed to place fabric samples on under uniaxial tension was used to prevent the edge curling observed in the Instron™ test rig while obtaining local transverse and axial strain effects. This method is highly invasive and far from ideal as results will be affected by preventing the fabric curling. However this curling effect will not be observed when the fabric is being used as a reinforcing over the graft, thus it was deemed acceptable under the current circumstances. The following areas could have affected the experimental results collected:

- The straining of one side sometimes produced a non-uniform, unevenly distributed strain from one sample end to the other (see Figures C.3 and C.4 in Appendix C).
- Frictional interaction between the flat bed and the fabric.
- The use of a stitch line and pins to produce the uniaxial strain produces a non-uniform displaced edge.

It would be ideal to visually monitor the local stress-strain relation while the fabric is tested in the Instron™ test rig, however, this was not possible due to the edge curling observed. The use of the flat bed to prevent the fabric edges curling, gives an indication of the local strains due to axial loading. Traditional engineering methods employed to measure local strain, such as strain gauges, would be redundant due to their highly invasive nature and the weak deformable fabrics tested.

The non-uniform displaced edge produced by using stitch lines and pins could have been prevented by using the custom built tensile test jaws and holder to provide the clamped edge and defined axial strain.

14.6 Circumferential and longitudinal tensile tests

The circumferential and longitudinal tensile tests were employed to gain the transverse stress-strain characteristics of the fabric reinforcing prototypes.

Circumferential. Several problems arise with the circumferential tensile test method, model correlation and assumptions used. The tensile test pins for the tests are only supported from one side (see Figure 12.4). Bending at this point may have occurred during testing thereby affecting the results. No bending was observed during testing at low strains, however at the higher strains ($> 25\%$) slight bending was observed. Thus, only physical data under 25 % circumferential strain was used to ensure that this did not affect the results. From Figure 12.5, a reduction in fabric circumferential stiffness is observed between 50 and 75 N/m. It is unclear whether this is due to fabric deformation or the sample slipping over the pins in the lateral direction. To eliminate the latter, it may be useful to prevent the fabric moving in the lateral direction by having a frictional surface on the pin, this would however, prevent circumferential strain. Thus,

it may be convenient to have this frictional surface on the apex of each pin preventing lateral motion, while still allowing circumferential strain. This could be achieved by etching fine micro grooves along the apex of each pin.

A soft contact model between the fabric and pin was implemented in the numerical model, this contact model was adjusted until a realistic solution was observed, however, no study was done to ensure the contact model was acceptable. Real time images of axial strain with circumferential tension could be captured to gain information on the relative motion between the pin and the fabric. This information could be used to calibrate the contact model.

Longitudinal. The longitudinal tensile tests were easily implemented, however the clamping of the sample ends prior to testing is not ideal as this introduces stress-strain effects. Thus, a better method of holding the ends of the test samples without introducing stress is required. Figure 14.2 shows a sectional view of a test jaw which is proposed to ensure the circular shape remains during physical testing. The proposed test jaw can easily be manufactured and implemented.

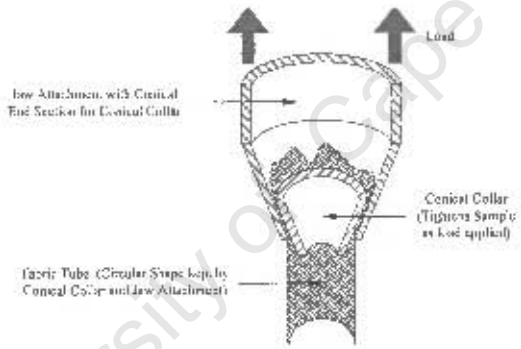

Figure 14.2: Schematic of sectioned longitudinal tensile test end-clamp to ensure tubes circular shape remains during testing

14.7 Compliance testing

14.7.1 Non-reinforced and fabric reinforced graft samples

The method of manufacture and preparation of the porous graft samples and fabric reinforcing can be found in Chapters 7 and 12. While every process is carefully controlled and rigorously followed, a high percentage of inconsistent porous graft and fabric samples are produced. Once samples are produced they go through a quality control process which eliminates unfit samples, even so, with the high expense and time to manufacture these samples, it is not always possible to obtain or use consistent samples, thus a degree of deviation is observed. A large qualitative variation in texture and feel was observed from one sample to the next, especially in the porous grafts, where non-compliant and complaint regions were easily distinguishable. This is mainly due to inconsistent bead packing in the graft rig (Section 7.2.3). With the onset of a semi-

automated manufacturing process much of these inconsistencies can be eliminated [9]. These inconsistencies contribute to the large variation in compliance results. Even though the mechanical properties of the porous structures were assessed in Section 10.2.1, this was done on samples cut from bead cast rods as it was not possible to get the required test sample sizes from the grafts.

A variation in mechanical properties is also observed in the prototype reinforcing samples produced. From the circumferential and longitudinal tensile tests (Section 12.2), it is observed that the standard deviation between samples is low in the low strains where the fabric reinforcing physically operates. The required longitudinal straining of the reinforcing over the graft could also contribute to the variation of graft test samples produced. Slight differences were observed in reinforced graft samples produced, even though care was taken to ensure the fabric reinforcings were not over strained, twisted or loose.

Graft anastomotic attachment was prepared by bonding the samples to e-PTFE graft samples (Figure 7.17). The bond produced is non-compliant, however, sample lengths (50 mm) ensured that anastomotic compliance did not affect the readings at the sample centre.

The variation in graft P vs. $\triangle d/d_0$ samples can be observed in Figure 13.3, where the standard deviation in results for the non-reinforced 90-106 μm grafts is slightly higher than the reinforced graft samples. However, with the 125-150 μm samples the opposite occurs. There is also little significant difference between the various pore sized graft samples used, only significant differences were observed between the 90-106 and 125-150 μm reinforced and non-reinforced pore size grafts ($p = 0.018$ and 0.053 respectively). With the addition of prototype I, a marked reduction in compliance is seen and a slight nonlinear stiffening effect observed. The slight nonlinear stiffening seen with the addition of prototype I, is due to the almost linear response the fabric reinforcing displays in the circumferential tensile tests as illustrated in Figure 12.6.

14.7.2 Luminal latex liners

The use of latex liners or balloons to line the porous grafts for testing, brings about further complications. Its effect on the overall structure has to be analytically subtracted to give compliance values. From Figures 10.3 and 10.5, the Young's modulus of the latex liner is considerably high compared to the porous materials ($E_Y = 750$ kPa and $E_Y = 200$ kPa for the latex liner and the 125-150 μm porous material respectively). Figure 13.2 displays the physical compliance curves obtain for the latex liners and the porous grafts including the latex liner, one can see the latex liner contributes largely to the mechanics of the combined structure. Thus, a weaker material or thinner liners are required to reduce the mechanical contribution to the combined structure.

It is possible to produce weaker luminal liners; silicone liners were produced with a Young's modulus of 150 kPa and a wall thickness of 30 μm which were extremely compliant. However, they were difficult to produce and inconsistencies along the length of the silicone liners was an issue, where wall thickness could deviate by 20 μm. These silicone liners were produced by a similar dipping process as the latex liners, however once the silicone had cured they were

released from the mandrel by swelling them in a solvent.

Hydrogels packed in the pores of the graft wall could also be used in place of the latex liners. These hydrogels are weak in compression and tension, contributing little to the mechanics, while preventing pressure loss. The hydrogel can also be adjusted to give similar mechanical responses as a blood clot, thus, giving a possible simulated time based change in compliance with clotting. A weak PEG hydrogel was utilised in the pores of a graft sample in place of a latex liner, where it successfully prevented pressure loss through the graft wall to183 mmHg. This shows its possible application in preventing pressure loss at low pressures. However, the following problems were observed; 1. it was difficult to drive the hydrogel into the pores of the graft wall without causing deformation, 2. when trying to form the hydrogel in the pores rather than drive it into the pores, swelling was observed during the cross-linking or curing process, causing excessive deformation in the porous structures.

The latex liner was observed to collapse or crimp when placed inside the graft. This is due to the variation in diameter between the lumen and liner. When obtaining the static compliance curves for the latex liners (Section 13.2.1) an initially low diameter change was observed between 0 and 20 mmHg pressure. This initial small diameter change was attributed to the samples being axially strained by 10 % prior to the application of pressure. This axial strain would cause the latex liner to collapse due to a pressure drop in the system as the compliance rig flow circuit is a closed loop. Thus, this initial increase in pressure is used to get the internal pressure back to zero while small diameter changes are observed. The same initial small diameter change is seen in Figure 13.2 for the porous grafts. This could be due to the latex liner in the porous graft collapsing, however, the porous structure would not as it would allow water to draw through the pores between the latex liner and graft wall. This effect would offset the actual pressures measured during testing and could be contributing to the low physical compliance results observed, as true sampling pressures would be lower.

With the 10 % axial strain the latex liner could circumferentially contract more than the porous structure, thus, a discontinuity is likely to occur between the liner and the porous graft. This could contribute to the differences observed between the numerical solutions and physical data. This effect could be studied in the graft numerical model, if permanent contact between the latex liner and porous graft is not enforced.

14.7.3 Compliance rig

The compliance rig was designed in-house and utilises either a digital or ultrasound imaging technique to measure real time external or internal diameter change. However, ultrasound image resolution and recordings were difficult to use due to the scattering of the reflected ultrasound caused by the micro-pores of the graft structure (see Figure 7.12), thus, this technique was found to be ineffective.

When placing the graft samples in the rig the orientation of the sample can greatly affect the

results, especially when the porous structures have mechanical property variation in the circumferential direction. In this study graft orientation was random, however, it may have been better to have gained a number of compliance readings at various orientations, such as 0, 120 and 240^o for a single graft sample.

The head of water due to the water level in the water bath (see Figures 7.8 and 7.9) can also affect initial pressure readings. To ensure that no errors were incurred due to this, the pressure transducers were zero-set prior to placement of the graft sample. The graft samples were placed in the heated water bath for several minutes prior to testing to soak the water into the pores and allow the sample's temperature to stabilise. The graft samples do expand and soften slightly with increased temperature, however, this was not a concern as all testing and material characterisation was done at physiological temperatures.

A roller pump, a one way flow valve, proximal and distal windkessels, and linear needle valves are used to obtain physiological pressure and flow curves. The rig is sensitive to slight variations along the system and thus, without user familiarity it is difficult to obtain consistent pressure and flow curves. A wide range of flow patterns and systolic and diastolic pressures across the grafts can be achieved with the compliance rig, thus, it is possible to simulate various regions of the vasculature (see Figure 2.2). However, problems do arise in producing consistent curves from one graft sample to the next, due to the highly sensitive nature of the system to variations in graft compliance and back pressure. Certain sections of the compliance rig use compliant tubing, such as at the roller pump, these compliant sections including the windkessels absorb and dissipate energy, making it very sensitive to slight system changes. To reduce this effect and help produce controllable and consistent waveforms, rigid tubing and a programmable positive displacement piston pump, similar to those used by Holdsworth *et al.* [154] and Charara *et al.* [148], could be implemented.

Measuring the external diameter is not ideal for compliance calculations. The error incurred in assuming the graft's wall thickness remains constant is large and will result in reduced compliance values being obtained. External diameter measurements were made via a CCV camera connected to a microscope which focused on the graft sample (see Figure 7.9). Reliable measurements down to 9.26 μm could be made, which was considered reasonable for the purposes of this study (see Section 7.2.2).

Image refraction through the water surface could lead to variation in results, however, a rule was used to calibrate each measurement taken. Thus, the error due to refraction would be consistently observed. However, good correlations are observed between our visual method and a research group using ultrasound phase locked echo tracking (Section 7.3).

The analytical subtraction of the latex liner is also of concern. Some researchers neglect the effect of the latex liner, as they assume it is a weak membrane, while others such as ourselves test both the latex tube and then the combined latex tube and graft and then subtract the latex curve. This method is not ideal.

Human error and inconsistent test procedures can also affect results. Every effort has been made to ensure that rigorous procedures are adhered to.

14.8 Compliance results and correlations

Experimental and model compliance results have been obtained, however, the supply of prototype II reinforcing was limited and no physical data was obtained for this as an adventitial support. It would have been beneficial to have had compliance data for prototype II to further compare numerical data with experimental results.

For the non-reinforced numerical solutions, dynamic compliance values were 2.7, 6.5 and 16.0 %/100 mmHg higher than experimental observations, while prototype I reinforced numerical model compliance values were 5.3, 5.5 and 6.0 %/100 mmHg higher, with increasing pore size respectively. This data was obtained by adjusting for internal diameter and analytically subtracting the luminal latex (refer to Table 13.3). These differences were reduced and were observed to fall within the experimental results obtained for the non-reinforced and the 106-125 and 125-150 μm reinforced grafts, when correlations were made with static pressure and external diameter data (refer to Table 13.4). It can be seen from the static P vs. $\triangle d/d_0$ relations obtained (Figures 13.1, 13.8 and 13.9), the numerical models are over predicting diameter change with pressure. However, the effect of the reinforcing on the numerical solutions does follow the experimental data by showing a reduction in diameter change of between 3.6 to 4.5 % for the numerical data and 3.1 to 3.8 % for the physical data at 120 mmHg. Errors which could contribute to the difference in numerical and physical data are:

1. **Model error:**
   - The hyperelastic and hyperfoam material models are not accurately describing the physical situation. From Section 10.2, the hyperfoam material model solutions follow the tensile data to 30 % strain in compression and 55 % in tension, whilst only to 0.25 % in shear. These are all within the bounds of the physical strains observed by the porous structures. The rms errors for the mathematical expressions fitting the physical test data for the 90-106, 106-125 and 125-150 μm porous structures were 6.13, 5.56 and 4.99 % respectively. In the case of the latex liner and the hyperelastic material model the rms error for the mathematical expression fitting the physical test data was zero.
   - The fabric material models do not accurately model the physical situation. From Section 12.3, the solutions obtained from GA3 for prototypes I and II give very good solutions in the circumferential direction, while only giving good solutions at lower strains in the longitudinal direction. The models are deemed accurate for the requirements. However, no transverse strain data was optimised for, this may be contributing to the error observed. When the fabric is longitudinally strained to fit the graft sample, the fabric model obtained from GA3 for prototype I gives a 11.7 % circumferential strain while the physical situation would require 16.6 % in order for the fabric to fit the porous graft. Thus, there are

transverse strain variations observed between the fabric and the model used.

2. **Experimental error:**
   - The porous test data used to obtain the hyperfoam material models was produced from bead cast rods as opposed to sections cut from the grafts. Material properties could vary between the cast rods and grafts due to different bead packing configurations during the casting process.
   - The large variation in fabric and porous graft properties due to the intensive manual manufacturing process.
   - The longitudinal straining of the fabric over the graft sample, causes a stress state in both the fabric and porous structure prior to testing.
   - The axial strain applied to the graft sample prior to compliance testing and the closed loop system (constant volume) would cause the latex liner to collapse under negative pressures, affecting compliance readings.
   - The large variation in latex liner properties as observed by the large standard deviation in Figure 13.1.

When assessing the above and noting that the effect of the reinforcing on the numerical solutions follows the experimental data. The use of bead cast rods rather than graft samples used to obtain the porous test data and the hyperfoam material models is the most likely cause of error in the results observed.

14.9 In vivo models and future developments

A four-week in vivo primate study was done using prototype I on a 125-150 μm pore size graft to see the effect of the fabric reinforcing on healing response. H&E stains on explanted graft cross-sections revealed large FBGC activity around the fabric reinforcing fibers, which indicates a high inflammatory response. This response could be heightened due to mechanical shearing and frictional forces between the individual yarns as they respond to pulsatile loads. This initial in vivo study of the fabric reinforcing is premature to totally exclude the use of fabrics as a reinforcing, as much research has been done on the use of fabrics in the body, where inflammatory outcomes have been low. Thus, an optimal fabric structure type and material selection should be sought which reduces the inflammatory response. The use of mono-filament fibre fabrics to reduce the yarn interaction to single points could reduce this inflammatory response.

The desired effect over a period of time in vivo should also be considered, where it is hoped that the overall mechanics of the porous structure including tissue in-growth will mimic that of the host vessel after healing. With this comes the question; what are the initial mechanical properties required before implantation? With the current work we have looked at producing a graft which is similar to the common femoral artery and i.e. has a 6 %/100 mmHg compliance,

a nonlinear stiffening effect and a diastolic diameter of 4 mm. This would be ideal if the graft's mechanical properties degraded at the same rate as healing occurred. This controlled material degradation would be difficult to produce and will probably produce an inflammatory response. Thus, an initial compliance of 6 %/100 mmHg is not ideal, as mechanical changes to the graft will be observed, especially if rapid healing is induced by growth factors.

Chapter 15

Conclusions and Recommendations

15.1 Conclusions

Constitutive material models, numerical methods and genetic algorithms were used to assess and optimise fabric reinforced porous graft structures, the variables being the coefficients of a strain energy function used to describe the general characteristics of an ideal anisotropic elastic coarse knit fabric used to reinforce the porous grafts.

The genetic algorithm, GA1 is used to optimise the fabric constitutive model coefficients to obtain a 6 %/100 mmHg diameter compliance (C_d), a 4.0 mm diastolic diameter and a nonlinear stiffening characteristic in a dynamic numerical graft model.

Solutions were found for three porous graft types, namely; 90-106, 106-125 and 125-150 μm bead cast polyurethane structures. These solutions were then utilised in a static numerical graft model to obtain pressure-diameter relations, circumferential and longitudinal numerical tensile models were also used to obtain the transverse stress-strain requirements of the reinforcing solutions.

A nonlinear anisotropic elastic strain-energy function with ten coefficients was used to describe the material behaviour of coarse knit fabrics. A second genetic algorithm, GA2 and a uniaxial tensile numerical model were used to show that the strain-energy function could model a wide range of fabric characteristics, by simulating four diverse coarse knit fabric samples tested under uniaxial tension in both the warp and weft directions. Good solutions were obtained, however, the strain-energy function failed to describe fabrics with linear stress-strain relations.

It was not possible to produce fabrics displaying the transverse stress-strain relations obtained from GA1 due to time and cost constraints. However, two prototypes produced where chosen based on selection criteria to be used for experimental purposes.

These two prototype reinforcing tubes were then physically tested in the circumferential and longitudinal directions to obtain their transverse stress-strain characteristics. These stress-strain characteristics were then implemented in a third genetic algorithm, GA3, to obtain the prototypes' strain energy coefficients. The coefficients were then employed in numerical graft models to obtain numerical static and dynamic compliance data.

Only one prototype, prototype I was physically tested over the three porous graft types, however, comparing the numerical compliance data with experimental results, the numerical models typically predicted higher compliance values. Using internal diameter and analytically

subtracting the latex liner, the non-reinforced numerical compliance values were 2.7, 6.5 and 16.0 %/100 mmHg higher than the experimental results with increasing pore size respectively, while the reinforced numerical compliance values were 5.3, 5.5 and 6.0 %/100 mmHg higher. The differences were reduced to 0.4, 0.1 and 2.0 %/100 mmHg respectively, for the non-reinforced grafts and 1.5, 1.1 and 0.4 %/100 mmHg for the reinforced grafts, when the latex liner was not subtracted and external diameters used. The main reasons for the observed difference in numerical and physical results are the following:

- The use of bead cast rods rather than graft samples to obtain the hyperfoam material models used to describe the porous structures.
- The inconsistent graft test samples used.
- The high mechanical contribution of the luminal latex liner used to prevent pressure loss through the porous structures.
- The error in analytically subtracting the latex liner from the static compliance curves.
- The error in assuming no compression through the porous graft wall to obtain internal diameter measurements from external diameter data.
- The failure of the fabric model coefficients obtained from GA3 to accurately describe the behaviour of the prototypes.

Finally, the specific objectives of the present study as set out in Section 1.2 have been achieved.

15.2 Recommendations

Much can be done to improve the numerical models, genetic algorithms, samples and the experimental techniques. The following are recommended:

15.2.1 The hyperfoam material model

- Hyperfoam material model should be fitted to tensile, shear and compressive test data for porous graft samples and not bead cast rods.

15.2.2 The fabric constitutive model

- Implement a different strain energy function described in (14.1) and (14.4).
- Develop time dependent material constitutive relations for tissue in-growth and material degradation.
- Implement anisotropic viscoelasticity and plasticity.

15.2.3 Finite element models

- Implement higher order elements.
- Model fabric with shell elements.
- Study the effect of axial load vs. fixed strain on compliance using the graft model.

- Allow relative motion between the fabric, latex and porous structures in the graft model.
- Study the effect of longitudinally straining the fabric over the porous graft.
- Validate the soft contact model used in the circumferential tensile model.

15.2.4 The GAs and optimisation

- Implement further partial objective functions into GA1 to minimise wall compression and obtain specific longitudinal compliance.
- Reduce GA simulation times by implementing penalties prior to analysing numerical models.
- Reduce GA simulation times by starting with coarse meshed finite element models and refining the element mesh with increased generations.

15.2.5 Graft samples and fabric reinforcings

- Develop GA1 fabric reinforcing solutions to experimentally validate the numerical solutions obtained.
- Develop fabric samples which match the external diameter of the graft samples.

15.2.6 Circumferential and longitudinal tensile tests

- Develop high friction surface on apex of circumferential test pins.
- Develop longitudinal tensile end clamp as shown in Figure 14.2.
- Implement real time image capturing technique to obtain transverse stain data with circumferential and longitudinal tension.

15.2.7 The compliance rig and testing

- Develop mechanically weak hydrogels or consistent silicone liners.
- Develop computer controlled displacement pump with feedback loop to replace roller pump.
- Develop a method of removing micro-bubbles from the porous grafts to reduce ultrasound image scatter.

15.2.8 In-vivo studies

- Investigate the effect of tissue in-growth on fabrics and porous structures under physiological conditions.

Bibliography

[1] Sauvage L. R. AndBerger K. E., Mansfield P. B., Wood S. J., Smith J. C., and Overton J. B. Future directions in the development of arterial prosthesis for small and medium calibre arteries. *Surgical Clinics of North America*, 54(1), 1974.

[2] Niklason L. E. and Langer R. S. Advances in tissue engineering of blood vessels and other tissues. *Transplant Immunology*, 5(4):303–306, 1997.

[3] Burkel W. E. The challenge of small diameter vascular grafts. *Medical progress through technology*, 14:165–175, 1988.

[4] Flemma R. J., Mullen D. C., and Leply D. *Artocoronary Vein Bypass Grafting*. Appleton-Century-Crofts, N.Y., 1978.

[5] Huynh T., Abraham G., Murray J., Brockbank K., O-Hagen P., and Sullivan S. Remodelling of an acellular collagen graft into a physiological responsive neovessel. *Nature Biotechnology*, 17:1083–1086, 1999.

[6] Hayashi K., Takamizawa K., Saito T., and Kira K. Elastic properties and strength of a novel small-diameter, compliant polyurethane vascular graft. *Journal of Biomedical Materials Research (Applied Biomaterials)*, 23:229–244, 1989.

[7] Lyman D. J., Fazzio F. J., Voorhees H., and Robinson G. Compliance as a factor effecting the patency of a copolyurethane vascular graft. *Journal of Biomedical Materials Research*, 12:337–345, 1978.

[8] Mooney D. J., Baldwin D. F., Suh N. P., Vacanti J. P., and Langer R. Novel approach to fabricate porous sponges of poly d, l-latic-co-glycolic acid without the use of organic solvents. *Biomaterials*, 17(14), 1996.

[9] Bezuidenhout D. *Porous Polymeric Superstructures as In-Growth Scaffolds for Tissue-Engineered Vascular Prosthesis*. PhD thesis, Stellenbosch University, 2001.

[10] Zilla P. and Greisler H. P. *Tissue Engineering of Vascular Prosthetic Grafts*. R. G. Landes Company, Austin, Texas U.S.A, 1999.

[11] How T. V., Guidon R., and Young S. K. Engineering design of vascular prosthesis. *Proc. Instn. Mech. Eng.*, 206, 1992.

[12] Hayashi K. Experimental approaches on measuring the mechanical properties and constitutive laws of arterial walls. *J. Biomech. Eng.*, 115:481–487, 1993.

[13] Baird R. N., Kidson I. G., L'Italien G. J., and Abbott W. M. Dynamic compliance of arterial grafts. *Am. J. Physiol.*, pages H568–H572, 1977.

[14] Stewart S. F. C. and Lyman D. J. Effects of vascular Graft/Natural artery compliance mismatch on pulsatile flow. *J. Biomech.*, 25:297–310, 1992.

[15] Hasson J. E., Megerman J., and Abbott W. A. Increased compliance near vascular anasta-

mosis. *J. Vasc. Surg.*, 2:419–423, 1985.

[16] Seifert K. B., Albo D., Knowlton H., and Lyman D. J. Effect of elasticty of prosthetic wall on patency of small-diameter arterial prosthesis. *Surg. Forum.*, 30:206–208, 1979.

[17] Weston M. W., Rhee K., and Tarbell J. M. Compliance and diameter mismatch affect the wall shear rate distribution near end-to-end anastomosis. *J. Biomech.*, 29:187–198, 1996.

[18] Ballyk P. D., Ojha M., Walsh C., and Butany J. Suture-induced intramural stresses and intimal hyperplasia. *Advances in Bioengineering*, 33:213–214, 1996.

[19] Ballyk P. D., Walsh C., Butany J., and Ojha M. Compliance mismatch may promote graft-artery intimal hyperplasia by altering suture-line stresses. *J. Biomech.*, 31:229–237, 1998.

[20] Hess F., Jerusalem C., and Braun B. The endothelialisation of a fibrous polyurethane microvascular prosthesis after implantation in the abdominal aorta of the rat. *J. Cardiovasc. Surgery*, 24, 1986.

[21] MacKellar I. The mechanical design aspects of a small diameter vascular prosthesis. Master's thesis, University of Cape Town, 1998.

[22] Hughes A. G. Mechanical design aspects of a small diameter vascular graft with structured porosity. Master's thesis, University of Cape Town, December 1999.

[23] Fung Y. C. and Liu S. Q. Strain distribution in small blood vessels with zero stress state taken into consideration. *Am. J. Physiol.*, 264:H544–H552, 1992.

[24] Fung Y. C. and Liu S. Q. Determination of the mechanical properties of the different layers of blood vessels in vivo. *Proc. National academy of science USA*, 92:2169–2173, 1995.

[25] Demiray H. A quasi-linear constitutive relation for arterial wall materials. *J. Biomech.*, 29:1011–1014, 1996.

[26] Carmines D. V., McElhaney J. H., and Stack R. A piece-wise non-linear elastic stress expression of human and pig coronary arteries tested in vitro. *J. Biomech.*, 24:899–906, 1991.

[27] Takamizawa K., Hayashi K., and Matsuda T. Isometric biaxial tension of smooth muscle in isolated cylindrical segments of rabbit arteries. *American Journal of Physiology*, 263 (Heart Circ. Physiol. 32):H30–H34, 1992.

[28] Dobrin P. B. and Mrkvicka R. Estimating the elastic modulus of non-atherosclerotic elastic arteries. *Journal of Hypertension*, 10:S7–S10, 1992.

[29] Yu Q., Zhou J., and Fung Y. C. Neutral axis location in bending and young's modulus of different layers of arterial wall. *American Journal of Physiology*, 34:H52–H60, 1993.

[30] Haas K. S., Phillips S. J., Comerota A. J., and White J. V. The architecture of adventitial elastin in the canine infrarenal aorta. *The anatomical record*, 230:86–96, 1991.

[31] Langewouters G. J., Wesseling K. H., and Goehard W. J. A. The static elastic properties of 45 human thoracic and 20 abdominal aortas in vitro and the parameters of a new model. *J. Biomech.*, 17:425–435, 1984.

[32] Fung Y. C. *Biomechanics: Mechanical Properties of Living Tissue*. Springer-Verlag, New York, 2nd edition, 1984.

[33] Choung C. J. and Fung Y. C. Compressibility and constitutive equations of arterial wall in radial compression experiments. *J. Biomech.*, 17:35–50, 1984.

[34] Takamizawa K. and Hayashi K. Strain energy density function and uniform strain hypothesis for arterial mechanics. *J. Biomech.*, 9:293–300, 1987.

[35] Wu S. G. and Lee G. C. On non-linear viscoelastic properties of arterial tissue. *ASME J. Biomech. Eng.*, 106:42–47, 1984.

[36] Young J. T., Vaishnav R. N., and Patel D. J. Non-linear anisotropic viscoelastic properties of canine arterial segments. *J. Biomech.*, 10:549–559, 1977.

[37] Bergel D. H. *Cardiovascular Fluid Dynamics*, volume 2. Academic Press, 1972.

[38] Mills C.J., Gabe I.T., Gault J.H., Mason D.T., Ross Jr. J., Braunwald E., and Shillingford J.P. Pressure-flow relationships and vascular impedance in man. *Cardiovascular Res.*, 4:405–417, 1970.

[39] Rushmer R. F. *Cardiovascular Dynamics*. W. B. Saunders, Philadelphia, 3rd edition, 1970.

[40] Rhodin J. A. G. Architecture of the vessel wall. In *Handbook of Physiology, Section 2: The Cardiovascular System*, volume II Vascular Smooth Muscle. American Physiological Society Bethesda, MD, 1980.

[41] Levy B. I. The mechanical properties of the arterial wall in hypertension. *Prostaglandins, Leukotrienes and essential fatty acids*, 54:39–43, 1996.

[42] L'italien G. J., Chandrasekar N.R., and Lamuraglia G. M. Biaxial elastic properties of rat arteries in vivo: Influence of vascular wall cells on anisotropy. *American Journal of Physiology*, 267 (Heart Circ. Physiol. 36):H574–H579, 1994.

[43] Langewouters G. J., Wesseling K. H., and Goedhard W. J. A. The pressure dependent dynamic elasticity of 35 thoracic and 16 abdominal human aortas in vitro described by a five component model. *J. Biomech.*, 18:613–620, 1985.

[44] Von Maltzahn W. W., Besdo D., and Wiemer W. Elastic properties of arteries: A nonlinear two-layer cylindrical model. *J. Biomech.*, 14:389–397, 1981.

[45] Mohan D. and Melvin J. W. Failure properties of passive human aortic tissue 1: Uniaxial tension tests. *J. Biomech.*, 11:887–902, 1982.

[46] Humphery J. D. Mechanics of the arterial wall: Review and directions. *Critical Reviews in Biomedical Engineering*, 23, 1995.

[47] Choung C. J. and Fung Y. C. On residual stresses in arteries. *J. Biomech.*, 108:189–192, 1986.

[48] Hearn E. J. *Mechanics of Materials*, volume 1. Butterworth-Heinemann, Oxford, 2nd edition, 1996.

[49] Hearn E. J. *Mechanics of Materials*, volume 2. Butterworth-Heinemann, Oxford, 1995.

[50] Chuong C. J. and Fung Y. C. Three-dimensional stress distribution in arteries. *J. Biomech.*, 105:268–274, 1983.

[51] Fung Y. C. *Stress-Strain History Relations of Soft Tissues in Simple Elongation.* Prentice-Hall, Englewoods Cliffs, N.Y., 1972.

[52] Hutchinson K. J. Effect of variation of transmural pressure on the frequency response of isolated segments of canine carotid arteries. *Circulation Res.*, 35:742–751, 1974.

[53] Newman D. L., Bowden N. L. R., and Gosling R. G. The dynamic and static elastic properties of the aorta of the dog. *Cardiovasc. Res.*, 9:679–684, 1975.

[54] Greenwald S. E., Newman D. L., and Denyer H. T. Effect of smooth muscle activity on the static and dynamic elastic properties of the rabbit carotid artery. *Cardiovasc. Res.*, 16:86–94, 1982.

[55] Dehoff P. H. On the nonlinear viscoelastic behaviour of soft biological tissues. *J. Biomech.*, 11:35–40, 1978.

[56] Decraemer W. F., Maes M. A., Van Huyes V. J., and Van Peperstraete P. A non-linear viscoeleastic constitutive equation for soft biological tissues. *J. Biomech.*, 13:559–564, 1980.

[57] Lyman D. J., Albo D., Jackson R., and Knutsen K. Development of a small diameter vascular prosthesis. *Trans. Am. Soc. Artif. Intern. Organs*, XXIII, 1977.

[58] Kidson I. G. and Abbott W. M. Low compliance and arterial graft occlusion. *Circulation*, 58(3):I1–I4, 1978.

[59] Kidson I. G. The effect of wall mechanical properties on patency of arterial graft. *Annals of the Royal College of Surgeons of England*, 65:24–29, 1983.

[60] Belz G. G. Elastic properties and windkessel function of the human aorta. *Cardiovascular Drugs and Therapy*, 9:73–83, 1995.

[61] O'Rourke M. F. and Brunner H. R. Introduction to arterial compliance and function. *Journal of Hypertension*, 10:S3–S5, 1992.

[62] Walden R. and L'italien G.J. et al. Matched elastic properties and successful arterial grafting. *Arch. Surgery*, 115:1166–1169, 1980.

[63] Tai N. R. M., Giudiceandrea A., Salacinski H. J., Seifalian A. M., and Hamilton G. In vivo femoropopliteal arterial wall compliance in subjects with and without lower limb vascular disease. *J. of Vacsular Surgery*, 30:936–945, 1999.

[64] Rosset E., Brunet C., and Rieu R. Viscoelastic properties of human arteries, methodology and preliminary results. *Surgical and Radiologic anatomy*, 18:1996, 1996.

[65] Gupta B. S. and Kasyanov V. A. Biomechanics of human common carotid artery and design of novel hybrid textile compliant vascular grafts. *J. Biomed. Mat. Res.*, 34:341–349, 1997.

[66] Millam R. Design of an adventitial type of reinforcing of prosthetic vascular grafts through mechanical affirmed material and structural modulation. Master's thesis, University of

Cape Town, 2001.

[67] Tai N. R., Salacinski H. J., Edwards A., Hamilton G., and Seifalian A. M. Compliance properties of conduits used in vascular reconstruction. *British Journal of Surgery*, 87:1516–1524, 2000.

[68] Martz H., Beaudoin G., Paynter R., King M., Marceau D., and Guidoin R. Physiochemical characterisation of a hydrophilic microporous vascular graft. *Journal of Biomedical Materials Research*, 21:399–412, 1987.

[69] Kowligi R. R., Von Maltzahn W. W., and Eberhart R. C. Fabrication and characterisation of small-diameter vascular prostheses. *Journal of Biomedical Materials Research (Applied Biomaterials)*, 22:245–256, 1988.

[70] Muller-Glauser W., Lehmann K. H., Bittmann P., Bay U., Dittes P., Von Segesser L., and Turina M. A. Compliant small diameter vascular prosthesis lined with functional venous endothelial cells. *ASAIO Trans*, 34(3):528–531, 1988.

[71] Uchida N. and Kambic H. et al. Compliance effects on small diameter polyurethane graft patency. *Journal of Biomedical Materials Research*, 27:1269–1279, 1993.

[72] Edwards A., Carson R. J., Bowald S., and Quist W. C. Development of a microporous compliant small bore vascular graft. *Journal of biomaterials application*, 10:171–187, 1995.

[73] Chen J. H., Laiw R. F., Jiang S. F., and Lee Y. D. Microporous segmented polyurethane vascular graft: Dependency of graft morphology and mechanical properties on compositions and fabrication conditions. *Journal of Biomedical Materials Research (Applied Biomaterials)*, 48:235–245, 1999.

[74] Peterson L. H., Jensen R. E., and Parnell J. Mechanical properties of arteries in vivo. *Circulation research*, 8:622–639, 1960.

[75] Mangoni A. A. and Mircoli L. et al. Heart rate-dependence of arterial distensibility in vivo. *J. of Hypertension*, 14:897–901, 1996.

[76] MacWilliams B. A., Hoffman A. H., and Savilonis B.J. Variation of arterial compliance within the cardiac pressure pulse. *J. of Biomechanics*, 31:867–871, 1998.

[77] Seifalian A. M., Giudiceandrea A., Schmitz-Rixen T., and Hamilton G. *Noncompliance: The Silent Acceptance of a Villain*, chapter 2, pages 45–58. 1999.

[78] Conti J. C. and Strope E. R. et al. Frequency dependent radial compliance of latex tubing. *Biomedical Science Instrumentation*, 33:524–529, 1997.

[79] Hayashi K., Handa H., Nagasawa S., Okumura A., and Moritake K. Stiffness and elastic behavior of human intracranial and extracranial arteries. *J. Biomechanics*, 13:175–184, 1980.

[80] Kawasaki T., Sasayama S., Yagi S. I., Asakawa T., and Hirai T. Non-invasive assessment of the age related changes in stiffness and major branches of the human arteries. *Cardiovascular Research*, 21:678–687, 1987.

[81] Binns R. L., Ku D. N., and Stewart M. T. Optimal graft diameter: Effect of wall shear stress on vascular healing. *J. of Vascular Surgery*, 10:326–37, 1989.

[82] Weinberg C. and Bell E. A blood vessel model constructed from collagen and cultured vascular cells. *Science*, 231:397–400, 1986.

[83] L H. N., Paquet S., Labbe R., Germain L., and Auger F. A complete biological tissue-engineered human blood vessel. *FASEB J.*, 12:47–56, 1998.

[84] L H. N., Germain L., and Auger F. Tissue engineering. *Science*, pages 1621–1622, 1999.

[85] De Cooman R., Vandeweerdt P., Berghmans H., and Koningsveld R. Solution spinning of fibres with orientated porosity. *J. Appl. Poly. Science*, 60:1127–1135, 1996.

[86] Zhang Z., Marios Y., Guidoin R. G., Bull P., Marios M., How T., Laroche G., and King M. W. Vascugraft polyurethane arterial prosthesis as femoro-popliteal and femoro-peroneal, structural and chemical analysis of four excised grafts. *Biomaterials*, 18(2), 1997.

[87] Gibson L. J. and Ashby M. F. *Cellular Solids: Structure and Properties*. Pergamon Press, 1988.

[88] Ferry J. D. *Viscoelastic Properties of Polymers*. Wiley, N.Y., 1961.

[89] Hu J. L. and Teng J. G. Computational fabric mechanics: Present status and future trends. *Finite Elements in Analysis and Design*, 21:225–237, 1996.

[90] Hatch K. L. *Textile Science*. West Publishing, N.Y., 1993.

[91] Lai W. M., Rubin D., and Krempl E. *Introduction to Continuum Mechanics*. Pergamon Press, N.Y., 3rd edition, 1993.

[92] Malvern L. E. *Introduction to the Mechanics of a Continuum Medium*. Prentice-Hall, Englewood Cliffs, New Jersey, 1969.

[93] Holzapfel G. A. *Nonlinear Solid Mechanics. A Continuum Approach to Engineering*. John Wiley and Sons, Chichester, 2000.

[94] Hibbit, Karlsson, and Sorensen Inc. *ABAQUS, Version 5.8, Theory Manual*. 1997.

[95] Ogden R. W. *Non-Linear Elastic Deformations*. John Wiley and Sons, N.Y., 1984.

[96] Rivlin R. S. and Saunders D. W. Large elastic deformations of isotropic materials: VII experiments on the deformation of rubber. *Phil. Trans. Roy. Soc. Lond.*, A243:251–288, 1951.

[97] Rivlin R. S. Large elastic deformations of isotropic materials; IV: Further developments of the general theory. *Philos. Trans. Roy. Soc. London Ser.*, A241:379–397, 1948.

[98] Mooney M. A theory for large elastic deformation. *J. Appl. Phys.*, 11:582–597, 1940.

[99] Swanson S. R. A constitutive model for high elongation elastic material. *J. Eng. Mat. Tech. ASME Trans.*, 107:110–114, 1984.

[100] Alexander H. A constitutive relation for rubber-like material. *Int. J. Eng. Sci.*, 6:549–563,

1968.

[101] Gadala M. S. A unified numerical treatment for hyperelastic and rubber-like constitutive laws. *Comm. Appl. Numerical Methods*, 7:581–587, 1991.

[102] Storåkers B. On material representation and constitutive branching in finite compressible elasticity. *Journal of the Mechanics and Physics of Solids*, 34(2):125–145, 1986.

[103] Mehrabadi M. M. and Nemat-Nasser S. Some basic kinematical relations for finite deformations of continua. *Mech. Mater.*, 6:127–138, 1987.

[104] Vaishnav R. N., Young J. T., and Patel D. J. Distribution of stresses and of strains-energy-density through the wall thickness in a canine aortic segment. *Circ. Res.*, 32:577–583, 1973.

[105] Treloar L. R. G. *The Physics of Rubber Elasticity*. Clarendon Press, Oxford, 2nd edition, 1958.

[106] Haas R. Annual report. *National Advisory Committee for Aeronautics, Germany*, 1917.

[107] Peirce F. T. Geometry of cloth structure. *J. Text. Inst.*, 28:T45, 1937.

[108] Kawabata S., Postle R., and Niwa M. Objective specification of fabric quality, mechanical properties and performance. *Textile Machinery Society of Japan*, 1982.

[109] Hu J. L. and Newton A. Modelling of tensile stress-strain curves of woven fabrics. *J. Chin. Text. Univ.*, 10:46–61, 1993.

[110] Hearle J. W. S., Grosberg P., and Backer S. *Structural Mechanics of Fibers, Yarns and Fabrics*, volume 1. Wiley-Interscience, N. Y., 1969.

[111] Grosberg P. *In Structural Mechanics of Fibers, Yarns and Fabrics*. John Wiley Interscience, England, 1969.

[112] Alsawaf F. B. *A Model for Textile Tensile Curves*. PhD thesis, University of Manchester Institute of Science and Technology, 1985.

[113] Hearle J. W. S. and Shanahan W. J. An energy method for calculations in fabric mechanics, parts 1 and 2. *J. Text. Inst.*, 69:81–100, 1978.

[114] Sun W. *Constituitive Modeling of Composites Incorporating Nonlinear and Three Dimensional Effects*. PhD thesis, Drexel University, 1992.

[115] Mathews J. H. *Numerical Methods for Mathematics, Science and Engineering*. Prentice Hall Inc., Englewoods, N.J., 1992.

[116] Bais-Singh S. and Goswami B. C. Theoretical determination of the mechanical behaviour of spun-bound nonwovens. *J. Text. Inst.*, 86:271–288, 1995.

[117] Bais-Singh S. and Goswami B. C. Prediction of the biaxial tensile deformation behavior of spun-bound nonwovens. *Text. Res. J.*, 1997.

[118] Collier J. R., Collier B. J., Toole G. O., and Sargrand S. M. Drape prediction by means of finite element analysis. *J. Text. Inst.*, 82:96–107, 1991.

[119] Kim J. H. *Fabric Mechanics Analysis Using Large Deformation Orthotropic Shell Theory*. PhD thesis, North Carolina State University, 1991.

[120] Gan L., Steven G. P., and Ly N. A finite element analysis of the draping of fabric. *6th Int. Conference on Finite Element Methods, University of Sydney*, pages 402–414, 1991.

[121] Yu W. R., Kang T. J., and Lee J. K. Drape properties of woven fabrics. In *Proc. 2nd Asian Textile Conf.*, pages 455–459, 1993.

[122] Kang T. J., Lee J., Yu W. R., and Oh K. H. Prediction of woven fabric deformation using finite element method. *Proc. Int. Symp. on Fiber Science and Technology, Hong Kong*, pages 480–481, 1994.

[123] British Standards Handbook 11. *Methods of Test for Textiles*, 1974.

[124] Cook R. D., Malkus D. S., and Plesha M. E. *Concepts and Applications of Finite Element Analysis*. John Wiley and Sons, N. Y., 3rd edition, 1989.

[125] Burnett D. S. *Finite Element Analysis*. Addison-Wesley, Reading, 1987.

[126] Crisfield M. A. *Non-Linear Finite Element Analysis of Solids and Structures*, volume 2 Advanced Topics. John Wiley and Sons, N.Y., 1997.

[127] Belytschko T., Liu W. K., and Moran B. *Nonlinear Finite Elements for Continua and Structures*. John Wiley and Sons Ltd. England, 2000.

[128] Lindfield G. and Penny J. *Numerical Methods Using Matlab*. Ellis Horwood, N.Y., 1995.

[129] Ward A. and Seering W. An approach to computational aids for mechanical design. *Proceedings of the International Conference on Engineering Design*, 2:591–598, 1987.

[130] Faires J. D. and Burden R. L. *Numerical Methods*. PWS Publishing, Boston, 1993.

[131] Mitchell M. *An Introduction to Genetic Algorithms*. MIT Press, Cambridge, Massachusetts, 1996.

[132] Dorea C. C. Y. Stopping rules for a random optimisation method. *SIAM Journal of Control and Optimisation*, 28:841–850, 1990.

[133] Zuckerman D. Optimal stopping in a continuous search model. *Journal of Applied Probability*, 23:514–518, 1986.

[134] Holland J. H. *Adaptation in Natural and Artificial Systems*. MIT Press, Cambridge, Massachusetts, second edition, 1992.

[135] Goldberg D. E. *Genetic Algorithms in Search, Optimization, and Machine Learning*. Addison-Wesley, 1989.

[136] Rawlins G. J. E. *Foundations of Genetic Algorithms*. Morgan Kaufmann, San Mateo, CA, 1991.

[137] Akyildiz I. and Shonkwiler R. Simulated annealing for throughput optimization in communication networks with window flow control. *IEEE-ICC Conference Proceedings*, 3:728–738, 1990.

[138] Carlson S. E., Shonkwiler R., and Ingrim M. Component selection using genetic algorithms. *Advances in Design Automation 1993 Proceedings*, 1:471–476, 1993.

[139] Davis L. *Handbook of Genetic Algorithims.* Van Nostrand Reinhold, N.Y., 1991.

[140] Richardson J., Palmer M., Liepins G., and Hilliard M. Some guidelines for genetic algorithms and penalty functions. *Proceedings of the Third International Conference on Genetic Algorithms, San Mateo, CA*, pages 191–197, 1989.

[141] Michalewicz Z. and Janikow C. Z. Handling constraints in genetic algorithms. *Proceedings of the Fourth International Conference on Genetic Algorithms, San Mateo, CA*, pages 151–157, 1991.

[142] Michalewicz Z. A survey of constraint handling techniques in evolutionary computational methods. *Proceedings of the Fourth Annual Conference on Evolutionary Programming, CA*, pages 135–155, 1995.

[143] Powell D. and Skolnick M. Using genetic algorithms in engineering design optimization with non-linear constraints. *Proceedings of the Fifth International Conference on Genetic Algorithms, San Mateo, CA*, pages 426–431, 1993.

[144] Shonkwiler R. and Van Vleck E. Parallel speed-up of monte carlo methods for global optimization. *Journal of Complexity*, 10:64–95, 1994.

[145] Skalak S. C., Shonkewiler R., Babar S., and Aral M. Annealing a genetic algorithm over constraints. *Proceedings of IEEE Systems, CA*, Oct. 11-14, 1998.

[146] Shonkwiler R., Mendivil F., and Deliu A. Genetic algorithms for the 1-d fractal inverse problem. *Proceedings of the Fourth International Conference on Genetic Algorithms, San Mateo, CA*, pages 495–501, 1991.

[147] Liu D. K., Yang Y. L., and Li Q. S. Optimum positioning of actuators in tall buildings using genetic algorithms. *Computers and Structures*, 81:2823–2827, 2003.

[148] Charara J., Ruel J., Lemay J., and Doillon C. J. Development of a flow simulator to study haemodynamic behaviour of natural and artificial blood vessels under physiologic flow conditions. *Journal of Medical Engineering and Technology*, 23(3):83–95, 1999.

[149] Giudiceandrea A., Salacinski H. J., Tai R. M., Punshon G., Hamilton G., and Seifalian A. M. Development and evaluation of an ideal flow circuit: Assessing the dynamic behaviour of endothelial cell seeded grafts. *Journal of Artifical Organs*, 3:16–24, 2000.

[150] Golledge J., Turner R. J., Harley S. L., Springall D. R., and Powell J. T. Development of an in vitro model to study the response of saphenous vein endothelium to pulsatile arterial flow and circumferential deformation. *Eur. J. Vasc. Endovasc. Surg.*, 13:605–612, 1997.

[151] Schima H., Tsangaris S., Zilla P., Kadletz M., and Wolner E. Mechanical simulation of shear stress on the walls of peripheral arteries. *J. Biomechanics*, 23(8):845–851, 1990.

[152] Schima H., Tsangaris S., Zilla P., Fasol R., and Kadletz M. *Simulation of pulsatile wall shear stress in peripheral arteries by means of a mock circulation.*, pages 189–194. Karger, N. Y., 1987.

[153] Law Y. F., Cobbold R. S. C., Johnston K. W., and Bascom P. A. J. Computer-controlled pulsatile pump system for physiological flow simulation. *Medical and Biological Engineering and Computing*, pages 590–595, 1987.

[154] Holdsworth D. W., Rickey D. W., Drangova M., Miller D. J., and Fenster A. Computer-controlled positive displacement pump for physiological flow simulation. *Medical and Biological Engineering and Computing*, pages 565–570, 1991.

[155] Labadie R. F., Antaki J. F., and Williams J. L. et al. Pulsatile perfusion system for ex-vivo investigation of biochemical pathways in intact vascular tissue. *American J. of Physiology*, 270:H760–768, 1996.

[156] Brant A. M., Rodgers V. G. J., and Borovetz H. S. Measurement in-vitro of pulsatile arterial diameter using a helium-neon laser. *J. of Applied Phsiology*, 62(2):679–683, 1987.

[157] Hoeks A. P. G., Brands P. J., Willigers J. M., and Reneman R. S. Non-inavasive measurement of mechanical properties of arteries in health and disease. *Proc. Instn. Mech. Engrs.*, 213(H):195–202, 1999.

[158] Roman M. J., Pini R., Pickering T. G., and Devereux R. B. Non-invasive measurements of arterial compliance in hypertensive compared with normotensive adults. *J. Hypertension*, 10(6):S115–S118, 1992.

[159] Meister J. J., Tardy Y., Stergiopulos N., Hayoz D., Brunner H. R., and Etienne J. D. Non-invasive method for the assessment of non-linear elastic properties and stress of forearm arteries in vivo. *J. Hypertension*, 10(6):S23–S26, 1992.

[160] Stadler R. W., Karl W. C., and Lees R. S. New methods for arterial diameter measurement from b-mode images. *Ultrasound in Medicine and Biology*, 22(1):25–34, 1996.

[161] Giannattasio C., Failla M., and Mangoni A. A. et al. Evaluation of arterial compliance in humans. *Clinical and Experimental Hypertension*, 18(3 and 4):347–362, 1996.

[162] Wu S. M., Shau Y. W., Chong F. C., and Hsieh F. J. Non-invasive assessment of arterial distension waveforms using gradient-based hough transform and power doppler ultrasound imaging. *Medical and Biological Engineering and Computing*, 39:627–632, 2001.

[163] Igo S. R., Meador J. W., and Frazier O. H. Comparitive in vitro evlauations of vascular graft compliance during dynamic loading. *American Society of Artificial Internal Organs Transactions*, 34:785–788, 1988.

[164] Sonoda H., Urayama S. I., Takamizawa K., Nakayama Y., Uyama C., Yasui H., and Matsuda T. Compliant design of artifical graft: Compliance determination by new digital x-ray imaging system-based method. *Journal of Biomedical Materials Research*, 60:191–195, 2002.

[165] Stok W., De Groot E., Kastelein J.J.P., and Karemaker J.M. M-mode ultrasound imaging of arterial wall movement and arterial wall thickness of distal carotid arteries in atherosclerosis atudies. In *Abstract to the 4th Pulse Wave Analysis Congress*, London 2001.

[166] Murgo J. P., Cox R. H., and Peterson L. H. Cantilever transducer for continuous measurement of arterial diameter in-vivo. *J. of Applied Physiology*, 31(6):948–953, 1971.

[167] American National Standard Association for the Advancement of Medical Instrumentation. *Cardiovascular Implants - Vascular Prosthesis*, aami standard edition, 1994.

[168] ISO International Standard 7198. *Cardiovascular Implants-Tubular Vascular Prosthesis*, 1998.

[169] Hibbit, Karlsson, and Sorensen Inc. *ABAQUS, Version 5.8, Users Manual*, volume I. 1997.

[170] Hibbit, Karlsson, and Sorensen Inc. *ABAQUS, Version 5.8, Users Manual*, volume II. 1997.

[171] Hibbit, Karlsson, and Sorensen Inc. *ABAQUS, Version 5.8, Users Manual*, volume III. 1997.

[172] Writing UMATs and VUMATs. In *ABAQUS User's Conference*, Newport, Rhode Island, 1996. Hibbitt, Karlsson and Sorensen, Inc.

[173] Swokowski E.W. *Calculus with Analytic Geometry*. Prindle, Weber and Schmidt Publishers, third edition, 1984.

[174] Gamble J., Matthias L., Meyer G., Kaur P., Russ G., Faull R., Berndt M, and Vadas M. Regulation of in vitro capillary tube formation by anti-intergrin antibodies. *J. Cell Biol.*, 121(4):931–943, 1993.

[175] Kline S. J. and McClintock F. A. Describing uncertainties in single-sample experiments. *Mech. Eng.*, page 3, 1953.

[176] National Institute of Health, Publication no. 86-23. *Guide for the Care and Use of Laboratory Animals*, Bethesda, Maryland, USA, 1985.

[177] Gadala M. S. Recent advances in numerical modeling of constitutive relations. *Finite Element in Analysis and Design*, 24:171–185, 1997.

[178] Holzapfel G. A., Gasser T. C., and Ogden R. W. A new constitutive framework for arterial wall mechanics and a comparitive study of material models. *Journal of Elasticity*, 61:1–48, 2000.

Appendix A

Mesh Sensitivity Analysis Results

A.1 Graft parametric study results

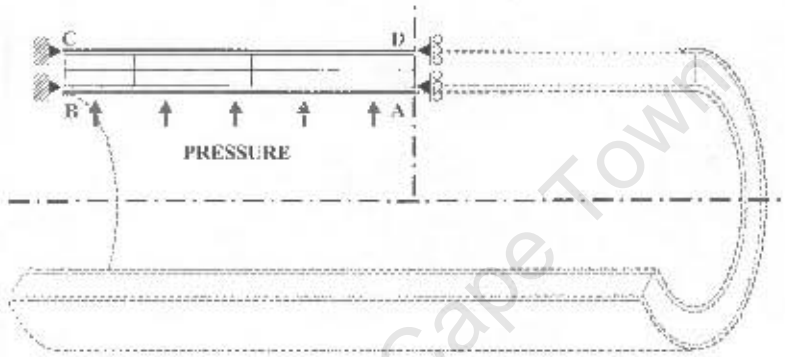

Figure A.1: Schematic of graft numerical model and critical points used in parametric study

			Model	A	B	C	D	L	I	G	H
			Mesh	[illegible]	[illegible]	[illegible]	[illegible]	[illegible]	[illegible]	[illegible]	[illegible]
			Elements #	193	213	306	474	529	616	799	2000
			Difference	0	10	30	174	192	198	300	1384
Material	Point	Description									
Porous Polymer Graft	A	S22	Circumferential	17240	47071	44089	10142	40197	48004	48284	48780
		S11	Axial	28900	05100	29105	20224	28220	29088	[illegible]	[illegible]
		S33	Radial	-41806	-41955	-41458	-41673	-41835	[illegible]	[illegible]	[illegible]
		S12	Shear	6.01E-03	9.9E-02	5.96E-04	5.5E-04	5.79E-04	1.43E-04	3.03E-04	3.03E-04
	B	S22	Circumferential	28847	28845	29007	28334	29007	28966	28961	[illegible]
		S11	Axial	30 [illegible]	[illegible]	[illegible]	30713	30782	30966	30[illegible]	[illegible]
		S33	Radial	5241	1440	1447	1405	1419	1347	[illegible]	[illegible]
		S12	Shear	1.09E-03	6.35E-05	1.70E-04	1.10E-04	1.67E-04	4.96E-05	4.30E-05	4.11E-05
	C	S22	Circumferential	7.0	4230	4304	1029	-1021	332	4328	4071
		S11	Axial	38259	41[illegible]	[illegible]	47000	47008	51346	51977	133080
		S33	Radial	[illegible]	[illegible]	[illegible]	5[illegible]	[illegible]	[illegible]	[illegible]	[illegible]
		S12	Shear	15269	9.43E-[illegible]	3.[illegible]	4.313	-8.271	[illegible]	-12.543	8.351
	D	S22	Circumferential	3[illegible]	[illegible]	[illegible]	[illegible]	[illegible]	[illegible]	[illegible]	[illegible]
		S11	Axial	34[illegible]	3[illegible]	[illegible]	2[illegible]	[illegible]	2[illegible]	2[illegible]	[illegible]
		S33	Radial	4[illegible]	3847	[illegible]	341	3414	3106	3[illegible]	92
		S12	Shear	16.848	[illegible]	[illegible]	6.320	7.270	6.243	6.655	-2.344
Fabric Reinforcing	C	S22	Circumferential	2[illegible]	[illegible]	[illegible]	27[illegible]	27[illegible]	27[illegible]	27[illegible]	[illegible]
		S11	Axial	2[illegible]	[illegible]	[illegible]	[illegible]	2[illegible]	[illegible]	[illegible]	[illegible]
		S12	Shear	-1.11E-01	[illegible]	[illegible]	-7.07E-04	-8.51E-04	-1.81E-04	[illegible]	[illegible]
	D	S22	Circumferential	3148	[illegible]	2[illegible]	2[illegible]	2[illegible]	2[illegible]	2[illegible]	[illegible]
		S11	Axial	17[illegible]	[illegible]	8[illegible]	8[illegible]	[illegible]	[illegible]	[illegible]	[illegible]
		S12	Shear	[illegible]	[illegible]	[illegible]	[illegible]	[illegible]	[illegible]	[illegible]	[illegible]
	Other	Pressure	kPa	[illegible]	[illegible]	[illegible]	[illegible]	[illegible]	[illegible]	[illegible]	[illegible]
		Strain Energy	J	[illegible]	3.87[illegible]	3.877	3.877	3.877	3.876	3.876	3.876
		Von Mises Stress	kPa	4.[illegible]	[illegible]	[illegible]	4.328	4.328	4.330	4.337	4.332
		CPU Time	[illegible]	[illegible]	[illegible]	[illegible]	[illegible]	[illegible]	[illegible]	[illegible]	[illegible]
% Differences to 2000 Element Model	A-Graft	S22	%	3.[illegible]	[illegible]	[illegible]	1.[illegible]	1.[illegible]	0.[illegible]	0.[illegible]	-
		S11	%	[illegible]	[illegible]	[illegible]	1.[illegible]	1.[illegible]	0.[illegible]	0.[illegible]	-
		S33	%	[illegible]	[illegible]	[illegible]	[illegible]	0.[illegible]	[illegible]	[illegible]	-
	C-Fabric	S22	%	[illegible]	[illegible]	[illegible]	0.[illegible]	0.[illegible]	0.[illegible]	[illegible]	
		S11	%	.97	[illegible]	[illegible]	[illegible]	0.[illegible]	[illegible]	0.[illegible]	-
	Other	Pressure	%	[illegible]	[illegible]	[illegible]	[illegible]	0.[illegible]	0.[illegible]	0.[illegible]	
		Strain Energy	%	3.[illegible]	[illegible]	[illegible]	0.[illegible]	0.[illegible]	0.[illegible]	0.[illegible]	

Table A.1: Graft model parametric study results

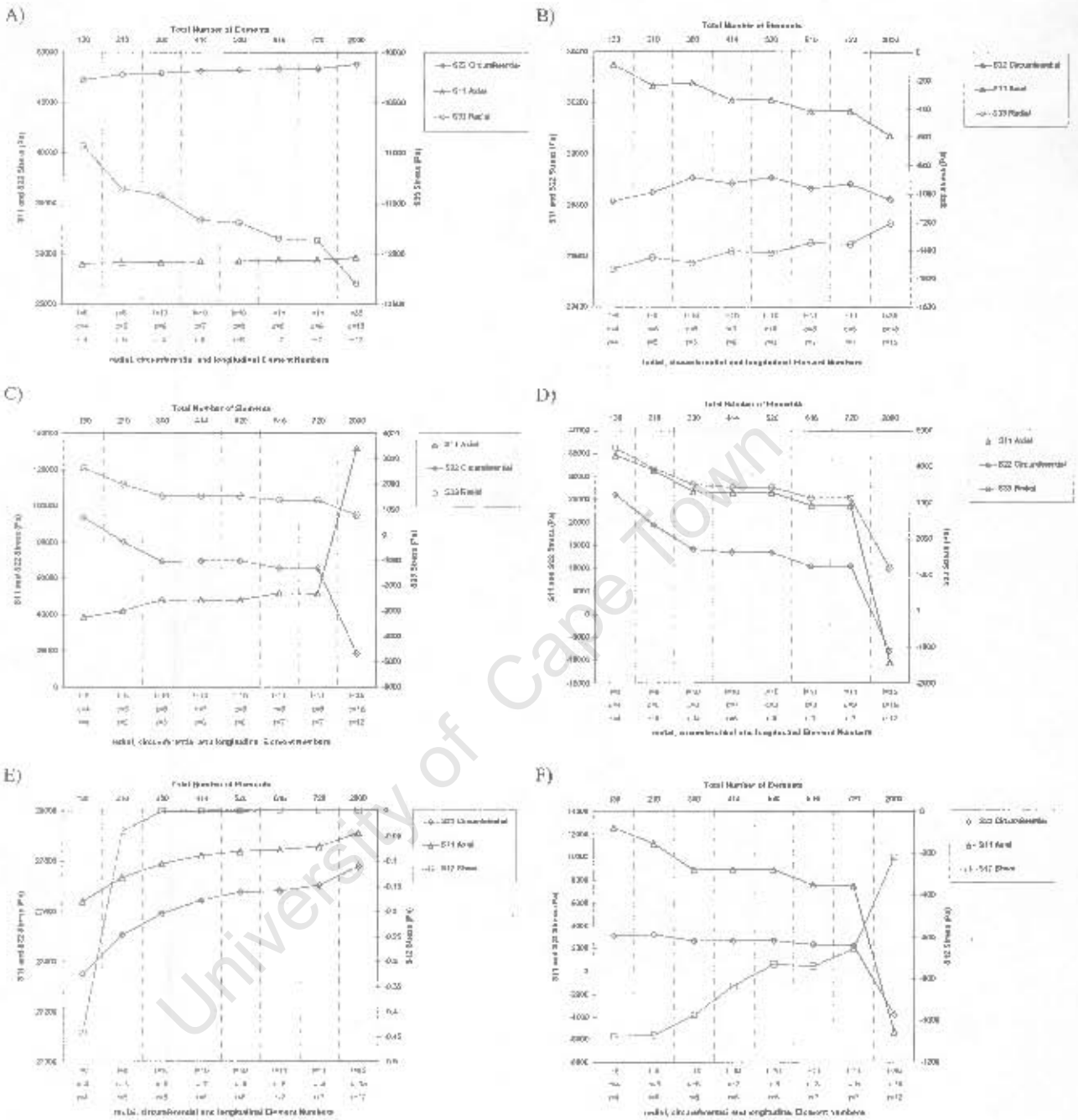

Figure A.2: Variation in graft numerical model stress values at critical points: (a) point A^G, (b) point B^G, (c) point C^G, (d) point D^G, (e) point C^F and (f) point D^F with increased element numbers

A.2 Uniaxial tensile model parametric study results

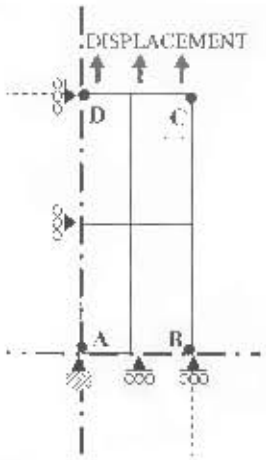

Figure A.3: Schematic of uniaxial tensile numerical model and critical points used in parametric study

			Model	A	B	C	D	E	F	G	H
			Mesh	x=5 y=15	x=7 y=14	x=9 y=7	x=10 y=20	x=11 y=28	x=12 y=24	x=13 y=27	x=24 y=50
			Local Mesh	x=2 y=2	x=3 y=3	x=3 y=2	x=3 y=4	x=4 y=3	x=3 y=4	x=5 y=5	x=10 y=11
			Element #	60	98	153	270	378	392	561	1200
			Difference	0	45	55	47	75	42	98	972
Material	Point	Description									
Fabric	A	S22	Axial	1409.0	1440.0	2480.0	2452.0	3461.0	3480.0	2479.0	2479.0
		S11	Transverse	1.0	11.7	11.0	11.5	11.0	11.7	11.4	11.3
		S12	Shear	0.352	0.372	0.023	0.014	0.020	0.020	0.010	0.001
	B	S22	Axial	2050.0	2067.7	2075.0	2075.0	2072.0	2071.0	2071.0	2071.0
		S11	Transverse	-44.0	-44.0	-43.7	-43.5	-43.7	-43.8	-43.7	-43.7
		S12	Shear	9.6	9.7	9.5	9.6	9.9	9.9	9.8	9.8
	C	S22	Axial	1540.0	1730.0	1434.0	1437.0	1416.0	1407.0	1426.0	1376.0
		S11	Transverse	-3.0	-42.4	-41.7	-41.6	-41.5	-41.5	-41.5	-39.8
		S12	Shear	-42.527	-41.349	-41.5	-41.6	-41.5	-41.5	-41.5	-41.2
	D	S22	Axial	1047.35	1126.78	1031.01	1031.01	1026.0	1026.0	1027.0	1027.0
		S11	Transverse	2.1417	3.0.3.1	3.0.3.1	3.0.3.1	3.0.3.1	3.0.3.1	3.0.3.1	3.0.3.1
		S12	Shear	3.0.3.1	3.0.3.1	3.0.3.1	3.0.3.1	3.0.3.1	3.0.3.1	3.0.3.1	3.0.3.1
	Other	Force/Length	N/m	30.173	30.525	30.675	31.167	31.736	31.170	31.170	31.170
		U1 @ Local Point	m	12.754	12.754	12.754	12.754	12.754	12.754	12.754	12.754
		U2 @ Local Point	m	-3.125	-3.125	-3.125	-3.125	-3.125	-3.125	-3.125	-3.125
	CPU Time		s	1.204	1.156	1.344	1.156	1.203	1.156	1.203	1.203
% Differences to 1200 Element Model	A	S22	%	40.81	40.49	41.29	41.17	41.36	41.36	41.01	-
		S11	%	-7.28	-4.91	-3.07	-1.97	-2.43	-1.74	-1.91	-
		S12	%	-82.607	-61.631	-38.61	-39.1	-17.13	-15.9	-1.572	-
	B	S22	%	-0.47	-0.27	-0.16	-0.13	0.03	0.02	0.02	-
		S11	%	3.03	1.16	0.2	1.67	0.74	0.4	0.7	-
		S12	%	-0.60.24	-3.01	-2.35	-0.33	-0.39	-0.19	-0.14	-
	Other	Force/Length	%	8.40	4.22	4.20	5.82	3.91	1.50	-0.12	-
		U1 @ Local Point	%	0.73	0.00	-0.01	0.00	0.00	0.00	0.00	
		U2 @ Local Point	%	-4.17	-0.12	-0.08	-0.16	-0.08	-0.08	-0.08	

Table A.2: Uniaxial tensile model parametric study results

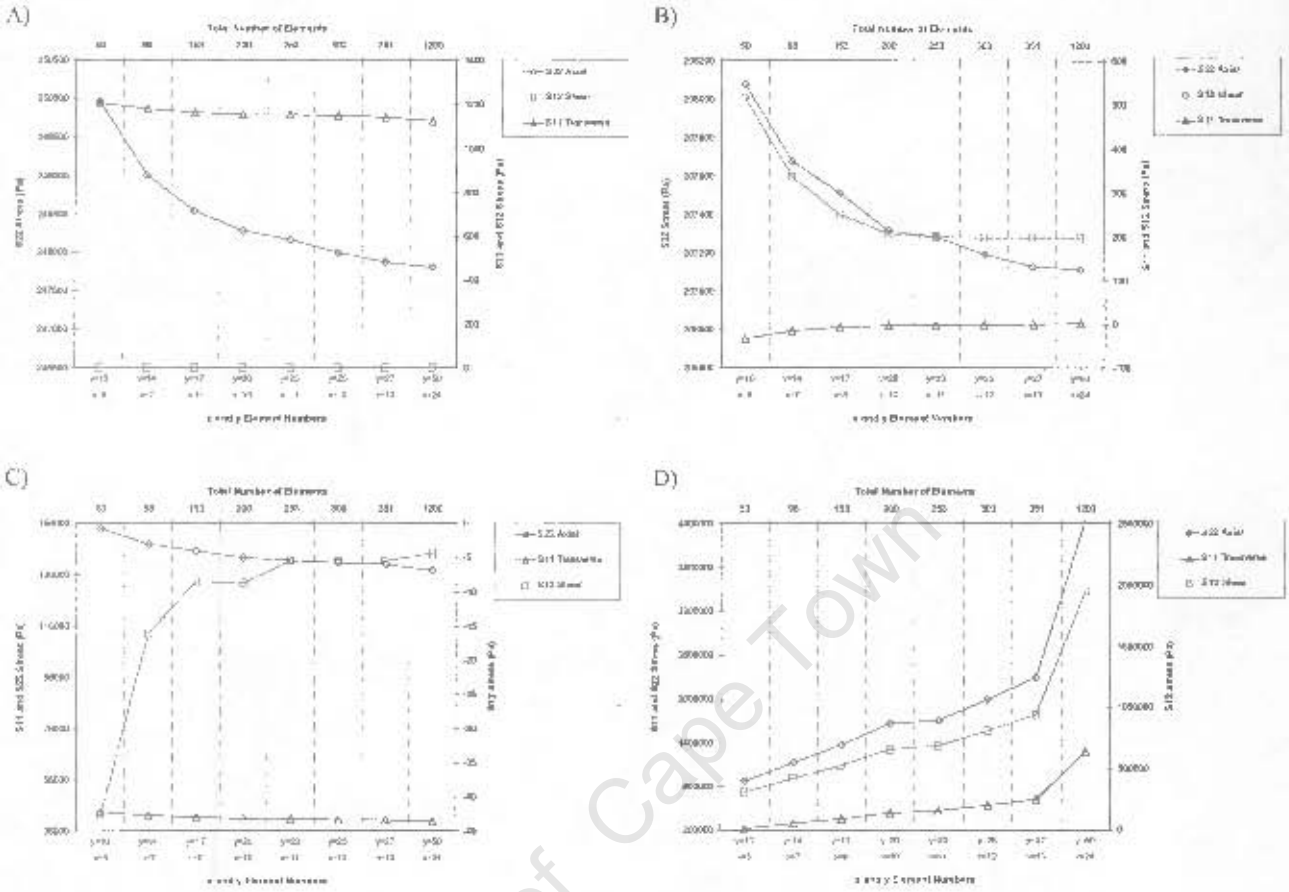

Figure A.4: Variation in uniaxial tensile numerical model stress values at critical points; (a) point A^F, (b) point B^F, (c) point C^F and (d) point D^F with increased element numbers

A.3 Circumferential tensile model parametric study results

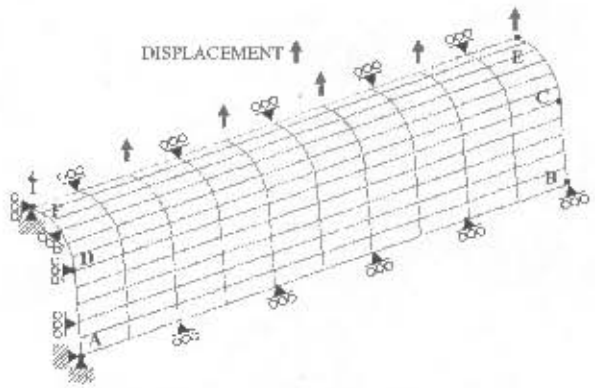

Figure A.5: Schematic of circumferential tensile numerical model and critical points used in parametric study

			Model	A	B	C	E	G	I	J
			Mesh	n=4 e=2 l=5	n=7 e=6 l=10	n=10 e=16 l=10	n=10 e=15 l=20	n=14 e=16 l=28	n=20 e=24 l=28	n=28 e=30 l=39
			Elements	20	100	200	320	600	800	1856
			Difference	0	80	100	320	80	200	1056
Material	Point	Description								
Fabric	A	σ_{22}	Circumferential	59215	61301	58024	54384	54400	54400	53745
		σ_{11}	Axial	7284	8471	8170	8028	8210	8196	7786
		σ_{12}	Shear	1053	1228	640	852	0	0	144
	B	σ_{22}	Circumferential	22132	21804	21696	21050	21000	21000	20540
		σ_{11}	Axial	3214	3716	3971	4167	4140	4140	4246
		σ_{12}	Shear	1547	1734	1388	1440	1440	1440	1477
	C	σ_{22}	Circumferential	64660	64784	62336	62115	62145	62220	62168
		σ_{11}	Axial	7801	10870	11431	10200	11000	11000	10844
		σ_{12}	Shear	2145	4152	4302	4238	4238	4241	4274
	D	σ_{22}	Circumferential	60748	61279	60030	62204	62200	62204	62139
		σ_{11}	Axial	7202	9967	10674	11400	11400	11400	11340
		σ_{12}	Shear	-3.38E-02	-3.97E-02	-4.02E-04	-1.08E-04	-4.04E-05	-4.97E-05	-8.89E-05
	F	σ_{22}	Circumferential	36371	37042	36800	36409	36407	36396	36386
		σ_{11}	Axial	7401	12550	12764	12646	12569	12512	12155
		σ_{12}	Shear	2.16E-02	-1.31E-03	2.28E-04	-1.19E-03	-1.16E-05	-4.05E-01	6.12E-04
	I	σ_{22}	Circumferential	47086	48376	46035	38660	42172	41998	40972
		σ_{11}	Axial	9400	10537	9221	9155	9141	9251	9258
		σ_{12}	Shear	3027	3037	3585	3408	3799	3721	3761
	Other	Fibre Length	L_f	5.154	5.312	5.647	5.815	5.694	5.845	5.945
		Fibre Length Standard Deviation	σ_{L_f}	4.8...	4.9...	1.91...	2.0...	1.9...	1.9...	1.9...
		Void Fraction	V_f	7.4...	7.5...	7.7...	7.7...	7.7...	7.7...	7.7...
	CPU Time									
Direction										
% Difference to 1056 Element Model	A	σ_{22}	%	1.60	1.62	1.93	1.41	1.4...	1.3...	
		σ_{11}	%	1.0e+27	1.0e+27	7.0E-01	5.3E-02	7.5E-04	2.0E-03	
		σ_{12}	%	1647.01	1.1e+4	1.1e+4	6.7E-01	6.2E-01	1.1e+4	
	B	σ_{22}	%	39.85	37.71	36.82	31.04	31.50	31.50	
		σ_{11}	%	1.0e+27	4.3E-02	4.1e+15	2.7E-15	2.8E-30	2.8E-31	
		σ_{12}	%	1894.59	1656.73	1200.10	1183.70	1.2E-03	4.7E-04	
	Other	Fibre Length	%	8.54	8.61	9.02	10.02	9.71	9.91	
		Fibre Length Standard Deviation	%	6.09	6.20	1.70	1.68	1.68	1.68	
		Void Fraction	%	11.38	2.61	2.30	1.19	1.19	1.19	

Table A.3: Circumferential tensile model parametric study results

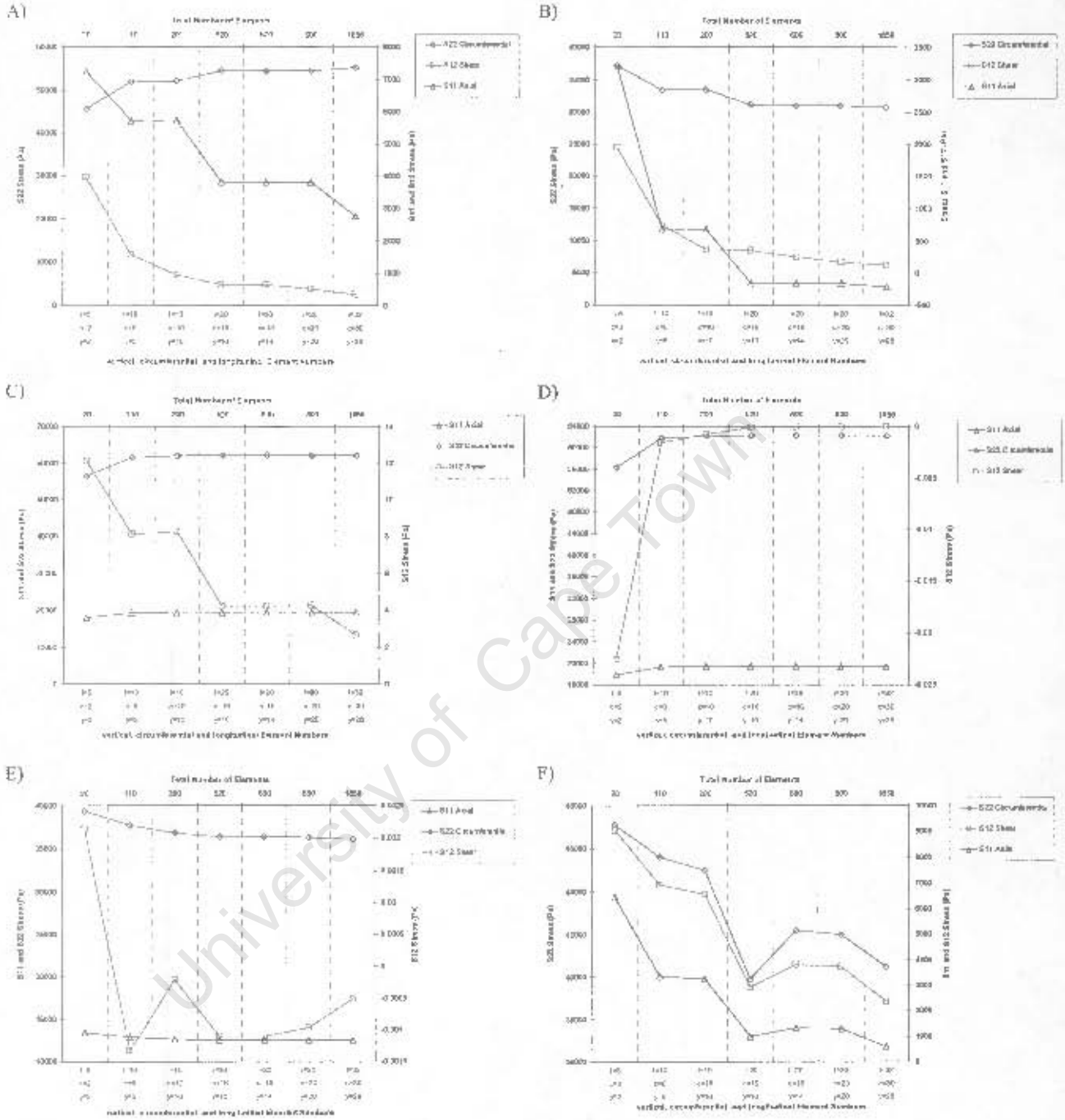

Figure A.6: Variation in circumferential tensile numerical model stress values at critical points; (a) point A^F, (b) point B^F, (c) point C^F, (d) point D^F, (e) point E^F and (f) point F^F with increased element numbers

A.4 Longitudinal tensile model parametric study results

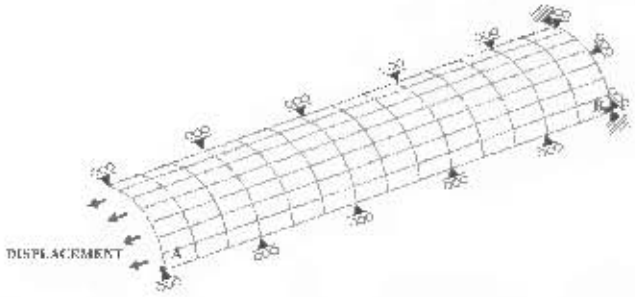

Figure A.7: Schematic of longitudinal tensile numerical model and critical points used in parametric study

			Model	A	B	C	D	E	F	G	H
			Mesh	c=4 l=15	c=10 l=20	c=12 l=25	c=14 l=26	c=16 l=30	c=17 l=35	c=18 l=38	c=20 l=40
			Element #	98	200	300	392	480	585	684	1020
			Difference	0	102	100	92	88	105	204	2035
Material	Point	Description									
Fabric	A	S22	Circumferential	2760.07	2731.85	2707.60	2.69E+03	2.68E+03	2.66E+03	2.65E+03	2.64E+03
		S11	Longitudinal	1.31E+03	1.31E+03	1.30E+03	1.30E+03	1.29E+03	1.29E+03	1.28E+03	1.28E+03
		S12	Shear	20.65	20.50	20.39	20.31	17.83	16.58	15.69	7.31
	B	S22	Circumferential	3003	3002	3.00E+03	3095	3097	3096	3.09E+03	3.09E+03
		S11	Longitudinal	2.10E+03	2.10E+03	2.10E+03	2.10E+03	2.10E+03	2.10E+03	2.10E+03	2.10E+03
		S12	Shear	106.42	66.89	42.41	33.07	27.74	23.37	19.48	4.17
	Other	Principal stress	%	82.27	84.11	84.87	85.04	85.28	85.68	86.02	87.36
		Axial Strain	%	30	40	40	40	40	40	40	30
		Circumferential Strain	%	-58.149	-58.34	-58.048	-58.036	-58.028	-58.019	-58.015	-58.034
	CPU Time			1.764	2.418	3.009	3.420	3.972	4.512	5.208	8.184
Deviation											
% Differences to 2605 Element Model	A	S22	%	-2.36	-1.93	-1.03	-0.23	0.23	0.53	0.71	
		S11	%	27.1%	-20.26	-13.4%	-10.2%	-11.4%	-10.4%	-9.1%	-
		S12	%	426.2%	225.3%	97.4%	58.0%	16.6%	128.7%	125.7%	-
	B	S22	%	0.4%	0.1%	0.1%	0.0%	0.0%	0.0%	0.0%	-
		S11	%	-0.5%	-0.2%	0.0%	0.0%	0.0%	0.0%	0.0%	
		S12	%	417.6%	229.4%	106.3%	71.0%	36.0%	43.8%	50.0%	
	Other	Principal stress	%	0.02	0.01	0.00	0.00	0.00	0.00	0.00	
		Axial Strain	%	0.00	0.00	0.00	0.00	0.00	0.00	0.00	
		Circumferential Strain	%	0.41	0.26	0.07	0.01	0.01	0.02	0.03	-

Table A.4: Longitudinal tensile model parametric study results

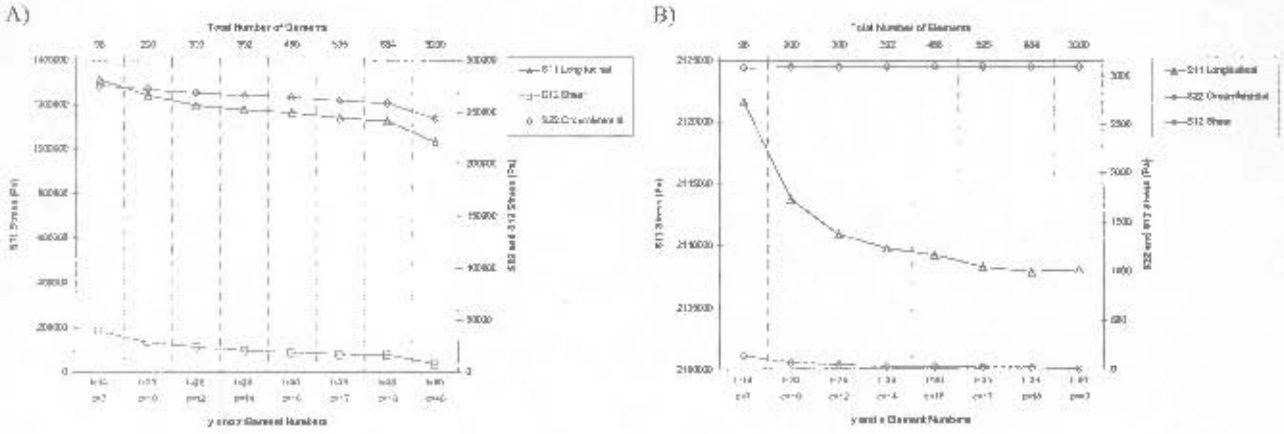

Figure A.8: Variation in longitudinal tensile numerical model stress values at critical points; (a) point A^F and (b) point B^F with increased element numbers

Appendix B

Fabric Patch Test Results

B.1 Fabric single element fabric model parameter changes

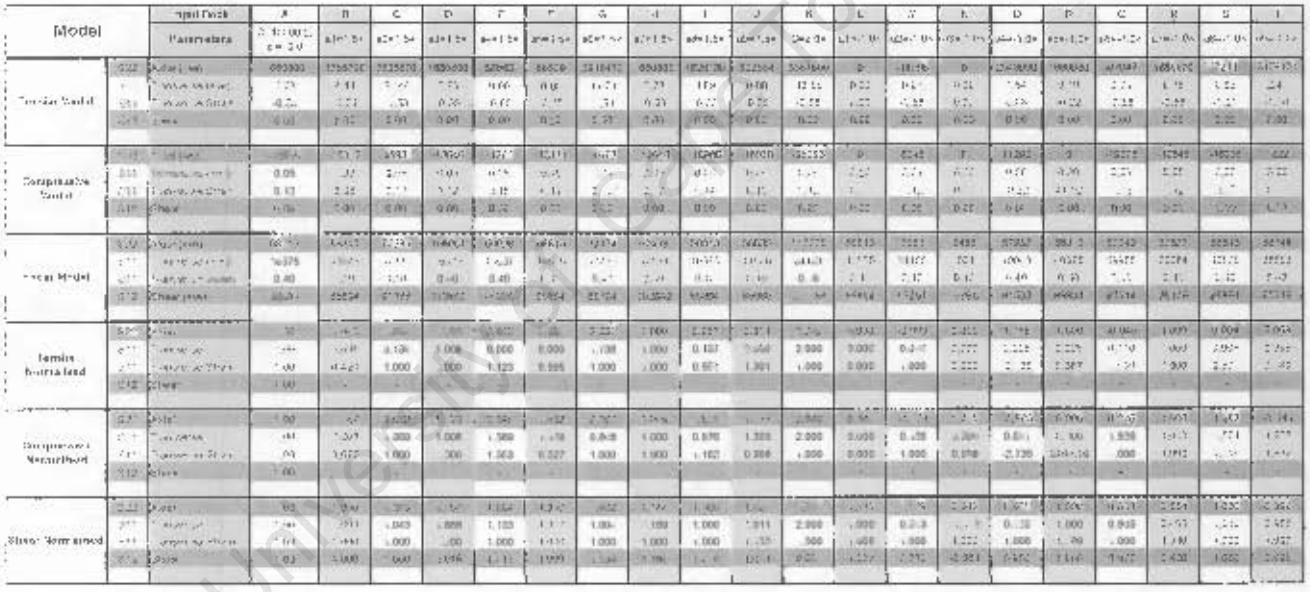

Table B.1: Fabric model patch test results with variation in model coefficents

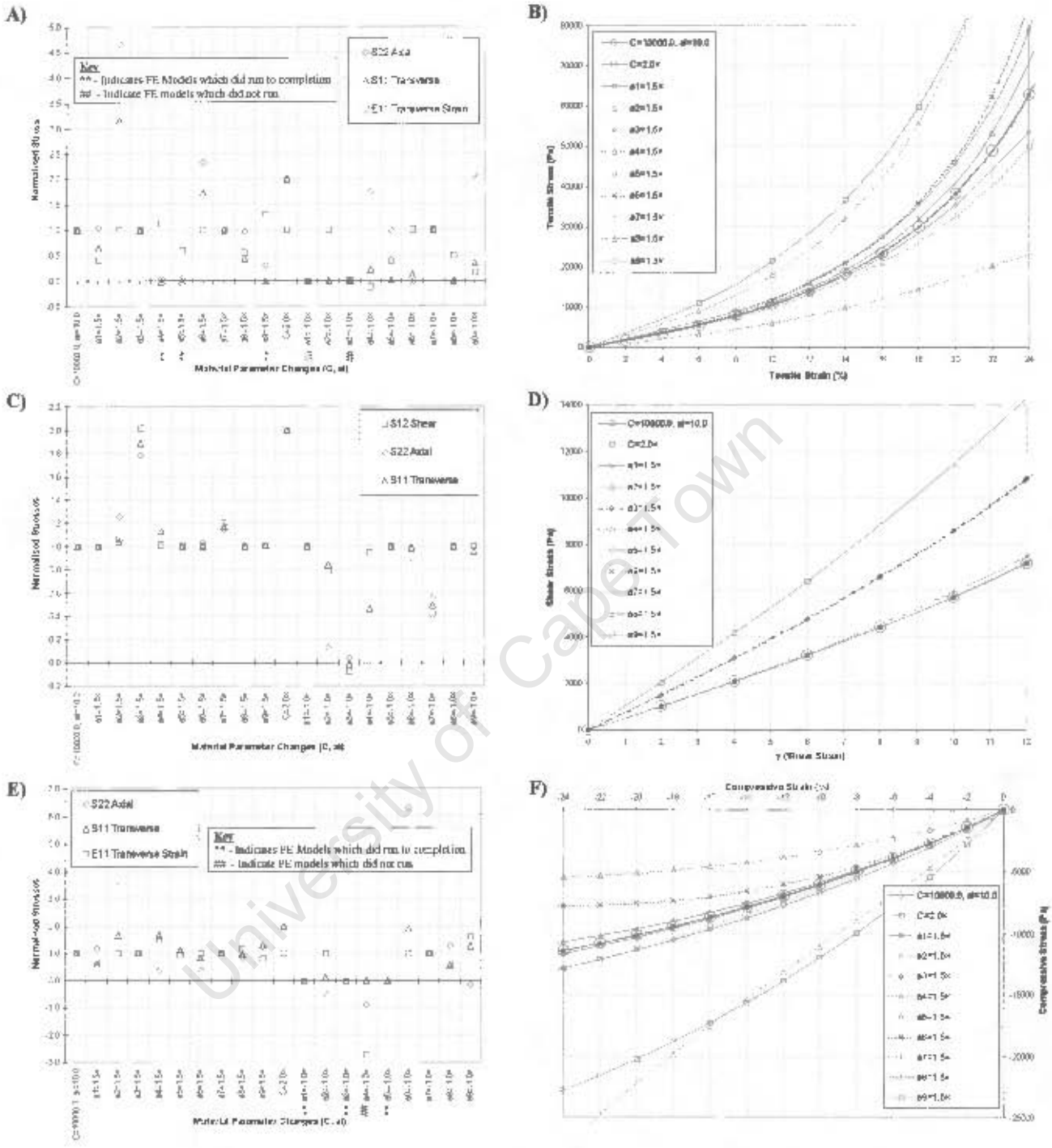

Figure B.1: Fabric coefficient variation patch test results; (a), (c) and (e) normalised variation of stress and strains with coefficient variation for tensile, shear and compressive models respectively. (b), (d) and (f), corresponding graphs

Appendix C

GA2 Uniaxial Tensile Model Results vs. Test Data and SEM Images

C.1 SEM images of uniaxial tensile fabric samples

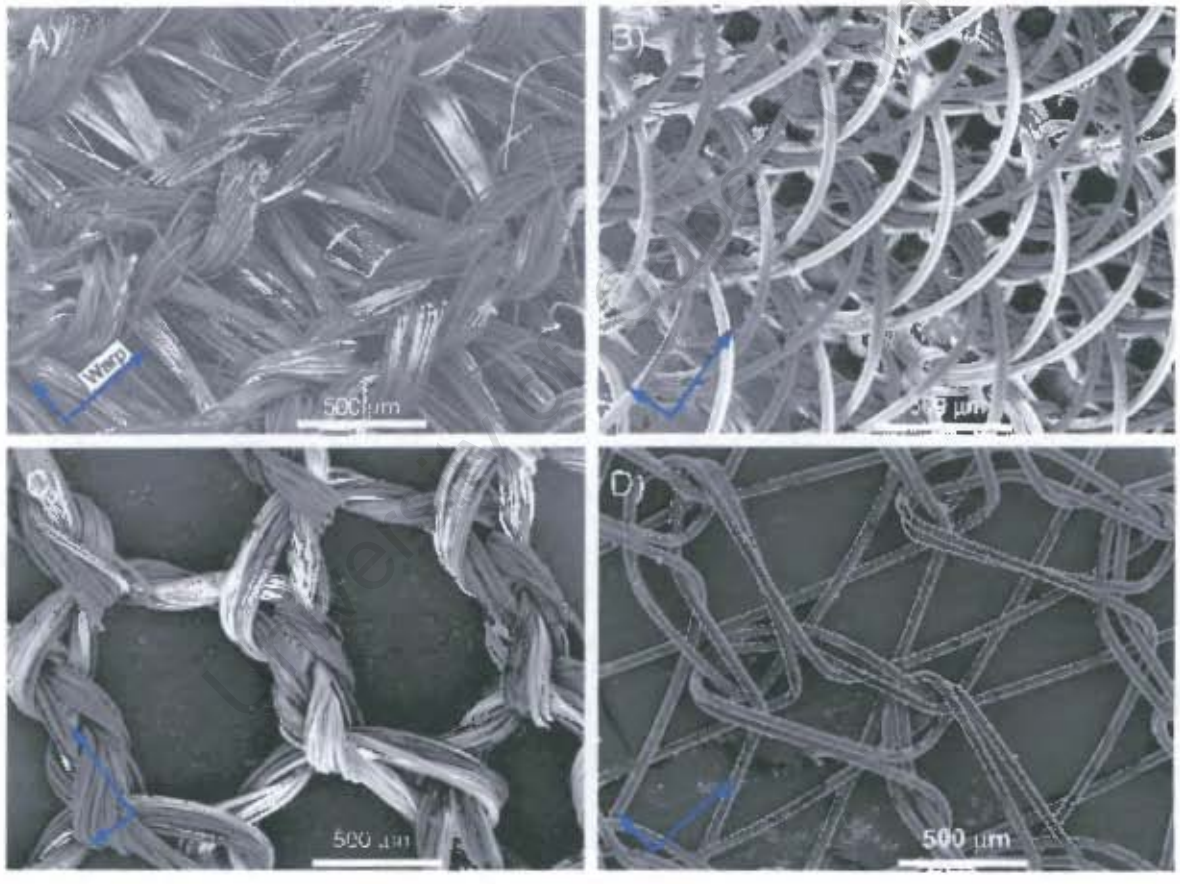

Figure C.1: SEM images (50×) of uniaxial tensile fabric test samples; (a) sample 1: basic warp knit, (b) sample 2: warp knit with Lycra® support, (c) sample 3: coarse warp knit and (d) sample 4: monofilament warp knit (Arrows indicate warp/weft direction)

C.2 Uniaxial tensile test vs. numerical model data

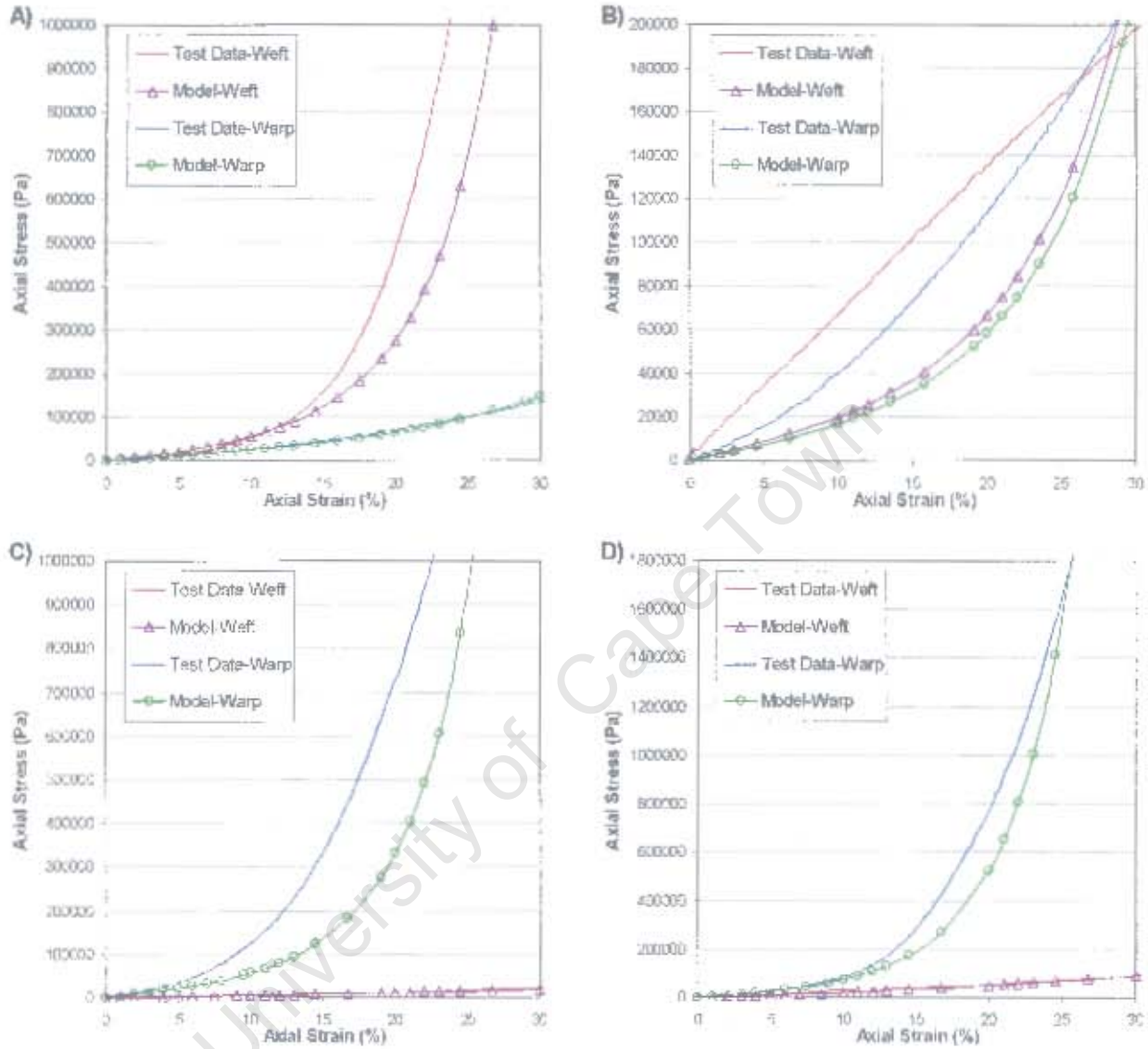

Figure C.2: Uniaxial tensile test data vs. numerical model data for; (a) sample 1, (b) sample 2, (c) sample 3 and (d) sample 4

C.3 Transverse strain vs. numerical model data

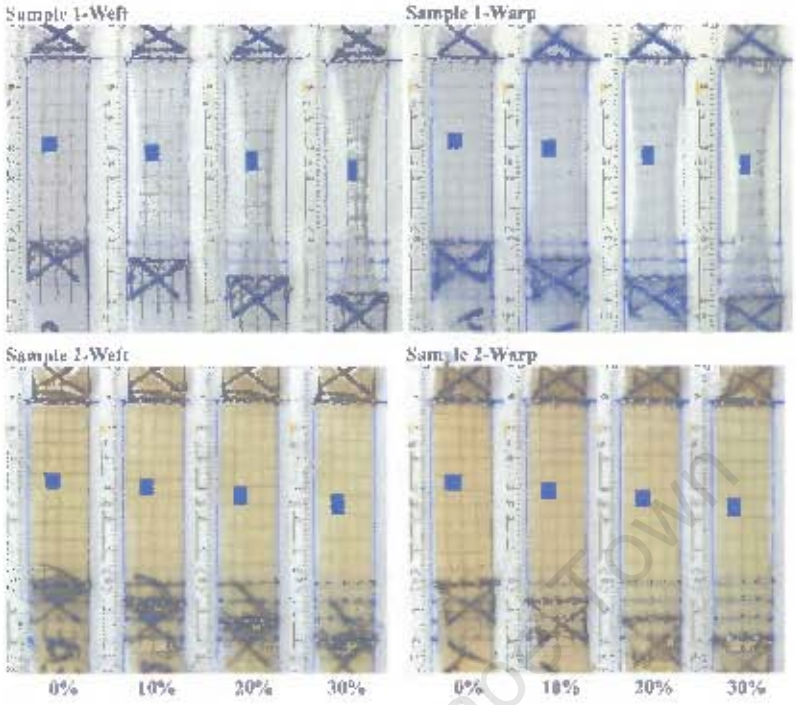

Figure C.3: Transverse strain vs. axial strain images for uniaxial fabric samples 1 and 2 in the weft and warp directions

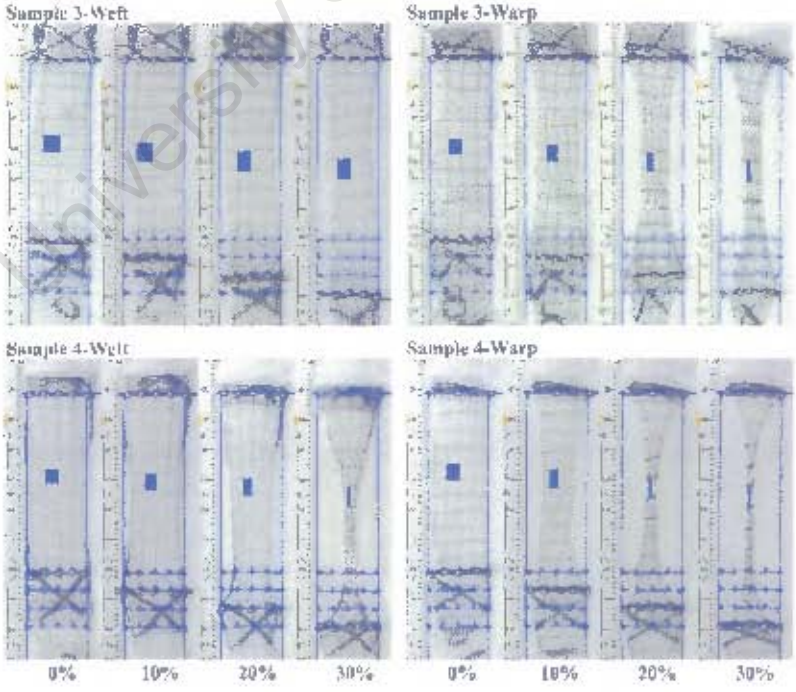

Figure C.4: Transverse strain vs. axial strain images for uniaxial fabric samples 3 and 4 in the weft and warp directions

Sample	Fabric Direction	Axial Strain 0%	7%	27%	37%
1	Weft	0.0	-11.2	-28.3	-44.7
	Warp	0.0	-5.6	16.7	-30.6
2	Weft	0.0	-5.3	10.7	-15.8
	Warp	0.0	-5.1	-10.3	-15.4
3	Weft	0.0	-9.5	-16.7	-23.8
	Warp	0.0	-26.5	-47.1	-64.7
4	Weft	0.0	-19.4	-44.4	-77.8
	Warp	0.0	-39.4	-66.7	87.9

Table C.1: Transverse strain vs. axial strain for localised grid on fabric samples

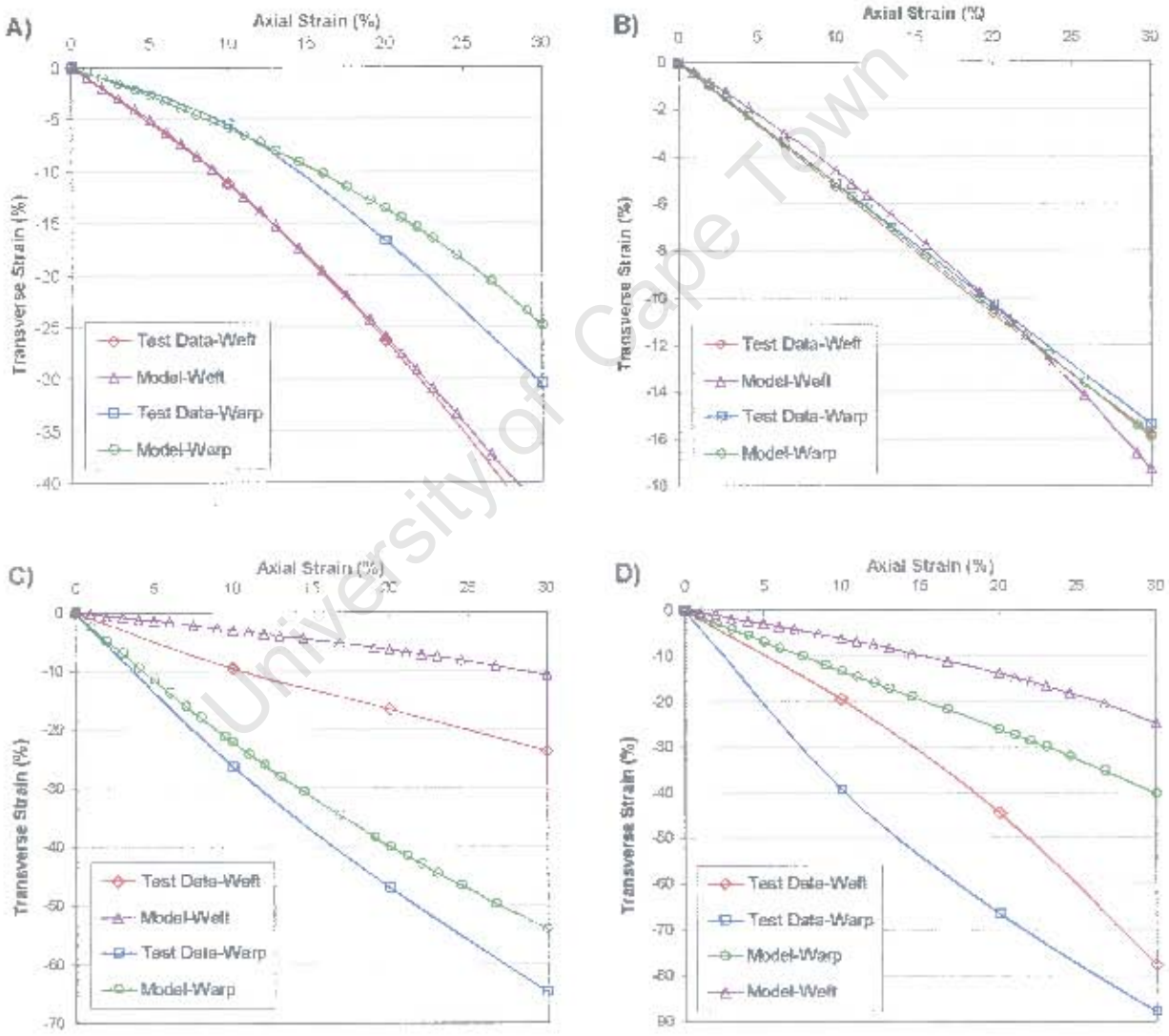

Figure C.5: Transverse strain data vs. numerical model data for; (a) sample 1, (b) sample 2, (c) sample 3 and (d) sample 4

Appendix D

GA1 Optimised Adventitial Reinforced Graft Results

D.1 Dynamic data

D.1.1 90-106 μm pore sized graft structures

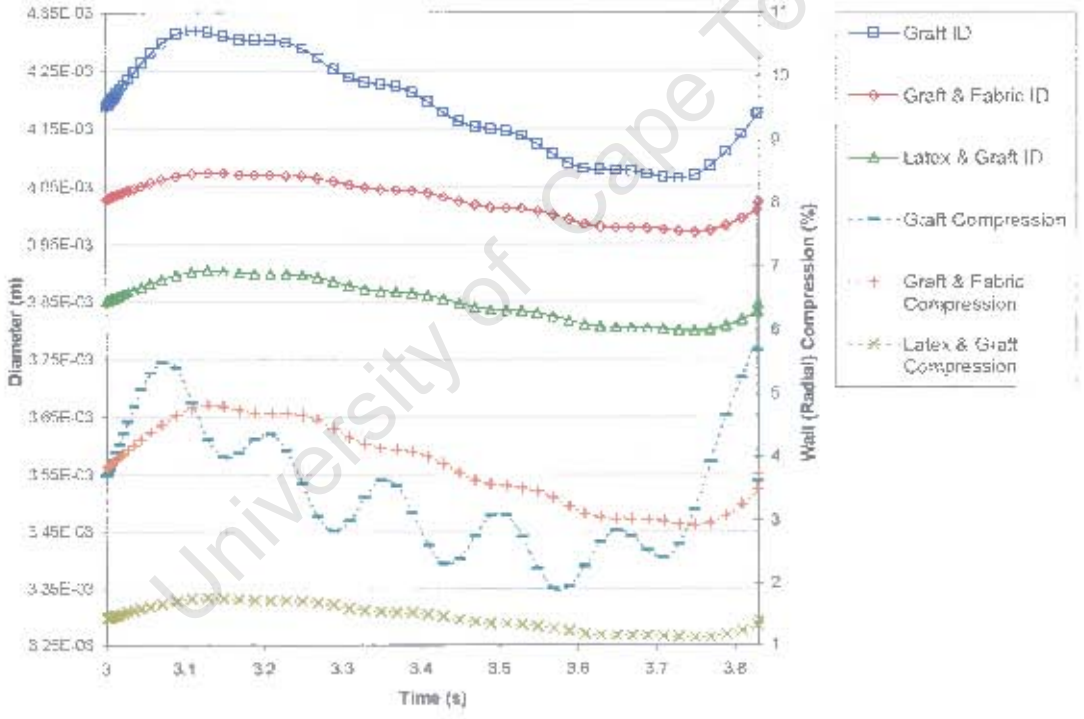

Figure D.1: Internal diameter and wall compression curves vs. time obtained during dynamic pressure step for 90-106 μm pore sized graft, graft and fabric with graft with latex

Graft Type		Graft		Graft & Fabric 1		Graft & Fabric 2		Graft & Fabric 3		Graft & Latex		Graft & Latex & Fabric	
Description	Units	Internal D	External D	Internal D	External D	Internal D	External D	Internal D	External D	Internal D	External D	Internal D	External D
Initial Diameter	mm	5.00	5.20	4.84	5.00	5.00	5.20	5.00	5.20	5.00	5.20	5.00	5.20
Diastol													
Pressure	mmHg	80.4		80.4		80.4		80.4		80.4		80.4	
Diameter	mm	4.06	5.43	3.97	5.53	3.98	5.34	3.98	5.34	3.80	5.18	3.78	5.18
Wall Compression	%	1.81		2.93		2.81		2.91		1.13		1.21	
Fabric Circumferential Strain	%	8.50		8.51		8.85		8.84		3.87		3.91	
Systol													
Pressure	mmHg	119.8		119.8		119.8		119.8		119.8		119.8	
Diameter	mm	4.10	5.66	4.07	5.41	4.10	5.48	4.09	5.47	3.90	5.28	3.89	5.26
Wall Compression	%	5.68		4.80		4.80		4.81		1.76		1.93	
Fabric Circumferential Strain	%	13.73		8.15		8.67		8.43		5.09		5.23	
Compliance	%/(mmHg)	16.62	10.86	2.50	3.45	7.10	4.02	4.75	3.79	7.03	4.72	5.49	4.21

Table D.1: Compliance, diameter and fabric circumferential strain values at diastolic and systolic pressures for 90-106um composite grafts

D.1.2 106-125 μm pore sized graft structures

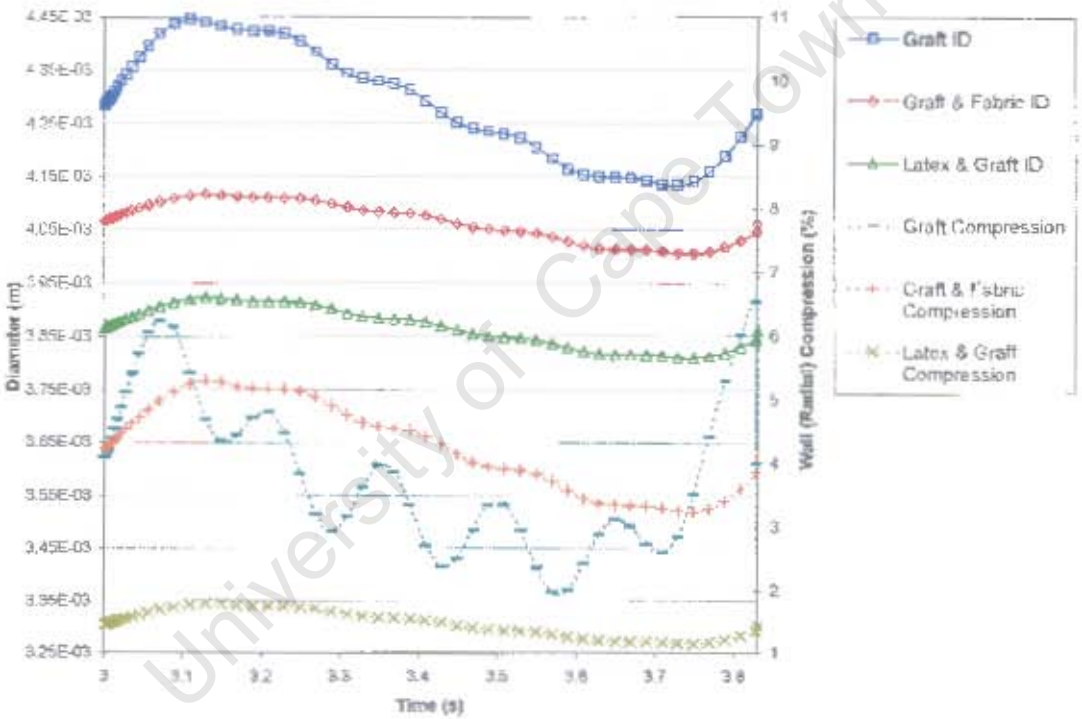

Figure D.2: Internal diameter and wall compression curves vs. time obtained during dynamic pressure step for 106-125 μm pore sized graft, graft and fabric with graft with latex

Graft Type		Graft		Graft & Fabric 1		Graft & Fabric 2		Graft & Fabric 3		Graft & Latex		Graft & Latex & Fabric	
Description	Units	Internal D	External D	Internal D	External D	Internal D	External D	Internal D	External D	Internal D	External D	Internal D	External D
Initial Diameter	mm	5.00	5.20	4.84	5.00	5.00	5.20	5.00	5.20	5.00	5.20	5.00	5.20
Diastol													
Pressure	mmHg	80.4		80.4		80.4		80.4		80.4		80.4	
Diameter	mm	4.15	5.49	4.00	5.36	3.98	5.34	3.97	5.32	3.81	5.19	3.80	5.22
Wall Compression	%	1.67		1.74		2.91		2.84		1.11		1.65	
Fabric Circumferential Strain	%	4.82		4.79		4.92		4.41		2.05		1.23	
Systol													
Pressure	mmHg	119.8		119.8		119.8		119.8		119.8		119.8	
Diameter	mm	4.45	5.78	4.12	5.44	4.10	5.40	4.07	5.40	3.92	5.30	3.90	5.27
Wall Compression	%	6.91		5.01		4.86		4.85		1.79		100.03	
Fabric Circumferential Strain	%	15.02		8.85		8.67		8.85		5.14		5.36	
Compliance	%/(mmHg)	16.24	10.23	7.12	3.04	7.10	4.30	6.75	3.78	7.49	5.05	6.60	4.19

Table D.2: Compliance, diameter and fabric circumferential strain values at diastolic and systolic pressures for 106-125um composite grafts

D.1.3 125-150 μm pore sized graft structures

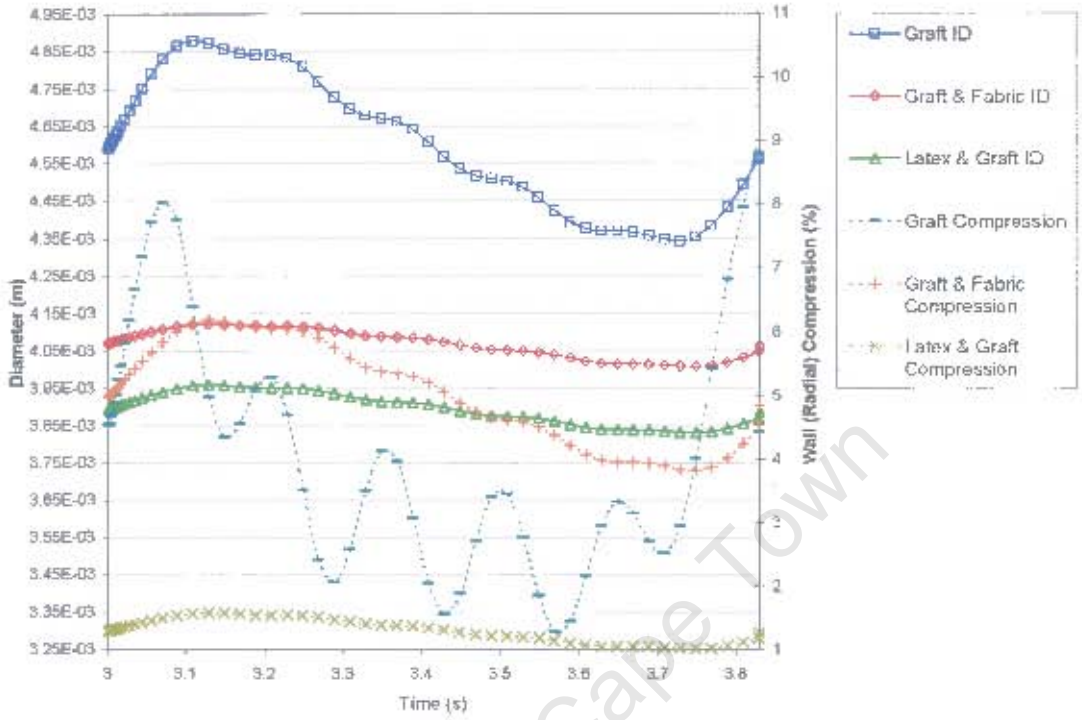

Figure D.3: Internal diameter and wall compression curves vs. time obtained during dynamic pressure step for 125-150 μm pore sized graft, graft and fabric with graft with latex

Description	Units	Graft		Graft & Fabric		Latex & Graft		Graft & Latex		Graft & Latex	
		Internal D	External D	Internal D	External D	Internal D	External D	Internal D	External D	Internal D	External D
Initial Diameters	mm	3.90	5.70	3.89	5.90	3.89	5.90	3.89	5.92	3.90	5.92
Diastol											
Pressure	mmHg	80.4		80.4		80.4		80.4		80.4	
Diameter	mm	4.09	5.43	3.97	5.33	3.98	5.34	3.98	5.34	3.80	5.16	3.79	5.15
Wall Compression	%	1.91		2.93		2.91		2.91		1.13		1.21	
Fabric Circumferential Strain	%	8.50		6.81		6.88		6.94		3.67		3.51	
Systol											
Pressure	mmHg	119.6		119.6		119.6		119.6		119.6		119.6	
Diameter	mm	4.32	5.68	4.07	5.41	4.10	5.43	4.09	5.42	3.90	5.28	3.89	5.26
Wall Compression	%	5.88		4.52		4.91		4.91		1.76		1.93	
Fabric Circumferential Strain	%	13.13		6.13		8.57		6.43		5.59		5.23	
Compliance	%/mmHg	16.02	10.06	5.80	3.65	7.10	4.03	6.78	3.79	7.03	4.72	6.43	4.21

Table D.3: Compliance, diameter and fabric circumferential strain values at diastolic and systolic pressures for 125-150um composite grafts

D.2 Static data

D.2.1 90-106 μm pore sized graft structures

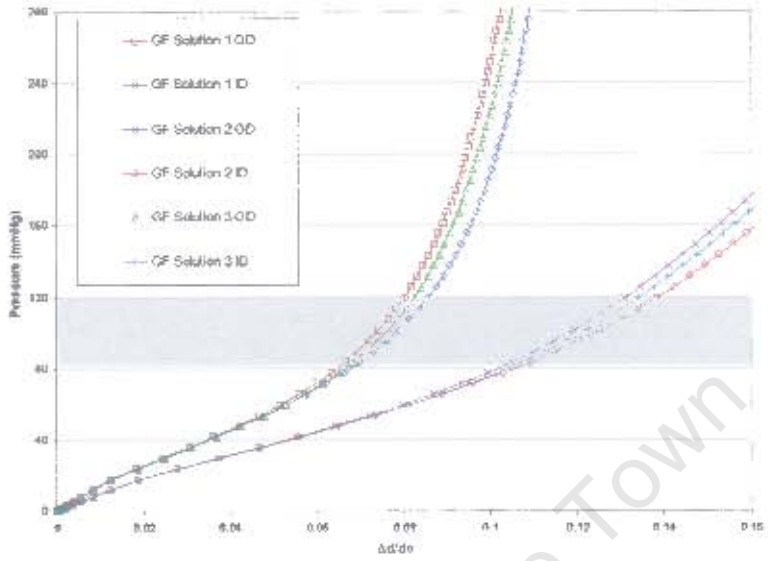

Figure D.4: GA1 static P vs. $\triangle d/d_0$ fabric reinforced model solutions for 90-106 μm pore sized graft

D.2.2 106-125 μm pore sized graft structures

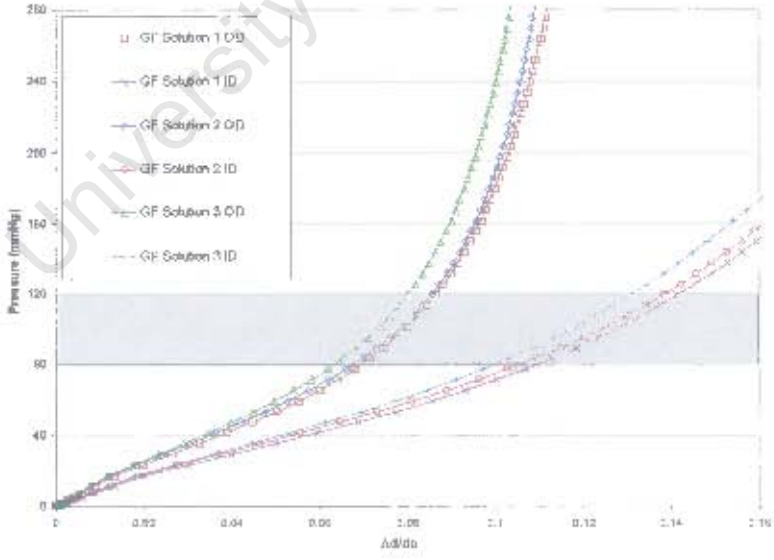

Figure D.5: GA1 static P vs. $\triangle d/d_0$ fabric reinforced model solutions for 106-125 μm pore sized graft

D.2.3 125-150 μm pore sized graft structures

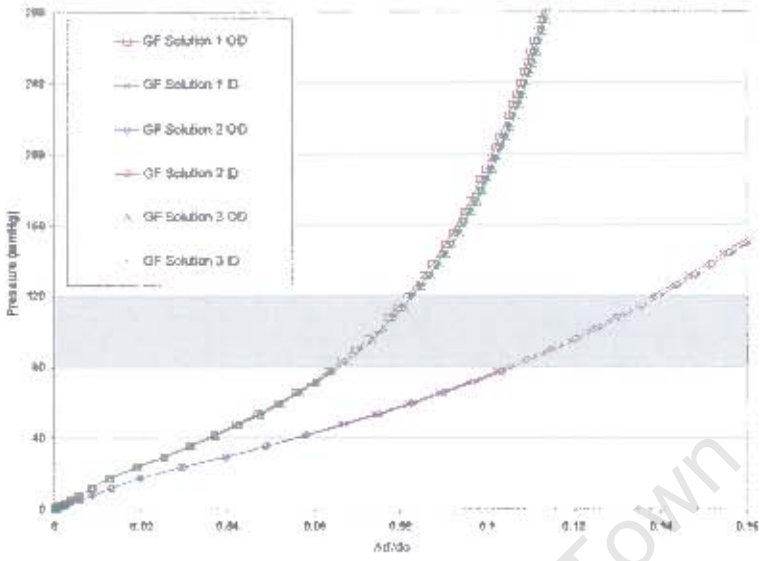

Figure D.6: GA1 static P vs. $\Delta d/d_0$ fabric reinforced model solutions for 125-150 μm pore sized graft

D.3 Comparisons between various pore sized graft structures

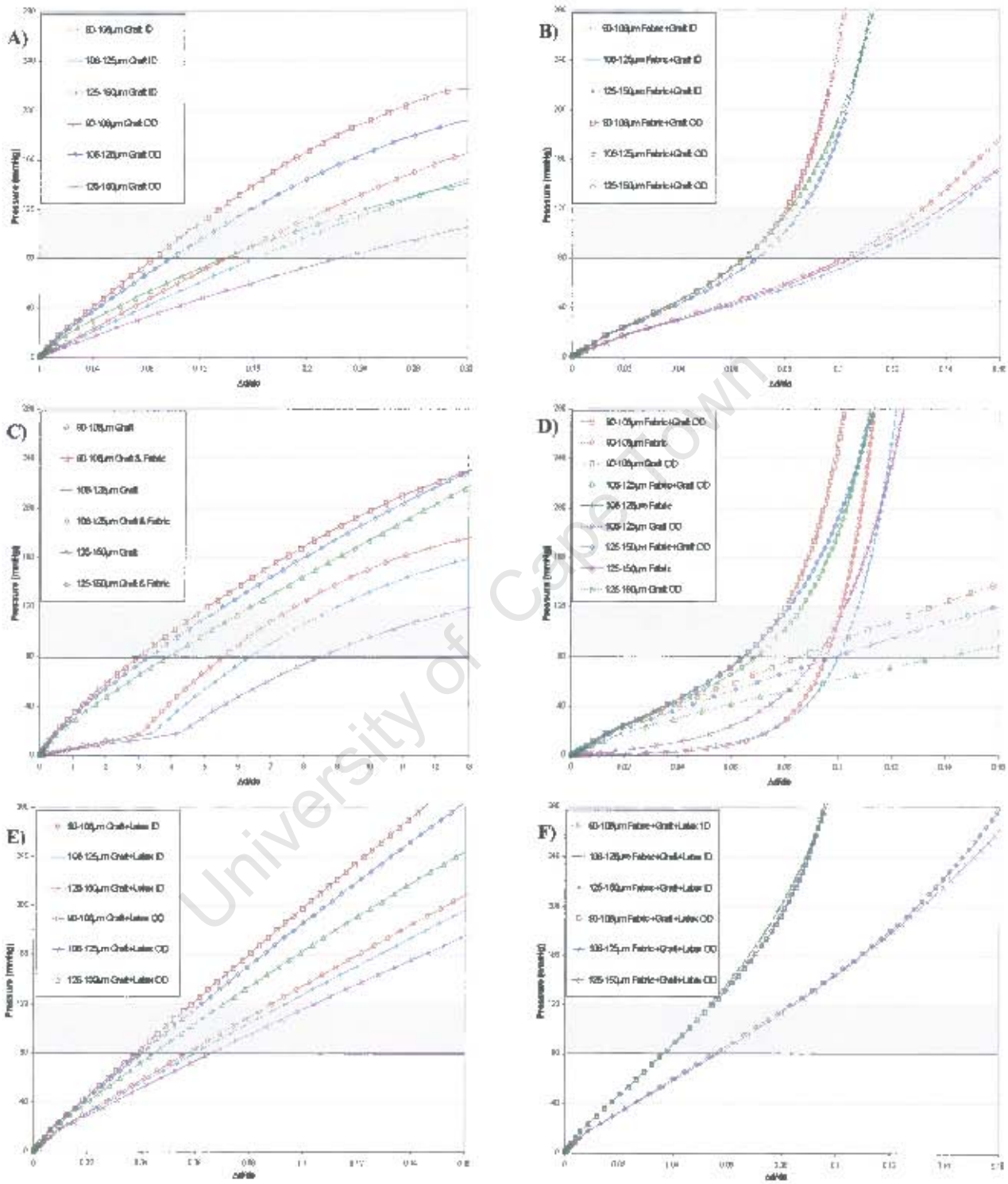

Figure D.7: Static P vs. $\Delta d/d_0$ comparisons between pore sized graft groups and GA1 fabric reinforced model solutions for; (a) graft only, (b) graft & fabric, (c) compression, (d) fabric (e) graft & latex and (f) graft & fabric & latex

Appendix E

GA1 Circumferential and Longitudinal Model Results

E.1 Comparisons between various pore sized graft structures

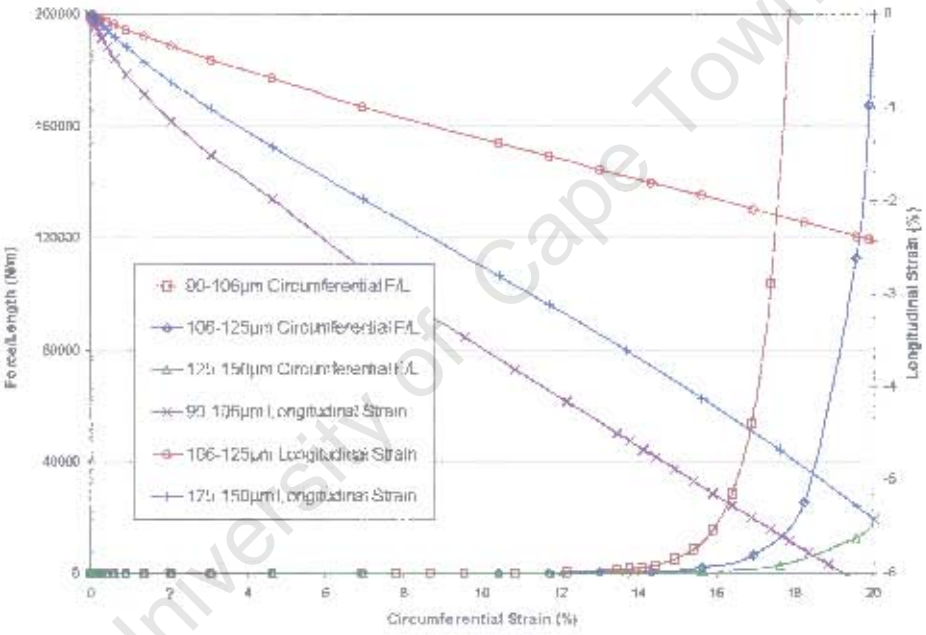

Figure E.1: Circumferential force per unit length and longitudinal strain curves vs. circumferential strain

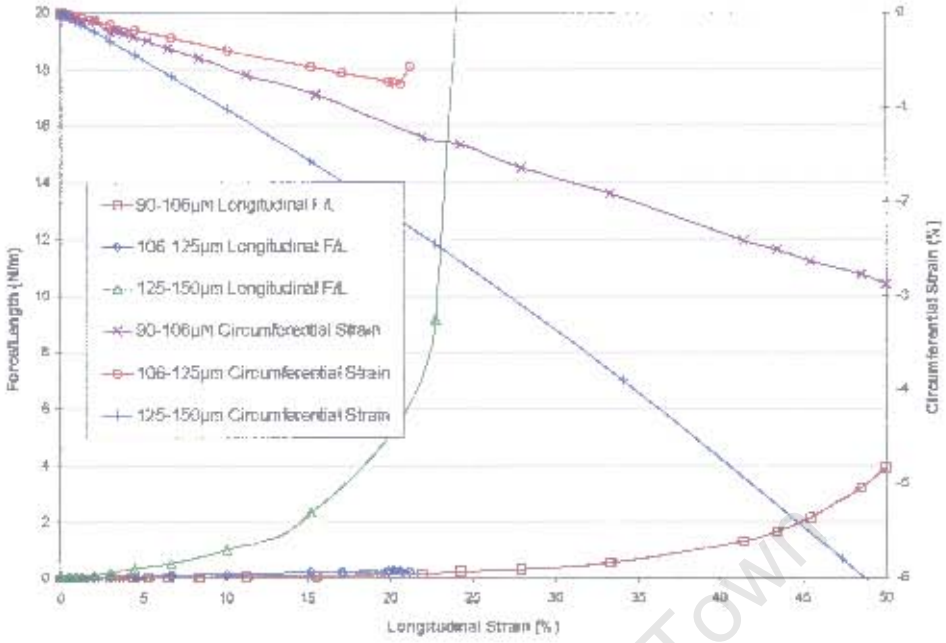

Figure E.2: longitudinal force per unit length and circumferential strain curves vs. longitudinal strain

E.2 Individual pore size solutions

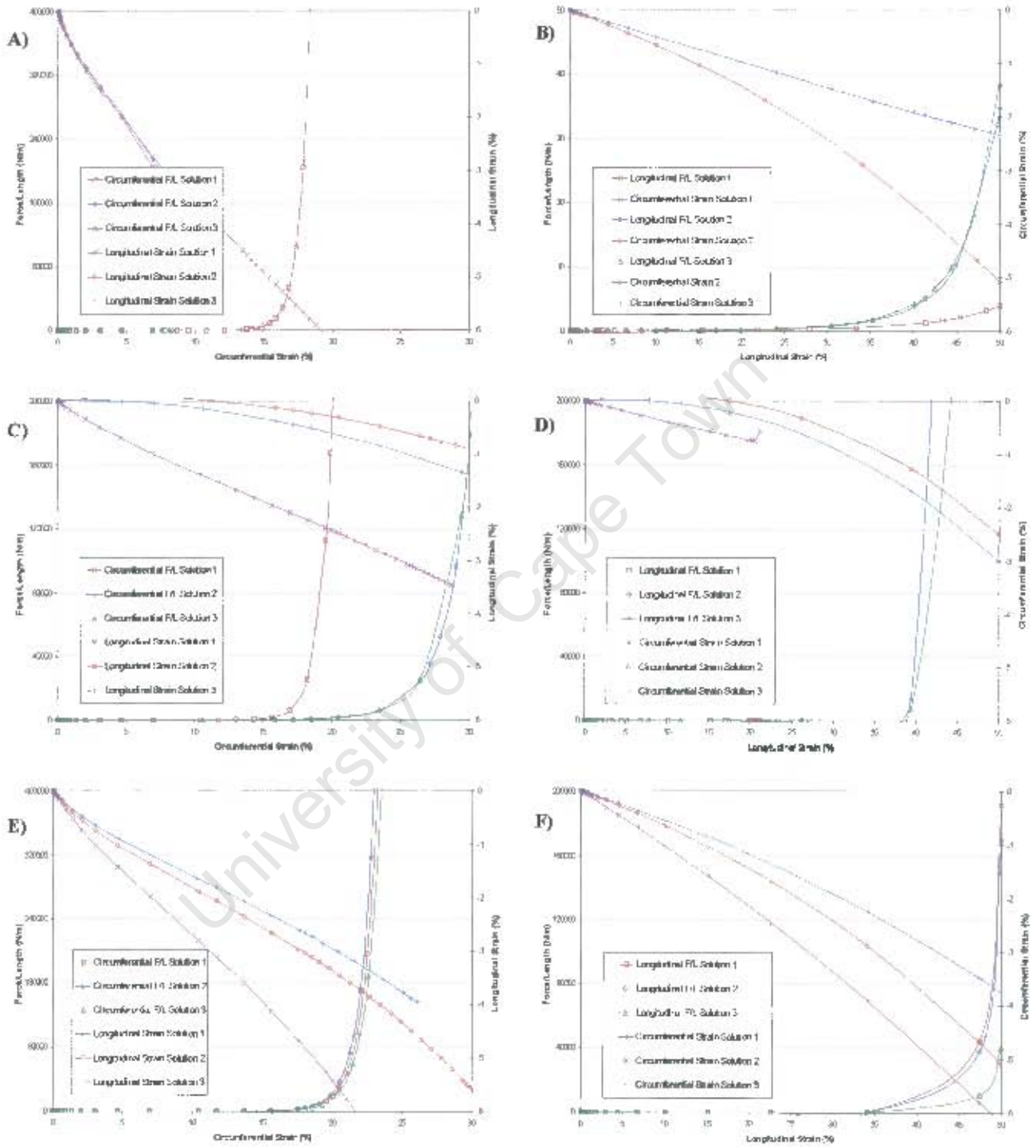

Figure E.3: Circumferential and longitudinal force per unit length vs. strain for (a) & (b) 90-106 μm, (c) & (d) 106-125 μm and (e) & (f) 125-150 μm

Appendix F

Static and Dynamic Compliance Data for Graft Samples

F.1 Static data

F.1.1 90-106 μm static compliance curves

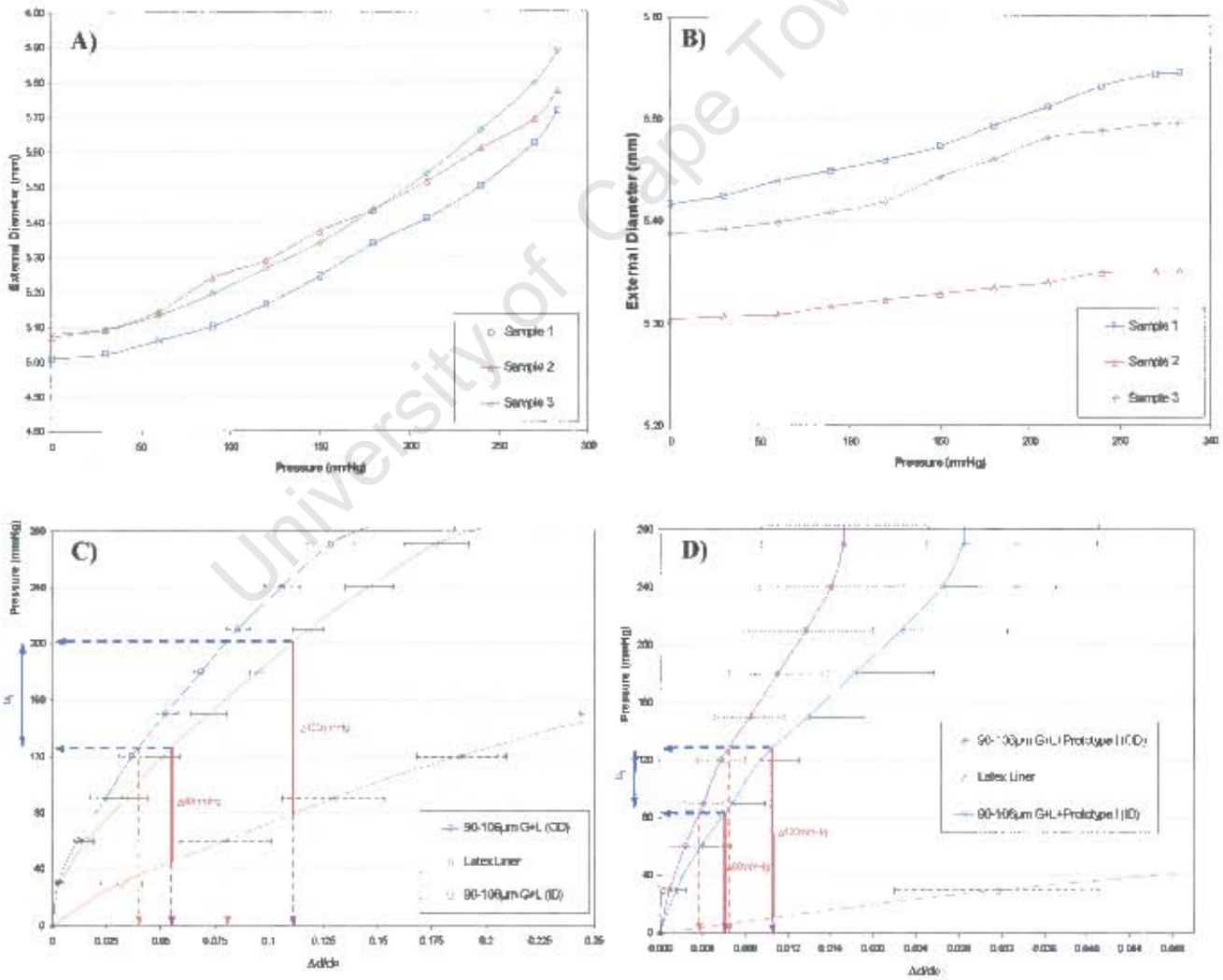

Figure F.1: Static P vs. d curves for 90-106 µm graft samples; (a) with latex liner, (b) with latex and prototype I. (c) & (d) compiled static P vs. $\Delta d/d_0$ for (a) & (b)

F.1.2 106-125 μm static compliance curves

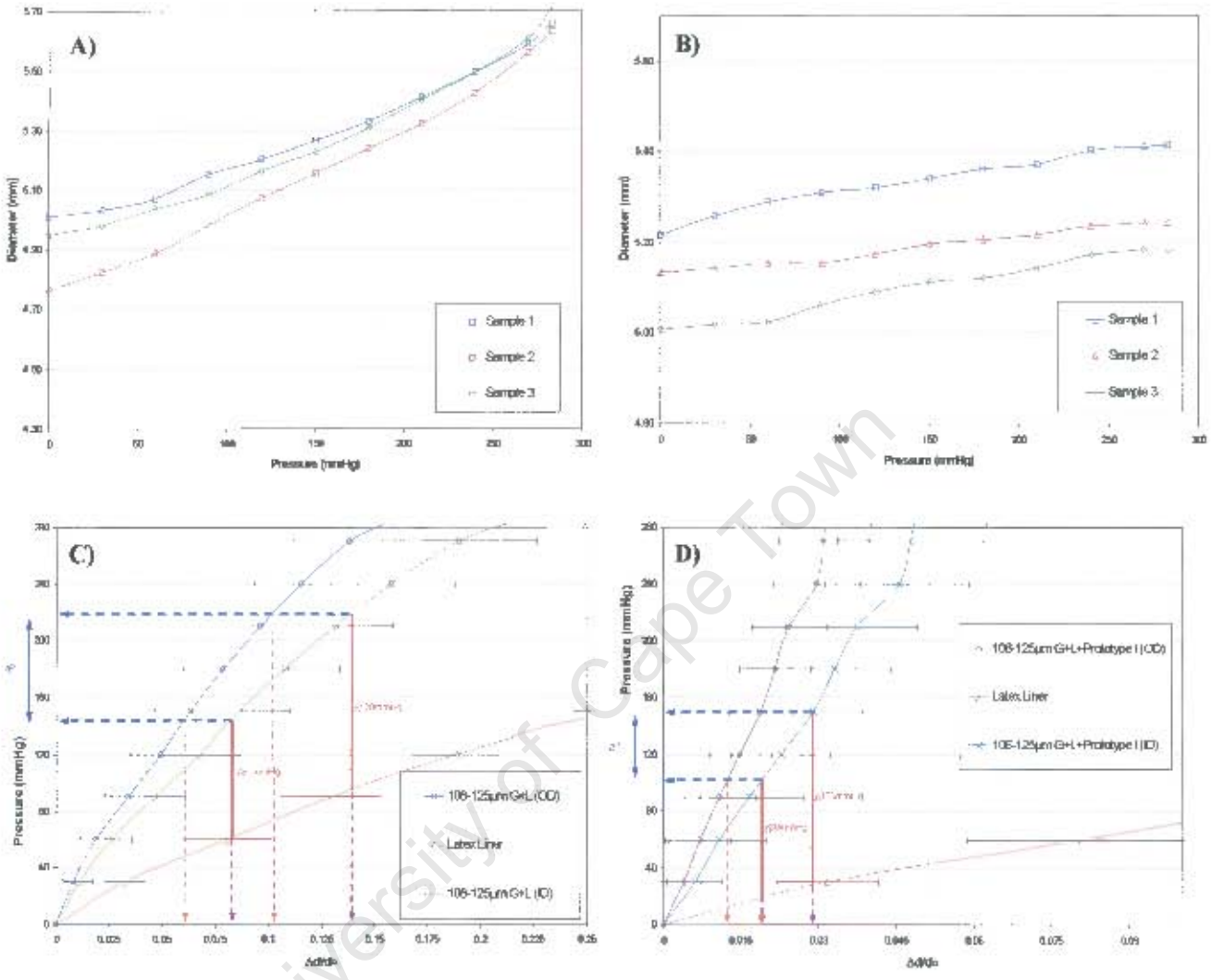

Figure F.2: Static P vs. d curves for 106-125 µm graft samples; (a) with latex liner, (b) with latex and prototype I. (c) & (d) compiled static P vs. $\Delta d/d_0$ for (a) & (b)

F.1.3 125-150 μm static compliance curves

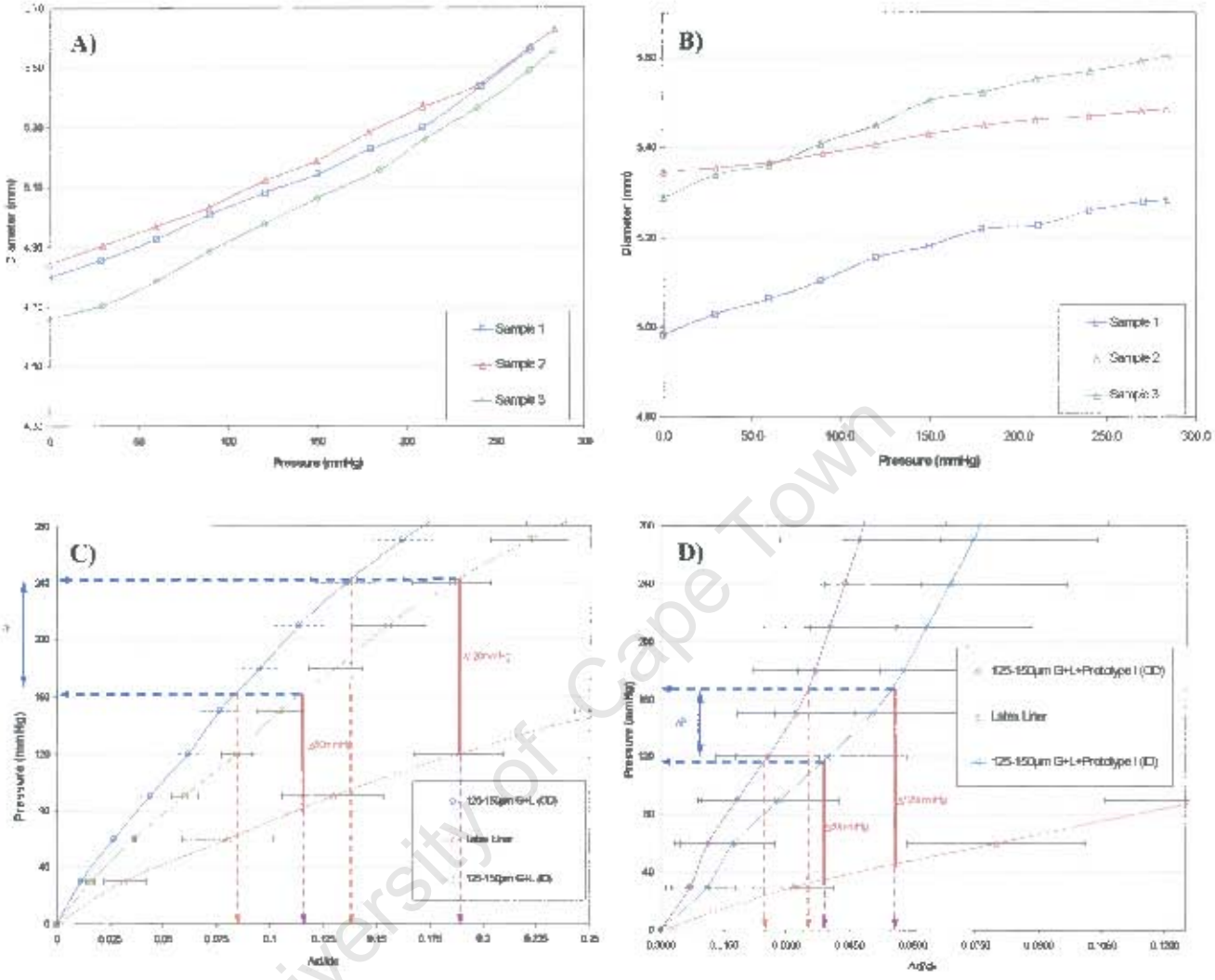

Figure F.3: Static P vs. d curves for 125-150 μm graft samples; (a) with latex liner, (b) with latex and prototype I. (c) & (d) compiled static P vs. $\triangle d/d_0$ for (a) & (b)

F.2 Dynamic data

F.2.1 Dynamic compliance curves

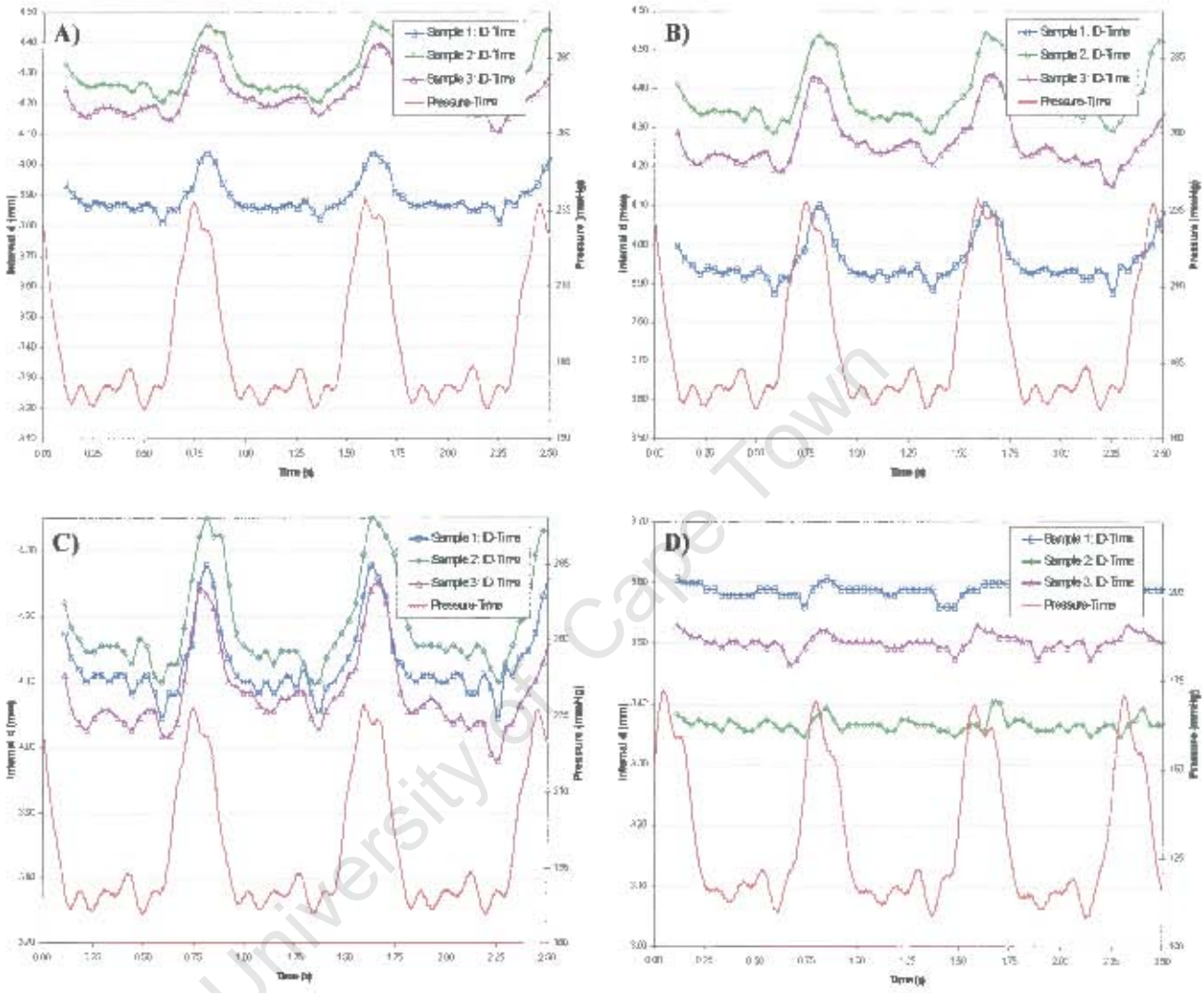

Figure F.4: Dynamic P and internal diameter curves with time for graft samples with latex liner. (a) 90-106 μm, (b) 106-125 μm, (c) 125-150 μm and (d) 125-150 μm with prototype 1

F.3 Compiled compliance data

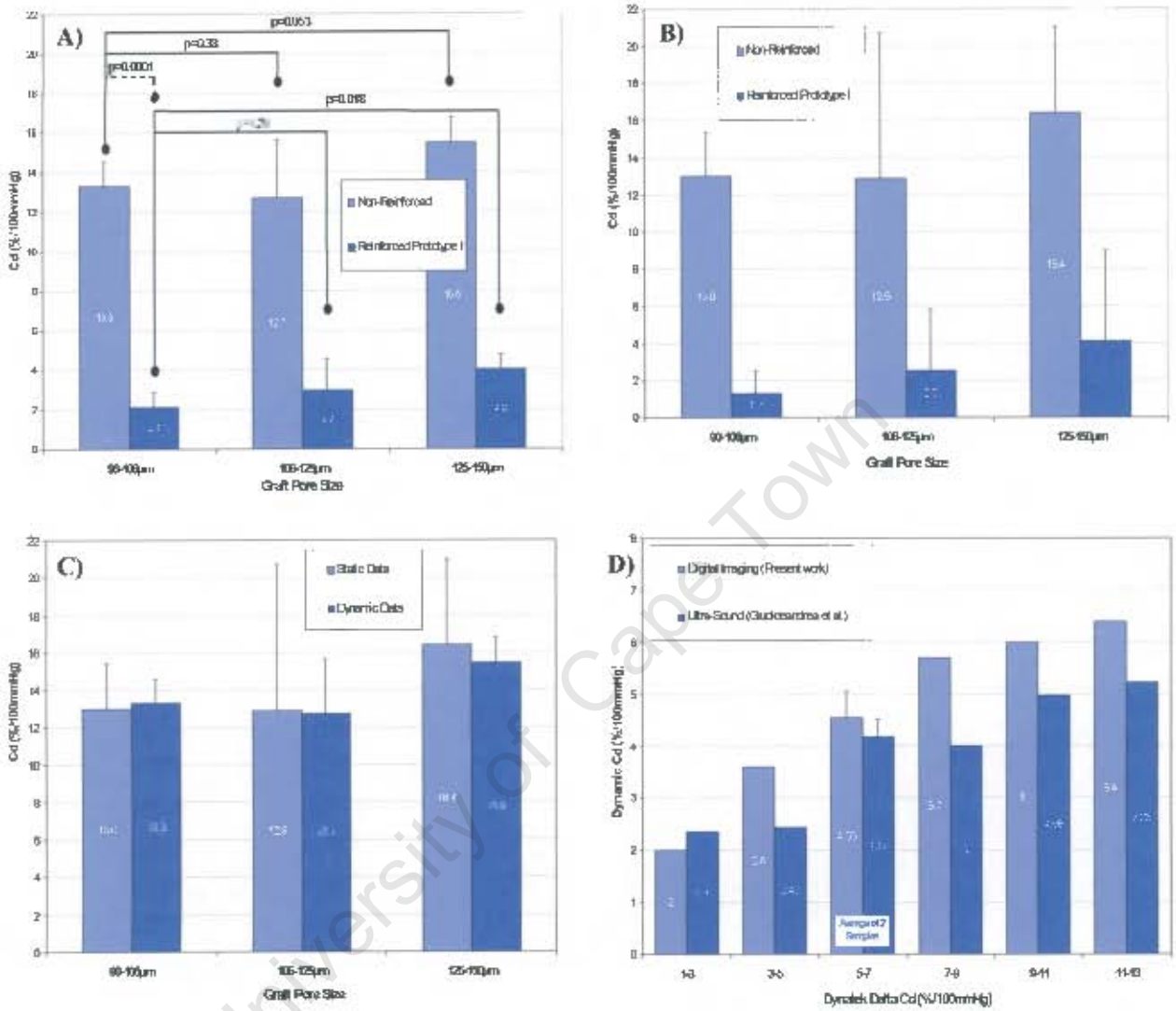

Figure F.5: Compiled barcharts; (a) dynamic reinforced vs. non-reinforced, (b) static reinforced vs. non-reinforced, (c) static vs. dynamic (non-reinforced) and (d) ultrasound vs. imaging methods

Description	Dynamic Data								Static Data	
Sample #	Sample 1	Sample 2	Sample 3	Cd (ID)	Stdev	T-Tests			Cd (ID)	Stdev
Non-Reinforced						50-106µm	106-125µm	125-150µm		
50-106µm	12.2	14.7	13.5	13.5	1.2	0.0001	0.36	0.06	13.0	2.4
106-125µm	9.4	15.0	13.8	12.7	2.9		0.015	0.10	12.9	7.8
125-150µm	14.3	15.2	16.9	15.5	1.3			0.0001	16.4	4.6
Reinforced										
Prototype I						50-106µm	106-125µm	125-150µm		
50-106µm	2.1	2.9	1.4	2.1	0.8		0.292	0.010	1.3	1.2
106-125µm	1.3	4.6		3.0	1.6			0.747	2.5	3.3
125-150µm	3.3	4.2	4.7	4.0	0.7				4.1	4.9

Table F.1: Compiled compliance test data for graft samples

Perception	Reported Data			
Lycotek Data	Digital Imaging	Stdev	Ultra-Sound	Stdev
1-3	2	-	2.36	-
3-5	3.6		2.43	-
5-7	4.55	0.5	4.17	0.35
7-9	5.7	-	4	-
9-11	6	-	4.98	-
11-13	6.4	-	5.23	-

Table F.2: Compliance test data for silicon grafts

Appendix G

Compliance Conversions

G.1 Volume to diameter compliance

Volume compliance C_V defined by

$$C_V = \frac{\Delta V}{V \Delta P} \times 100 \times 100 \qquad (\%/100\,\text{mmHg})\,, \tag{G.1}$$

where V is the internal volume of a vessel, ΔP is the change in pressure and ΔV the change in internal volume due to ΔP. The volume of a unit length l of a vessel is given by

$$V = \frac{\pi d_i^2}{4} \times l\ , \tag{G.2}$$

where d_i is the internal diameter of the vessel. When the pressure rises by ΔP the diameter increases by Δd_i, and the fraction change in volume $\frac{\Delta V}{V}$ is

$$\begin{aligned} \frac{\Delta V}{V} &= \frac{\pi(d_i + \Delta d_i)^2 - \pi d_i^2}{\pi d_i^2} \\ &= \frac{2 d_i \Delta d_i + \Delta d_i^2}{d_i^2} \\ &= \frac{2\Delta d_i}{d_i} + \frac{\Delta d_i^2}{d_i^2}\ . \end{aligned}$$

The term $\frac{\Delta d_i^2}{d_i^2}$ is small with respect to $\frac{2\Delta d_i}{d_i}$ so it can be disregarded. Thus

$$\frac{\Delta V}{V \Delta P} \simeq \frac{2\Delta d_i}{d_i \Delta P}\ . \tag{G.3}$$

But the definition of Diameter Compliance (C_d) is

$$C_d = \frac{\Delta d_i}{d_i \Delta P} \times 100 \times 100 \qquad (\%/100\,\text{mmHg})\,. \tag{G.4}$$

Thus

$$C_v \approx 2 C_d \tag{G.5}$$

G.2 Internal to external diameter compliance

Assuming that the vessel wall has thickness w and is incompressible, from equation (G.4) we

have

$$\begin{aligned} C_d^{int} &= \frac{\Delta d_i}{d_i \Delta P} \times 100 \times 100 \\ &= \frac{\Delta d_i}{d_e} \times \frac{d_e}{d_i} \times \frac{1}{\Delta P} \times 100 \times 100 \ . \end{aligned}$$

But $\Delta d_i = \Delta d_e$, as wall thickness does not vary. Thus

$$C_d^{internal} = \frac{d_e}{d_i} \times C_d^{external} \ . \tag{G.6}$$